Processes and feedbacks associated with iceberg calving and subaqueous terminus morphology, Tasman/Haupapa Glacier, New Zealand

Jessie L. Lindsay

Supervisors: Dr Heather Purdie and Dr Wolfgang Rack

A thesis submitted in partial fulfillment of the degree of

Master of Science in Geography

University of Canterbury, Christchurch, New Zealand

Abstract

Global deglaciation is increasing the number of glaciers that are forming or have formed proglacial lake. Deglaciation is also changing the size of proglacial lakes in temperate settings, resulting in more glaciers losing mass via iceberg calving. In order to better estimate future ice volume change, we need to understand processes driving calving in freshwater environments. Calving is an important process influencing the mass balance of a glacier, as the calving process is a cause of high rates of ablation in comparison to melt out rates alone. The calving rate and magnitude of iceberg calving can be influenced by the presence of subaqueous ice ramps. Some calving glaciers form subaqueous ice ramps or 'ice feet' due in part to differences in the rates of subaerial and subaqueous calving. Spatial and temporal variation of these subaqueous features indicate that other processes also exert control. Photographic and satellite imagery was combined with bathymetric and limnological surveys from Tasman Glacier (2013-2018) to explore the processes that drive spatial and temporal variability in iceberg calving and subaqueous terminus morphology, the relationships between near-terminus surface velocity, iceberg calving and subaqueous morphology.

A large number of calving events in spring and summer are associated with an increase in surface velocity and lake level fluctuations. One significant calving event over a 10-day period had a surface velocity of 0.39 md-1 ± 0.04 md-1. This was followed by a 58.97% decrease over a 20-day interval post calving event. Lake level increased on the day of the calving. Lake levels increased from 7.17.84 m ± 0.02 m to 719.93 m ± 0.10 m over a 5-day period. Increases in surface velocity and lake levels did not always result in major calving activity. Velocity or lake level increase may not always be an indication that a large calving event is imminent. The lack of large calving events after some surface velocity increases indicates that large calving events

are likely a result of multiple processes. Velocity and calving have a strong relationship with subaqueous morphology. Velocity varies spatially across the terminus with lower velocities on the eastern side of the terminus. The slower velocity combined with the increase in lateral drag at the margins of the glacier means that calving events are less frequent resulting in a more stable setting. Faster surface velocities are found in the central region of the terminus, result in a higher longitudinal strain rate and therefore higher calving rate.

A higher aerial calving rate than subaqueous calving rate leads to the formation of subaqueous ice ramps which are subject to subaqueous melt and buoyant calving processes. In order to prevent floatation, the terminus needed to exceed 23 m ± 5 m. The central ice cliff section does not meet H_F, but the terminus is unlikely to be buoyant due to cliff height exceeding the floatation thickness at each margin. As such, the dominant form of subaqueous calving is driven by buoyant calving rather than from the disintegration of a floating ice tongue.

The distribution of ramp lengths from 2013 – 2018 are commonly between 40 – 120 m in length (n=170) with the next largest group (n=12) between 120 – 200 m, only three ramps have been identified as greater than 200 m over the five-year survey time. From 2013-2018 a limited number of ice ramps exceeded 200 m in length, suggesting that ice ramps greater that 200 m are highly prone to buoyant calving, given that no ice ramp has exceeded 380 m during the 6-year survey period.

Findings to date indicate the primary driver of subaqueous ice ramp formation is the faster aerial calving rate over subaqueous calving. Spatial and temporal variation in velocity, lake

limnology and subglacial hydrology also drive the formation and calving of subaqueous morphology but on a lesser scale than that of aerial calving.

Acknowledgements

This thesis would not be what it is or even exist without a small village of people that helped me through the process. Thank you to Dr Heather Purdie and Dr Wolfgang Rack, you have both been incredibly patient and generous with your knowledge and time. Thank you Heather for letting me tag along on field trips to Tasman and providing interesting conversations and clarity on processes at Tasman/Haupapa Glacier. Thank you, Wolfgang for all your support with all things remote sensing. The level of support I received from both of you made studying long distance easy.

To team MacGyver, otherwise known as the technical staff in the Geography Department. Thank you to Paul Bealing, Justin Harrison, Nick Key and John Thyne for answering numerous questions on field equipment, processing methods and helping me trouble shoot software issues while I was on campus for my short processing trips from Invercargill.

Thank you also to Dr Brian Anderson from Victoria University for providing time lapse photos of the terminus, time series data on lake level fluctuations and interesting conversations on extracting terminus heights from time lapse photos.

A special thanks to Jerry Lemon and the team at Glacial Explorers for allowing the use of their boats and juggling the schedules so we would always have the best weather window. Thank you also for helping transport gear to and from the lake for each survey.

To all my colleagues at Land and Water Science, thank you for allowing me to work on my MSc on a part time basis and for acting as a sounding board for my processing ideas. Allowing me time away from the office to get my thesis over the line despite everyone's busy schedule is much appreciated.

Thank you to Dr Trevor Chinn, a wealth of knowledge on all things glacial, including the entire history of Tasman, thank you for sending through multiple surveys and reports and for the interesting conversation at SIRG – I left with more questions than answers.

Thanks also to Simon & Tracey Gow and Martin Kane for your help with ideas and coding superpowers to help process large amounts of data and thank you to Johnny & Rushani Violet Bowman for your proofreading prowess and showing me the joys of formatting.

My data processing trips up to Christchurch wouldn't have been easy without the continual support of my friends who let me stay, they not only put up with my odd working hours but also helped with proof reading, a special thank you Sarah and Rachel who frequently hosted

me.

Julie, Sarah, Stacey, Julian, Bryony and Paul thank you for helping me keep it all together and for picking up the pieces when I didn't quite keep it together. Your words of support and encouragement kept me going through both my undergraduate and my postgraduate studies. Thank you to all my friends and family that have put up with me while I have worked on my thesis, your support and continual interest in my progress has helped get me over the line.

Finally thank you to Bronwyn Colquhoun, my mentor, rock and friend, I would not have started this journey without your help.

Table of Contents

Table of Figures

Chapter 1

1.0 Introduction

1.0.1 Overview

Globally, glaciers are retreating at unprecedented rates, and are expected to make the most significant contribution to global sea level rise in the near future (Zemp et al., 2015). An important process that influences loss of mass from glaciers globally is calving, whereby volumes of ice break away or collapse from a glacier terminus. Temperate mountain glaciers make up less than 1% of the world's ice volume, but currently account for approximately one third of observed sea level rise (Gardner et al., 2013). Temperate glaciers are more sensitive to climate-related fluctuations in temperature and precipitation than those in subpolar or continental areas (Radic & Hock, 2014). Current research predicts that these glaciers will be a major contributor to sea level rise during the 21st century (Larsen et al., 2015; Meier et al., 2007; V. Radic et al., 2013) and will cause alterations in the hydrological cycle that will impact populations at local and regional levels (Radic & Hock, 2014). Runoff from temperate glaciers contributes to, and supplements, local river systems, especially during periods of low river flow (Valentina Radic et al., 2008). Alterations to the hydrological cycle resulting from changes in glacial conditions can contribute to an intense demand on water resources, impacting ecosystems, hydro-generation and agricultural water supplies, especially in regions with large populations (Radic et al., 2013; Rohl, 2006).

A consequence of the current global rapid glacial retreat, is that an increasing number of glaciers are developing proglacial lakes. Freshwater lakes influence ice dynamics, terminus morphology and physical stability in both temperate and ice sheet margins (Carrivick & Tweed, 2013). It is predicted that proglacial lakes will increase in both numbers and volume

causing rapid ablation in a short timeframe (Carrivick & Tweed, 2013). The formation of proglacial lakes at the terminus of a retreating glacier can modify that glacier's previous response to climate through an increased rate of calving and terminus retreat (Funk & Röthlisberger, 1989; Warren & Aniya, 1999), thereby partially decoupling and accelerating the retreat process from climate. There is evidence of this happening on the south-eastern Tibetan Plateau (SETP), where changes in climate have produced warmer temperatures and altered precipitation, enabling the retreat and thinning of mountain glaciers (Kaab, Berthier, Nuth, Gardelle, & Arnaud, 2012; Song, Ke, Huang, & Richards, 2015; Song, Sheng, Ke, Nie, & Wang, 2016).

Knowledge of the processes driving terminus morphology and the expansion of freshwater lakes (Carrivick & Tweed, 2013; Immerzeel, Pelliciotti, & Bierkens, 2013; Liu et al., 2015; Miles, Willis, Arnold, Steiner, & Pellicciotti, 2017) has been predominantly developed in a marine setting (Luckman et al., 2015; Mernild, Liston, & Hiemstra, 2014; Rignot, Fenty, Xu, Cai, & Kemp, 2015; van der Veen, 2002). However, it is known that calving rates and subaqueous melt rates are orders of magnitude lower in freshwater environments (Boyce, Motyka, & Truffer, 2007; Truffer & Motyka, 2016a; van der Veen, 2002; Warren, Benn, Winchester, & Harrison, 2001). While calving is a complex process that involves multiple processes that operate at different scales at different times of the year, similar calving patterns have been observed at Tasman/Haupapa Glacier, and these can be related to ice cliff and buoyancy conditions (van der Veen, 2002; Boyce et al,. 2007). Benn & Astrom (2018) have suggested that these observational similarities could be combined with a detailed process-based understanding of calving mechanics, resulting in simple calving laws that can reliably predict ice front locations.

1.0.3 Research aim

The aim of this thesis is to provide an integrated view of processes that effect near terminus velocity, calving, and subaqueous morphology at Tasman Glacier.

1.0.4 Research Objectives

This research will address the following:

1) **Are there relationships between near-terminus surface velocity, iceberg calving and subaqueous terminus morphology?**

Previous research has highlighted important linkages between surface velocity and iceberg calving (Benn & Astrom, 2018), due to the relationship between velocity, tensile stress and crevasse development (Benn & Astrom, 2018). Because of the impact surface velocity can have of the rate calving, multiple studies have used remote sensing techniques such as satellite imagery to map the velocity variation through feature tracking algorithms (Redpath 2013, Kaab et al., 2016, Herman et al. 2011). Although highly accurate surface velocity measurements can be made using a series of stakes on the glacier surface, these measurements are often of inconsistent spatial and temporal resolutions, in that they require multiple field trips to collect data from stakes that have generally been placed only on the most accessible parts of a glacier resulting in low spatial coverage (Scherler et al. 2008). Satellite imagery has, therefore, become more widely used, as it provides global coverage, allowing for mapping of quantitative changes in spatial and temporal velocity patterns (Yan et al, 2018). However, the quality of the imagery and the significance placed on the results of the spatial and temporal velocity patterns will always be influenced by the time interval between images and the method used to derive velocity.

This study aims to highlight temporal and spatial variation in surface velocity, derived from Sentinel satellite imagery with a spatial resolution of 10 m. Previous studies of surface velocity at Tasman/Haupapa Glacier have used satellite imagery with 15 m resolution (Quicey et al. 2009; Herman et al. 2011; Redpath et al. 2013; Haritashya et al. 2015). The higher resolution of the Sentinel imagery may be able to further refine velocity patterns at the near terminus.

For this study, the spatial and temporal variation in subaqueous morphology using bathymetric survey methods outlined by Purdie et al. (2016). Bathymetric surveys from 2013-2015 (Purdie et al. 2016) and 2016-2018 (this study) are assessed to help understand how the subaqueous morphology evolves over time in relation to velocity and calving events at the terminus of Tasman/Haupapa Glacier.

2) Do the limnological characteristics of the lake influence subaqueous morphology?

Based on the relationships between water temperature, subaqueous melting and subaqueous terminus morphology this study will use a combination of vertical temperature profiles, lake surface temperature, lake level time series data and satellite imagery to identify processes and lake conditions that could affect the development of subaqueous morphology. It has been suggested that limnological characteristics enhance both subaqueous melt and calving rates, and that conductivity temperature depth casts could be useful when combined with high-frequency multibeam sonar to map subaqueous processes. Repeatable bathymetric surveys of the near terminus at Tasman/Haupapa glacier from 2013 - 2018 can help identify whether the spatial and temporal calving patterns identified by Dykes (2013) are linked to the subaqueous morphology and hydrology.

1.0.5 Thesis structure

This thesis is broken into 6 chapters. The first chapter is an overview of the importance of research on glaciers calving into freshwater lakes and outlines the research aim and objectives. The second chapter provides a literature review on calving, velocity and subaqueous morphology, with a focus on calving processes in freshwater lakes. Chapter 3 outlines the study area at Tasman/Haupapa Glacier and explains how the calving terminus has evolved over the years as the lake expanded. The methodology used in this study is set out in chapter four, in particular feature tracking process and uncertainty analysis used to derive surface velocity from satellite imagery, and the identification of lake conditions and terminus morphology. Research results are presented in chapter 5. Chapter 6 discusses the relationships between velocity, calving and subaqueous morphology using a series of diagrams that show how the processes spatially and temporally integrated at the terminus. Lake characteristics and how they influence subaqueous morphology is also discussed and demonstrated in a diagram as well as recommendations for future work.

Chapter 2 – Literature Review

2.0 Mass balance

2.0.0 Glacier mass balance

The mass balance of a glacier is the net result of accumulation (the glacier gains mass) and ablation (the glacier loses mass), as shown in Figure 1. The two areas are separated by the Equilibrium Line Altitude (ELA) where annual net accumulation and ablation are equal (Benn & Evans, 2010).

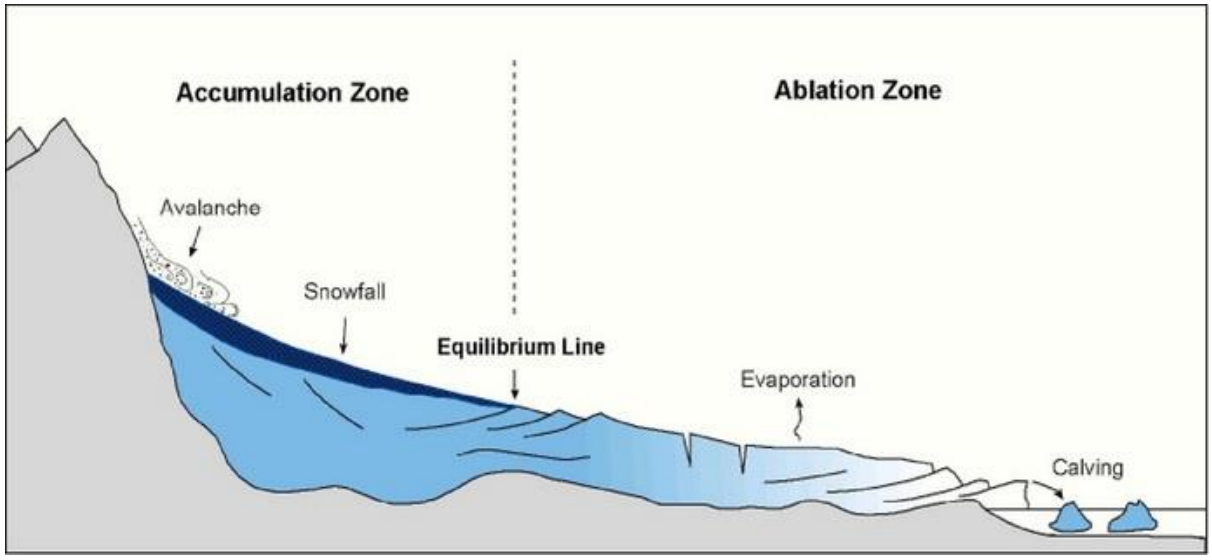

Figure 1 : Diagram showing the different components that make up mass balance, the accumulation side of the glacier gains mass while the ice in the ablation zone loses mass. From Garinger Earth Science 2014-2015. Retrieved March 08, 2019 from https://garingerearthsci.weebly.com/uploads/3/7/7/3/37738075/glacial_diagram.jpg

A positive mass balance indicates that the glacier is gaining mass (net accumulation is greater than net ablation). A negative mass balance (net ablation is greater than net accumulation) indicates the glacier is losing mass. Precipitation falling as snow is an important factor influencing mass gains in the accumulation area. Some of the highest rates of accumulation through precipitation occur in mountainous maritime regions (Benn and Evans, 2010). Wind processes and avalanche material can also contribute to and influence the net mass of the

accumulation area. Mass lost in the ablation area is influenced by a combination of processes at the terminus through melting, evaporation and calving.

2.0.1 Ablation through calving

Calving is the process of volumes of ice breaking away or collapsing from a glacier terminus. Calving is an important process influencing the mass balance of a glacier, as the calving process is a cause of high rates of ablation in comparison to melt out rates alone. Current models use mass balance to help understand how glaciers are responding to changes in climate and how they may respond to future climatic conditions. The most notable example of this is at the polar ice sheets where calving is the dominant reason for mass loss of the ice sheets (Benn, Warren, & Mottram, 2007; Rohl, 2006). The Arctic and Antarctic area has been heavily researched as it contains approximately 87% of the worlds fresh water supply (van der Veen, 2002).

Research into calving in freshwater settings has increased in recent times in areas such as Alaska, Patagonia, and Bridge Glacier in British Colombia. This glacier shares glacial characteristics similar to Tasman Glacier in New Zealand. The Bridge Glacier has experienced retreat as a consequence of rapid calving from 1991 - 2013. Through the use of a distributed energy balance model, calving patterns of the glacier (specifically the percentage of ablation resulting from calving) was studied. Across individual seasons, calving was found to be responsible for ~49% of ablation, but ice lose from calving was a lot less when averaged over multiple seasons from 1984-2013, with only 10 – 25% of ablation attributed to calving (Chernos, Koppes, & Moore, 2016). The calving characteristics of Bridge Glacier were found to be similar to that of other lake terminating glaciers. A period of down-wasting of buoyant

termini is followed by a rapid step like retreat. This pattern may be common among glaciers that calve in freshwater settings, suggesting ta temporal control on calving behaviour (Chernos et al. 2016). However spatial and temporal relationships of subaqueous features such as ice ramps could be examined further. Chernos et al. (2016) acknowledged ice ramps at glaciers terminating in freshwater settings, such as the Mendenhall Glacier in Alaska and the Yakutat Glacier, exhibit different subaqueous calving characteristics.

2.1 Calving processes

The laws of calving glaciers are yet to be fully defined. This is due to the complex nature of glacier calving that can vary over geographical settings. Calving termini can be fully buoyant or remain grounded, some have subaqueous ice ramps or ice shelves, and some termini can experience all these variables at different stages of calving. Current models use mass balance to help understand how glaciers are responding to changes in climate and how they may respond to future climatic conditions, but are normally limited or tailored to a specific glacier geometry Benn and Evans (2010). Although it is not possible to precisely model all the details for every calving event, calving laws based on empirical or theoretical considerations are the optimum method for detailing ice loss through calving (Benn & Astrom 2018).

Calving rates and ice dynamics have previously been modelled using the 'master' and 'slave' theory (Benn et al. 2007) and can be argued two ways. The first is that ice dynamics is considered the 'master' process, where changes in the dynamics up glacier trigger changes in the 'slave' process of calving, thereby affecting terminus stability. The second form of this theory is the reverse, whereby calving processes are considered the 'master' process that triggers a change in ice dynamics up glacier (Benn et al. 2007). The accepted empirical

approaches to quantify the calving rate depends on if the calving processes is considered the 'master' or 'slave'.

The "water depth" model was derived from a large dataset that included a sample of 12 Alaskan tidewater water glaciers assessed by (Brown et al. 1982). This model assumes that ice dynamics are the 'slave' process that trigger changes in the near terminus with calving rate considered the 'master'. The study found a strong correlation between the rate of calving and depth of water for all 12 glaciers (Eq. 1). The depth to water model stipulates that there is a linear relationship between calving rate and water depth at the terminus (Brown et al. 1982). The model uses independent variables from the glacier, along with ice velocity to predict the changes in terminus position (Benn et al. 2007). This model has been widely accepted for predicting calving processes on grounded tidewater glaciers.

Water depth equation (1):

$$U_C = a + b\, D_W \quad (1)$$

Where U_C is the calving rate, a and b are empirically derived calving coefficients and D_W is the width averaged water depth. The depth to water model predicts calving rates well when annually averaged data is used but not when seasonal variation is taken into consideration. The linear relationship between calving and water depth also breaks down during periods of rapid glacial retreat (Van der Veen,2002; Vieli et al 2001). It was suggested by Van der Veen, (2002) that where termini experience periods of floatation the calving mechanism would be similar to that of floating ice shelves, however the depth to water model does not allow for the difference between grounded and floating terminus.

A new calving model was put forward by Van der Veen, (1996) the "height above buoyancy" model. This model treated calving as the 'slave' process whereby changes in terminus position were instigated by changes in the ice dynamics – the 'master' process. The height above buoyancy model stipulates that the terminus will become buoyant if it exceeds the floatation thickness of the terminus (Eq 2). If the terminus thins below the floatation thickness (H_O) the terminus will become buoyant and calving is likely to commence until the terminus has reached a stable position where the height above buoyancy criterion exceeds the floatation thickness.

To establish if the terminus of a glacier is buoyant or not can be calculated from equation (2) ; the buoyancy depends on the thickness of the glacier.

Floatation thickness equation:

$$Hf = \frac{\rho w}{\rho i} Dw \quad (2)$$

Where H_f is the floatation thickness, ρ_w is the water density (1000kg m^{-3}), ρ_i is the density of the glacier ice (917 kg m^{-3}) and D_w is the water depth.

This calculation is limited for predicting calving dynamics due to the complex interactions with other glacier dynamics such as subglacial hydrology, ice acceleration, ice fracture patterns and the energy exchanges between ice and water bodies (Benn et al. 2007; Cuffey & Paterson, 2010). The controlling factor for the terminus of the glacier to remain above buoyancy (H_O) is determined by the height of the terminus shown below (Eq. 3) where H_T is the ice thickness at the terminus.

Height above buoyancy equation:

$$H_O = H_T - \frac{\rho w}{\rho i} Dw \quad (3)$$

The height above buoyancy model does not attempt to calculate calving rates but rather sets the boundary conditions for which calving would be instigated (van der Veen, 2002). This model is unable to be used when assessing ice shelves, and therefore cannot be used in a marine environment, as the height above buoyancy is considered zero (Benn et al. 2007). The model also fails to explain calving events on termini that greatly exceed the floatation thickness.

Despite the limitations in both empirically derived models outlined above, they have shown robust but often opposing conclusions such as the results derived from the same 17 year-long dataset from the Colombia Glacier (Meier,1994,1997; van der Veen, 1996). Both models are successful in explaining components of calving rates in certain circumstances and environments, but a single unifying calving law has yet to be established. Calving is not an isolated process. If unifying calving themes are to be identified in order to solidify the laws of calving, then other glacial processes such as subglacial hydrology, basal drag, lateral drag and longitudinal stress need to be considered (Benn & Evans, 2010).

2.2 The hierarchy of calving processes

Ablation due to calving is driven by two dominant processes. Mechanical and thermodynamic processes dictate the interactions between ice and water in relation to calving (Truffer & Motyka, 2016b). A hierarchy of mechanical processes that instigate calving was divided into

first, second and third orders of control by Benn et al. (2007). Strength of strain rates and velocity were listed as the first order of control, which in turn determine the location of fracture propagation, listed as a second order of control, along with thermal under cutting and buoyant flexure. Subaqueous morphology (specifically ice ramps) were listed as a third order of control because aerial calving processes (in the first and second orders) determine rates (Benn et al. 2007). The mechanical and thermal processes that effect ice dynamics and calving processes are examined in the following sections.

2.3 Mechanical

There are 4 main mechanical processes identified by Benn et al. (2007) whereby calving events can occur:

1. Stresses associated with surface velocity gradients
2. Force imbalance at terminal ice cliffs
3. Thermal undercutting
4. Torque from buoyant processes

2.3.0 Stresses associated with surface velocity

Velocity is an important component when assessing the calving rate of glaciers. By establishing the velocity gradients and the proportions of basal drag, lateral drag and longitudinal strain near the terminus, the location of calving margins can be identified to help explain the calving settings of the termini (Benn & Evans, 2010). The relationships and positive feedback loops are demonstrated below in Figure 2.

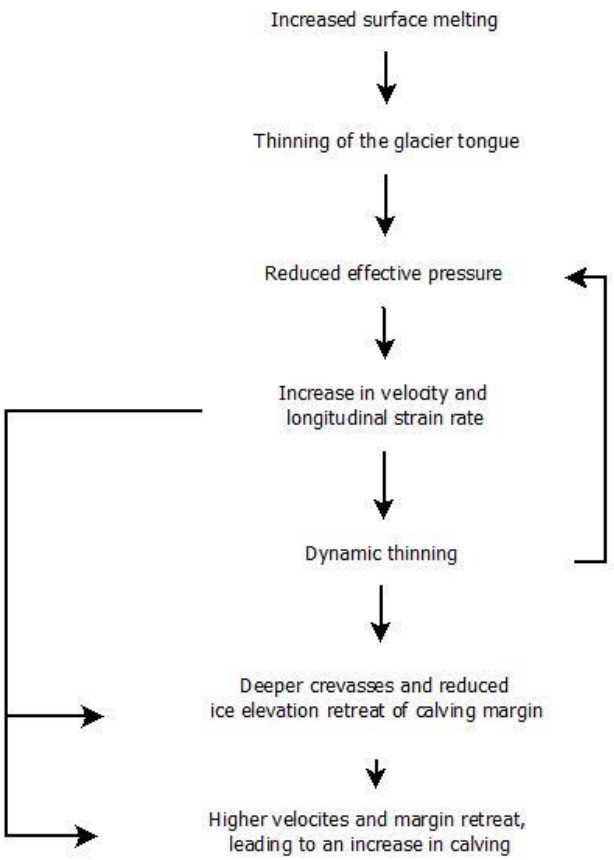

Figure 2: Positive feedback loops identified that result from effective pressure-dependent basal motion and longitudinal strain rates on calving and dynamic thinning. (Benn et al. 2007)

The movement of glaciers at its lower speeds can be attributed to internal deformation through ice creep and regelation slip. In glaciers with higher velocities, the increased speed can be related to basal slip, where the ice of the glacier can separate or slide over the bed and produce deformation in the basal sediment, depending on the type of bed the glacier is residing on i.e. hard or soft (Cuffey & Paterson, 2010). Where the terminus is grounded, there will typically be an increase in ice velocity in the near terminus region. This can be attributed to a reduction in basal drag as the glacier approaches floatation (Benn & Evans, 2010; van der Veen, 2002). Calving rates of a grounded terminus often increase with an increase in seasonal velocity. During the spring and summer months more meltwater input to the subglacial drainage system increases water pressures, leading to greater speed and in order for the

terminus to remain grounded the calving rate must increase accordingly (van der Veen, 2002).

A differential ice flow at the surface that is faster than ice flow near the base of the glacier can result in an over steepening at the near terminus. Differential ice flow stretches the ice, allowing for propagation of crevasses, sometimes down to the glacier base. Preferential calving can occur along these lines of weakness (Figure 3).

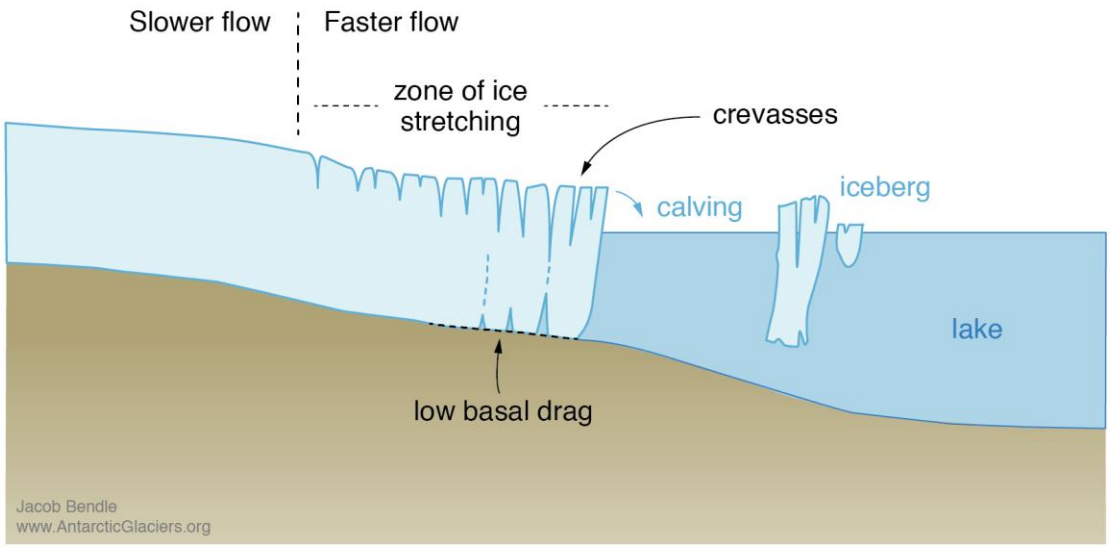

Figure 3: Diagram showing calving processes due to a heavily crevassed terminus. From AntarcticGlaciers.org – Explaining the science of Antarctic glaciology. Retrieved March 08, 2019, from http://www.antarcticglaciers.org/glacier-processes/glacial-lakes/calving-of-freshwater-glaciers/

If tensile stresses are large enough for the crevasses to propagate to depth in the ice, this can trigger calving events. When identifying factors that control or contribute to the location of calving, crevasse and velocity patterns are considered the first order of control (Benn et al. 2007).

2.3.1 Force imbalance at terminal ice cliffs

Force imbalance at the terminus can initiate calving. This is due to the differences in pressure as the terminus ends in both freshwater or marine settings. The water produces an opposing

force on the subaqueous ice, whilst no opposing pressure is produced on the aerial terminus ice (Figure 4). The differences in pressure can create a build-up of tensile and shear stresses, leading to the development of crevasses.

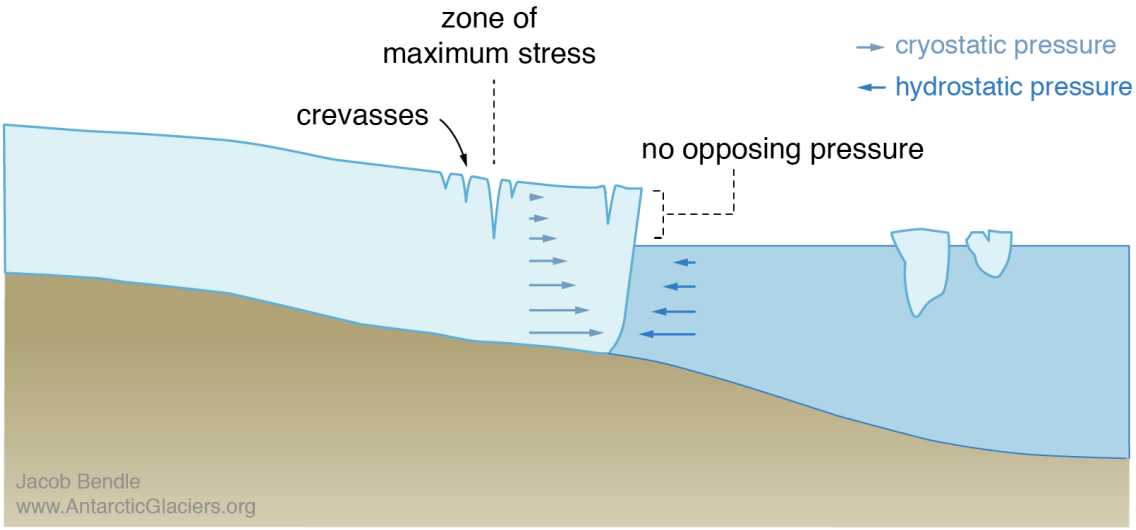

Figure 4: Diagram showing calving resulting from force imbalances. From AntarcticGlaciers.org – Explaining the science of Antarctic glaciology. Retrieved March 08, 2019, from http://www.antarcticglaciers.org/glacier-processes/glacial-lakes/calving-of-freshwater-glaciers/

2.3.2 Thermal undercutting

Calving can also be instigated through thermal erosion. Where ice is in contact with water, melting will engineer the formation of thermal notches. Thermal notches develop in both tidal and temperate conditions but are often inhibited during the winter months if the water freezes over. The rate at which ice melts at the waterline is dependent on the type of water circulation. Where there is only minor variation in the vertical temperatures in the water column, ice melt rates are thought to be small, this process is known as free convection. The opposite of this is forced convection, common in temperate tidewater settings, where intense upwelling of meltwater from the bed of the glacier drives convection currents. This results in higher energy fluxes and therefore higher melt rates than those associated with free convection (Benn & Evans, 2010). Glaciers in tidewater settings have been found to have a

much higher waterline melt rates than glaciers in freshwater settings. This can be attributed to the greater effects of currents and wave characteristics that may not be present at the same intensity in freshwater lake settings (Rohl, 2006).

Thermal erosion at or below the water line can undercut ice cliffs, removing support from the subaerial part of the ice cliff at the terminus and causing an increase in stress, that can result in calving of undercut pillars (Benn & Evans, 2010) (Figure 5).

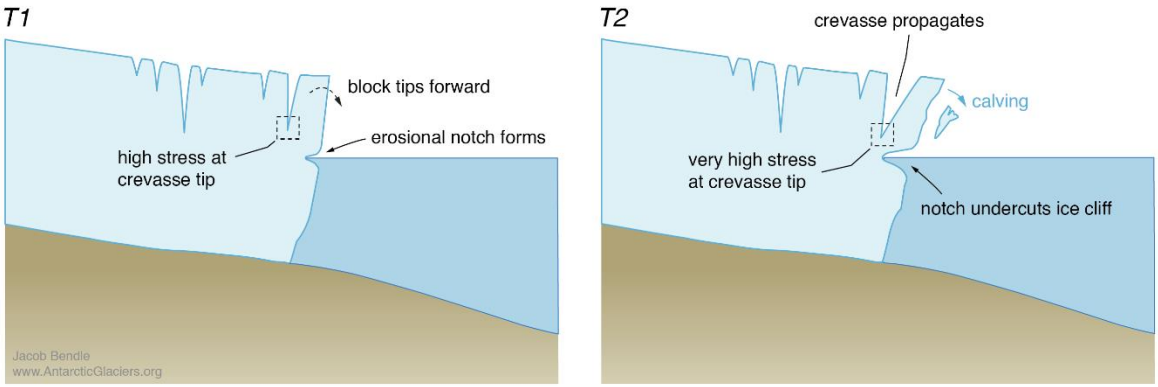

Figure 5: Diagram showing calving processes due to thermal notch development, water erodes ice at the waterline removing support of the subaerial ice cliff. From AntarcticGlaciers.org – Explaining the science of Antarctic glaciology. Retrieved March 08, 2019, from http://www.antarcticglaciers.org/glacier-processes/glacial-lakes/calving-of-freshwater-glaciers/

It was found by Rohl, (2006) that the effectiveness of this process was in part controlled by the ice melt rate and the location along the terminus where the melting was occurring. The spatial variation of ice melt is dependent on a number of factors, including water circulation patterns and variations in water levels, such as fluctuations in lake levels from rain events and water stratification (Benn & Evans, 2010;Rohl 2006).

2.3.3 Torque from buoyant forces

Calving rates can be influenced by ice thickness and water depth. van der Veen (2002) suggested that that calving rates can be inversely proportional to the height above buoyancy

(Eq. 2). If down-wasting of the glacier causes it to thin below the floatation thickness, the terminus can become buoyant. A buoyant terminus is not in equilibrium (Benn & Evans, 2010). If bending stresses cannot be accommodated through deformation, then basal crevasses may form at the base of the ice tongue as seen in Figure 6 below.

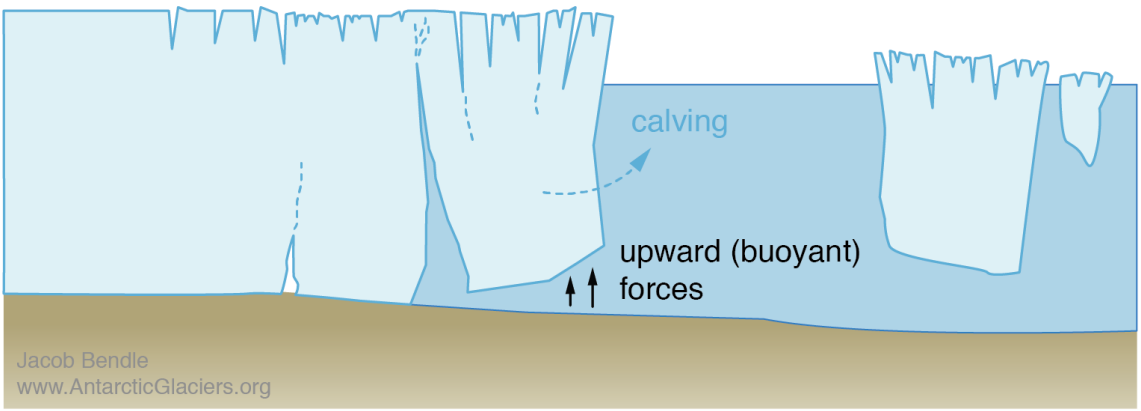

Figure 6: Diagram showing calving processes due to bouancy, this shows buoyancy calving to depth. From AntarcticGlaciers.org – Explaining the science of Antarctic glaciology. Retrieved March 08, 2019, from http://www.antarcticglaciers.org/glacier-processes/glacial-lakes/calving-of-freshwater-glaciers/

Glaciers in freshwater settings can sustain terminus buoyancy for longer periods than their tidewater counterparts. This is due to the lower order of magnitude perturbations experienced in a closed system. A freshwater glacier can sustain a steady buoyant terminus and accommodate slow perturbations, examples of this have been recorded at the Mendenhall Glacier where the floating terminus remained intact for ~2 years (Boyce et al. 2007), and at the Yakutat Glacier which sustained a floating terminus ~3km long for over a decade (Trussel et al. 2013). It has been documented that calving in these settings is triggered by an increase in buoyant forces acting on the terminus tongue. This results in rare but high magnitude calving events (Boyce et al. 2007).

The Mendenhall Glacier in Alaska calves into a proglacial lake. The buoyant terminus of the

glacier had an increase in net upward forces, causing upward warping and raising thermal notches out of the water. The glacier did not reach hydrostatic equilibrium and as a result underwent a series of large calving events. The Bridge Glacier in British Colombia also exhibited periods of low frequency, high magnitude calving events. This type of calving pattern supports the concept that glacier dynamics respond to large calving events by alleviating terminus instability and inhibiting future calving (Venteris, 1999; Benn et al. 2007).

Buoyant forces can also cause subaqueous calving of ice feet or ramps that extend out from the terminus. Studies have shown that a subaqueous calving event is often preceded by a subaerial calving event (Boyce et al. 2007). This pattern was observed at Tasman Glacier in New Zealand at the end of 2015, and again in early 2018, when a portion of the subaqueous ice ramp calved and was followed by a large subaerial calving event off the main ice cliff. This pattern is thought to be related to a sudden reduction in the pressure on the subaqueous ice feature which then increases the net upward forces acting on the subaerial ice, triggering subaerial calving if hydrostatic equilibrium is not achieved (Benn & Evans, 2010).

2.3.4 Summary of mechanical processes

By identifying which series of processes are acting on the terminus, the calving settings at the near terminus can be explained. Mechanical calving processes relate to the first and second order of controls of the calving hierarchy as set out by Benn et al. (2007). The processes may vary in magnitude across time and space, as they have at Tasman/Haupapa Glacier, which underwent a period of rapid calving followed by a period of low frequency but high magnitude calving events (Purdie et al. 2016; Dykes et al. 2011). Subaqueous morphology, the third order of control outlined by Benn et al. 2007 is dependent on the first and second orders of control,

however the structure of subaqueous ice ramp development is also dependent on thermodynamic processes.

2.4 Thermodynamics

Thermodynamic processes affect lake temperature, currents, density differences and suspended sediment concentrations (Truffer & Motyka, 2016a). The thermodynamic processes of a glacier can determine the formation of subaqueous morphology and subsequent calving of subaqueous morphology. Calving glaciers can form underwater ice ramps or 'ice feet' (Figure 7) and although this is thought to be due in part to differences in the rates of subaerial and subaqueous calving rates previously identified (Robertson, Benn, Brook, Fuller, & Holt, 2012), spatial and temporal variability of these subaqueous features indicate that other processes such as thermodynamics also exert control (Purdie et al. 2016; Robertson et al. 2012).

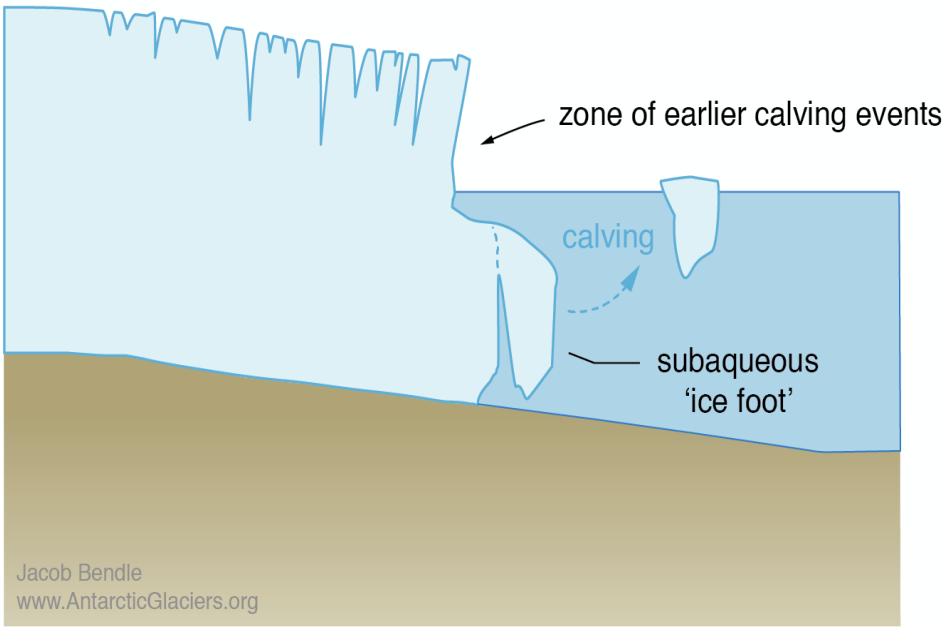

Figure 7: Diagram showing buoyant calving of subaqueous ice ramps, ice ramps may develop from a difference in subaerial and subaqueous calving rates. From AntarcticGlaciers.org – Explaining the science of Antarctic glaciology. Retrieved March 08, 2019, from http://www.antarcticglaciers.org/glacier-processes/glacial-lakes/calving-of-freshwater-glaciers/

Subaqueous morphology such as ice ramps and ice toes will buoyantly calve once the subaqueous ice feature exceeds the critical shear stress of the ice (Hunter & Powell, 1998), and the point at which the ice exceeds the critical shear stress will vary depending on physical processes.

Thermodynamic processes that control subaqueous melt rates are dependent on the heat transfer and conductivity through the water body (Truffer & Motyka, 2016b). Subaqueous melt rates of tidewater glaciers differ from those of freshwater lakes. In tidewater glaciers, subaqueous melt is driven mainly through density differences between subglacial meltwater and seawater. The mixing of these waters forms a buoyant discharge by incorporating the warm ocean water with the glacial meltwater. This enables heat to transfer from the water to the ice thereby enhancing melting at the calving front (Motyka, Hunter, Echelmeyer, & Connor, 2003).

Freshwater glaciers experience smaller perturbations overall, making them more stable than glaciers in a tidal setting (Boyce et al. 2007). For glaciers calving in freshwater settings, the buoyancy of the subglacial meltwater is much lower than that of a tidewater glacier. This is related to very small density differences between the subglacial meltwater and the water in the lake, which limits up-welling and heat exchange and inhibits subaqueous melting. Freshwater glaciers can produce floating ice tongues and infrequent but large calving events due to flatter topography, lower velocity and strain rates and less crevassing (Truffer & Motyka, 2016a). Due to this more stable setting, subaqueous morphology such as ice ramps can develop up to 300 m in freshwater settings, compared with open tidewater systems where reports of long ice ramps are not as common (Robertson et al. 2012). This is attributed in part to the closed heating and cooling system in a proglacial lake, compared with the

greater heat transfer opportunities caused by ocean currents in open tide water systems (Truffer & Motyka, 2016b).

Sugiyama et al. (2016) studied the thermal structure of three calving glaciers ending in proglacial lakes in Patagonia to better understand subglacial processes between ice and water. They found that the thermal structure of the lakes showed a significant difference when compared with data collected from glacial fiords. This was due to the water density being controlled primarily through suspended sediment concentrations instead of through water temperature, which is the dominant control in tidal settings (Sugiyama et al. 2016).

They found that heat transfer in the upper ~180m of the lake was active, due to wind-driven circulation mixing, however cold glacial water filled the area near the bottom of the lake which had no efficient heat transfer to the ice-water interface. This meant there is no upwelling current from the subglacial discharge (Figure 8.). This separation of the two layers was due to the turbid glacial water being denser that ambient lake water (Sugiyama et al. 2016). This temperate structure of proglacial lakes that have an upper mixed warmer layer overtop a denser cooler layer has the potential to create subaqueous features such as ice ramps and toes when the cooler water is trapped by topographical features.

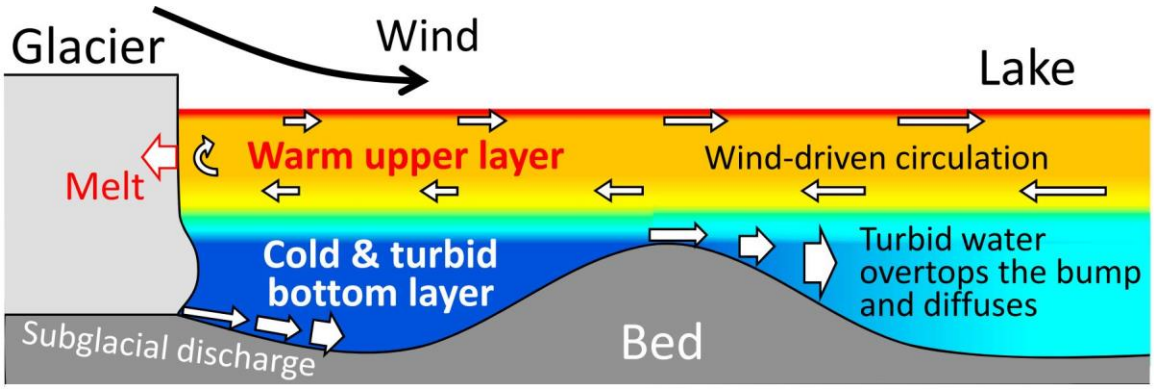

Figure 8: One example of thermal stratification with cool water near the base of the glacier which is contained be a topographical feature and warm water mixing at the top. Ice toes and ramps can form from this preferential melting. Figure adapted from (Sugiyama et al. 2016).

2.4.0 Subaqueous Melt Rates and Calving

An assessment of thermodynamic processes can help establish a subaqueous melt rate in glaciers that calve into proglacial lakes. The subaqueous melt rate is a key process that can be used to help explain spatial and temporal variation in subaqueous morphology. Modeling by Slater et al. 2015 showed that submarine hydrology had a significant effect on submarine melt rates in a tidewater glacier and that subglacial hydrology in a distributed system could produce more melt than that of a channelised system. This indicates that subglacial hydrology is a controlling factor on the spatial distribution of melt, which may also impact the development of subaqueous morphology and rate of calving.

The main controls on subglacial meltwater in freshwater settings are dependent on the temperature and pressure of the lake as well as sediment concentrations (Sugiyama et al. 2016). Glaciers terminating into lakes, such as the Yakutat Glacier in Alaska, have cold temperatures and lack density driven currents, so ablation rates can be calculated purely through surface mass balance. This differs markedly from the processes acting on the terminus at Tasman/Haupapa Glacier New Zealand, where subaqueous melt processes play a role in the variation of calving and terminus morphology (Gulley, Benn, Screaton, & Martin,

2009). At Tasman Glacier, Purdie et al. (2016) noted that a large iceberg showed evidence of circulation derived melting, indicating that changes in subglacial hydrology and or convection currents may influence the locations along the terminus where ramps can form.

2.5 Influence of Supraglacial Ponds

Relationships between supraglacial pond distribution and surface velocity and hydrology (Gulley et al. 2009; Hoffman & Price, 2014; Immerzeel et al. 2014; Miles et al. 2017) may influence calving processes and near terminus morphology. The development of supraglacial ponds on the near terminus of a debris covered glacier can often precede rapid calving. Small individual ponds may coalesce to form larger ponds, eventually forming or enlarging an existing proglacial lake (Chikita and Yamada, 2005; Rohl, 2008). Evidence of this happening was recorded in the late 1990's at the Khumbu Glacier where Naito's et al (2000) modelling found that ponds were now persisting through the year and in some cases were coalescing to forming larger ponds in the lower terminus region. Observations of pond development on the Eastern margin of the Khumbu Glacier by Watson et al 2016 supported the idea that the glacier may be entering a transitional phase that will enhance lake development.

Despite making up a small percentage of the glacier surface supraglacial ponds are an important component of ablation processes. It was found at the Lirung Glacier, a debris covered glacier in Langtang in the Himalayas the ice cliffs accounted for up to 18% of the ablation rate, despite the supraglacial ponds only covering 2% of the area of the glacier (Sakai et al. 2000). The persistence of supraglacial ponds is often dependent on the hydraulic connection of the englacial drainage system, which is in turn controlled by the position of the englacial conduits and supraglacial topography (Miles et al. 2017).

Debris covered glaciers can insulate ice from melting providing the debris cover exceeds a few centimeters in thickness, however if the debris cover is thin then the melt rate can accelerate and enhance melting due to a lower albedo. This results in the formation of supraglacial ponds (Benn et al. 2012). The irregular topography of debris covered glaciers causes the debris thickness to fluctuate. The development of supraglacial ponds is largely controlled by the gradient of the glacier and the surface velocity. The presence of supraglacial ponds has previously been recorded on glaciers with surface gradients <10° (Miles et al. 2017). In New Zealand supraglacial ponds have developed on glaciers with a surface gradient of < 2° (Rohl, 2008). In areas with a low surface gradient water can accumulate in depressions forming supraglacial ponds (Miles et al. 2017). Mapping in the Langtang Valley of Nepal from 1999-2013 using a combination of remotely sensed ASTER imagery and high-resolution UAV data demonstrated that surface velocity speeds and supraglacial ponds on the Langtang glacier were decreasing approximately 12km from the terminus (Kraaijenbrink, Shea, Pellicciotti, Jong, & Immerzeel, 2016). It was found that there was no distinct spatial distribution of supraglacial ponds on the glacier and linked high pond densities to low gradients and low velocities.

The formation of ice cliffs can also enhance the formation and development of supraglacial ponds. Ice cliffs can be formed from the slumping of debris slopes, which in turn exposes the ice, enhancing melting processes. Ice cliffs can also be formed through surface subsidence from the collapse of englacial voids or through calving into supraglacial lakes (Benn et al. 2012). The exposure of ice cliffs around the margins of supraglacial ponds can enhance the ablation process through ice cliff retreat as a result of calving processes or back-wasting from melt out processes (Benn et al. 2012). When the ice is exposed through slumping of slopes or from surface subsidence the exposed ice is typically dirty, resulting in a low albedo. The dirty

ice can readily absorb the incoming radiation causing melting. Subsequent melt rates can also be enhanced by the long wave radiation emitted from the surrounding warm debris surface (Sakai et al. 2002).

Multiple studies have recorded seasonal variation in supraglacial pond formation, drainage and water temperatures (Rohl, 2008; Narama et al. 2017; Watson, 2016; Miles et al. 2017). The total pond area on a debris covered glacier is often the largest at the onset of the melt season (Miles et al. 2017; Watson et al. 2016), followed by a decrease later in the season resulting from a greater degree of connectivity to the englacial drainage network (Narama et al. 2017). While small and temporary ponds have little effect on changing ice dynamics, large supraglacial ponds can influence the rate and direction of the ice flow. Supraglacial ponds can exist in areas of high surface velocity however these ponds are typically temporary with high surface velocities creating a strain on the pond walls. This will eventually result in fractures and crevasses leading to drainage of the pond (Rohl, 2008) which influences the glaciers' hydrology system, changing it from a slow distributed system to a fast channelised system and enhancing the velocity and deformation of the glacier (Mair, Nienow, Sharp, Wohlleben, & Willis, 2002).

The relationships between englacial conduits, ice cliffs, and glacial lakes are highlighted as key factors that control ablation on debris covered glaciers. Future research should focus on the interaction of these relationships to further understand the dynamics of debris covered glaciers (Immerzeel et al. 2014) and also on supraglacial pond persistence and recurrence over seasonal periods and how this interacts with englacial systems. Seasonal variation in ponds on the glacier may have an important link to the hydrology and mass balance of the glacier

(Miles et al. 2017).

2.6 Summary

This literature review has outlined the concepts of calving, with a specific focus on glaciers that calve into lakes. Calving, velocity and the development of subaqueous morphology are not the result of a single process, but a combination of several processes acting at different spatial and temporal scales. The nature of calving is complex, with glaciers enduring multiple mechanical and thermodynamic stresses that act on the near terminus. This complex nature may mean that no one uniform calving law will be able to explain calving at all types of glaciers, and while exact models may only be specific to the geometry of each individual glacier, there are still similarities between processes that can be used to help explain the behavior of glaciers.

The number of temperate glaciers that are forming or have formed proglacial lakes has risen in recent years. This is particularly notable in the Himalaya region, where glaciers are important factor in the hydrological cycle, providing fresh water for villages in the catchment and for agricultural purposes. These glaciers are not always easily accessible making it difficult to obtain high spatial and temporal surveys of lake bathymetry and full limnological assessments.

Tasman/Haupapa Glacier is a debris covered glacier that terminates into a freshwater lake in the Southern Alps of New Zealand. The glacier has been through a significant period of downwasting, eventually transitioning to a calving glacier that terminates in a proglacial lake. This glacier lake is easily accessible allowing for high resolution surveys to be conducted on

an annual basis. Findings at Tasman Glacier on how processes such as calving, velocity, pond formation and lake limnology effect the development of subaqueous morphology can be compared with processes at other temperate glaciers to help predict how the ice dynamics will respond in the changing climate.

Chapter 3 – Study Site

3.0 Tasman/Haupapa Glacier

The Tasman/Haupapa Glacier is a debris-covered, calving glacier located on the eastern side of the Southern Alps in Aoraki Mount Cook National Park of New Zealand. It is New Zealand's longest glacier at ~23km in length, contains a third of the total ice volume in New Zealand (Chinn, 2001), and is ~600m thick (Hart, 2014). Despite the insulating effects of the debris cover, the glacier experienced a period of down-wasting, eventually developing a lake in the late 1980s. The proglacial lake, Lake Tasman, is over 5 km in length and up to 240 m deep (Purdie et al. 2016). Tasman/Haupapa Glacier has an actively calving terminus, retreating at a rate of ~140 m per year (Purdie et al. 2016).

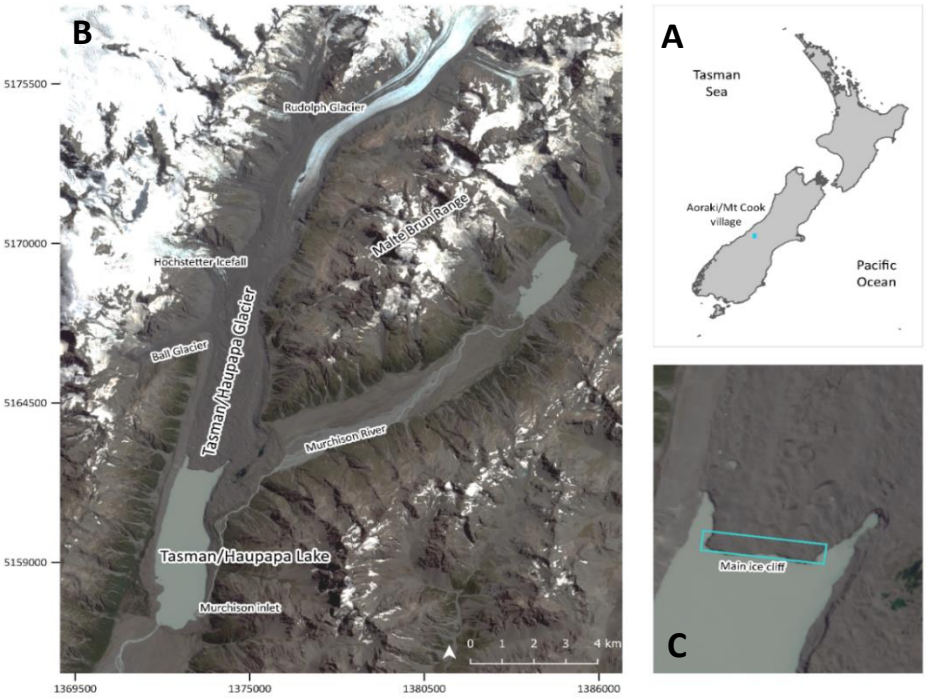

Figure 9: Study site A: Tasman/Haupapa Glacier is located on the eastern side of the Southern Alps of New Zealand and is situated in the Aoraki/Mt Cook National Park. The extent of the study area is shown in the blue box. B: Extent of Tasman/Haupapa Glacier from where the annual surface velocity was calculated. The main trunk of Tasman/Haupapa is fed by a number of tributaries. This study focuses on the ice below the Hochstetter confluence. C: This is the portion of the terminus that is referred to as the main ice cliff in the

following chapters.

3.1 Velocity

3.1.0 Surface velocity trends from previous research at Tasman/Haupapa Glacier

Surface velocity surveys at Tasman/Haupapa Glacier date as far back as 1891 (Table 1). Brodrick recorded a maximum surface velocity of 0.46 md $^{-1}$ below Ball Hut. Anderton (1975) measured surface velocities using stakes between 1971 and 1972 below Ball Hut, where it was estimated the glacier had thinned ~180 m since 1891. Surface velocities at the site measured 0.24 md $^{-1}$, showing Tasman/Haupapa Glacier had slowed considerably in this area since it was surveyed by Brodrick (1891).

Table 1: Surface velocity record of Tasman/Haupapa Glacier for regions of the Hochstetter, Ball Glacier region and the full glacier.

Reference	**Location and year(s)**	**Velocity (md^{-1})**
Brodrick (1891)	Ball glacier region	0.46
Anderton (1975)	Ball glacier region 1971 - 1972	0.24
Kirkbride (1995)	Ball glacier region 1971	0.01
Kirkbride (1995)	Ball glacier region 1986	0.27
Kirkbride (1995)	Terminus region 1986	0.009
Kirkbride and Warren (1999)	Terminus region 1995	0.07
Kaab et al. (2002)	Main trunk of glacier 2000-2001	0.14
Quincey and Glasser (2009)	Hochstetter region 2002, 2006 and 2007	0.41
Herman et al. (2011)	Full glacier 2002,2006	0.24
Redpath et al. (2013)	Hochstetter region 2009,2010,2011	0.41
Redpath et al. (2013)	Above the Hochstetter 2009,2010,2011	0.82
Haritashya et al. (2015)	Full glacier 2002,2006,2007,2009,2010,2012,2014	0.01
Haritashya et al. (2015)	Full glacier 2002,2006,2007,2009,2010,2012,2014	0.03
Horgan et al. (2015)	Terminus and Ball Glacier region 2012 - 2014	0.40
Purdie et al. (2018)	Hochstetter region	0.25

From 1957 - 1986 Kirkbride, (1995) used photogrammetry to survey the movement of boulders on the glacier surface. These measurements were supplemented with a survey of the surface velocity using surface markers. Photographs from 1957, 1971 and 1986 were used as image pairs to map the movement of boulders down the terminus. Time intervals between each image needed to be large in order to reduce the measurement error of tracking the boulders, this meant each photo had a time interval on 14-15 years. The long-time interval meant that interannual variation in the surface velocity could not be inferred. It was also observed that flow lines at the near terminus would converge towards the areas of the terminus featuring thermokarst erosion, suggesting that glacier velocity is influenced by these features.

By 1995 the glacier was showing signs of acceleration after years of stagnation (Kirkbride and Warren, 1999). The increase in surface velocity was linked to the propagation of new crevasses forming at the near terminus indicating an extending ice flow towards the centre of the lake. The development of these crevasses at the near terminus provide lines of weakness, which are then exploited by stresses leading to a period of rapid calving (Kirkbride and Warren, 1999). The increase in surface velocity observed prior to the faster calving period by Kirkbride and Warren, (1999) in this instance supports the theory that ice dynamics may be the master process and calving the slave process.

From 2000 onwards multiple surface velocity surveys have been conducted using remote sensing methods. Surface velocity assessments for Tasman/Haupapa Glacier using 15 m resolution ASTER (Advanced Spaceborne Thermal Emission and Reflection Radiometer)

satellite imagery was conducted by Kaab et al. (2002); Quincey & Glasser, (2009); Herman et al. 2013; Redpath et al. (2013); Haritashya, Pleasants, & Copland, (2015).

Both Kaab et al. (2002) and Quincey & Glasser, (2009) found surface velocity decreased from the Hochstetter confluence down towards the near terminus. Surface velocity near the terminus was found to be nearly stagnant by Quincey & Glasser, (2009) and Herman et al. (2011). The images used by Quincy & Glasser, (2009) to discern surface velocity had a 16-day time interval, which may have been too long an interval to see small fluctuations in velocity at the near terminus. Redpath et al. (2013) found that Tasman/Haupapa Glacier exhibits dynamic variation in surface velocity. Annual measurements were taken from 2009–2011. Velocities varied from 0.41 md^{-1} around the Hochstetter, to less than 0.14 md^{-1} towards the near terminus. Redpath et al. (2013) suggest that seasonal variation in surface velocity may occur within short (annual) timeframes. These findings showed the Tasman/Haupapa Glacier increases and decreases in velocity within annual time frames, and that seasonal variation may occur (Redpath et al. 2013).

The contrast in findings was put down to the large time interval between the measurement periods from the studies by Kaab et al. (2002) and Quincey & Glasser, (2009). By having an interval of 3-4 years apart any interannual spatial or temporal variation will may be lost by assuming the flow velocity evolved during the test period in a monotonic way (Redpath et al. 2013).

3.1.1 Spatial variation in velocity

The studies mentioned above have shown that surface velocity varies down the glacier. Surface velocity at the outer margins is generally slower than velocity in the centre of the glacier due in part to the lateral drag from the sides of the valley. An increase in velocity can result in the propagation of crevasses creating areas across the terminus that are more susceptible to calving. Kirkbride & Warren, (1997) suggested that an increase in velocity, which in turn enhances crevasse formation, was required for a faster calving rate to commence. Areas of the terminus that are heavily crevassed influence the pattern of subaerial calving, by calving more frequently than areas with less crevasse propagation. An increase in aerial calving rate may influence the location of the development of subaqueous morphology, given that they can form in areas where aerial calving exceeds subaqueous calving and melt processes (Robertson et al. 2012).

Glacier velocity "speed up" events resulting from surface meltwater and rainfall events that reach the bed of the glacier are well documented (Horgan et al. 2015; Meier et al. 2007; Truffer & Motyka, 2016a). Over a 26-month period Horgan et al. (2015) used GNSS time series to record a number of speed up events that exceeded 0.4 md^{-1}, which occurred in relation to rain events (Horgan et al. 2015). The speedup events resulted from rain rates ranging from 328mmh^{-1} – 353mmd^{-1}. Large rain events in the Mt Cook region that exceed 100 mm per day are not uncommon, suggesting speed up events on Tasman/Haupapa Glacier are a regular occurrence and are likely to influence increases in velocity at the near terminus which can drive calving rates.

The acceleration observed in these events was associated with the growth of water-filled cavities and an increase in bed separation at the bed of the glacier (Horgan et al. 2015). The findings of this study highlight that temporal variation and fast short-term acceleration in surface velocity, in relation to rainfall events, could be observed over small time intervals (hours and days), instead of the multi-year time intervals used in satellite imagery surface velocity surveys.

3.2 Calving

By 1998 a rapid onset of calving was demonstrated by an accelerating and extending ice flow (Kirkbride and Warren, 1999). An extensive series of arcuate crevasses at the very edge of the main ice cliff of the terminus were present – evidence of longitudinal stretching indicating that the Tasman/Haupapa glacier was on the brink of rapid calving (Kirkbride & Warren, 1999). It was suggested by Kirkbride and Warren, (1999) that in order for rapid calving to commence there needed to be significant development of crevasses at the terminus. Without this concentrated fracture propagation, the calving rate is likely to be slower, as calving is controlled mainly by waterline melt. It was predicted by Kirkbride and Warren (1999) that once rapid calving commenced, the potential for the Tasman/Haupapa Glacier to advance would be greatly reduced, given that temperatures have been rising since 1945 (Hochstein et al. 1995; Kirkbride & Warren, 1999). Kirkbride and Warren, (1999) hypothesized that the mass loss at Tasman/Haupapa could cause recession of much as 15km and that the rapid calving of Tasman/Haupapa Glacier would surpass a threshold not recoverable at a century timescale and potentially even a millennial timescale.

Research conducted by Dykes (2013) identified spatial and temporal calving patterns at Tasman/Haupapa Glacier. Dykes (2013) found that a number of supraglacial ponds formed on the Western margin of the Tasman/Haupapa Glacier. The ponds were hydrologically connected to the main englacial system and could expand in size due to an increase in water circulation, contributing to ice loss. The drainage of ponds also lead to a change in terminus geometry. Drainage of ponds can cause an increase in the buoyancy at the terminus which can alter the dynamics and stress regime. It is thought that this may have contributed to the unsteady retreat of the terminus with the western embayment becoming isolated from the central terminus.

Dykes (2013) studied calving rates between 2000-2008 and found two distinct periods of retreat. The rate of calving from 2000-2006 caused a slow retreat rate of 0.09 md^{-1} compared with a faster calving and retreat rate of 0.27 md^{-1} from April 2006 – January 2007. Spatial variation in the calving rates across the terminus were also evident across the main ice cliff which had a rapid retreat rate of 0.10 – 0.70 md^{-1}. This contrasted with the eastern embayment ice cliff with a retreat rate of 0.02 – 0.13 md^{-1}. It was suggested by Dykes (2013) that spatial variation in cliff retreat indicated additional processes were contributing to the increase in retreat rate at the main ice cliff.

Dykes (2013) identified several factors that contributed to the variability of calving across a spatial and temporal scale, these were related to terminus geometry, subaqueous morphology, thermal notch development and changing climate on diurnal and seasonal scales. Different combinations of these factors has determined the timing and style of calving at Tasman/Haupapa Glacier.

3.3 Lake conditions

Tasman/Haupapa Lake has formed from the rapid retreat of the Glacier since the late 1980s. A series of seismic surveys and radio echo soundings found that during the period 1973-1993 the glacier underwent a significant period of downwasting and the terminus disintegrated rapidly (Hochstein et al. 1995). The formation of the lake initiated with meltwater ponds forming on top of the glacier seen from as early as 1973 (Figure 10). These ponds coalesced to form a lake, with the first calving events taking place ~1991 (Kirkbride & Warren, 1999). Minor calving events took place through the early 1990's with lake levels deepening.

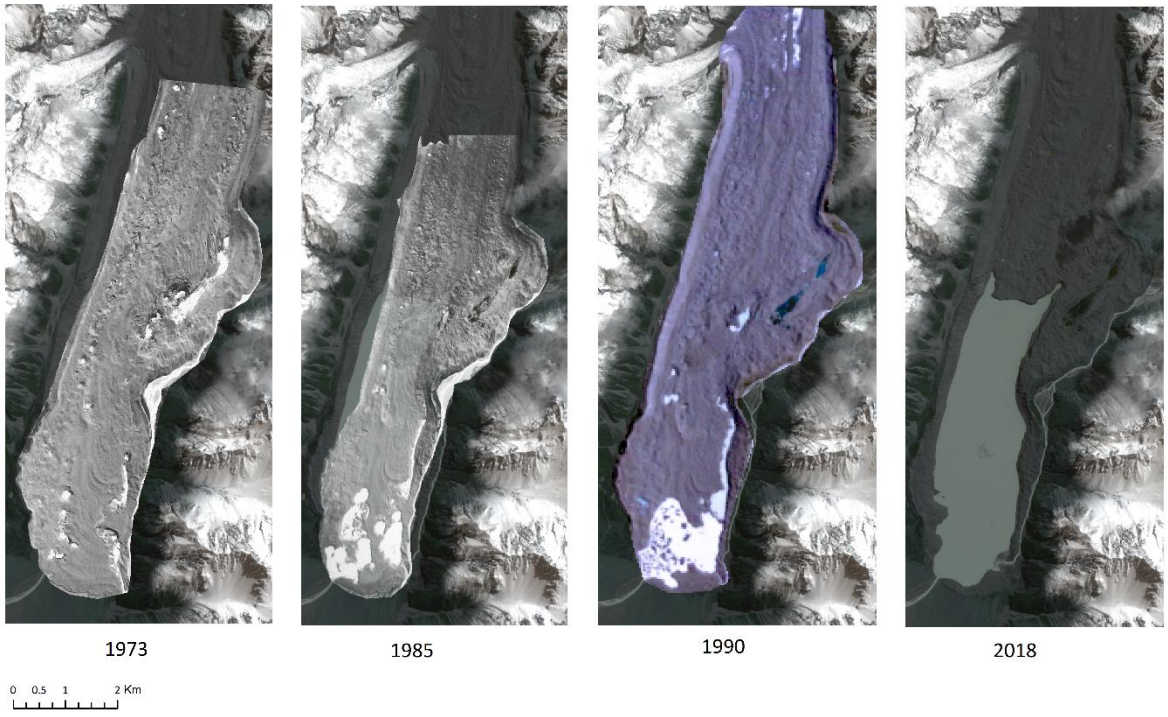

Figure 10: The progression of ponds forming in 1973 through to the coalescence of the ponds to form the beginnings of Lake Tasman. Photos retrieved from the Crown historic aerial photo archive: https://www.linz.govt.nz/about-linz/what-were-doing/projects/crown-historic-aerial-photo-archive-scanning-project

As the lake size has expanded, the glacier has continued to experience downwasting and the terminus has retreated further back from its Little Ice Age position. The valley walls that once supported the glacier have become destabilized, increasing the amount of slumping onto the glacier (Kirkbride & Warren, 1999).

Rohl, (2006) studied processes controlling the rate of thermal undercutting at Tasman/Haupapa Glacier. In a survey between 2001 – 2003, 17 thermal notches were measured at 14 locations. Rohl, (2006) found that undercutting off the ice cliff was driven by melt at the waterline, but that spatial variation and rate of the melt were key processes that would enhance calving (through thermal undercutting). The key control for temporal variation in thermal notch development is water temperature; limited notch development occurs in winter compared with spring and summer. The spatial variation in distribution of notches is determined by a number of processes, such as circulation, cliff geometry, debris supply and water level fluctuation (Rohl, 2006). It was found by Dykes, (2013) that the development of thermal notches was more advanced along the main ice cliff than in the eastern embayment ice cliff. It was suggested that the enhanced thermal notching on the main ice cliff may lead to larger subaerial calving events, which in turn would increase the retreat rate of this part of the terminus (Kirkbride & Warren, 1997; Rohl, 2006).

3.4 Terminus morphology

During the 1990's evidence of the development of subaqueous ice features started to emerge. Previously subaqueous features were recorded by Hochstein et al. (1995) who identified a vertical ice cliff along the main ice cliff in 1993. Subaqueous morphology measured by Purdie & Fitzharris, (1999) in the summer of 1995 identified vertical ice cliffs as well as ice shelves and ramps with gentle slopes across the main terminus, suggesting spatial variation in the processes that drive the formation of subaqueous features. It was found by Rohl, (2006) during surveys conducted between 2001 - 2003 that a subaqueous ice ramp extended the length of the terminus, with the exception of the eastern end.

Robertson et al. (2012) conducted a series of sub-bottom profiles with echo sounding and sonar, studying the development and morphology of ice ramps. Robertson et al. (2012) found an ice ramp that extended up to 400 m from the terminus, with a surface area of 0.49km^2 and covered the full width of the terminus, the surface of the ramp was covered in ~5-10m of debris. Similar findings were also identified by Dykes et al. (2013) who also surveyed the lake in 2008 and found subaqueous morphology in similar locations (Figure 11).

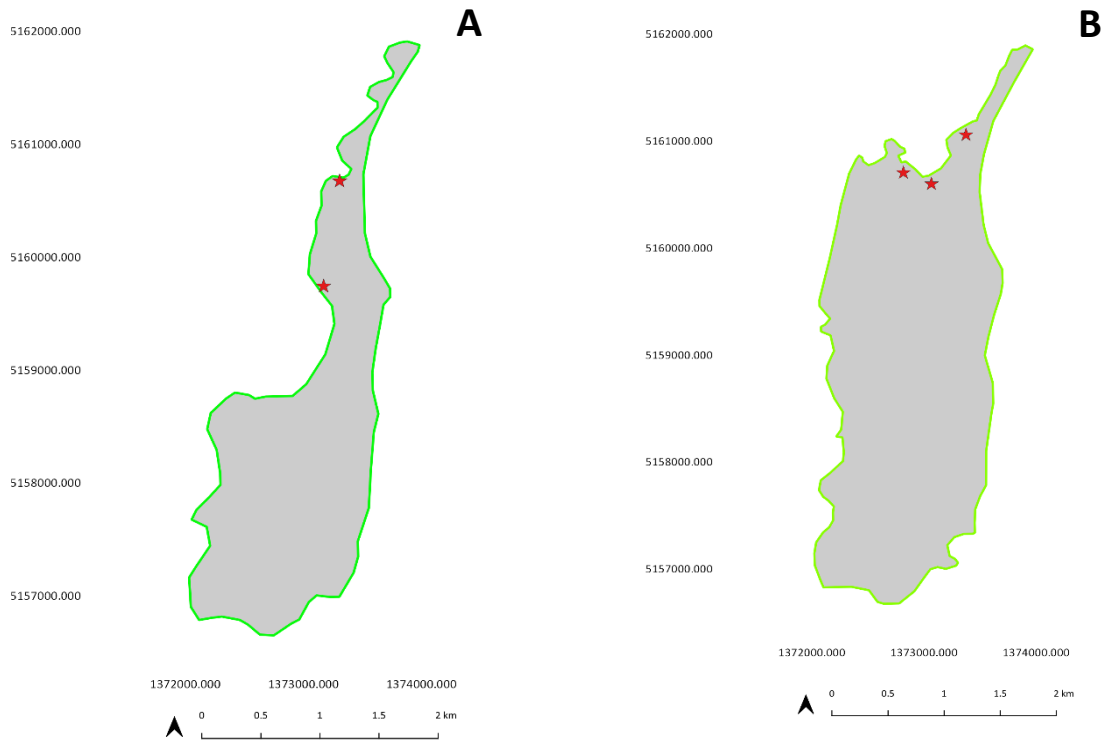

Figure 11: A: Mapped subaqueous features on the Eastern side of the terminus in 2003 by Rohl (2005). B: Ice ramps present in 2008 across the main ice ramp by Dykes et al. (2013) and Robertson et al. (2012) found ice ramps forming along the Eastern side of the terminus as well as the main ice front in 2008. Ramp locations identified by the red stars are general locations only of where ice ramps may have formed according to literature descriptions.

The rate of ramp evolution is not only controlled by the differences in subaerial and subaqueous calving but also through buoyancy forces, water temperature and insulating effects of debris (Robertson et al. 2012). The buoyant calving and buoyancy forces of subaqueous features can be suppressed if mass, such as debris is added to the ice ramp (Hunter & Powell, 1998). The debris settling on the ramp acts as an insulator, slowing down the melting and thinning process; under these conditions, the ramp can extend up to hundreds of metres from the terminus of the glacier (Robertson et al. 2012). Glacial environments where ice ramps have formed and been maintained often contain sediment rich meltwater (Hunter & Powell, 1998), the thick sediment cover acts as an insulator to buried ice; debris layers only need to be greater than 30mm for this to occur (Kirkbride & Deline, 2013). Understanding these processes that drive the development of subaqueous features will allow a better understanding of how subaqueous processes will affect the retreat of Tasman/Haupapa Glacier.

Previously, the formation of ice ramps at glaciers has been associated with areas of englacial discharge and sediment ramps (Hunter & Powell, 1998). Evidence of englacial discharge was found on a ramp that broke off at the Johns Hopkins Glacier in Alaska. The resulting iceberg had a rilled surface which was consistent with buoyant meltwater rising along the ice cliff (Hunter & Powell, 1998). Icebergs from ramp calving events at Tasman/Haupapa Glacier have also been reported by Purdie et al. (2016) with evidence of rills up the front of the ramp and thermal notches on the top of the ramp.

Thick sediment cover enables ice ramps to overcome buoyancy processes (Hunter & Powell, 1998). Observations and measurements at Tasman/Haupapa Glacier by (Warren & Kirkbride, 1998) documented boulders and stones falling from the debris rich glacier into the lake and onto a projecting ice ramp ≤4m from the near vertical terminus. They suggested that the formation of the ice ramps at Tasman/Haupapa Glacier was due to rapid melting at the waterline, leading to a greater retreat rate of the subaerial ice cliff compared with the subaqueous ice cliff. Purdie (1996) suggested that areas with no subaqueous ramps were where the terminus experienced deeper crevassing due to greater pressure release. Deeper crevassing lead to parts of the terminus calving at full depth instead of the subaerial calving processes that dominated the other areas of the terminus.

Ice ramps have the potential to affect the calving rates of the Tasman/Haupapa Glacier. The location of the ice ramps may be linked to subaqueous hydrology (Purdie et al. 2016). In research conducted by Robertson et al. (2012) it was found that the ice ramps evolve and move over time, likely growing and disintegrating in relation to subaerial retreat rates. The temporal and spatial variation in ice ramp development highlights the benefit of pursuing further research at Tasman/Haupapa Glacier using, remote sensing techniques, to better understand the dynamics and feedback mechanisms that operate between calving rates, subaqueous hydrology and subaqueous landforms.

3.5 Summary

Despite a number of glaciers in the Mt Cook National park developing proglacial lakes, calving processes and showing a collective pattern of retreat, they are staggered in their developmental process, highlighting that non-climatic forces can influence the calving process (Hochstein et al. 1995). The geometry of each glacier is different, with variables such as mass balance, subglacial drainage and ice flow dynamics affecting how the glacier responds to changes in climate. The differences in glacier geometry may help explain why the retreat pattern of glaciers in the Mt Cook National park are staggered. The unique geometry and staggered retreat rate of the glaciers also highlights the difficulty in developing a unifying calving law that is suited to all glacier types.

Chapter 4 - Methodology

4.0 Velocity

4.0.0 Details of satellite used to derive surface velocity

In order to calculate glacier surface displacement from 24 December 2015 - 21 February 2018 at Tasman/Haupapa Glacier, Sentinel-2A/B Level-1C satellite images were used. Repeat surveys of Tasman/Haupapa Glacier bathymetry and subsequent ice ramp locations start from 2013; however, Sentinel 2 imagery was only collected from the end of 2015 – the start of when data from Sentinel 2 was available. The Level-1C data consists of radiometric and geometric corrections (ESA website), the orthorectification process utilizes the PlanetDEM90 – a 90 m resolution Digital Elevation Model (DEM) (Kaab et al. 2016), produced by the Shuttle Radar Topography Mission (SRTM). The input data for the PlanetDEM90 has been improved and corrected for some mountain regions, desserts and parts of the United States of America, specific locations and dates of improvements are not specified. Further information on the orthorectification process for Sentinel satellite imagery has not been made available (Kaab et al. 2016)

The accuracy and level of detail obtained from the use of optical satellite imagery for feature tracking is limited by the spatial resolution of the sensor, the co-registration process of aligning satellite imagery from two different overpasses, the method used to orthorectify the images, and cloud conditions (Scherler 2008). It was also noted by Scambos (1992) that in order to achieve good co-registration between two sequential satellite images, the sun angle and azimuth should be nearly the same in both images. The Sentinel images in this study all have the same orbit path and thus the imagery is collected at similar times, with light conditions similar for short repeat pass times.

Sentinel imagery was selected over other imagery from optical satellites such as Landsat 8 and ASTER due to its ability to provide 10 m resolution in the near infra-red (NIR) band, whereas Landsat 8 and ASTER can only provide 15 m resolution and ASTER. Sentinel 2A and 2B orbit at an altitude of 786 km and are separated by 180° giving a repeat rate of 5 days if images from both satellites are used, or a 10-day repeat rate for each singular satellite. The satellites provide high resolution multi-spectral imagery and a more frequent repeat rate than Landsat or ASTER (Figure 12), giving a greater pool of images from which to select cloud free data.

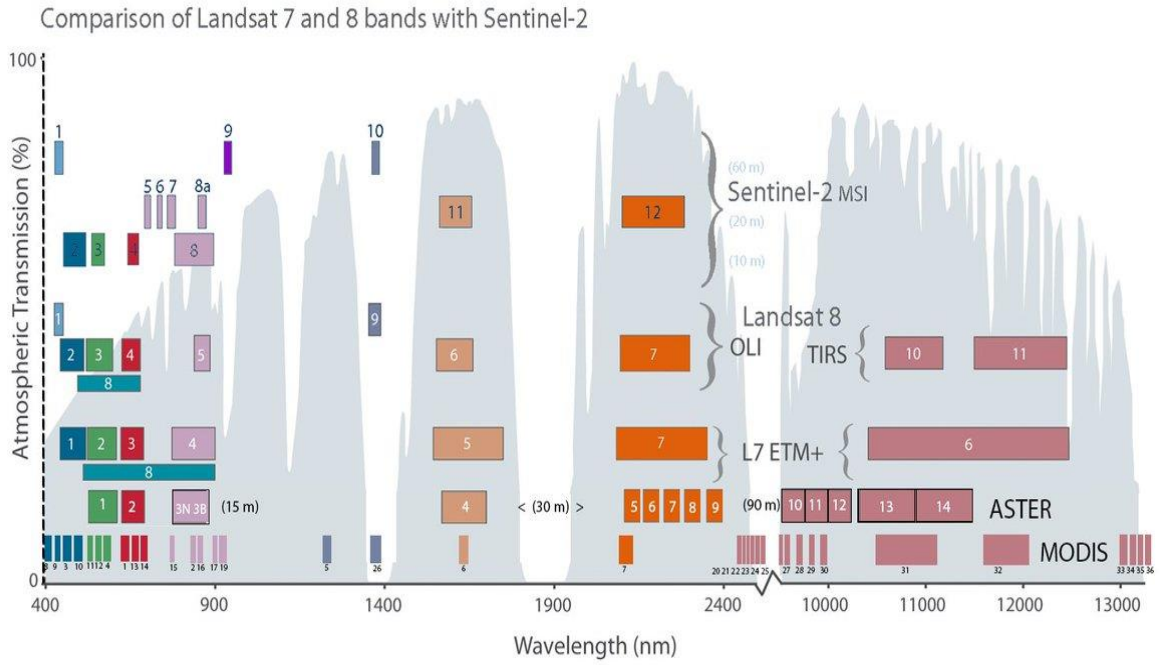

Figure 12: A comparison of the Sentinel-2 bands with Landsat, ASTER and MODIS showing the bandwidth for each satellite. The NIR band 8 from the Sentinel satellites has one of the widest bandwidths in the NIR at the highest resolution of 10 m. Figure retrieved from: https://twitter.com/USGSLandsat

The radiometric resolution is the satellite's ability to discern differences in light intensity, and the higher the accuracy of the image pixel values. Snow and ice have a lower spectral reflectance in the NIR range, so the NIR band can be used to highlight the contrast of an image to differentiate between snow, ice, water and rock (Kaab et al. 2014). For this study, for all 31 Sentinel images band 8 was selected (Figure 12), with a bandwidth of 842 nm and a spatial

resolution of 10 m.

4.0.1 Feature tracking process and uncertainty analysis

The feature tracking software Cosi Corr (Co-registration of Optically Sensed Images and Correlation) (LePrince et al. 2007) was used to extract surface displacement, producing 35 gridded velocity fields (Figure 13). The Sentinel images for this study were paired together sequentially to minimize large time gaps in-between images.

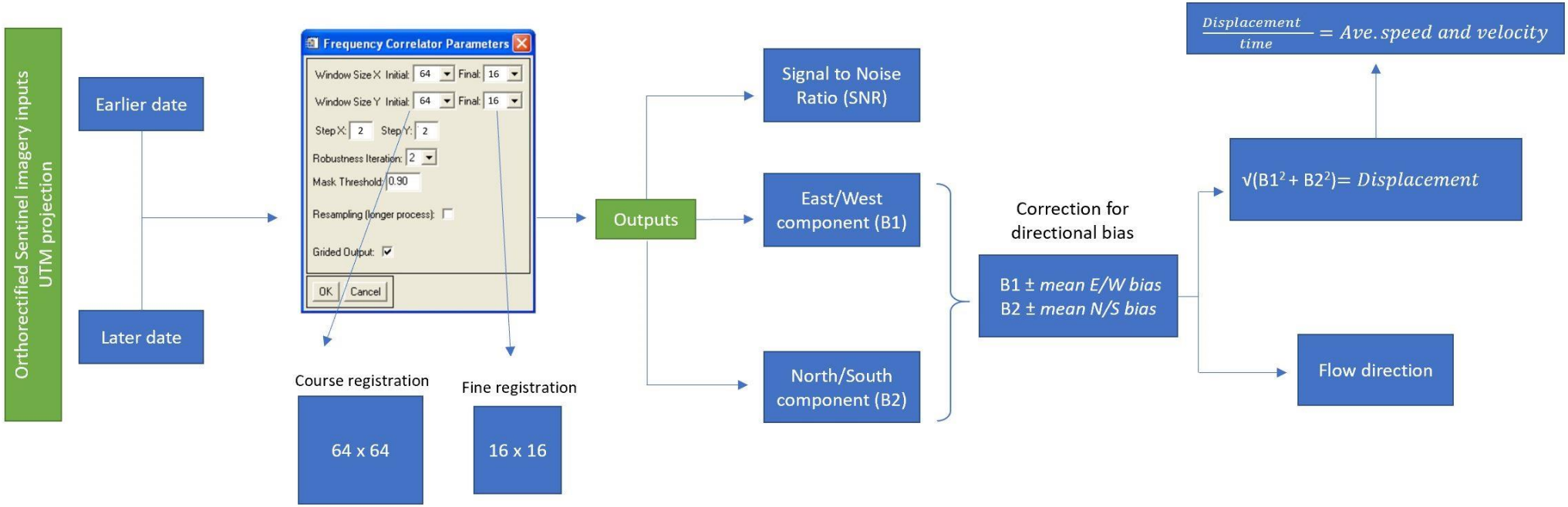

Figure 13: Workflow of creating displacement surfaces from Sentinel-2 imagery. Image 1 is always captured at the earlier date; image 2 is always captured at a later date. For the purposes of this study, where possible image 2 is the next sequential image. A frequency correlator is used to produce a North/South and East/West correlation and a Signal to Noise Ratio (SNR) image is produced showing areas of decorrelation. All imagery was processed using the settings shown in the 'Frequency Correlator Parameters' window. Directional bias is corrected for and gridded surface are produced of displacement and average speed and velocity. A vector field is also produced that shows the direction of flow.

Image correlation is achieved with an iterative, unbiased processor that estimates the phase plane in the Fourier domain by transforming a function of time into a function of frequency. The frequency correlator was used over the statistical correlator, as LePrince et al. (2007) states that although it is more sensitive to noise, it is more accurate when used with good quality images. The Fourier domain transforms both windows, the larger initial window detects the dominant displacement and the smaller windows are then used to iterate through correlations. The iteration process will stop if the correlation of the iteration deviates too much from the dominant displacement and the previous window correlation results are used (Kraaijenbrink et al. 2016).

Initially the size of the correlation window size was a course registration of 64 x 64 pixels, which was later reduced to a finer smaller window size of 16 x 16 pixels. The larger window size, the higher the bias in the marginal shear zone and steady rock areas. To minimize the bias the fine registration window is calculated by a window of 16 x 16 (160 x 160 m), reducing the bias at the glacier margins. However smaller windows increase noise, as the best compromise the window size of 16 x 16 was selected. A larger initial window size can help reduce noise in the image, but it can also reduce the level of relevant detail, by using a smaller final window size some of this level of detail can be retained (Kraaijenbrink et al. 2016).

Due to inaccuracy of orthorectification and changes in illumination, maximum achievable accuracy over ideal stable targets was determined by Leprince et al. (2007) with 1/50 of a pixel. This critically depends on the image quality, and cannot be achieved in the investigation area. The achievable coregistration accuracy for a changing target such as Tasman/Haupapa Glacier is likely lower (table 02).

Vector fields were created from the displacement map to assess the direction of ice flow and to help correlate the images. Images that were not well correlated had either an East/West (E/W) bias, and/or North/South (N/S) bias, identified by the direction of the arrows on non-moving parts of the images (such as bare ground). Corrections for the bias were made by subtracting and/or adding the mean E/W and N/S value to correct for the directional bias using band math.

The mean E/W bias and N/S bias statistics were generated from the basic statistics function in ENVI 5.1. Band math was used to discern the total displacement and hence velocity over the given time period for each pair of images. The equation below was used to calculated displacement.

Average velocity equation (4):

$$\frac{\sqrt{(B1^2 + B2^2)}}{time} = Average\ Velocity \tag{4}$$

For each velocity field, the displacement was divided by time, which was the number of days between the two images, all velocity values are presented as metres per day. This method produced a series of surface velocity fields showing the surface velocity of Tasman/Haupapa Glacier from 2015 – 2018. Images that had no cloud or very little cloud over Tasman/Haupapa Glacier were selected. As such, some of the images selected for processing had a cloud assessment > 50%, but were deemed acceptable to work with as Tasman/Haupapa Glacier itself had limited or no cloud cover.

Table 2: Sentinel 2A and 2B satellite images that were used to produce 35 gridded velocity surfaces. The N/S and E/W pixel corrections were applied to the E/W and N/S correlation image to correct for displacement bias on non-moving targets. The mean for the residual displacement (RD) images were calculated after the E/W and N/S corrections were made. The time interval and cloud assessment for each image are also included.

Imagery dates	Sentinel granule name	N/S bias correction	E/W bias correction	Mean RD (md^{-1})	Days between images	Cloud assessment (%)
24/12/2015	GS2A_20151224T223542_002643_N02.01	-0.12 ± 0.53	0.09 ± 0.55	0.04	10	43.13
03/012016	GS2A_20160103T223542_002786_N02.01					8.86
24/12/2015	GS2A_20151224T223542_002643_N02.01	1.14 ± 0.85	0.28 ± 0.75	0.12	40	43.13
2/02/2016	GS2A_20160202T223522_003215_N02.01					33.63
3/01/2016	GS2A_20160103T223542_002786_N02.01	-0.54 ± 0.62	0.23 ± 0.59	0.08	10	8.86
13/01/2016	GS2A_20160113T223532_002929_N02.01					33.63
3/01/2016	GS2A_20160103T223542_002786_N02.01	0.17 ± 1.30	0.14 ± 1.41	0.04	40	43.13
2/02/2016	GS2A_20160202T223522_003215_N02.01					19.97
13/01/2016	GS2A_20160113T223532_002929_N02.01	-0.04 ± 0.67	-5.53 ± 0.60	0.28	20	33.63
2/02/2016	GS2A_20160202T223522_003215_N02.01					19.97
2/02/2016	GS2A_20160202T223522_003215_N02.01	0.89 ± 0.67	-0.17 ± 0.60	0.04	40	19.97
13/03/2016	GS2A_20160313T223522_003787_N02.01					43.61
13/03/2016	GS2A_20160313T223522_003787_N02.01	-0.28 ± 1.05	0.27 ± 0.76	0.04	30	43.61
12/04/2016	GS2A_20160412T223522_004216_N02.01					6.13
12/04/2016	GS2A_20160412T223522_004216_N02.01	-1.00 ± 2.75	-0.26 ± 2.50	0.11	20	6.13

2/05/2016	GS2A_20160502T223542_004502_N02.01					20.75
2/05/2016	GS2A_20160502T223542_004502_N02.01	-0.40 ± 1.64	-0.90 ± 1.95	0.08	30	20.75
1/06/2016	GS2A_20160601T223552_004931_N02.02					3.29
01/062016	GS2A_20160601T223552_004931_N02.02	1.13 ± 4.80	-0.38 ± 3.91	0.07	50	3.29
21/07/2016	GS2A_20160721T223712_005646_N02.04					17.36
21/07/2016	GS2A_20160721T223712_005646_N02.04	-0.10 ± 1.80	0.21 ± 2.04	0.11	20	17.36
10/08/2016	GS2A_20160810T223712_005932_N02.04					28.15
10/08/2016	GS2A_20160810T223712_005932_N02.04	-1.88 ± 2.94	-0.62 ± 3.23	0.22	20	28.15
30/08/2016	GS2A_20160830T223712_006218_N02.04					17.87
30/08/2016	GS2A_20160830T223712_006218_N02.04	0.43 ± 1.57	0.61 ± 1.50	0.03	60	17.87
29/10/2016	GS2A_20161029T223712_007076_N02.04					5.84
29/10/2016	GS2A_20161029T223712_007076_N02.04	0.05 ± 1.05	0.36 ± 1.21	0.03	40	5.84
8/12/2016	GS2A_20161208T223702_007648_N02.04					65.13
8/12/2016	GS2A_20161208T223702_007648_N02.04	0.31 ± 0.99	-0.44 ± 1.01	0.02	50	65.13
27/07/2017	GS2A_20170127T223701_008363_N02.04					2.63
27/01/2017	GS2A_20170127T223701_008363_N02.04	-0.32 ± 0.73	-0.18 ± 0.67	0.03	30	2.63
26/02/2017	GS2A_20170226T223701_008792_N02.04					0.76
26/06/2017	GS2A_20170226T223701_008792_N02.04	-0.36 ± 0.60	-0.23 ± 0.57	0.04	20	0.76

18/03/2017	GS2A_20170318T223651_009078_N02.04					67.65
18/03/2017	GS2A_20170318T223651_009078_N02.04	-0.14 ± 0.64	0.06 ± 0.50	0.07	10	67.65
28/03/2017	GS2A_20170328T223701_009221_N02.04					5.81
28/03/2017	GS2A_20170328T223701_009221_N02.04	-0.65 ± 2.46	-0.83 ± 2.17	0.05	50	5.81
17/05/2017	GS2A_20170517T223711_009936_N02.05					7.64
17/05/2017	GS2A_20170517T223711_009936_N02.05	0.30 ± 0.79	0.20 ± 1.05	0.11	10	7.64
27/05/2017	GS2A_20170527T223711_010079_N02.05					12.11
27/05/2017	GS2A_20170527T223711_010079_N02.05	0.30 ± 0.79	0.20 ± 1.05	0.11	10	12.11
6/06/2017	GS2A_20170606T223701_010222_N02.05					2.43
6/06/2017	GS2A_20170606T223701_010222_N02.05	-0.55 ± 1.97	-0.41 ± 2.60	0.09	30	2.43
6/07/2017	GS2A_20170706T223701_010651_N02.05					38.82
6/07/2017	GS2A_20170706T223701_010651_N02.05	1.65 ± 1.08	0.04 ± 1.21	0.21	10	38.82
16/07/2017	GS2A_20170713T222541_010751_N02.05					13.34
06/072017	GS2A_20170706T223701_010651_N02.05	0.02 ± 2.51	-1.79 ± 2.46	0.07	30	8.86
15/08/2017	GS2A_20170815T223701_011223_N02.05					19.97
16/07/2017	GS2A_20170716T223701_010794_N02.05	1.78 ± 1.38	0.10 ± 1.55	0.08	30	64.95
15/08/2017	GS2A_20170815T223701_011223_N02.05					13.31
15/08/2017	GS2A_20170815T223701_011223_N02.05	0.43 ± 2.77	0.57 ± 3.13	0.06	50	13.31

4/10/2017	GS2A_20171004T223701_011938_N02.05					77.08
4/10/2017	GS2A_20171004T223701_011938_N02.05	0.22 ± 1.23	-0.44 ± 1.12	0.05	25	77.08
29/10/2017	GS2B_20171029T223649_003387_N02.06					26.22
29/10/2017	GS2B_20171029T223649_003387_N02.06	0.48 ± 0.62	0.29 ± 0.64	0.06	15	26.22
13/11/2017	GS2A_20171113T223701_012510_N02.06					31.88
29/10/2017	GS2B_20171029T223649_003387_N02.06	0.23 ± 0.67	0.17 ± 0.66	0.04	40	38.82
18/11/2017	GS2B_20171118T223649_003673_N02.06					13.31
13/11/2017	GS2A_20171113T223701_012510_N02.06	-0.22 ± 0.50	0.05 ± 0.50	0.13	5	31.88
18/11/2017	GS2B_20171118T223649_003673_N02.06					0.81
18/11/2017	GS2B_20171118T223649_003673_N02.06	-0.03 ± 0.56	-0.06 ± 0.54	0.07	10	0.81
28/11/2017	GS2B_20171128T223649_003816_N02.06					19.43
18/11/2017	GS2B_20171118T223649_003673_N02.06`	0.28 ± 0.88	-0.10 ± 0.80	0.04	25	
13/12/2017	GS2A_20171213T223701_012939_N02.06					15.73
28/11/2017	GS2B_20171128T223649_003816_N02.06	0.03 ± 0.63	0.45 ± 0.65	0.09	15	19.43
13/12/2017	GS2A_20171213T223701_012939_N02.06					15.73
13/12/2017	GS2A_20171213T223701_012939_N02.06	0.32 ± 0.78	0.31 ± 0.76	0.04	20	15.73
22/01/2018	GS2A_20180102T223701_013225_N02.06					55.15
22/01/2018	GS2A_20180122T223701_013511_N02.06	-0.06 ± 0.80	0.17 ± 0.81	0.03	30	2.74

21/02/2018	GS2A_20180221T223701_013940_N02.06	6.45

In order to understand how well correlated the surface velocity images were, the SNR images were assessed for decorrelation. LePrince (2007) outlined three sources of decorrelation: temporal decorrelation arising from drastic changes between images; decorrelation arising from shadowing effects; and decorrelation arising from features that are at the limit of the correlation window scale. This third type of decorrelation highlights a limitation in the feature tracking algorithm, whereby it is not able to produce a stable registration point between correlation windows (Leprince 2007). An example of the decorrelation from shadows and decorrelation of features that are at the window scale (such as lakes) is shown in Figure 14.

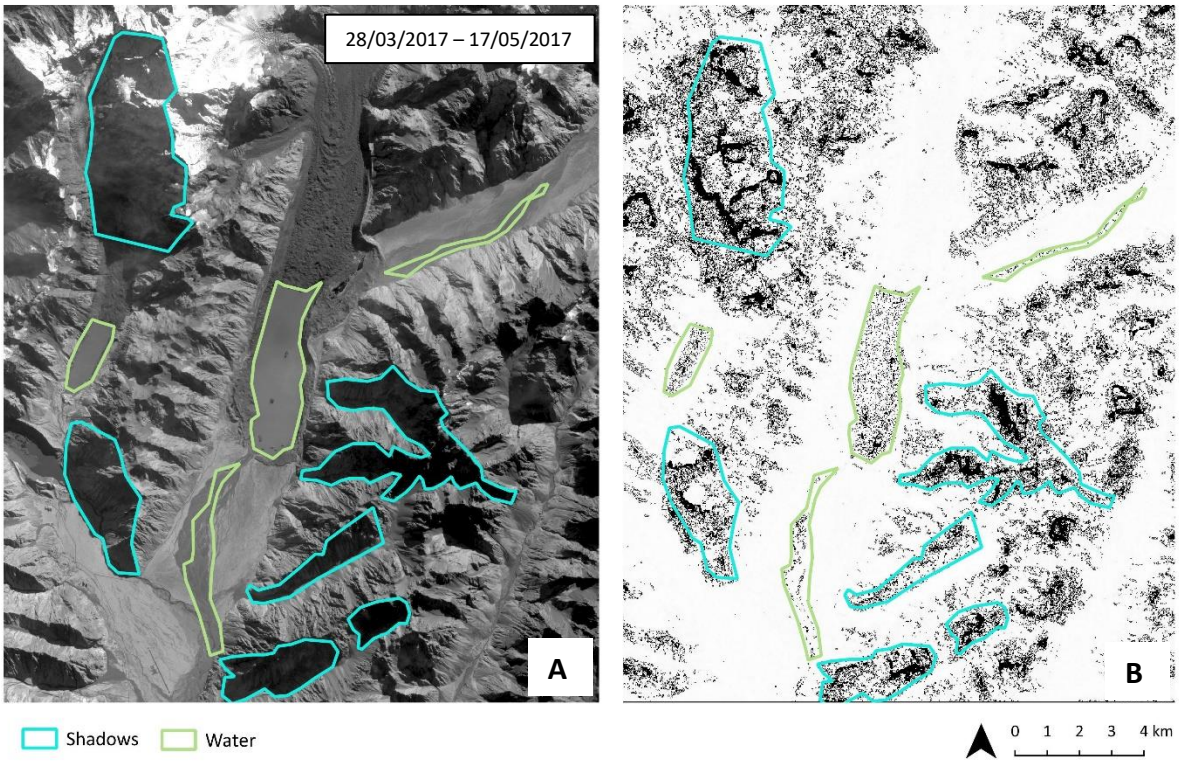

Figure 14: A: Areas of shadow and water are highlighted by polygons; the blue polygons show areas of shadow and the green polygons show areas of water. B: These same polygons are seen in the SNR image; the polygons show the areas of shadow and water are decorrelated.

By way of comparison, an image with very few shadows in the valleys and mountain sides shows fewer areas of decorrelation overall. Even so, bodies of water such as Tasman/Haupapa lake show up as an area of decorrelation (Figure 15). This is likely due to these features being

at the window scale.

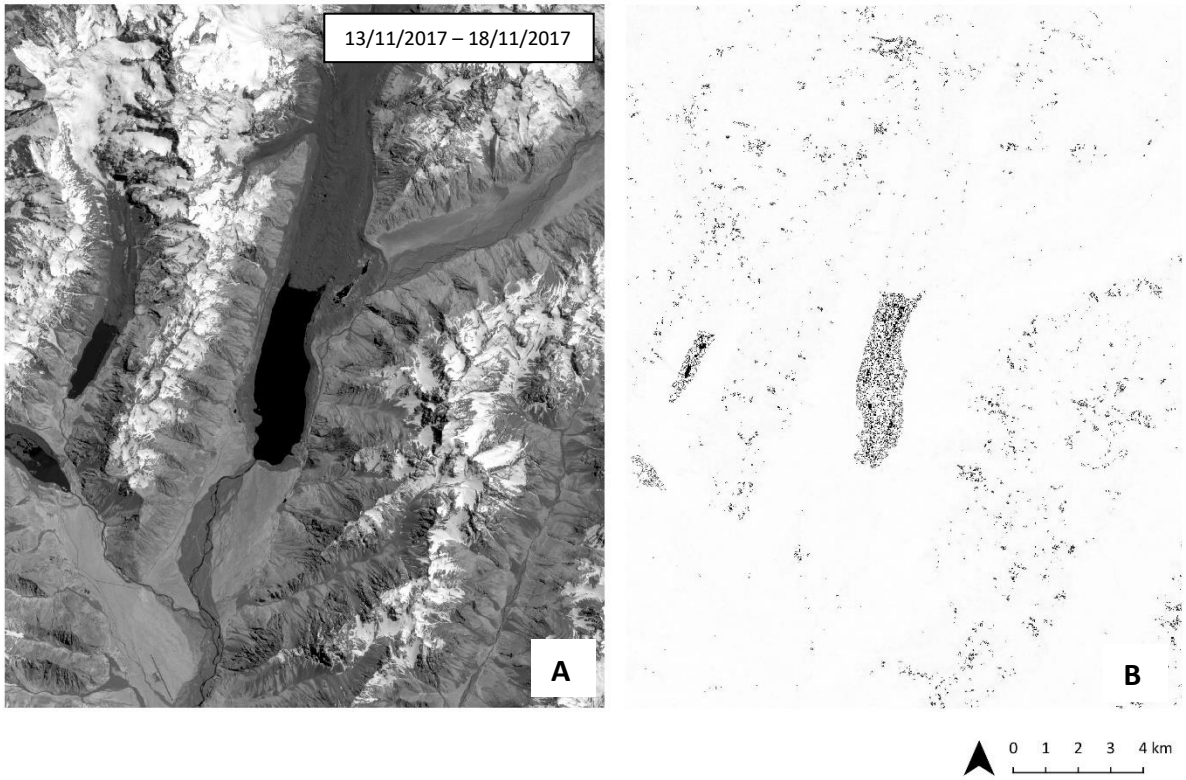

Figure 15: A: Sentinel image in band 8 with few shadows in the mountains. B: SNR image with very little decorrelation with the exception of water bodies such as lakes.

If the images are well correlated, any other offsets found in the imagery are the result of misregistration, topography, orbits and altitude (Berthier, 2005). The vector fields (Figure 16) were used to initially assess how well the images were co-registered. The size of the arrows corresponded to the size of the displacement recorded. If the image has good co-registration then stable areas such as roads or vegetated areas should not show displacement and will produce small vectors (Figure 16 A). If the vectors in these areas show a directional bias, then this needs to be corrected for.

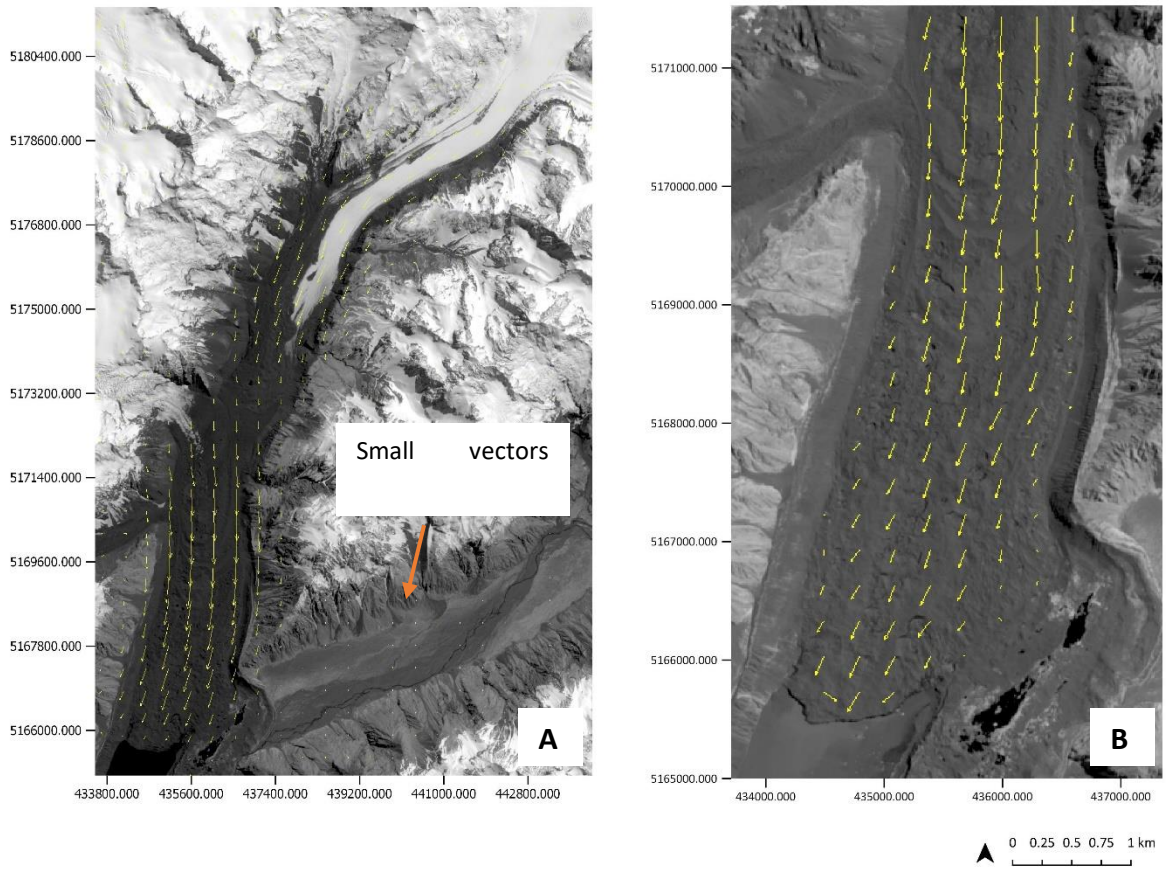

Figure 16: A: Vector arrows for the larger extent of the ablation zone. Small vector arrows over stable ground are highlighted by the orange arrow, the small size of the vectors suggests there is good coregistration between image 1 and image 2 (Fig 13). B: Smaller extent of the ablation zone below the Hochstetter showing displacement of pixels with vectors.

Polygons were created over stable land areas to assess how well coregistered the images were (Figure 17). Most of the polygons were concentrated on the western side of Tasman/Haupapa glacier and in the valley of the Murchison river, this was due to a higher of amount of stable land identified in these areas.

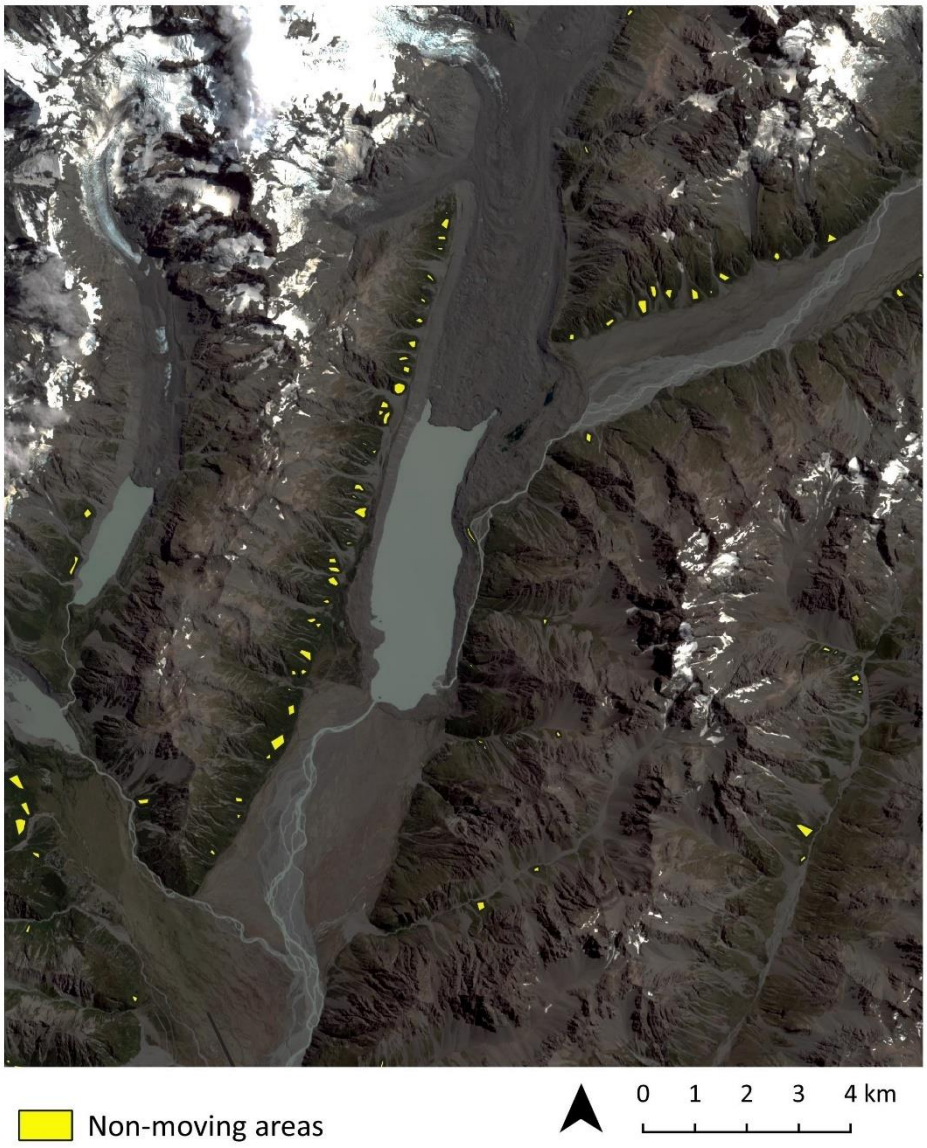

Figure 17: The yellow polygons are all considered non-moving areas such as vegetation. A total of 90 polygons are used to estimate how well co-registered the surface velocity images are.

These polygons covered ground deemed stable over the time period between satellite images. The polygons were dissolved using the 'Dissolve' tool in QGIS 3.6.2 so that the zonal statistics tool produced one mean and standard deviation for all polygons. If the images are well co-registered, then there should be no movement and the statistic should be zero. Zonal statistics was used to extract the standard deviation for all 35 velocity surfaces (Table 02). The best co-registered image had a mean residual of 0.02 m and the poorest co-registered image from 06/07/2017 – 16/07/2017 (Figure 18) had a mean residual of 0.21 m.

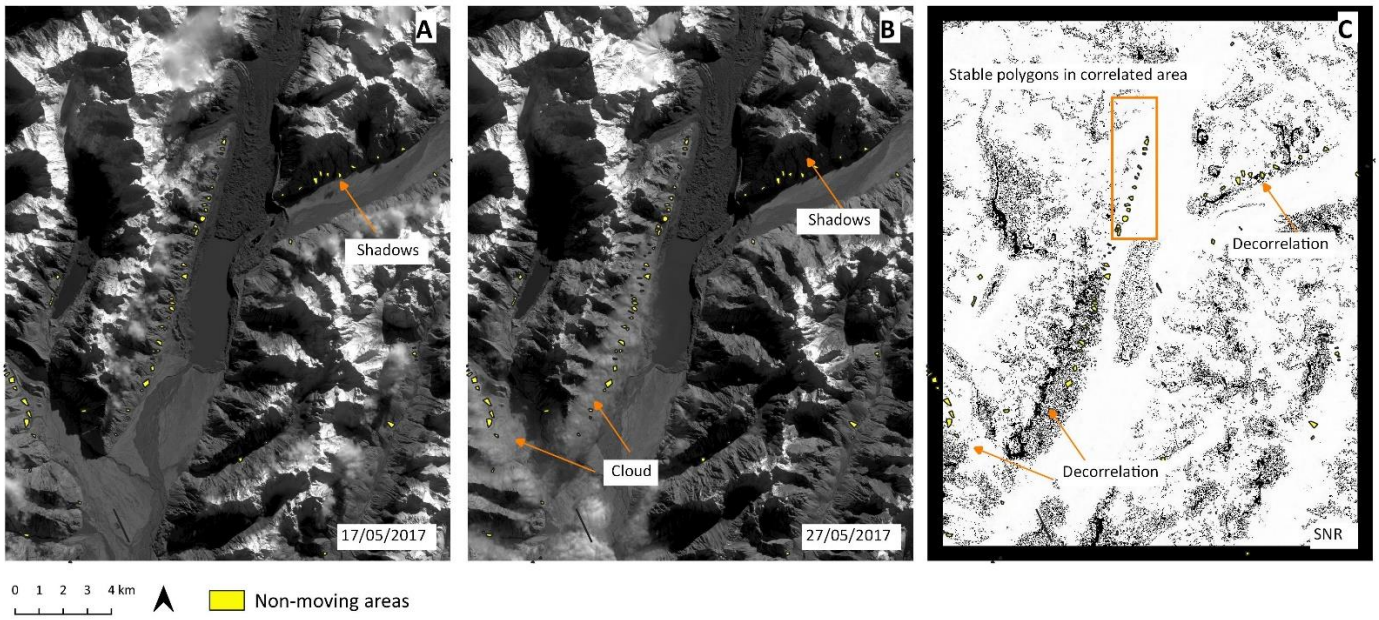

Figure 18: The 90 yellow polygons are all considered non-moving areas such as vegetation. A: image from 17/05/2017 identifies an area of dark shadow that coincides with the location of multiple polygons. B: Second image used in the feature tracking process from 27/05/2017, cloud is present at the same location as stable ground polygons. Shadows are also identified at the same location as stable polygons. C: Areas of decorrelation shown in black, these areas coincide with the cloud and shadows identified in A and B. A small subset of stable ground polygons inside the orange box were used to extract mean displacement. Area is white showing it is correlated.

If the polygons that cover stable ground are disrupted by cloud or shadows (Figure 18A,B), this will result in a poor correlation (Figure 18C), as such any polygons located in these areas were removed. The 18 polygons within the orange box (Figure 18C) were selected from the 90 stable ground polygons, as they covered ground that was well correlated. Zonal statistics were used to extract the mean from these areas, resulting in significantly less movement than initially calculated using the 90 polygons, some of which were affected by cloud and shadows.

This method of using multiple polygons across stable ground to test how well co-registered the images are relies on the images having limited imperfections and adequate coverage of stable ground across the whole image. The image from the 27/05/2017 only has 12.11% cloud coverage, but the cloud coverage is situated in the same location as >50% of the stable ground polygons, areas of the image with no cloud had few areas that could be identified as stable ground. It is noted that the bias correction applied here was assuming a linear relationship.

4.0.2 Surface velocity derived from Sentinel imagery

Where possible, Sentinel satellite images were paired sequentially (Table 2), and displacement was extracted, from which a surface velocity was derived using (Eq. (4)). For this study, eight region of interests (ROI's) were selected. One ROI covered the larger area of the ablation zone of Tasman/Haupapa Glacier, for which the surface velocity was calculated to determine average velocity patterns over a one-year time interval. A smaller ROI, of the glacier was used for all 35 velocity measurements. This smaller ROI was selected because changes in a glacier's surface velocity up-glacier may influence changes at the terminus. However, in the case of the Hochstetter, these changes were deemed to be too far away from the terminus to significantly influence changes at the terminus. Six small rectangular ROI's were created at different locations of Tasman/Haupapa Glacier. Point values were extracted from the centre of the glacier for each velocity surface. These points were placed in a scatter plot, from this inflections points in the data were used to identify the locations of the ROI polygons.

Mean surface velocities were calculated from six locations (Figure 19A). The mean surface velocity provided a one-year average for comparison with the surface velocity that was derived from the second ROI, which focuses on the lower part of the terminus below the Hochstetter confluence (Figure 19 B). Gridded velocity surfaces created from this ROI were used to analyse seasonal and spatial patterns in mean surface velocities from the three sites (Figure 19 B).

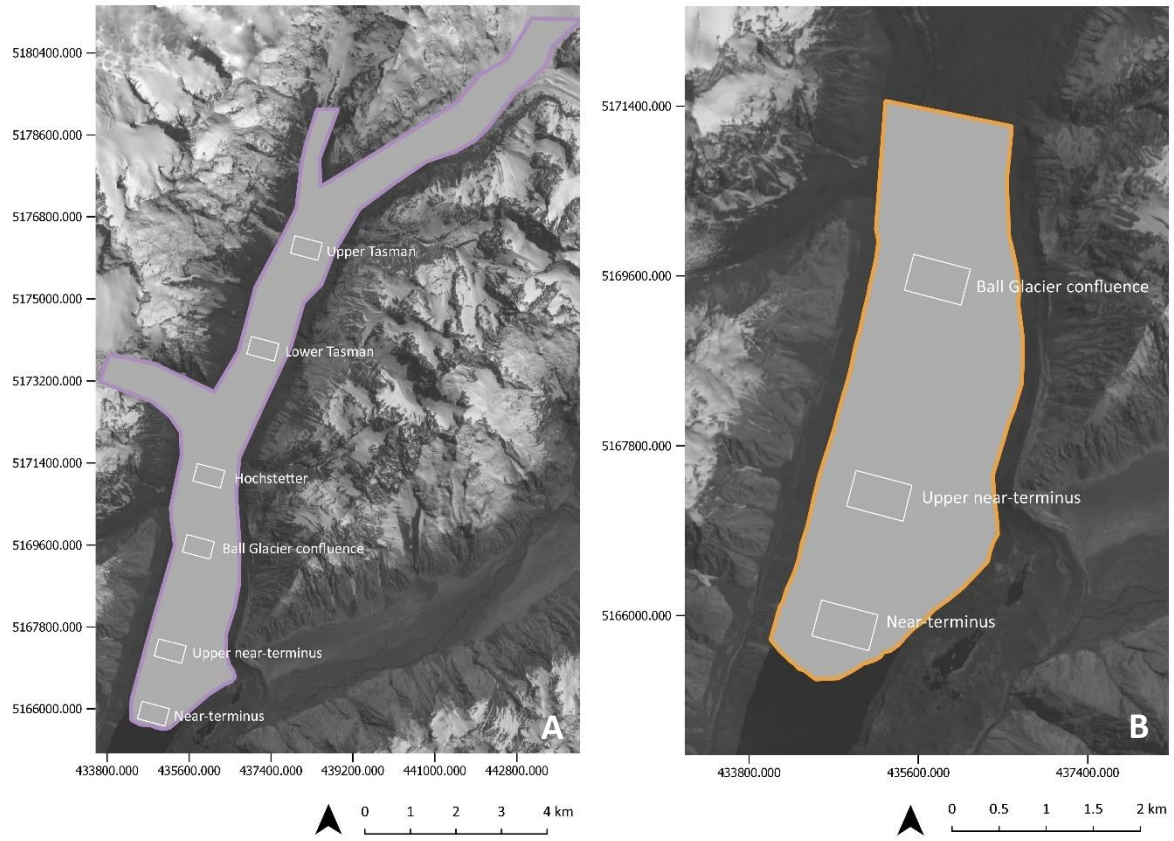

Figure 19: A: shows the extent that the one-year mean surface velocity is calculated for (purple outline). The location of all six rectangular polygons are shown with a white outline. Mean surface velocity was calculated from these rectangles, all rectangles are the same size. **B:** the smaller extent that starts below the Hochstetter confluence and ends at the terminus (orange outline).

All velocity gridded surface values were the same, so that any temporal variation between the surface velocity images would be comparable. In the results chapter, four surfaces (one per season) are presented for each of the 35 gridded surfaces mentioned above. These provide an example of how the glacier may respond during a particular season. Their time interval is 10 days for summer and spring, 20 days for winter and 30 days for autumn. All other velocity surfaces are available in appendix C. The surface velocity patterns for each season will therefore be partly affected by these differences in time intervals. Smaller time intervals may miss minor changes in velocity if the velocity change is slow, or they may average out sudden changes in velocity for longer time intervals. The velocity patterns also evolve as the season progresses, each gridded velocity measure being a snapshot of the glacier velocity at the specified time interval. Also, of relevance is the fact that due to the availability of satellite imagery the gridded velocity surfaces are from different times of the season.

To determine longitudinal variability in surface velocity, surface velocity was extracted at 293

points along 6 parallel lines spaced 20 m apart and extending 5.8 km up-glacier from the terminal face (Figure 20).

Figure 20: the six lines of points, each line of points started with 293 points. Points at the terminus were removed as the terminus retreated to exclude lake values.

During the feature tracking process for creating a displacement surface, a final 16 x 16 resampling window was used, meaning all pixels within 160 m^2 was used for the correlation process as correlation windows will search for a correlation in all directions (Kraaijenbrink et al. 2016). This means values near the edges of the glacier would be resampled with the edges of the moraine and other non-moving features, potentially affecting the velocity values near the edges of the terminus (Kraaijenbrink et al. 2016). However, all 6 transects were greater than 310 m from the edges of the terminus so pixel values for these transects were not

resampled with non-moving values.

The mean surface velocity was calculated for each individual transect using all 35 velocity values for that specific transect. Due to the retreat of the glacier, some transect values showed lake values. These values were removed so that only the surface velocity was recorded. The transects for each gridded velocity surface were plotted against the mean surface velocity of that transect. Single transect values were then compared with the mean transect values.

4.1 Calving

4.1.0 Quantifying iceberg calving from time lapse photography

To examine the relationship between calving events, rainfall and lake level change, calving events were recorded from time lapse photos of the terminus and compared with rainfall and lake level data from 20/07/2013 – 01/04/2018. The time series photos and lake level time series data used for this study was supplied by Dr Brian Anderson from Victoria University.

The camera that photographed the terminus was a Nikon D3200 that took 14 photos between 0800 hrs and 1800 hrs. Calving events that were identified from the times series photos. A calving event was any ice that broke off from the terminus. This created a large number of very small calving events. These small events could hide significant calving events that may be significant when plotted against rainfall and the velocity from the three sites on the terminus. An example of what was recorded as a small event and what was recorded as a large event is shown below in Figure 21.

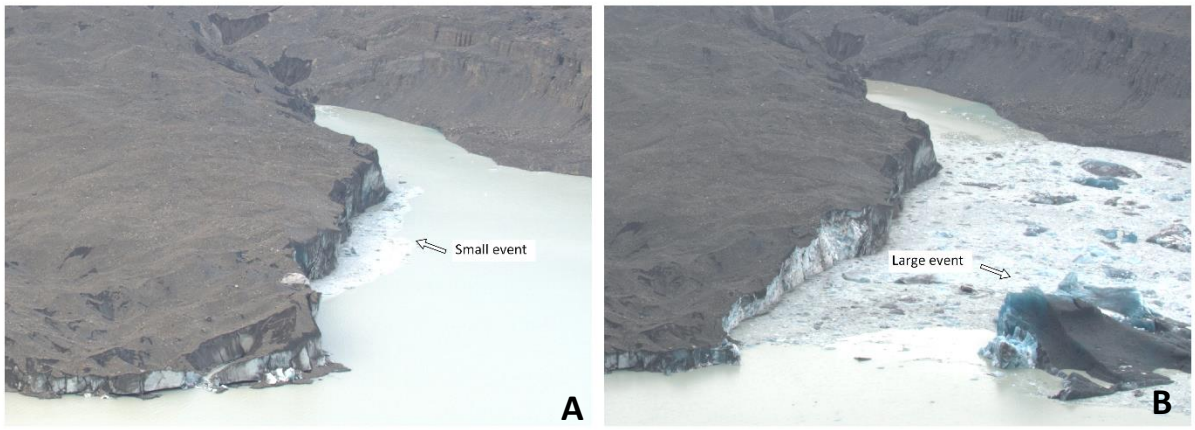

Figure 21: A: an example of what was recorded as a small event. B: an example of what was recorded as a large calving event.

For significantly large calving events, where a large portion on the terminus calved aerially and/or subaqueously, a large red diamond was plotted slightly above the other small calving events. The recording of calving events was limited to days with clear weather.

4.1.1 Comparison of Surface Velocity with Rainfall

To explore possible relationships between surface velocity and rainfall, daily rainfall data was collected from the National Climate Database (CliFlo) NIWA from the 24th December 2015 to the 21 February 2018 using data from the Mt Cook 18125 weather station. The rainfall data was then aligned with the dates of the velocity and calving event data. In order to establish if there was a relationship between calving, rainfall and velocity, calving events were plotted together with total 24 hr rainfall, mean velocity from the near-terminus, upper near-terminus and the Ball Glacier confluence. Calving events were also plotted against rainfall alone.

Mean rainfall was plotted against total velocity over 10, 20, 30, 40 and 50-day time intervals to align with the surface velocity data, to see if there was a significant relationship, and if the relationship was stronger or weaker as the length of days increased (Table 3). Mean values

were used to indicate the typical amount of rain that would fall over a specified time period.

Table 3: correlation, R^2 and p-values for the relationship between velocity and mean rainfall. No statistically significant relationship was found.

Time interval (days)	**10**	**20**	**30**	**40**	**50**
Correlation	0.61	0.12	0.38	0.79	0.88
R^2	0.37	0.01	0.14	0.62	0.78
P-value	0.15	0.80	0.46	0.21	0.31
Sample size	7	7	6	4	3

The Pearson correlation was used to calculate the correlation coefficient between average rainfall and mean velocity over set time intervals of 10, 20, 30, 40 and 50 days. The Pearson correlation evaluates the correlation coefficient between two variables for *n* number of samples. Variables are unrelated if the correlation is near zero. A paired samples t-test was used to calculate the p-value for each time interval. The α value was set at 0.05, any p-value above this value would lead to acceptance of the null hypothesis in that there was no statistically significant relationship between mean surface velocity and mean rainfall over *n* number of days.

4.2 Lake Conditions

4.2.0 Lake temperatures derived from satellite imagery

In order to assess the change in mean temperature of Tasman/Haupapa Lake from May 2013 through to June in 2017, imagery from Landsat 8 was used. Landsat 8 was launched 03 February 2016, and has a repeat orbit of 16 days, delivering ~650 scenes per day of the Earth. Landsat 8 carries on the Landsat program from Landsat 7 by continuing to collect moderate multispectral-resolution data of the earth's surface utilising two sensors: an Operational Land Imager (OLI), and Thermal Infrared Sensors (TIRS) containing two thermal bands. The two thermal bands (bands 10 and 11) have a spectral resolution of 100 m. This is resampled before

being made available at a spectral resolution of 30 m (Figure 12).

There were 29 Landsat 8 images used to derive mean surface lake temperatures of the whole lake. Band 10 was selected as the thermal band used to derive the surface temperature for all images. This band was selected over band 11 in order to minimise known errors arising from stray light, which may increase the reported surface temperature by as much as 8K in band 11, but by only 4K in band 10. Stray light occurs when thermal energy from outside the field of view enters the sensors and affects the data collected by bands 10 and 11. The stray light can be variable across scenes and is dependent on the radiance outside the field of view, meaning the end user of the product cannot correct for this error. The USGS/EROS who produce the products from the Landsat program are aware of the error and have tried to rectify it by applying a bias correction before releasing the thermal products but this correction still may lack precision and it is recommended that band 11 is not used in scientific studies (Barsi et al. 2014). Therefore, each Landsat 8 image was displayed using band 10 in the remote sensing software ENVI 5.1.

Table 4: Landsat 8 imagery used for mean lake temperatures and mean near terminus temperatures

File name	Image date	Cloud cover	Sun azimuth	Sun elevation
LC08_L1TP_075090_20130511_20170504_01_T1	11/05/2013	4.09	34.08	21.52
LC08_L1TP_075090_20130612_20170504_01_T1	12/06/2013	21.83	32.56	16.56
LC08_L1TP_075090_20130628_20170503_01_T2	28/06/2013	13.27	33.28	16.20
LC08_L1TP_075090_20130730_20170503_01_T1	30/07/2013	42.09	36.25	20.31
LC08_L1TP_075090_20130916_20170502_01_T1	16/09/2013	2.20	41.87	35.79
LC08_L1TP_075090_20131119_20180202_01_T1	19/11/2013	59.89	57.15	55.21

LC08_L1TP_075090_20131221_20170427_01_T1	21/12/2013	9.70	65.64	55.86
LC08_L1TP_075090_20140223_20170425_01_T	23/02/2014	54.32	55.68	43.05
LC08_L1TP_075090_20140311_20170425_01_T1	11/03/2014	65.34	50.09	38.53
LC08_L1TP_075090_20140327_20170424_01_T1	27/03/2014	61.98	44.74	33.80
LC08_L1TP_075090_20140514_20170422_01_T1	14/05/2014	41.47	34.27	20.69
LC08_L1TP_075090_20150821_20170405_01_T1	21/08/2015	18.71	39.19	26.02
LC08_L1TP_075090_20150906_20170404_01_T1	6/09/2015	1.39	41.06	31.60
LC08_L1TP_075090_20151008_20170403_01_T1	8/10/2015	34.48	45.91	43.63
LC08_L1TP_075090_20151109_20170402_01_T1	9/11/2015	55.67	54.20	53.14
LC08_L1TP_075090_20151227_20170331_01_T1	27/12/2015	16.25	66.61	55.09
LC08_L1TP_075090_20160128_20170330_01_T1	28/01/2016	64.11	63.84	49.50
LC08_L1TP_075090_20160213_20170330_01_T1	13/02/2016	12.07	59.40	45.66
LC08_L1TP_075090_20160229_20170328_01_T1	29/02/2016	17.44	53.99	41.40
LC08_L1TP_075090_20160316_20170328_01_T1	16/03/2016	11.99	48.38	36.82

LC08_L1TP_075090_20160417_20170326_01_T1	1/04/2016	74.05	43.19	32.09
LC08_L1TP_075090_20160807_20170322_01_T1	7/08/2016	14.11	37.60	22.13
LC08_L1TP_075090_20160908_20170321_01_T1	8/09/2016	2.40	41.32	32.66
LC08_L1TP_075090_20161229_20170314_01_T1	29/12/2016	43.74	66.76	54.78
LC08_L1TP_075090_20170215_20170228_01_T1	15/02/2017	3.98	58.51	44.96
LC08_L1TP_075090_20170420_20170501_01_T1	20/04/2017	23.14	38.28	26.63
LC08_L1TP_075090_20170506_20170515_01_T1	6/05/2017	32.18	35.33	22.42
LC08_L1TP_075090_20170607_20170616_01_T1	7/06/2017	5.59	33.02	16.76

To extract the mean temperature of the lake a polygon outline of the lake was digitized from the 2013/14, 2015, 2016 and 2017 imagery. A polygon for each year was created to account for terminus retreat. The imagery from 2013/2014 showed minimal retreat of the terminus, so one polygon from the 2013 imagery was digitized and used for both years.

Due to the low 30 m resolution of the Landsat imagery pixels around the edges of the lake may have consisted of both lake and moraine wall. Values from these pixels may not be a true representation of lake temperature. To avoid these pixels the lake polygons that were digitised from the imagery were made slightly smaller than lake boundary. Zonal statistics were run for each of the images using the lake polygon for each respective year.

4.2.1 Lake temperatures from Conductivity Temperature Density Probe

Variations in lake temperature at depth may affect how the locations of subaqueous ice ramps develop. To determine if temperature varied at depth and at different locations in the lake, a series of temperature-depth profiles were collected during the 2015 and 2016 surveys. The temperature-depth profiles were conducted with a Richard Branker Research (RBR) XR620 conductivity-temperature-density (CTD) probe. One temperature-depth profile was collected from the near terminus region in April 2015, with subsequent profiles being collected from the middle of the lake and from near the Murchison river inlet in September 2016 (Figure 22). The temperature-depth profiles at the top of the lake, near the terminus down to the Murchison inlet, show how temperature varies at depth, and how it varies at depth by location. Colder water temperatures at depth near the terminus may result from the proximity to the ice and/or subglacial hydrology. The profiles from the middle and bottom of the lake will identify if the temperature stratification is consistent with the temperature depth profile at the terminus.

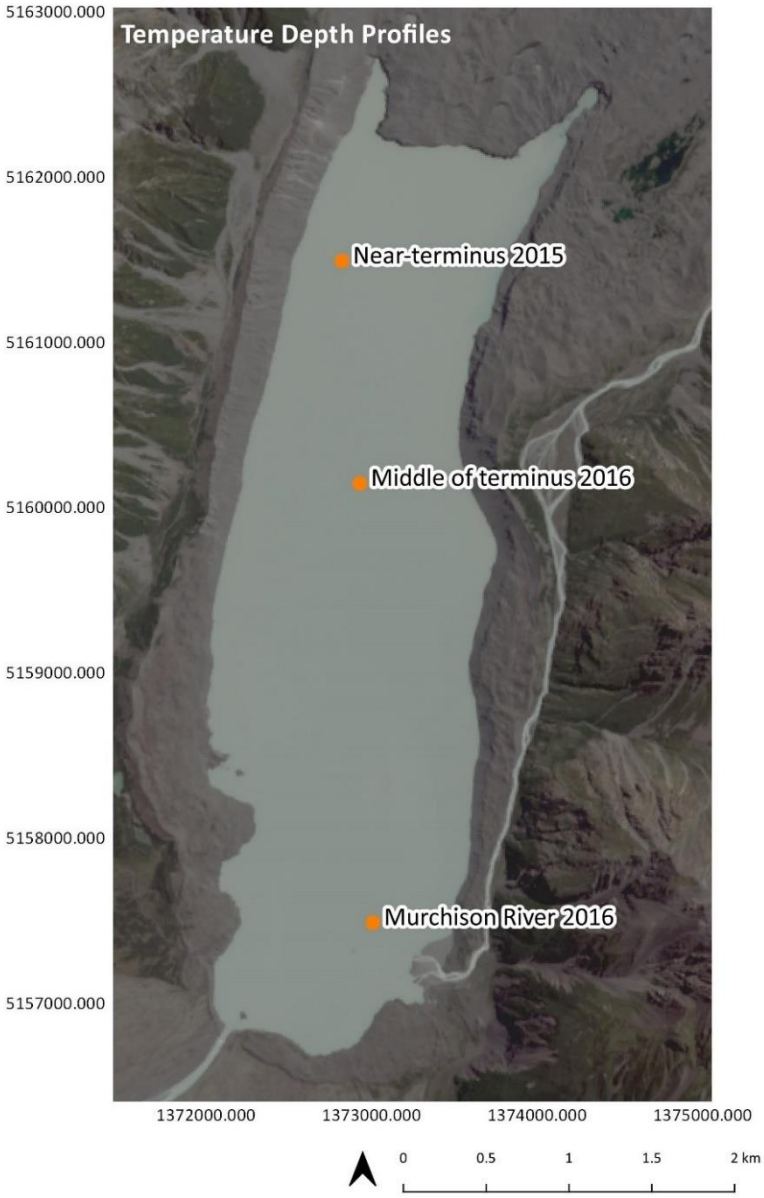

Figure 22: Locations of the temperature depth profiles from the 2015 and 2016 surveys. Each white cross marks the location from which a temperature depth profile was collected.

4.2.2 Identification of Water Seepage Tasman/Haupapa Lake

There is potential for different sources of water such as water plumes and seepages to influence ice melt and/or water circulation based on different water temperatures. In order to determine if lake conditions such as water plumes and seepage have an effect on terminus morphology, the frequency and location of plumes and water seepage were mapped from Sentinel satellite imagery.

During the 2018 survey water was seen entering the lake from the moraine wall. The water seeping through the moraine appeared to have different turbidity to the lake water, identified from the differences in colour in the lake water (Figure 23). Changes in water composition were also identified using B8 from Sentinel satellite imagery.

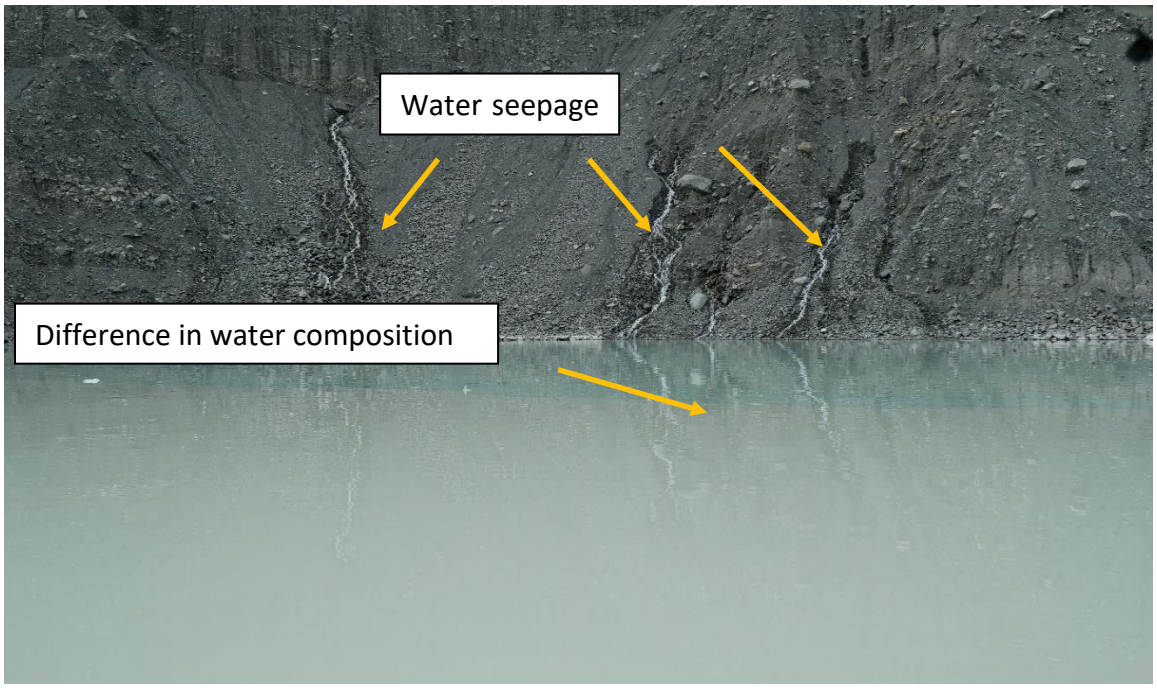

Figure 23: Water seepage entering into Lake Tasman/Haupapa from the moraine wall.

A collection of water plumes was identified in four of the Sentinel-2 images. Water seepage was identified in front of the terminus, from the sides of the moraine wall, and from the Murchison inlet. An outline was drawn around these seepage areas and placed next to the

image of the lake in B8 for comparative purposes. All four images are displayed in sequential order in Chapter 5.

4.2.3 Lake Level Fluctuations

Fluctuating lake levels can increase buoyant forces by increasing tensile stress at the terminus. Lake level fluctuations were looked at in conjunction with rainfall to see if a relationship to calving could be identified. Lake level data was provided by Dr Brian Anderson from Victoria University. The lake level was recorded for every minute, a daily average was calculated. The lake level fluctuation was then plotted against rainfall and calving from 2013 -2018. Lake levels were also plotted with calving and velocity to see if there was a relationship with increased surface velocity, lake levels and calving events.

4.3 Terminus Morphology

4.3.0 Bathymetric Ice ramp surveys at Tasman/Haupapa Glacier

Despite the fact that their existence was inferred in the late 1800s, there have still been only a few bathymetric surveys that have mapped subaqueous ice ramps or ice feet, in either tidewater or freshwater settings. Observations made by Wright, (1892) described subaqueous icebergs rising to the surface, anything up to hundreds of metres away from the terminus. Wright, (1892) proposed that these icebergs were the result of subaqueous ice-foot calving. Similar events were witnessed by Warren et al. (1995), where icebergs were witnessed rising up to the surface ~150 m from the terminus, supporting the existence of an ice foot protracting from the base of the glacier.

The paucity of available ice-ramp data and the infrequency of repeat surveys is in part due to the hazards faced when collecting data from an actively calving terminus, and also to the

difficulties associated with recording the existence of these features and mapping their extent given the technology available at the date of each survey. More recent surveys have been conducted mapping bathymetry and ice features using sensors such as CHIRP sub-bottomed sensors and echo sounders (Dykes et al. 2011;Robertson et al. 2012; Sugiyama, 2016).

Autonomous data collection methods are also an effective means of surveying ice ramp development. Such methods allow for repeat surveys to be conducted with high frequency, allowing researchers to collect data away from an active calving area (Neal et al. 2012). In June 1991 a remotely operated vehicle (ROV) was deployed near the terminus of the Muir Glacier in Alaska, where it observed evidence of an underwater ice foot (Hunter & Powell, 1998). The ROV was unable to directly record the ice ramp with video imaging due to large amounts of suspended sediment, but it was able to obtain close-up images of the grounding line and ice cliff. ROVs are limited in that they must still be tethered to the main boat, and the longer the tether, the more difficult it is to transmit information (Bowen et al. 2014). An ROV's imaging capability is also limited by environmental factors such as highly turbid waters.

Other types of autonomous vehicles such as remotely controlled boats equipped with sensors have proven effective in collecting bathymetry data at the near terminus, and can offer access into remote locations (Neal et al. 2012). A small remote-controlled sailing dingy ~2.3m in length was specifically built for collecting data near the terminus of glaciers, and was tested at Lille Gletscher in Western Greenland. The instrument was fitted with swath bathymetry, terrestrial laser scanning sensors, and real time kinematic (RTK) GPS for improved depth accuracy. The remote-controlled boat surveyed a section of the same area that a larger boat

had surveyed, and found that the data collected was of a similar quality. Initial design limitations included the top speed of the boat, which at 1.3 m/s was at times not capable of maintaining course in the water's currents. This had a knock-on effect on the boat's battery, its life shortened by having to make constant course corrections. As a result, surveying times were limited and field times extended by these limitations and the operators were always running the risk that weather and current conditions could deteriorate to the point where the capabilities of the ROV were exceeded.

At Tasman/Haupapa Glacier, evidence of subaqueous ice ramps have been recorded in several studies (Dykes et al. 2011; Purdie et al. 2016; Robertson et al. 2012). Subaqueous ice ramps were identified through observations and through the use of Compressed High Intensity Radar Pulse (CHIRP) sub bottomed profilers and duel frequency echo sounders attached to a piloted boat, surveys using these methods were conducted in 2008 and 2015 (Dykes et al. 2011; Robertson et al. 2012; Purdie et al. 2016).

Bathymetric surveys of Lake Tasman were collected for April 2013, May 2014, November 2015 (Purdie et al. 2016), October 2016 and April 2018 (this study, Figure 24). The results from these surveys, along with data from previously conducted surveys are presented in Chapter 5.

Following the methods of Purdie et al. (2016), in 2016 and 2018 a remote-controlled boat was used to survey lake depth using a Garmin GPSMAP 7407XSV with a dual-beam. This has an estimated accuracy of ± 5-10 m. To obtain accurate positioning, a Trimble R8 RTK-GNSS

antenna was mounted inside the boat with a horizontal uncertainty of ± 1.24 m (Purdie et al. 2016).

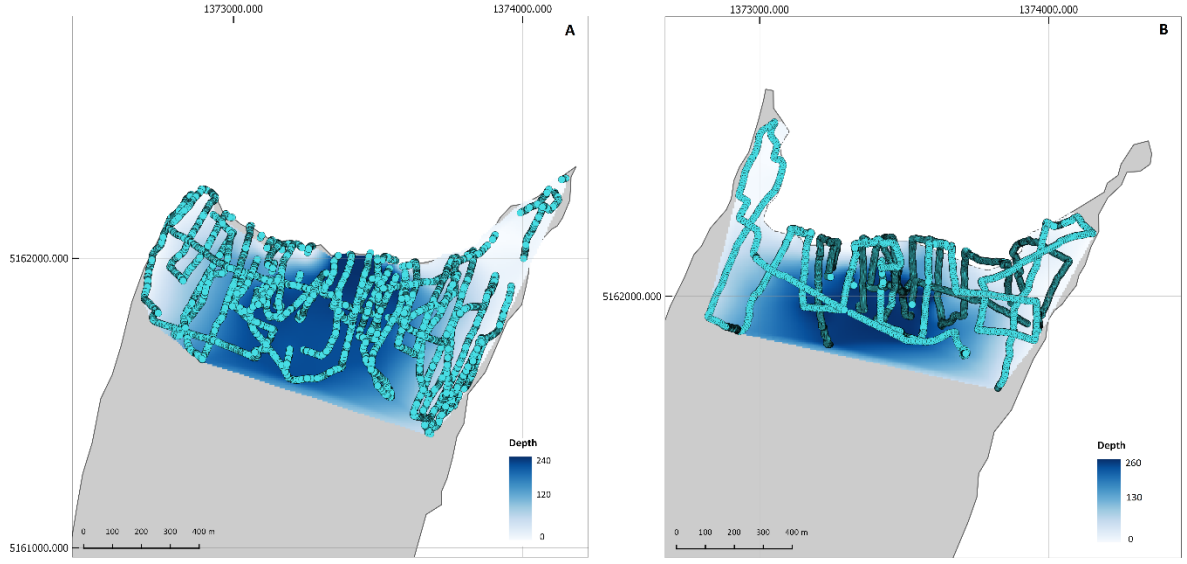

Figure 24: Bathymetry points collected using the Jettec boat from 2016 and 2018, surveys from 2013-2015 can be viewed in Purdie et al (2016).

A network adjustment was conducted in 2013 and subsequent surveys were corrected back to the 2013 lake level to make surveys comparable. All surveys were corrected for variations in sound velocity, turbidity and lake levels based on 2013 values as per Purdie et al. (2016). To ensure consistency between the earlier surveys by Purdie et al. (2016) and the surveys undertaken in 2016 and 2018, the point data collected by the jet boat was corrected for positioning and heave compensation. The data points were then imported into ArcGIS and interpolated using a triangular irregular network (TIN). An Inverse Distance Weighted tool that used a 'nearest neighbour' filter and mean focal statistics was used to produce a raster surface displaying average bathymetric depth. Methods for interpolation were replicated from the study of Purdie et al. (2016) to maintain consistency between surveys and make results from successive surveys comparable. The interpolated point data was then explored for the presence of subaqueous ice ramps using the 3-D viewer in QGIS. Ice ramp locations

were identified and digitized from the interpolated surfaces using the 'Terrain Profile' tool in QGIS 3.6. This tool would draw the elevation profile of the line drawn in front of the terminus and aided in identification of the horizontal extent of the subaqueous ice morphology.

4.3.1 Ice ramp distribution and length change – a comparison of different melt rates

The differences in ice ramp lengths were compared from surveys from 2013 – 2018, to see if they changed in length due to subaqueous melt processes. Assumptions made for this analysis were:

1) The ice ramps had not fully or partially calved in-between surveys, or regrown after partial calving.
2) All ice ramps used to compare length change from the 2018 survey were assumed to be new ice ramps that were not present during the 2016 survey.

Daily melt rates from Rohl, (2006) and Purdie et al. (1999) were used to calculate potential subaqueous and subaerial melt respectively. These melt rates were selected, as they were from surveys conducted at Tasman/Haupapa Glacier in 2001, 2003 and 1995-1996 respectively. The melt rate used from Rohl, (2006) was the only subaqueous ice melt rate used in this analysis. The melt rates from Purdie et al. (1999) were melt rates derived for bare ice melt and debris melt. It is noted that the melt rate may have changed over time as the lake expanded with the onset of rapid calving, which may have become the dominant process over melt rates for subaqueous ice ramp development.

4.3.2 Observations of recent subaqueous calving events from photos and CHIRP images

The photos and sonar images presented in Chapter 5 are used to provide more information

about subaqueous ice morphology. During the 2018 survey a subaqueous calving event took place overnight on the 11 April 2018. High-resolution photos were taken within 8 hours limiting time for erosion to occur, that would significantly change the morphological features of the icebergs. An interpretation of these ice features in relation to the processes acting on the subaqueous ice ramps has been provided in Chapter 5 in conjunction with CHIRP images.

Sonar homeport data was collected during the 2018 survey. The sonar recordings were loaded into Garmin Homeport 2.3.1, which is a trip planning software for marine devices. The sonar video recordings were replayed in Homeport, and screenshots of a selection of ramps were chosen from survey lines when the Jettec boat was heading towards the terminus. The sonar recordings generally produced the clearest sonar recordings of the ramps heading towards the terminus rather than recordings heading away from the terminus. This is thought to be due to the angles of the sonar which were facing away from the ice ramps heading back out from the terminus.

4.3.3 Estimating the Floatation Thickness of the 2016 Terminus using SfM

In order to assess the buoyancy of the terminus an estimate of the height of the terminus was needed. Structure from motion (SfM) was used to build a model of the terminus from 69 overlapping photos from the 2016 survey. From this model 17 height estimates were extracted to determine height above buoyancy (H_o).

During the 2016 survey, overlapping photos were recorded using the same methods outlined in Purdie et al. (2016) for the photos collected in 2013. There were 69 overlapping photos with their corresponding GNSS position, all photos had an overlap of ~80%. Photos were

recorded from the survey boat ~700m from the terminus at a slow speed. Structure from motion (SfM) was then used to create a 3-D representation of the terminus.

SfM generates a 3-D model from point data using a range of algorithms Javernick et al. (2014). Agisoft Metashape 1.5.2 was used to process the terminus model which generates models using a series of black box algorithms Javernick et al. (2014). These algorithms calculate the location and orientation of the camera from differential positions of numerous matched features (Carrivick et al. 2016).

Common points were identified from the 69 photos, the initial sparse point cloud from the 69 photos produced 64,879 tie points out of a possible 81,192 with a RMS reprojection error of 0.14 (0.74 pix) and a maximum reprojection error of 0.42 (26.49 pix). Estimates of the height of the terminus were taken using the measure tool in Agisoft Metashape 1.5.2 at 17 locations across the terminus using the dense point cloud. Height estimates have an error of ± 5 m and were based on the size of debris and boulders on the glacier surface.

Chapter 5 - Results

5.0 Velocity

5.0.0 Annual surface velocity

The annual surface velocity for the length of the Tasman Glacier over a one-year period from the 29/10/2016 – 29/10/2017. (Figure 25) shows greater surface velocity in the area of the Upper Tasman at the Rudolph confluence and at the Hochstetter confluence. The mean surface velocity at the Upper Tasman was 0.16 md^{-1} ± 0.04 md^{-1}, the surface velocity then slows considerably from the Lower Tasman (0.07 md^{-1} ± 0.01) whereby the ice flux becomes dominated by the input from the Hochstetter confluence. The Hochstetter confluence shows an increase in surface velocity as it enters the main trunk of the glacier. The surface velocity decreases down glacier with surface velocity slowing to 0.19 md^{-1} ± 0.01 md^{-1} at the Ball Glacier Confluence and 0.11 md^{-1} ± 0.01 md^{-1} at the Upper near terminus. A small increase in velocity is seen at the Near-terminus. The mean velocity of all sites are listed in Table 5.

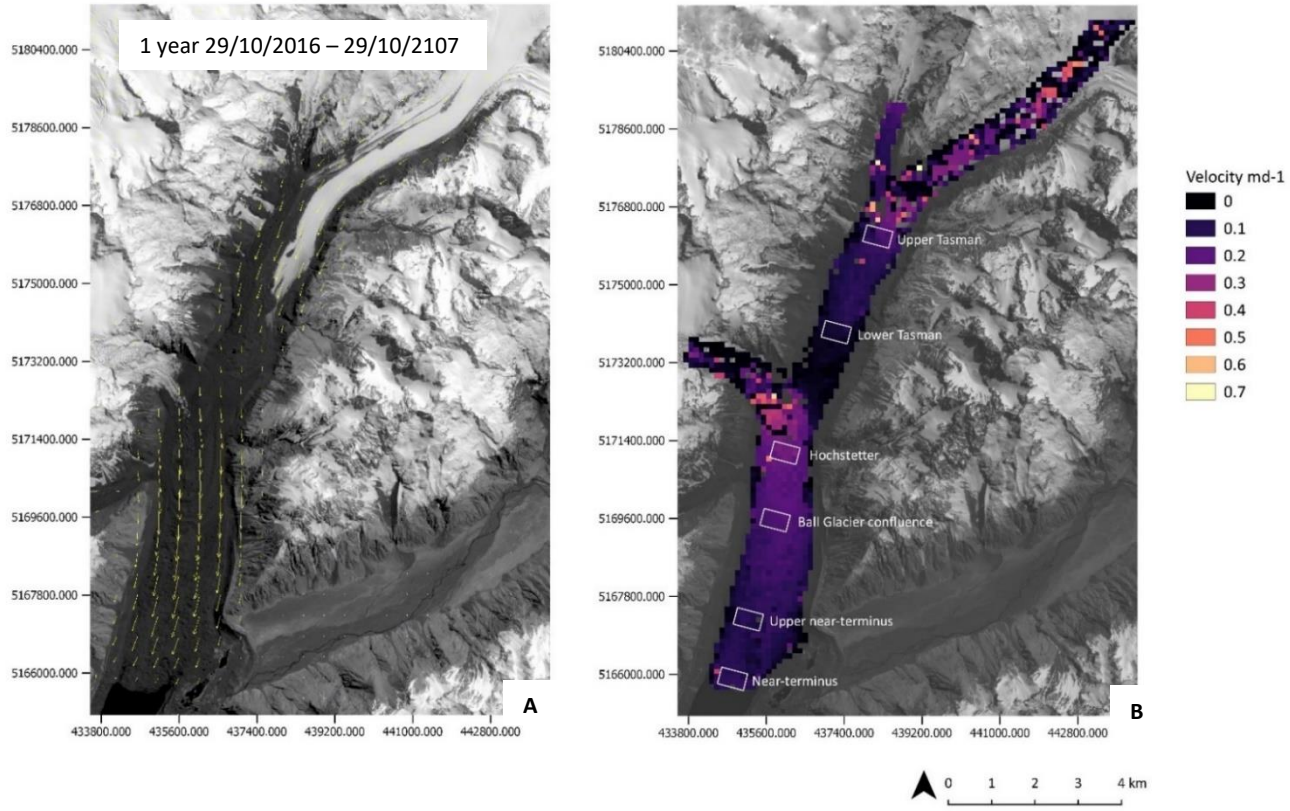

Figure 25: Annual average surface velocity from 29/10/2016 – 29/10/2017, the white rectangles were used to extract the mean surface velocity for each site.

Table 5: Mean annual surface velocity and standard deviation. Degree days and total rainfall have been calculated for the one year interval between 29/10/206 and 29/10/2019.

	Image dates	29/10/2016 - 29/10/2017
	Time interval	365
	Degree day	2485.47
Velocity (md^{-1})	**Lower near-terminus mean**	0.13
	Lower near-terminus SD	0.01
	Upper near-terminus mean	0.11
	Upper near-terminus SD	0.01
	Ball Glacier confluence mean	0.19
	Ball Glacier confluence SD	0.01
	Hochstetter mean	0.25
	Hochstetter SD	0.02
	Lower Tasman mean	0.07
	Lower Tasman SD	0.01
	Upper Tasman mean	0.16
	Upper Tasman SD	0.04
	Total rainfall (mm)	3894

5.0.1 Seasonal surface velocity

Seasonal surface velocity was determined for the region of the glacier below the Hochstetter confluence for 35 surface velocity images, four velocity surfaces are presented in this section to show how surface velocity varies seasonally (Figure 26, 23, 24 and 25), the remaining 31 velocity surfaces are displayed in appendix C.

During a 10-day time interval in summer (Figure 26) velocity was highest up glacier near the Ball glacier confluence. The centre of the glacier shows higher velocities than the margins of the glacier and an increase in velocity of 0.9 md^{-1} is present at the terminus. During a 30 day time interval in autumn (Figure 27) velocity was highest up glacier near the Ball glacier confluence, the centre of the glacier had slowed to 0.1 – 0.3 md^{-1} around the Upper near-terminus, but there was a small increase in velocity around the Near-terminus of 0.6 md^{-1}. For a 20 day time interval during winter (Figure 28) velocity is highest up glacier near the Ball glacier confluence, the centre of the glacier has slowed to 0.1 – 0.2 md^{-1} around the Upper near-terminus and there is a small increase in velocity around the Near-terminus between 0.3- 0.4 md^{-1}. Over a 10-day time interval during the middle of spring (Figure 29) different sections of the glacier show velocity starting to increase. These sections range from 0.4 to 0.6 md^{-1}. These areas are interspersed with areas with a velocity of 0.1 – 0.3 md^{-1}.

All 35 velocity measurements were used to plot mean velocity across seasons ranging from 2016 - 2018 from the Ball Glacier confluence, Upper near-terminus and the Near-terminus regions shown in Figure 30. The Ball Glacier confluence generally has the highest mean velocity compared with the Upper near-terminus and Near-terminus. The Upper near-

terminus is generally the slowest section of the glacier with the Near-terminus transect overall having a higher mean velocity than that of the Upper near-terminus.

The velocity trends from each site follows the same velocity increases and decreases but at different magnitudes, examples of this can be seen during the autumn seasons of 2016 and 2017 and in the summers of 2017 and 2018 (Figure 30). The transition between winter and spring in 2016 shows an acceleration at all three sites. Over a 20-day period from 21/07/2016 – 10/08/16 the surface velocity was 0.17 md^{-1} ± 0.07 md^{-1} at the Near-terminus which then increased to 0.27 md^{-1} ± 0.04 md^{-1} over the next 20-day period from 10/08/2016 – 30/08/2016. Surface velocity tends to show an increase in spring and summer and decreases in autumn and winter, an exception to this is the Ball Glacier confluence winter of 2017 which has a surface velocity of 0.34 md^{-1} ± 0.29 md^{-1} compared with the Near-terminus and Upper near-terminus which were 0.14 md^{-1} ± 0.05 md^{-1} and 0.18 md^{-1} ± 0.18 md^{-1} respectively. Later in the 2017 winter season the Ball Glacier confluence and Near-terminus sites saw large increase in velocity compared to the Upper near-terminus over a 10-day period, the surface velocity decreases again over a 40-day period to similar winter velocities found in 2016. Over this 40-day period from 06/07/2017 – 16/07/2017 the Upper near-terminus is significantly slower than that of the Ball Glacier confluence and Near-terminus region with a velocity of 0.06 md^{-1} ± 0.03 md^{-1}.

The 35 velocity surfaces had different acquisition dates of the satellite data which influences the time periods that surface velocity can be calculated for. The acquisition dates of the satellite imagery had time intervals ranging from 10, 20, 30, 40 and 50 days. No statistically

significant correlation was found between surface velocity and mean rainfall for any time interval (Table 6).

Table 6: correlation, R2 and p-values for the relationship between velocity and mean rainfall. No statistically significant relationship was found.

Time interval (days)	**10**	**20**	**30**	**40**	**50**
Correlation	0.61	0.12	0.38	0.79	0.88
R^2	0.37	0.01	0.14	0.62	0.78
P-value	0.15	0.80	0.46	0.21	0.31
Sample size	7	7	6	4	3

The relationship between velocity and rainfall over a 50-day time interval in Figure 31 had the strongest R^2 values of 0.78 and a p-value of 0.31, the 50-day time interval had the smallest sample size (n=3). The 10, 20 and 30-day time intervals has the smallest R2 values from 0.37, 0.01 and 0.14. These time intervals have the largest sample sizes ranging from 6-7.

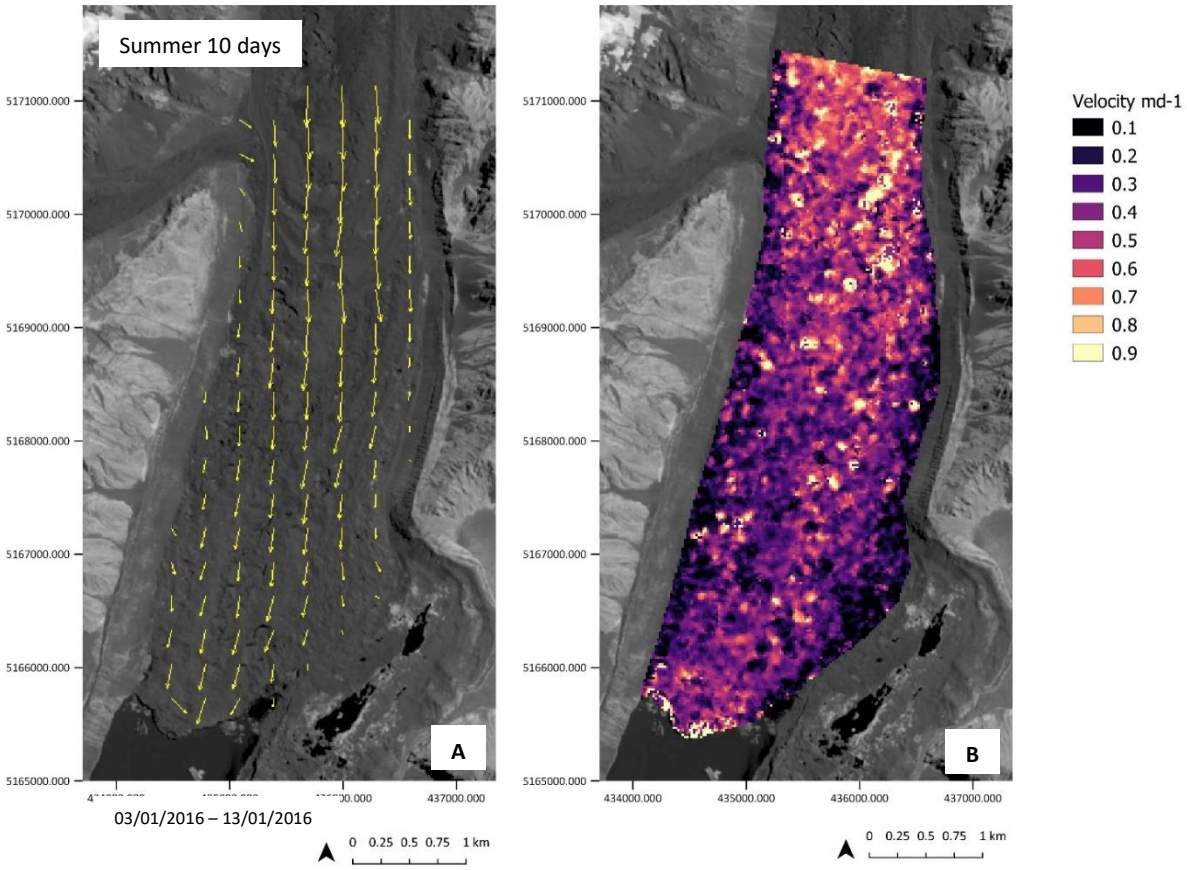

Figure 26: Surface velocity during summer over a 10-day time interval from 03/01/2016 – 13/01/2016, A. shows the vector arrows showing the direction of displacement. B. shows the surface velocity in md^{-1}.

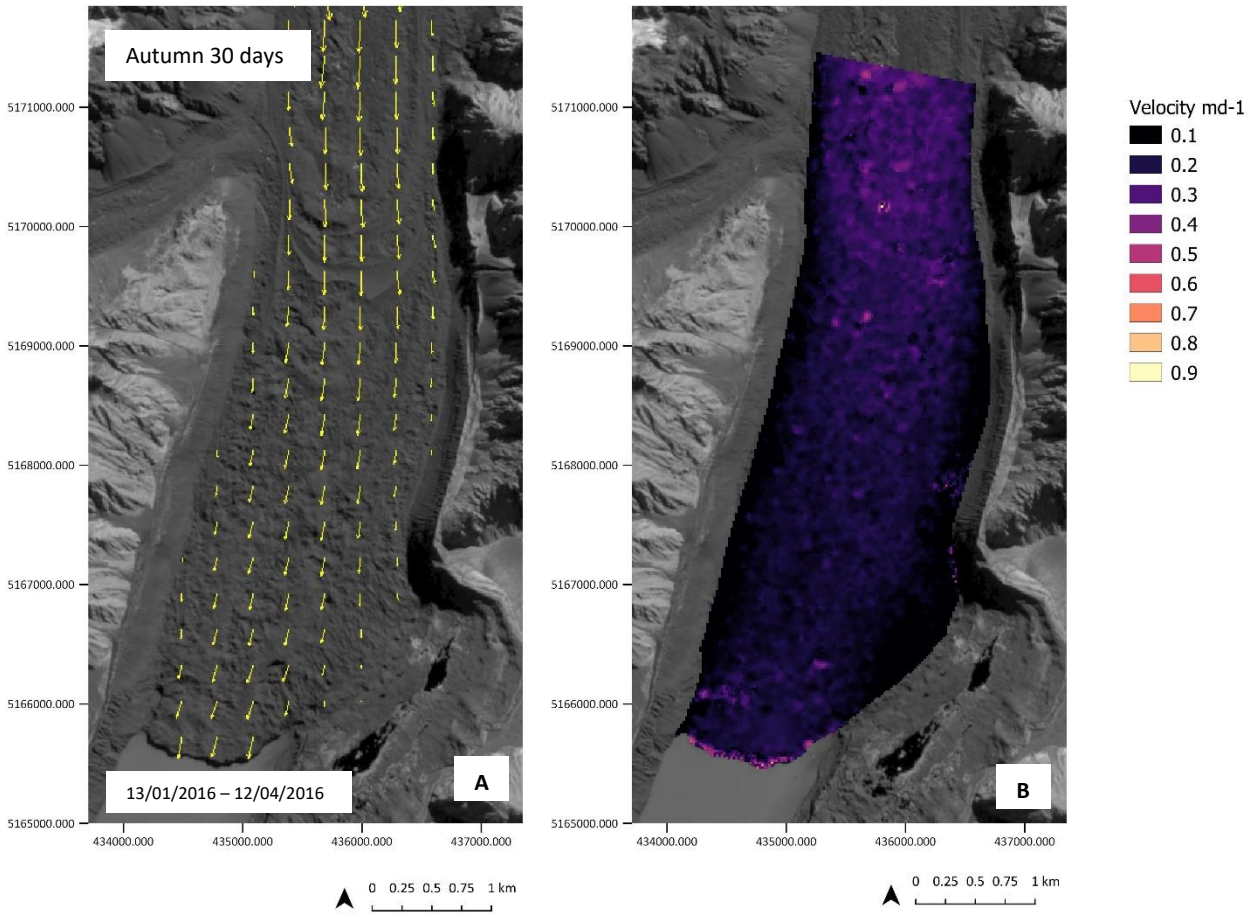

Figure 27: Surface velocity during autumn. Surface velocity is over a 30-day period from 13/03/2016 – 12/04/2016, A. shows the vector arrows showing the direction of displacement. B. shows the surface velocity in md^{-1}.

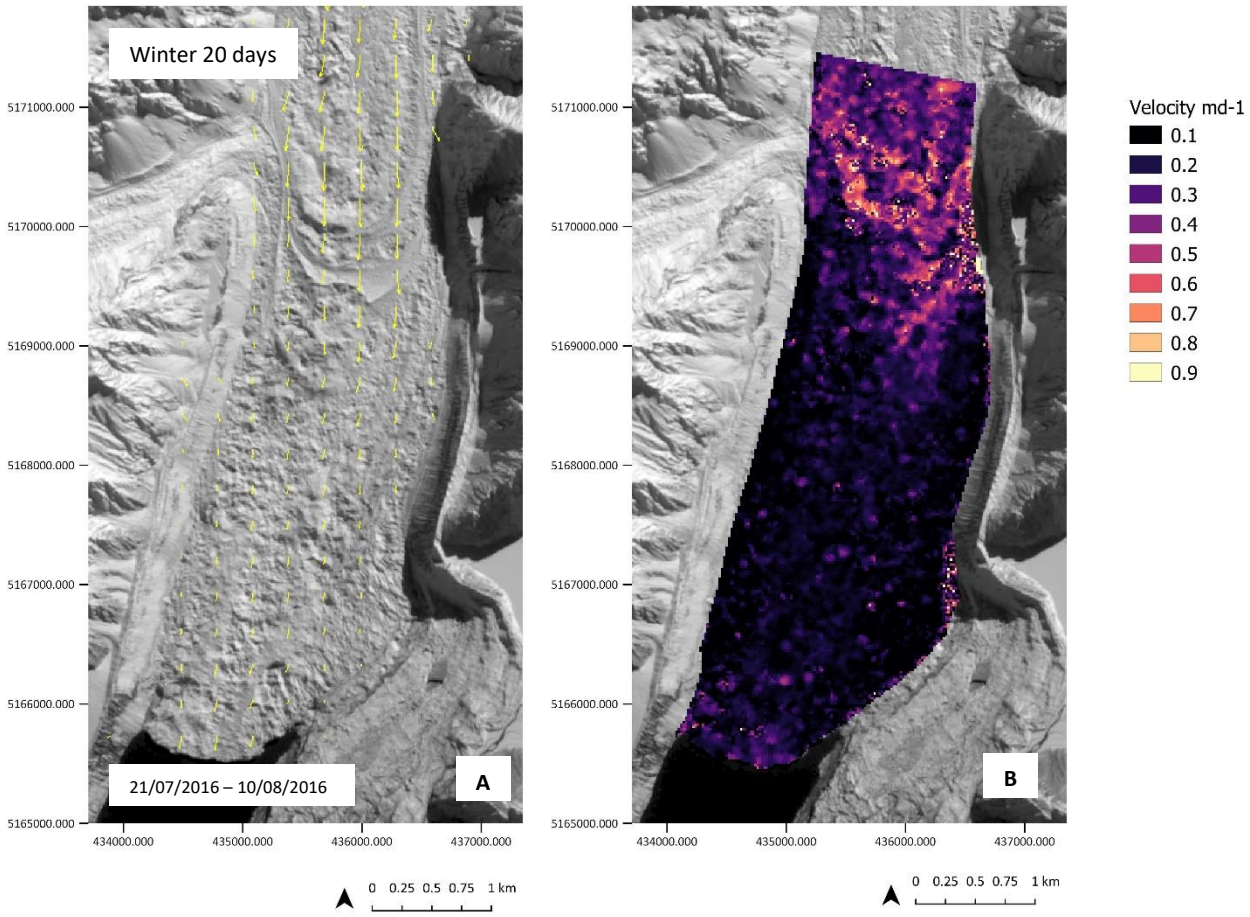

Figure 28: Surface velocity during the winter season, surface velocity is over a 20-day period from 21/07/2016 – 10/08/2016. A. shows the vector arrows showing the direction of displacement. B. shows the surface velocity in md^{-1}.

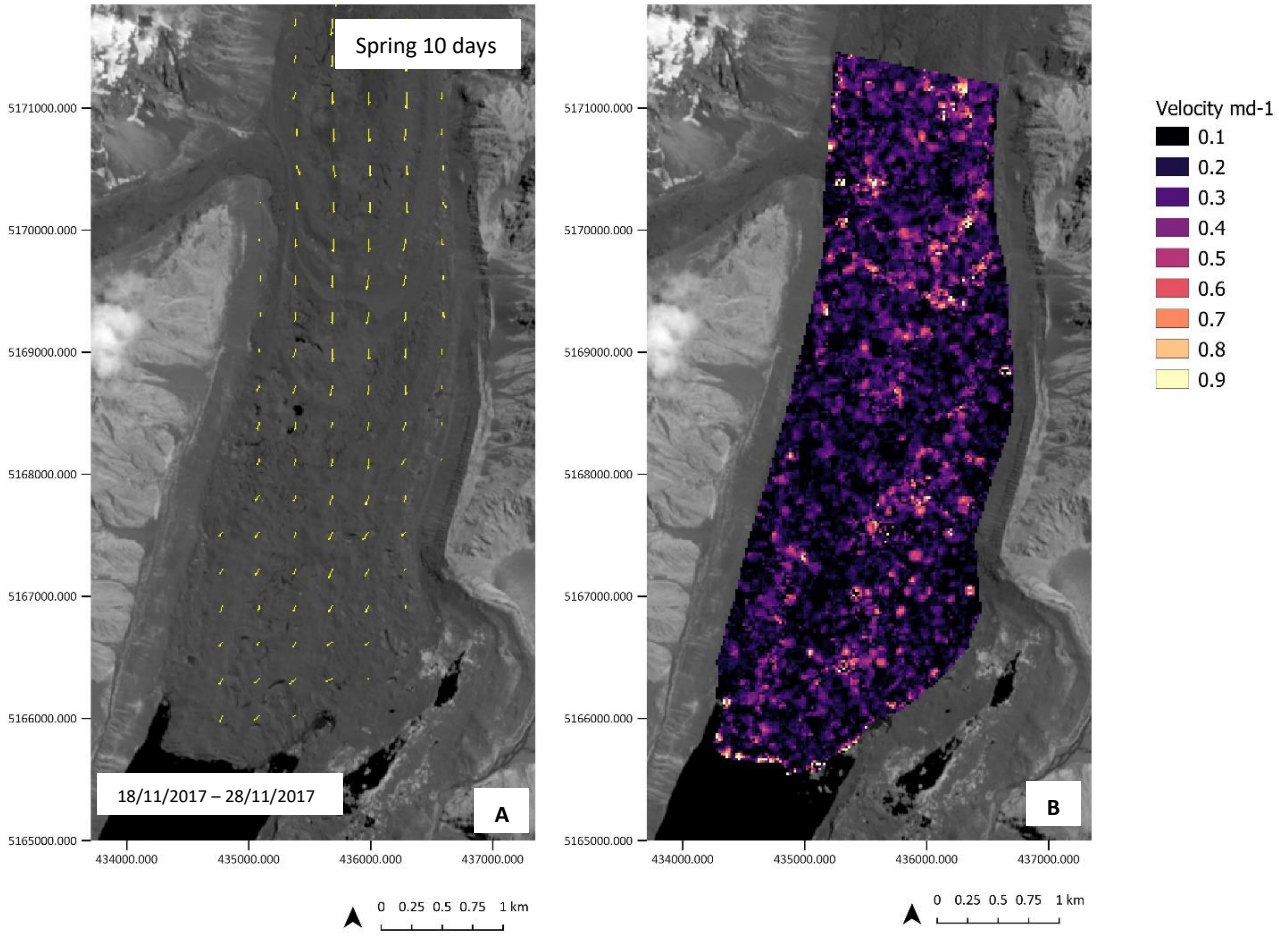

Figure 29: Surface velocity during spring. Surface velocity is over a 10-day interval from 18/11/2017-28/11/2017, A. shows the vector arrows showing the direction of displacement. B. shows the surface velocity in md^{-1}.

Table 7: The acquisition dates from the satellite images that were used to measure surface velocity are listed below along with mean and standard deviation of velocity (md^{-1}) for that time interval. The degree day and total rainfall was calculated for the total time interval of the image dates.

Image dates		Time interval (days)	Degree day	Velocity (md^{-1})						Total rainfall (mm)
				Near terminus mean	Near terminus SD	Upper-near terminus mean	Upper-near terminus SD	Ball Glacier confluence mean	Ball Glacier confluence SD	
24/12/2015	3/01/2016	10	148.57	0.14	0.11	0.16	0.17	0.20	0.18	4.60
24/12/2015	2/02/2016	40	535.27	0.39	0.11	0.35	0.16	0.47	0.23	383.60
3/01/2016	13/01/2016	10	134.47	0.39	0.04	0.36	0.07	0.37	0.11	96.20
3/01/2016	2/02/2016	30	394.97	0.23	0.04	0.20	0.04	0.23	0.06	381.80
13/01/2016	2/02/2016	20	272.17	0.16	0.04	0.16	0.07	0.22	0.05	286.00
2/02/2016	13/03/2016	40	594.87	0.18	0.03	0.14	0.03	0.20	0.05	412.20
13/03/2016	12/04/2016	30	326.57	0.19	0.03	0.17	0.02	0.23	0.02	263.80
12/04/2016	2/05/2016	20	194.07	0.16	0.04	0.12	0.03	0.18	0.05	156.40
2/05/2016	1/06/2016	30	161.65	0.22	0.04	0.22	0.03	0.30	0.06	803.80
1/06/2016	21/07/2016	50	145.05	0.10	0.02	0.10	0.01	0.13	0.05	678.40
21/07/2016	10/08/2016	20	22.07	0.17	0.07	0.14	0.05	0.25	0.11	231.00
10/08/2016	30/08/2016	20	190.60	0.27	0.04	0.25	0.05	0.28	0.07	45.60
30/08/2016	29/10/2016	60	394.50	0.12	0.03	0.11	0.03	0.15	0.03	620.20
29/10/2016	8/12/2016	40	338.97	0.12	0.04	0.13	0.05	0.19	0.06	602.40

8/12/2016	27/01/2017	50	523.46	0.18	0.04	0.14	0.04	0.26	0.04	933.80
27/01/2017	26/02/2017	30	387.24	0.15	0.03	0.13	0.04	0.20	0.04	373.20
26/02/2017	18/03/2017	20	241.47	0.14	0.03	0.12	0.03	0.16	0.05	16.60
18/03/2017	28/03/2017	10	123.70	0.13	0.05	0.12	0.05	0.18	0.08	36.20
28/03/2017	17/05/2017	50	376.75	0.16	0.03	0.14	0.02	0.18	0.02	364.00
17/05/2017	27/05/2017	10	29.98	0.14	0.05	0.18	0.15	0.34	0.24	35.60
27/05/2017	6/06/2017	10	18.44	0.14	0.05	0.18	0.15	0.34	0.24	10.40
6/06/2017	6/07/2017	30	54.07	0.15	0.02	0.17	0.07	0.18	0.07	272.40
6/07/2017	16/07/2017	10	0.43	0.41	0.29	0.18	0.08	0.38	0.10	30.60
6/07/2017	15/08/2017	40	56.30	0.14	0.08	0.09	0.02	0.15	0.08	539.20
16/07/2017	15/08/2017	30	55.87	0.14	0.08	0.09	0.02	0.15	0.03	508.80
15/08/2017	4/10/2017	50	238.42	0.18	0.06	0.15	0.04	0.19	0.03	664.20
4/10/2017	29/10/2017	25	202.24	0.13	0.04	0.12	0.04	0.18	0.05	99.00
29/10/2017	13/11/2017	15	146.62	0.14	0.07	0.15	0.09	0.21	0.08	196.80
29/10/2017	18/11/2017	20	202.78	0.43	0.27	0.41	0.26	0.42	0.30	202.20
13/11/2017	18/11/2017	5	65.71	0.15	0.05	0.14	0.06	0.21	0.07	0.00
18/11/2017	28/11/2017	10	159.01	0.20	0.11	0.18	0.11	0.25	0.14	5.40
18/11/2017	13/12/2017	25	388.94	0.12	0.05	0.11	0.06	0.17	0.10	104.60
28/11/2017	13/12/2017	15	245.78	0.19	0.13	0.17	0.11	0.26	0.13	99.20
13/12/2017	22/01/2018	40	579.97	0.27	0.07	0.24	0.08	0.35	0.08	212.00
22/01/2018	21/02/2018	30	442.56	0.19	0.06	0.17	0.06	0.26	0.09	614.40

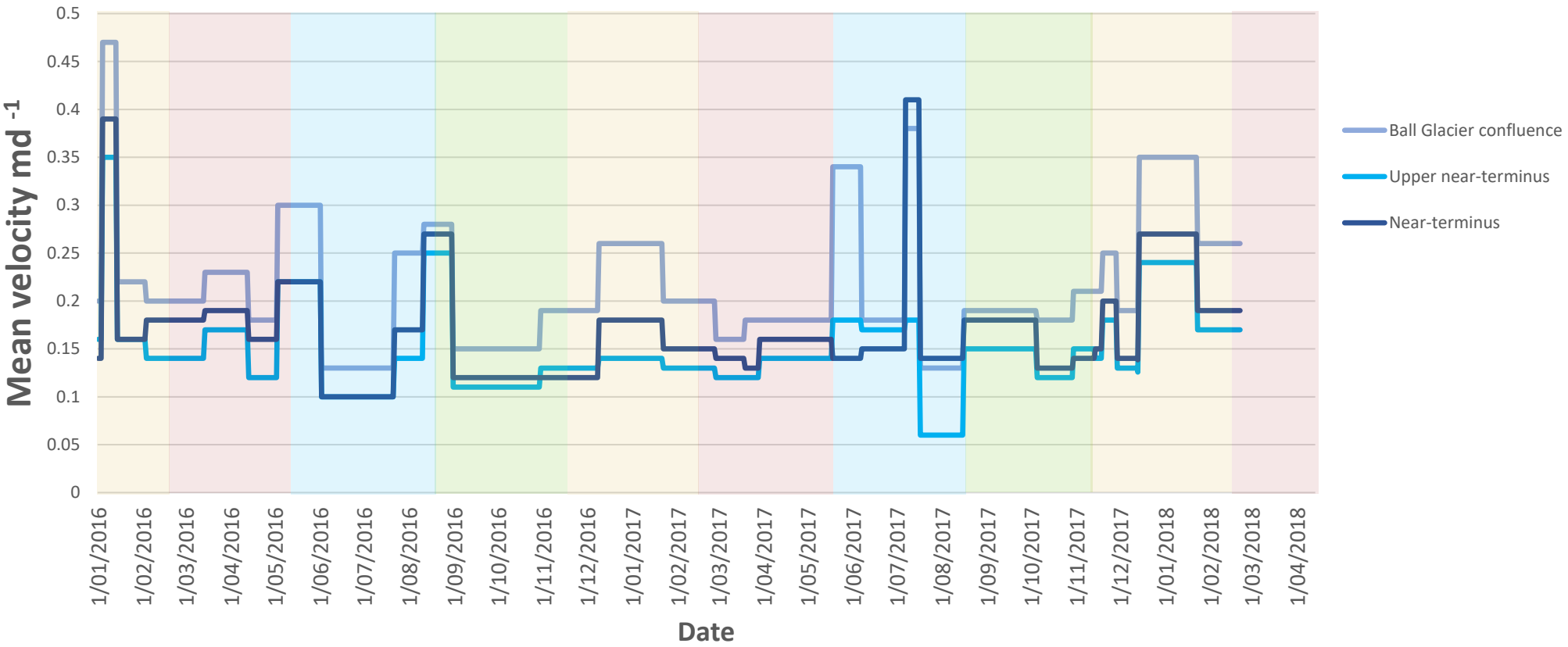

Figure 30: Mean seasonal variation in surface velocity at the Near-terminus (dark blue), Upper near-terminus (blue) and the Ball Glacier confluence (light blue). Summer is indicated by yellow, autumn by red, winter by blue and spring by green. The horizontal line indicates the time period in days for which the velocity measure was recorded.

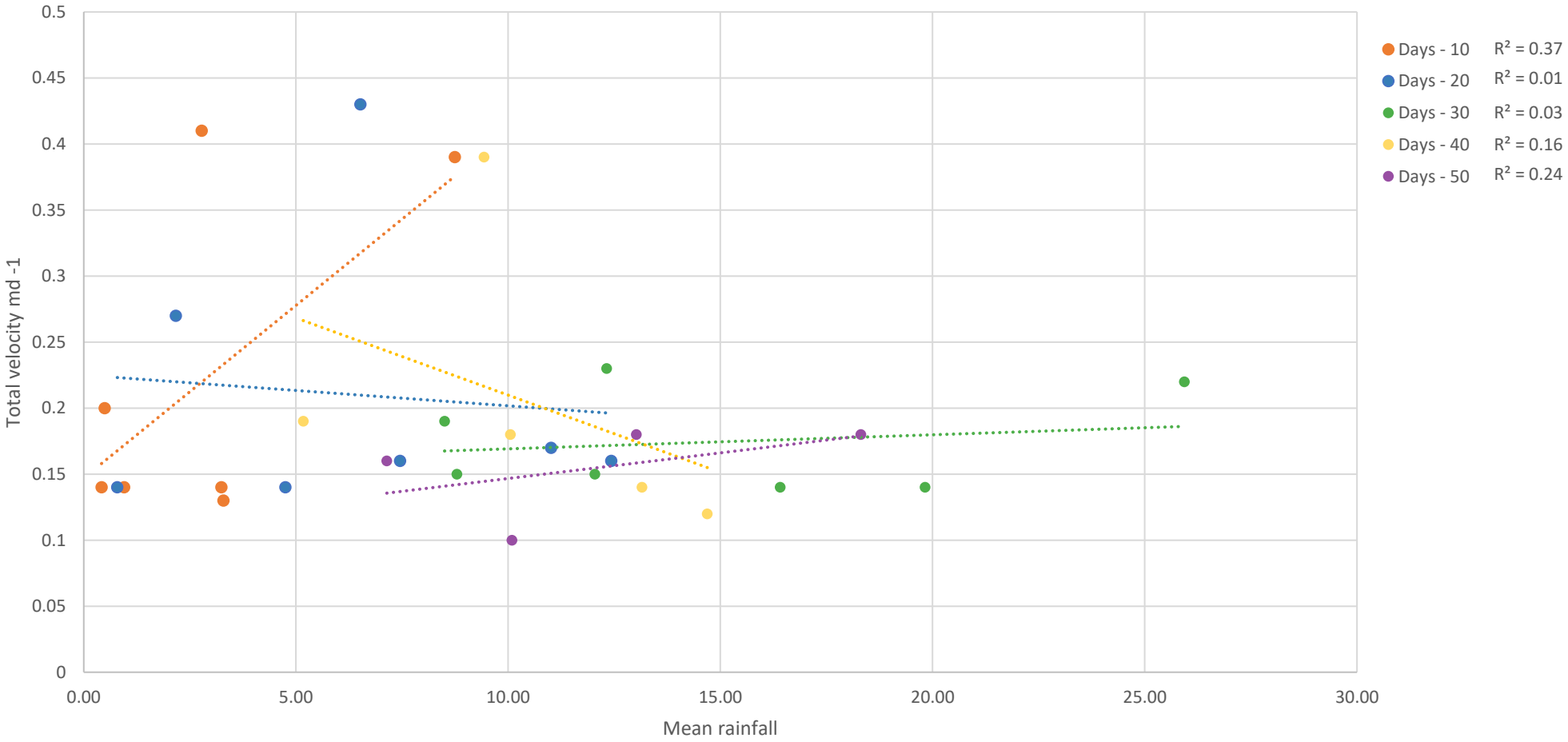

Figure 31:The relationship between total surface velocity over 10, 20, 30, 40 and 50-day intervals with mean rainfall. The dotted lines show the linear relationship between the variables.

5.0.2 Spatial and temporal variation in surface velocity

To explore how surface velocity varies spatially, velocity was determined along six longitudinal transects (Figure 32). The velocity of each transect, for each individual velocity surface was plotted against the mean of all 36 velocity values for that transect. The length of the transects was adjusted to account for terminus retreat. Two transects from the 06/07/2017 – 16/07/2017 over a 10-day period are displayed in Figure 33, all other transects for all 35 velocity surfaces can be viewed in appendix A and B.

Surface velocity was found to vary down the length and across the width of the glacier. The surface velocity was plotted with the mean velocity for each transect to identify areas of the glacier that varied from the mean surface velocity. Transect 1 in Figure 33 shows an acceleration of velocity reaching speeds of 1.00 md^{-1} and propagating 1.5 km up from the terminus (blue line). This acceleration exceeded the mean velocity (orange line) for this section of the transect, which had a surface velocity of 0.53 md^{-1} at the terminus and a surface velocity between 0.16 md^{-1} and 0.33 md^{-1} from 0.2 – 1.5 km up glacier. There was an area of significant slow velocity between 1.5-2.8 km up glacier when compared with the surface velocity up glacier of 2.8 km and down glacier of 1.5 km.

A similar pattern is seen in transect 4 in Figure 33 with the velocity exceeding the mean velocity which propagates 1.5 km up glacier. The mean velocity of the terminus was 0.81 md^{-1} and mean velocity 0.2-1.5 km up glacier ranged between 0.14-0.24 md^{-1}. The velocity 1.5 km up glacier reached speeds of 1.5 md^{-1}. There was an area that showed significant slow velocity 1.5-2.0 km. This area of slow velocity is 1.3 km smaller than that of transect 1 on the outer

margin. Velocity for this area ranged between 0.1 and 0.3 md^{-1}.

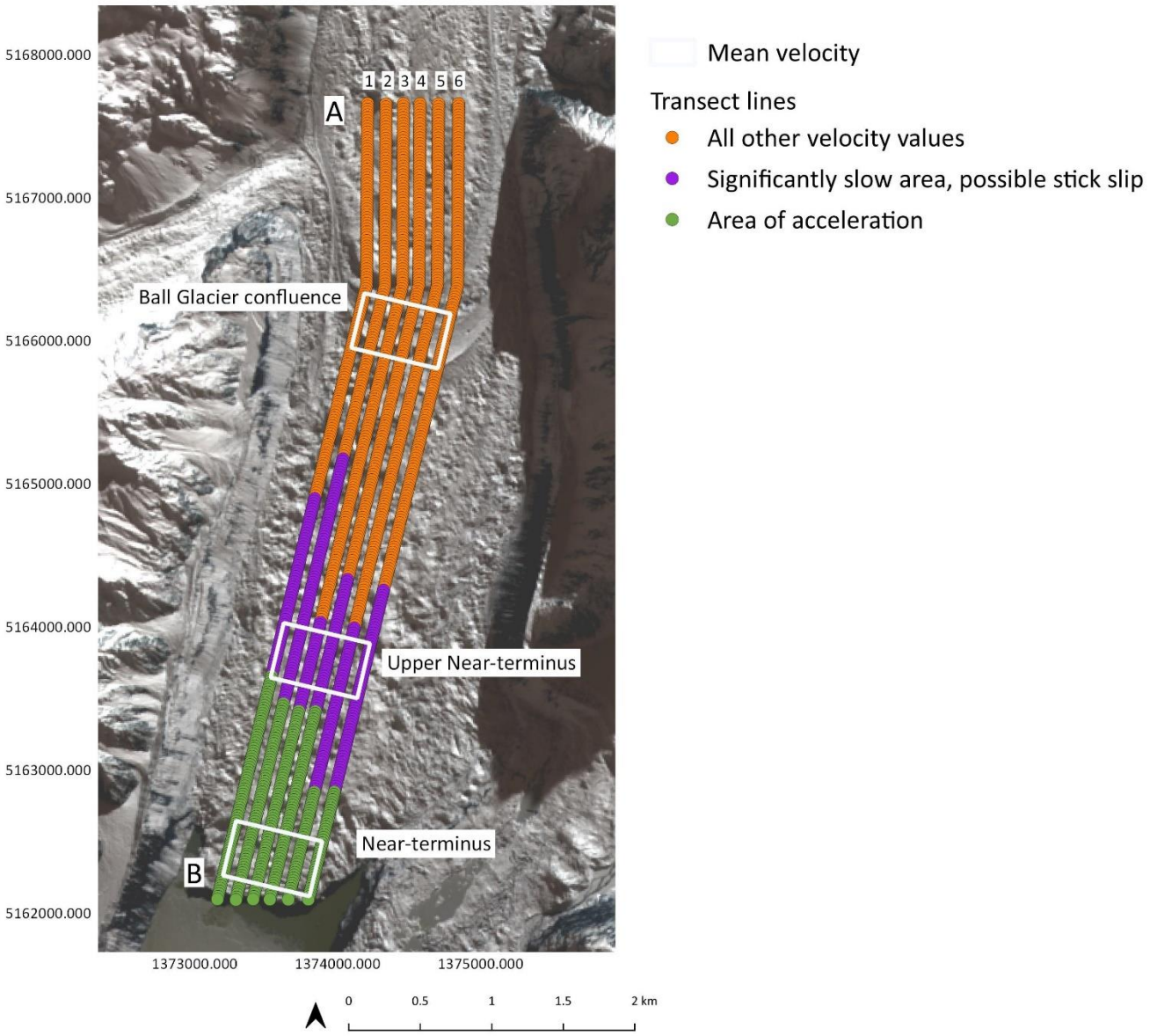

Figure 32: Longitudinal velocity variations were extracted for concentrated regions using the rectangular polygons with the white outline. Longitudinal velocity variations were also extracted along 6 profiles. All surface velocity profiles presented run from A, near the Ball Glacier confluence down to the terminus at B. Velocity profiles from 06/07/2017 – 18/11/2017 showed areas of acceleration at the near terminus (green points), significant slowdown/possible stick slip (purple points) and orange points show all other velocity values

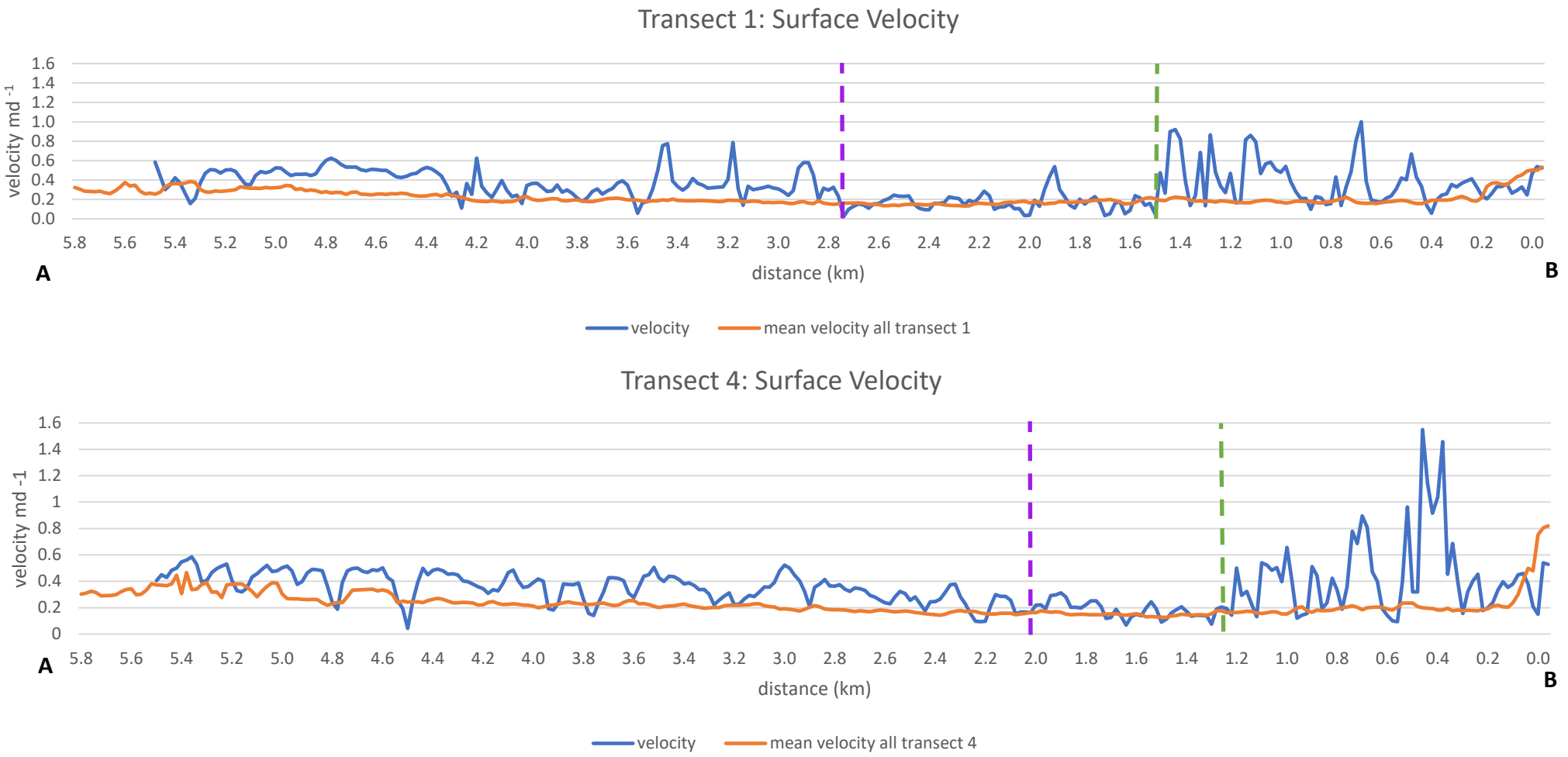

Figure 33: Longitudinal velocity profiles from 06/07/2017 – 16/07/2017 (time period of 10 days) The orange line indicates the surface velocity values extracted from all surface velocity images. The blue line is the surface velocity values extracted from each profile. Profiles run from A near the Ball Glacier confluence down to B at the terminus. The green dotted line shows the extent of the propagation of acceleration up from the terminus. The extent of the area with significantly slow velocity is shown be the purple dotted line.

5.1 Calving

5.1.0 Calving, rainfall, lake level and velocity

Calving events were identified in a series of time lapse photos of the terminus at Tasman/Haupapa Glacier from 20/07/2013 to 01/04/2018. A calving event was defined as any ice that fell off the terminus, as a result of this definition there were a lot of frequent but low magnitude ice calving events. Calving events are shown by the coloured diamonds in Figure 34 the colour of the diamond reflects the year the calving event took place, the grey bars reflect the total rainfall per day. The majority of calving events were found to take place during spring and summer. In the winters of 2014, 2016 and 2017 there were little to no calving events, the winter of 2015 recorded calving events, but they were very small in magnitude. No statistically significant relationship between calving a rainfall was found with an R^2 value of 0.0001 and a p-value of 0.60.

During summer in 2016 there is an increase in velocity to 0.39 md^{-1} ± 0.04 md^{-1} at the near terminus from 03/01/2016 – 13/01/2016 with a total rainfall amount of 96.2 mm (Figure 35). At the end of this 10-day period there was a large calving event. The lake level on the day of the large calving event increased from 717.84 m ± 0.02 m on the 21/01/2016 to 719.93 m ± 0.10 m by the 26/01/2016. During a 40-day period from 02/02/2016 – 13/03/2016 there was another large calving event on the 18/02/2016, which happened the day after a large rainfall event of 175.8 mm. Over this 40-day period there was not a sudden increase in velocity specifically related to the large rain event, velocity at the near terminus was 0.18 md^{-1} ± 0.03 md^{-1}. The lake level increased prior to this calving event from 717.53 m ± 0.01 m on the 14/02/2016 to 719.93 m ± 0.22 m the day before the major calving event on the 18/02/2016

when lake levels decreased slightly to 718.95 m ± 0.53 m.

During the winter months in 2016 the frequency of days with precipitation increased, over a 30-day period from 02/05/2016 – 01/06/2016 there was 803.8 mm of precipitation and velocity at the near terminus was 0.22 md^{-1} ± 0.04 md^{-1}. This decreased to 0.10 md^{-1} ± 0.02 md^{-1} over a 50-day time period that recorded 678.4 mm of precipitation. There was another large calving event towards the end of the year on the 01/11/2016. The calving event took place during a 60-day time interval with a mean velocity at the Near-terminus at 0.12 md^{-1} ± 0.03 md^{-1} and 620.2 mm total amount of precipitation was recorded.

The rainfall, calving events and mean velocity for 2017/2018 (Figure 37) shows a sudden increase in velocity at the near terminus over a 10-day time interval 06/07/2017 – 16/07/2017, total rainfall for this period was 30.6 mm with a velocity at the near-terminus of 0.41 md^{-1} ± 0.29 md^{-1}. In the summer of 2017, there was another large calving event recorded on the 28/12/2017, velocity during this 15-day time interval was 0.19 md^{-1} ± 0.13 md^{-1} with 99.2 mm of rain. After this large calving event a higher velocity was recorded over 40-day time interval at 0.27 md^{-1} ± 0.07 md^{-1} and 212.0 mm of rain was recorded. Lake levels prior to the large calving event on the 28/12/2017, were 717.05 m ± 0.04 m on the 13/11/2017, lake levels increased to 717.60 ± 0.02 m by the 29/11/2017, with a total rainfall over this period of 5.4 mm.

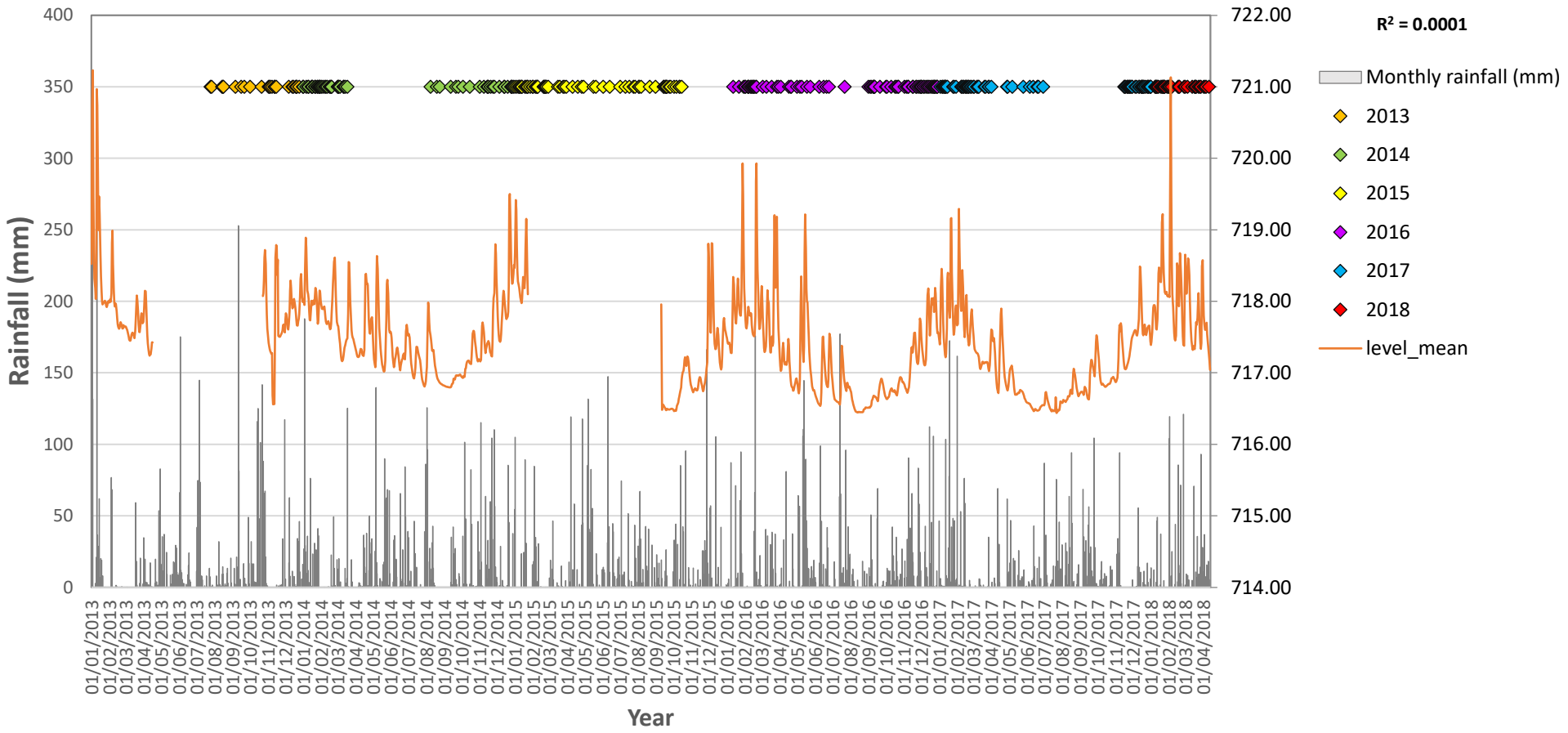

Figure 34: Comparison of rainfall with calving from 2013 - 2018. Calving events and lake level time-lapse photos and data were supplied by Dr Brian Anderson. Calving events are shown by coloured diamonds, each colour is specific to a year. Orange diamonds show calving events from 2013, green diamonds from 2014, yellow from 2015, purple from 2016, blue from 2017 and red diamonds for calving events in 2018. The orange line is the lake level between 2013-2018. Gaps in the line indicate when no lake level data was collected for that period.

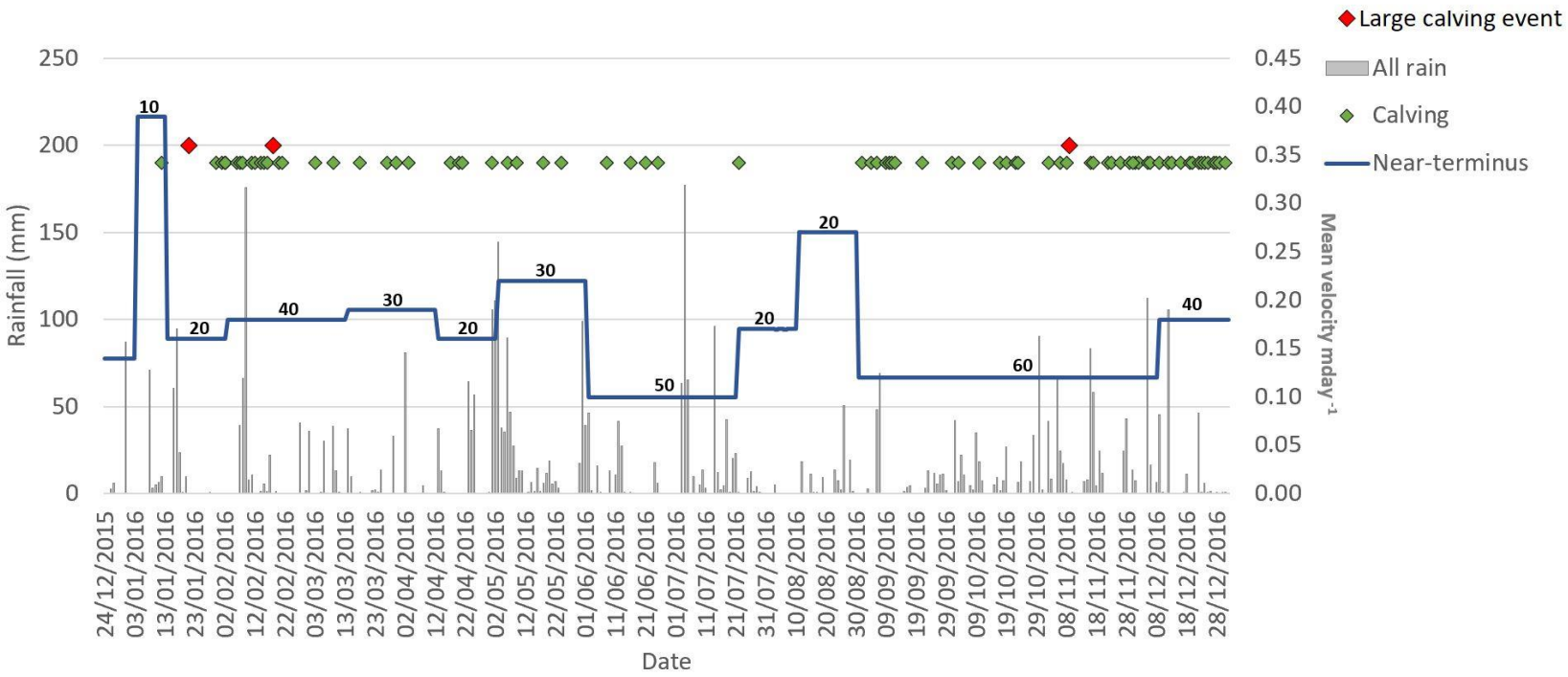

Figure 35: A comparison between surface velocity, calving events and rainfall. Surface velocity at the Near-terminus shown by the dark blue line, rainfall has been mapped in grey bars. Days that had calving events are mapped by green diamonds. The red diamonds show significantly large calving events. Calving events were recorded from time-lapse photos provided by Dr Brain Anderson. The numbers on the blue line show the number of days for each velocity measurement.

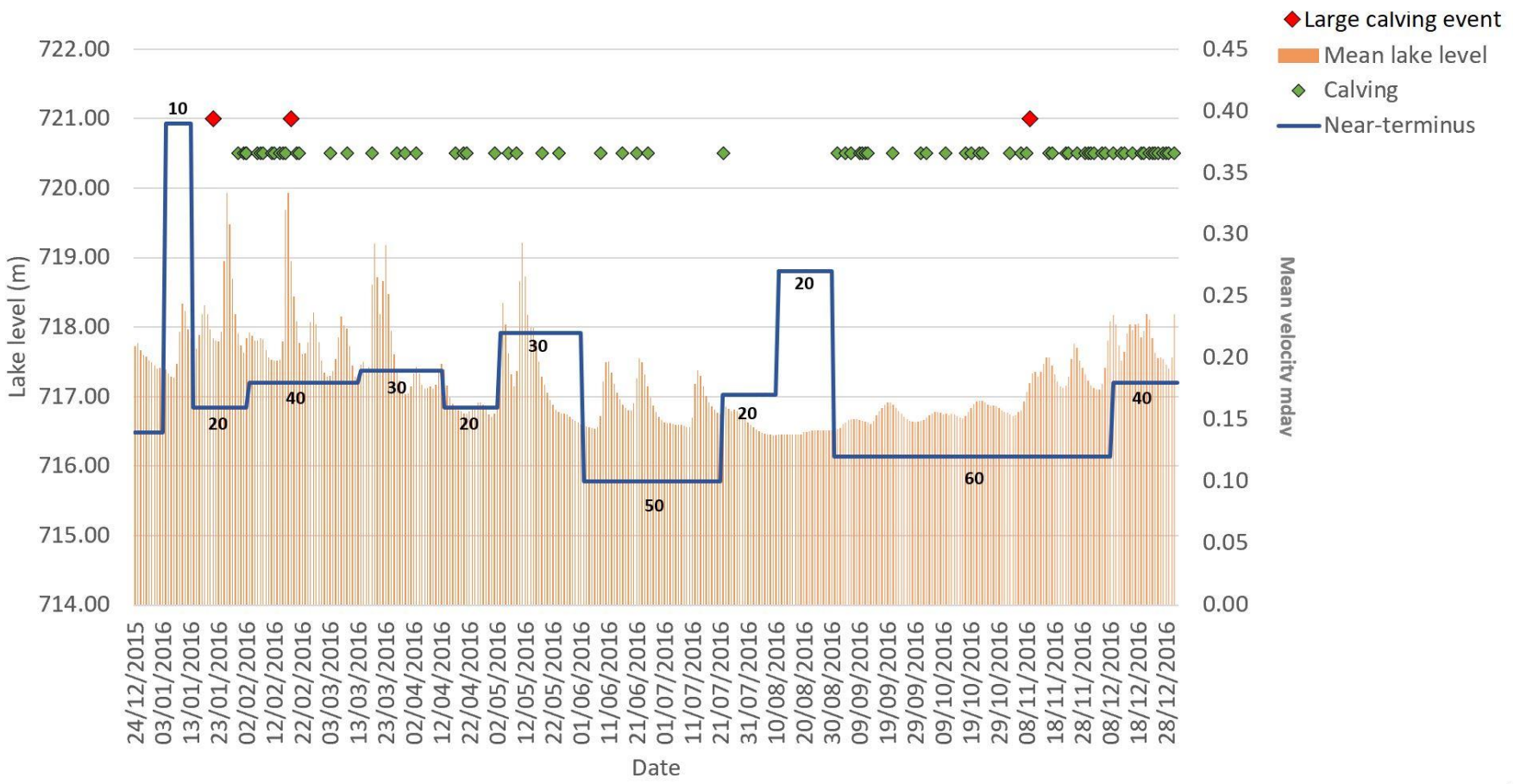

Figure 36: A comparison between surface velocity, calving events and lake level for 2016. Surface velocity at the Near-terminus shown by the dark blue line, mean lake level has been mapped in orange bars. Days that had calving events are mapped by green diamonds. The red diamonds show significantly large calving events. The number above the blue velocity line indicates the time interval in days.

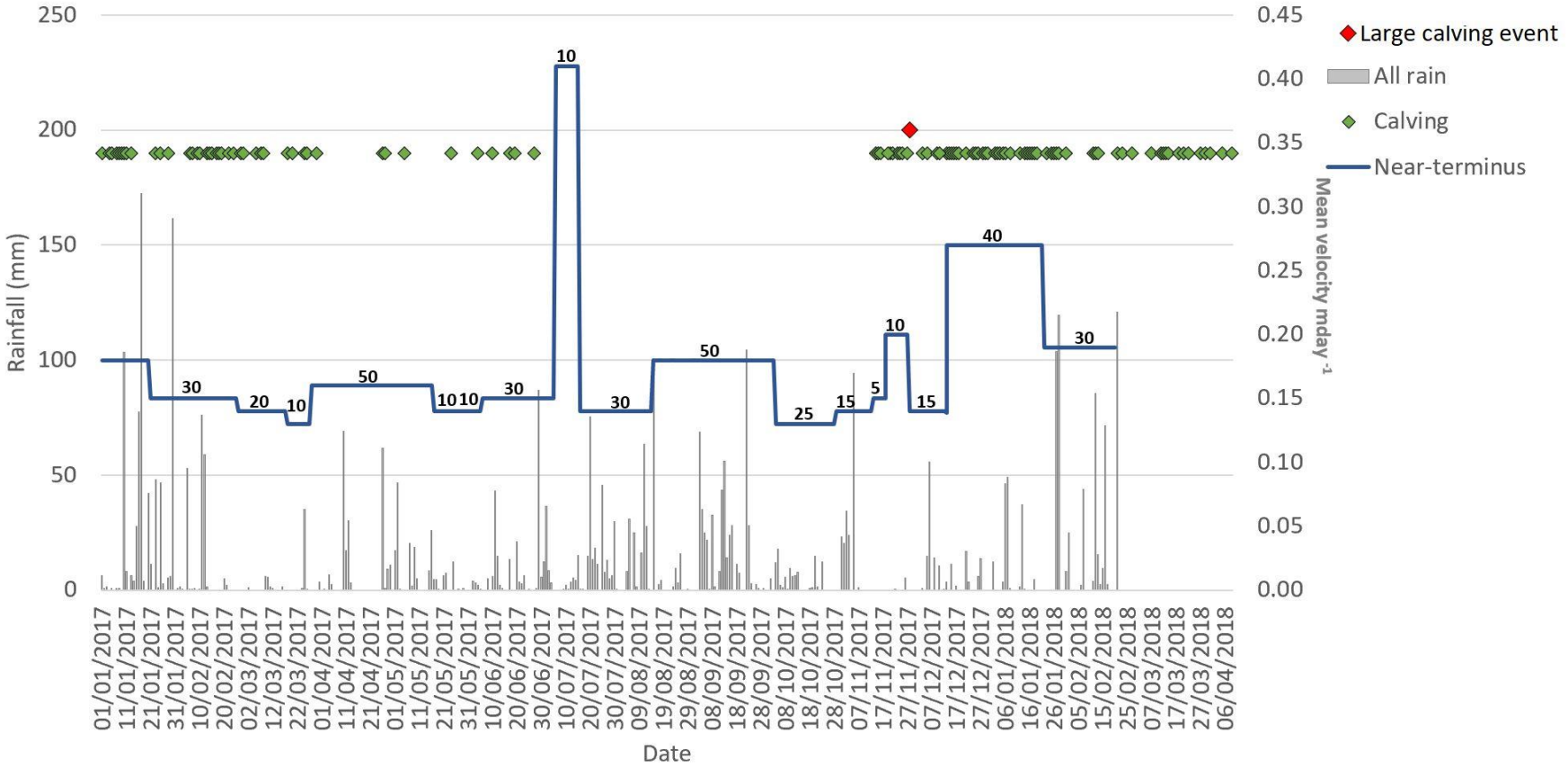

Figure 37: Surface velocity for 2017-2018 at the Near-terminus shown by the dark blue line, rainfall has been mapped in grey bars. Days that had calving events are mapped by green diamonds. The red diamonds show significantly large calving events. The number above the blue velocity line indicates the time interval in days.

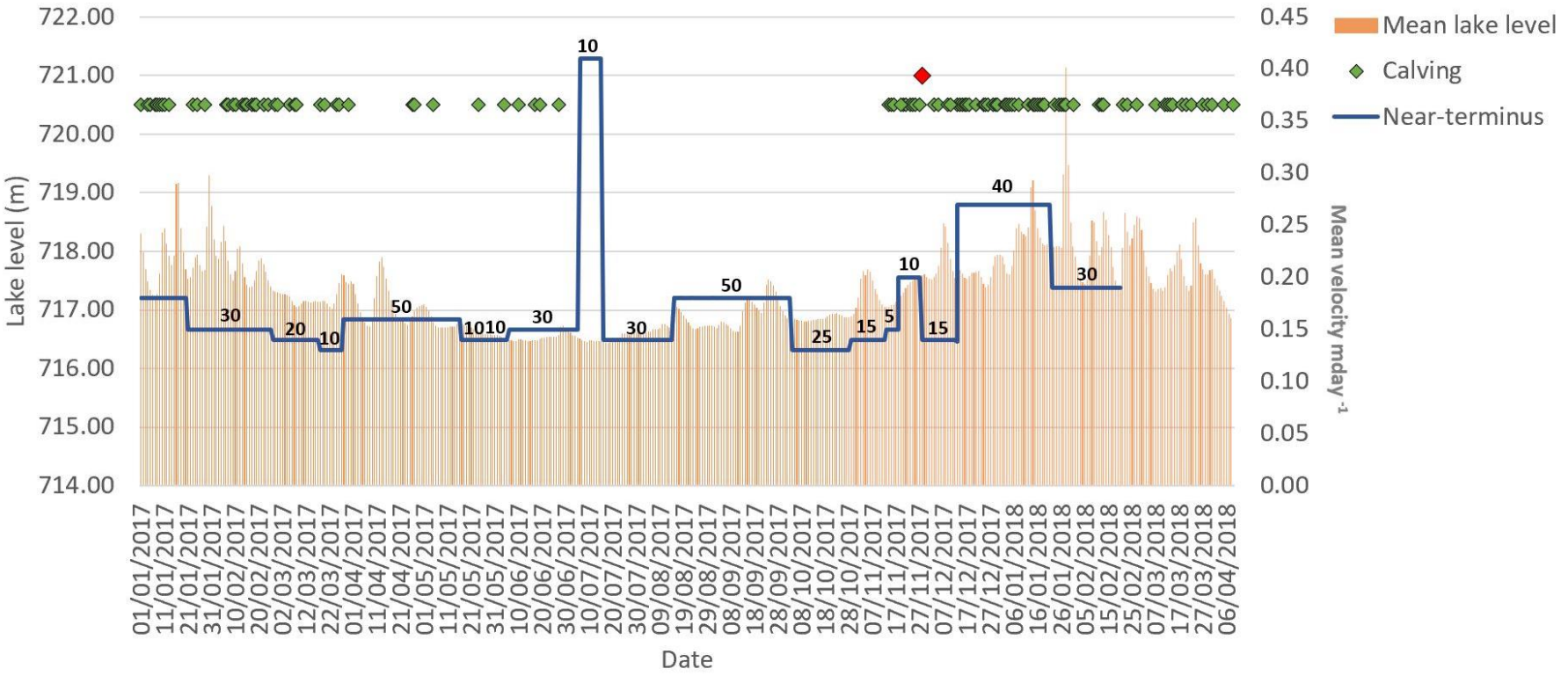

Figure 37: Surface velocity at the Near-terminus shown by the dark blue line, mean lake level has been mapped in orange bars. Days that had calving events are mapped by green diamonds. The red diamonds show significantly large calving events. The number above the blue velocity line indicates the time interval in days.

5.2 Lake conditions

Landsat 8 imagery was used to map the seasonal surface temperature variation from 2013 – 2017. Mean surface lake temperatures were extracted for the entire lake and for the near-terminus region from Landsat-8 imagery using the thermal band (Figure 38). The lake surface temperatures show strong seasonal variation with cool temperatures in the autumn and winter and warmer temperatures in the spring and summer. Mean lake winter temperatures ranged from -6.2°C and -1.6°C in 2013 and 2016 respectively and winter temperatures at the near terminus ranged from -6.0 and -0.7°C in 2013 and 2016. During the summer months in 2015 the mean lake temperature was 14.1°C. The lake surface temperatures show a rapid change in temperature gradient at the changing of the seasons. In 2013 the mean surface temperature increased by 13.88 °C at a mean rate of 0.12°C per day over a 113-day time interval between the 30/07/13 - 19/11/2013. This sharp increase in temperature was also seen in 2015 where the mean surface temperature increased by 12.95°C over a 113-day time interval at a mean rate of 0.11°C per day from the 06/09/15 - 27/12/2015. A steep decline in temperatures was evident when changing from autumn to winter, over a 65-day time interval from 11/03/2014 - 14/05/2014 the temperature dropped by 8.6°C at a mean rate of 0.13°C per day.

5.2.0 Surface temperature of lake

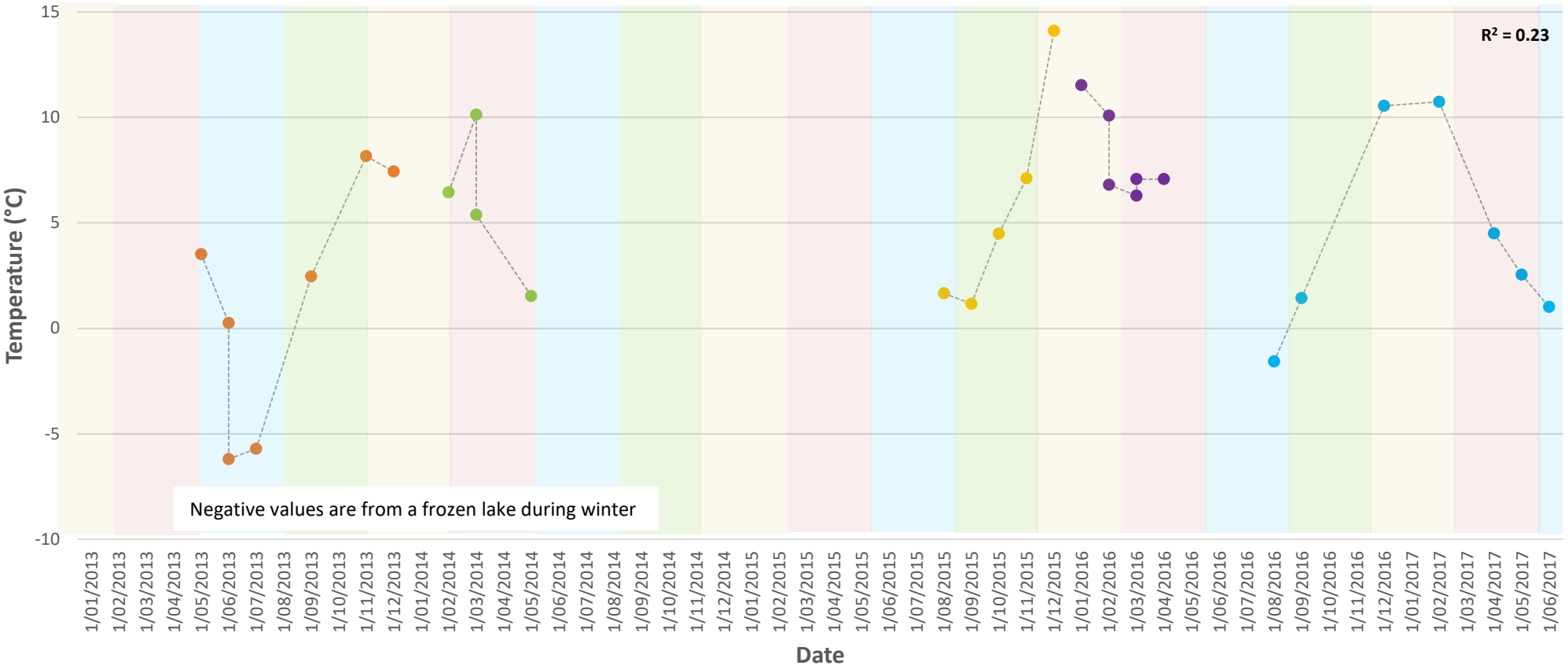

Figure 38: Mean surface temperatures derived from the thermal band in Landsat-8. The black line indicated mean surface temperature for the whole lake and the grey line indicates mean surface temperature for the near-terminus. The different coloured dots indicate the year and the coloured bars show the season. Yellow is summer, red is autumn, blue for winter and green for spring.

5.2.1 Temperature Profile Depths

Vertical temperature and conductivity profiles measured in autumn and spring (Figure 39) showed that the profile near the terminus from 2015 had temperatures at the near surface of ~2.0 °C and isothermal properties at depth, with minor variation in temperature at depth. The temperature depth profile near the terminus in 2015 has near surface temperatures of 2.0°C at a depth of 0-10 m. The temperature was isothermal from 10 – 90 m, with a change in temperature from 1.8°C to 1.6°C. The temperature profile starts decreasing in temperature at 175 m reaching 1.0°C at 200 m. The temperature at the maximum depth of the vertical temperature profile varied between 0.5 and 1.0 at 210 m.

The 2016 vertical temperature profile from the middle of the lake had a temperature between 1.7 – 1.5°C at 0-10 m depth. The profile shows an isothermal pattern from 10 – 110 m at a temperature of 1.4°C. From 100 – 200 m the temperature decreased from 1.4°C to 0.9°C.

Near the Murchison river inlet, the near surface temperature at 10 m was 1.6°C. The temperature remained the same at 1.5°C between 3 – 24 m, temperature then increased to 2.0°C near the lakebed at 30 m depth.

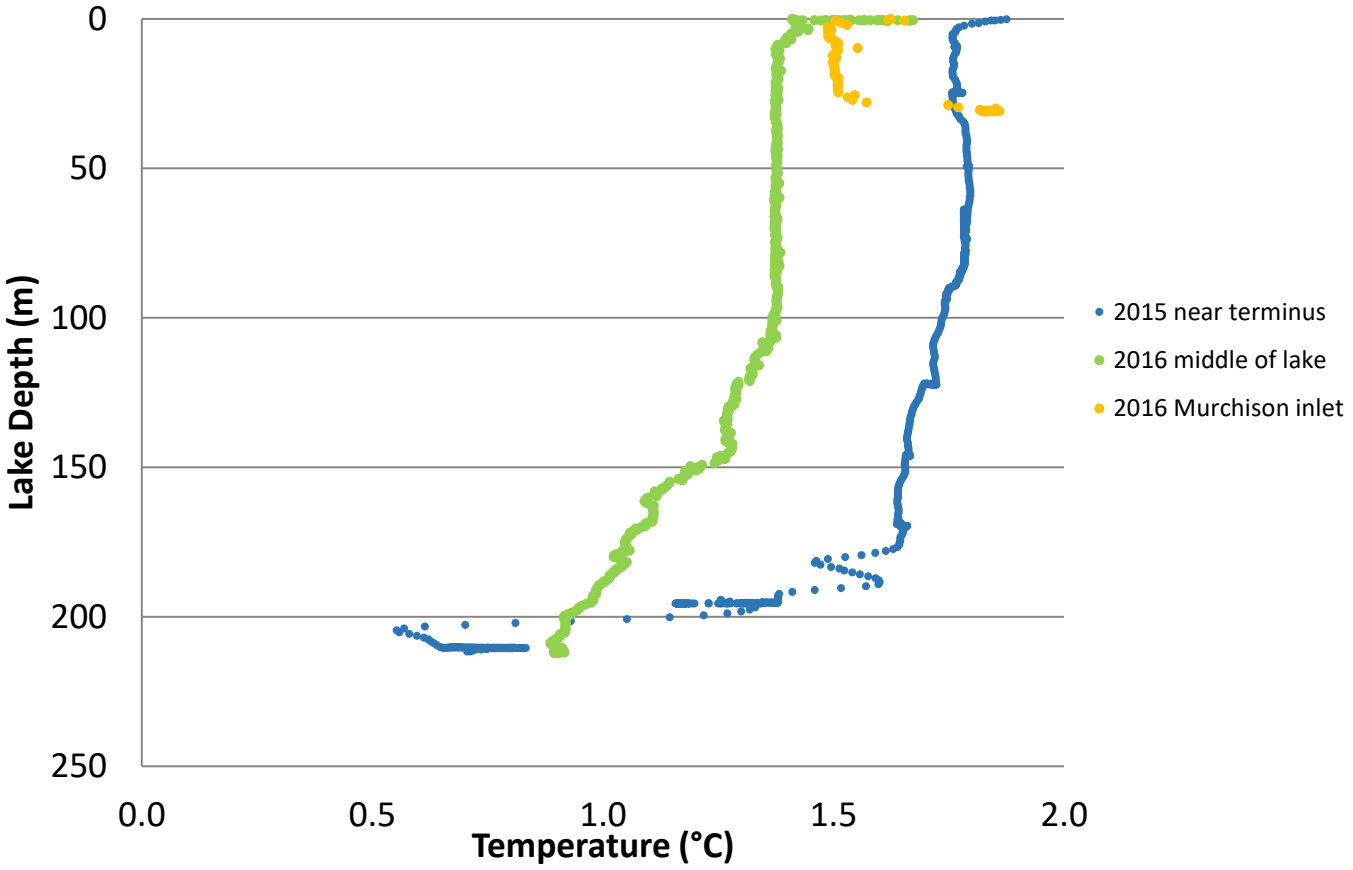

Figure 39: 2015 vertical temperature profile at the near-terminus is shown in blue, the 2016 vertical temperature profiles are in green and yellow respectively. The green lower was from the middle of the lake and the yellow lower was near the Murchison River inlet. The 2015 profile was collected in mid-autumn in April and the 2016 profiles were collected during the spring in September.

5.2.2 Water seepage

Evidence of water seepage was found from Sentinel 2 images. Sources of water contribution were identified as water plumes in the front of the terminus, seepage from the moraine walls, icebergs and the Murchison inlet. Water seepage can be seen near the eastern moraine at the terminus in Figure 40. Icebergs are also seen in the bottom half of the lake. A plume in front of the terminus was identified from one satellite image from 06/06/2017 (Figure 41) along with a minor contribution from the Murchison inlet. Small amounts of water seepage were also mapped from satellite imagery on the 18/03/2017, shown in Figure 42 on the east and west side of the terminus near the moraine walls.

Water seepage from the moraine wall near the terminus shown in Figure 43 was also recorded from photos taken during the 2018 survey. Also visible in the image is a previous lake level line highlighting that the lake level fluctuates when water inputs such as precipitation are large enough.

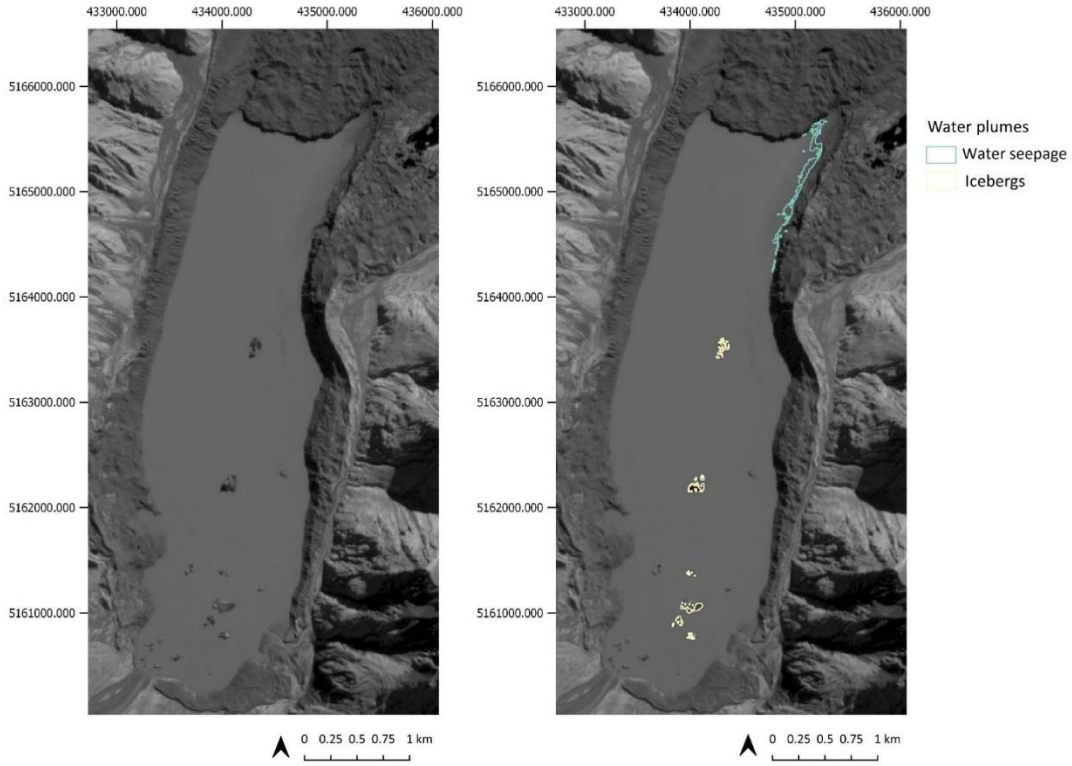

Figure 40: Sentinel satellite image from 12/04/2016, yellow outline are icebergs, light blue shows seepage near the moraine wall on the eastern side of the terminus.

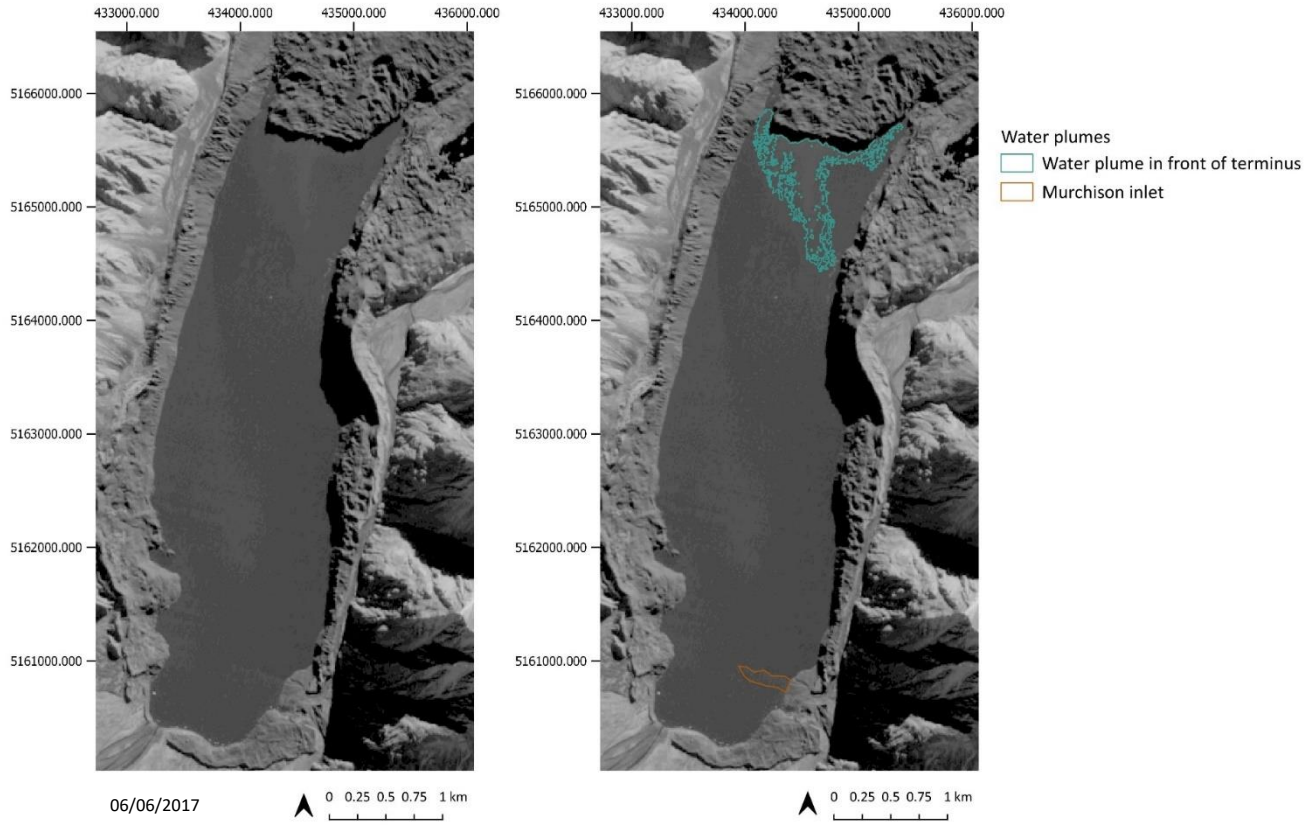

Figure 41: Sentinel satellite image from 06/06/2017. A plume in from of the terminus is digitised in dark green, with a contribution from the Murchison inlet in brown.

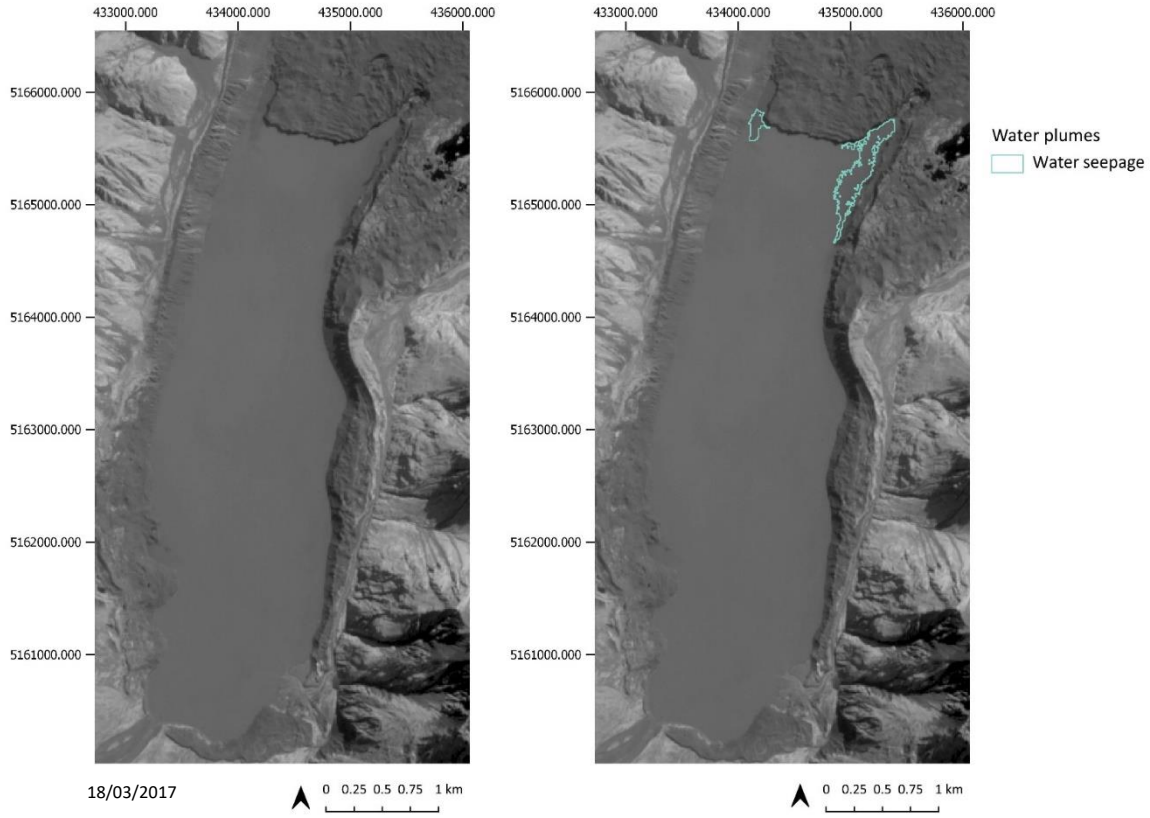

Figure 42: Sentinel satellite image from 18/03/2017, water seepage in light blue on the eastern and western sides of the moraine walls near the terminus.

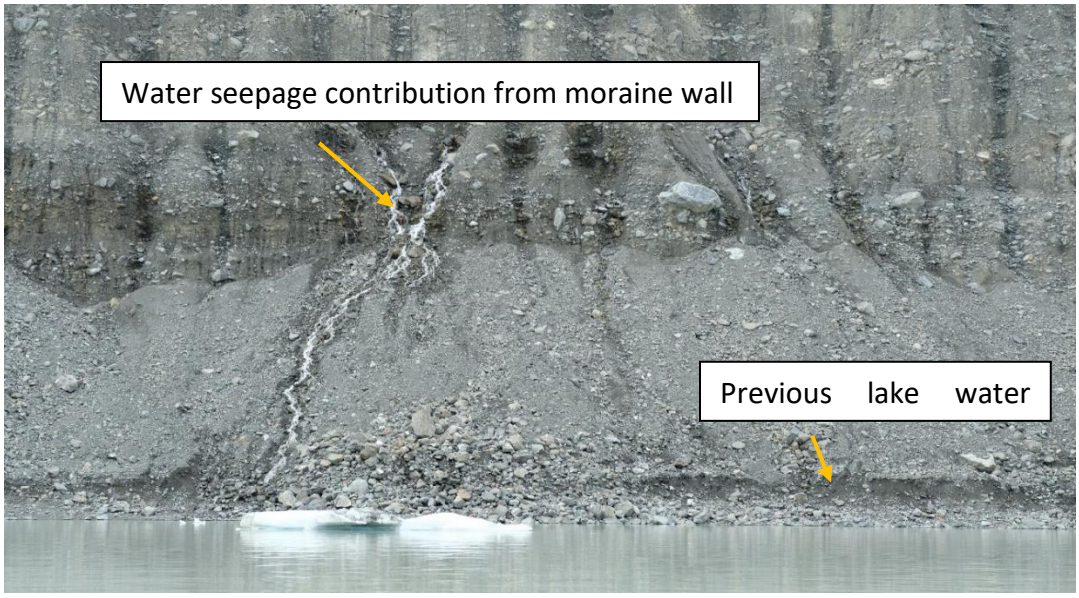

Figure 43: Water seepage contributing to Tasman lake during the 2018 bathymetric survey on the eastern moraine. A waterline of a previous level is shown in the white box.

5.3 Terminus morphology

5.3.0 Previous identification of subaqueous morphology

Bathymetric surveys of the lake near the terminal face were conducted in 2013, 2014, 2015 (Purdie et al. 2016), and in 2016 and 2018 (this study). Ice ramps were digitised across the width of the terminus. The digitised ice ramps in this chapter are not assumed to exist in isolation. The interpolated surface of the bathymetric surveys shows that the subaqueous morphology may be connected across the width of the terminus. The digitised ice ramps provide an indication of ice ramp length and profile.

Four ice ramps identified during the 2013 and 2014 surveys; it was assumed that the two 2014 ramps were the same ramps identified in the 2013 survey. All four ramps formed along the main face of the terminus (Purdie et al. 2016), and Fig 44 & 45, with ramps 1, 2 and 3 exceeding 100 m in length. Ramp 4, located on the eastern side, was the greatest in length reaching 175 m and 180 m in 2013 and 2014 respectively. In 2013 the maximum lake depth was 220 m, increasing to 240 m in 2014.

The 2015 survey in Figure 46 was the start of the higher resolution surveys allowing finer details of the ice ramps to be recorded. In 2015 9 ramps were digitised along the main face of the terminus. Profiles of ramps 7, 8 and 9 showed a large shelf feature towards the eastern side of the terminus, all three of these ramps exceeded 200 m in length. Profiles of ramps 1-6 had a steeper gradient with shelf features, the extent of these ramps ranged between 120 m and 200 m

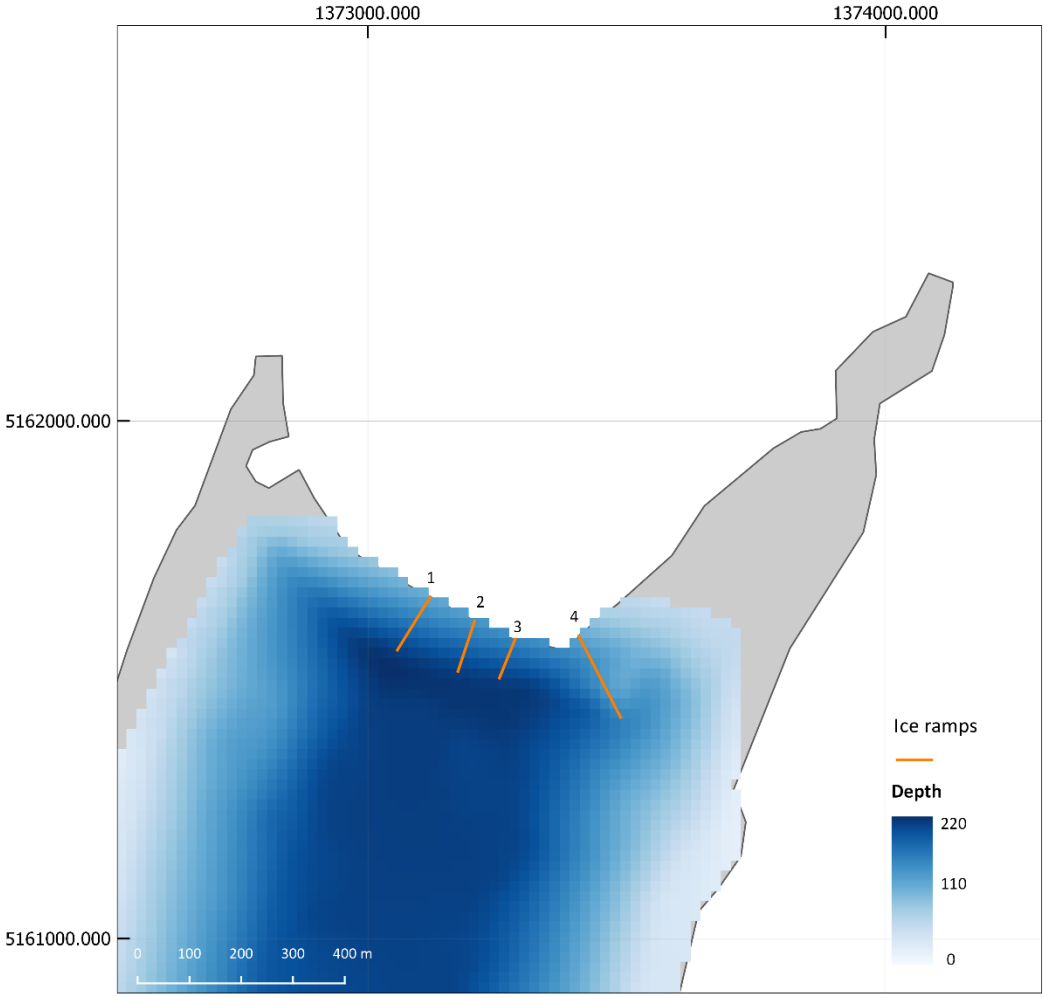

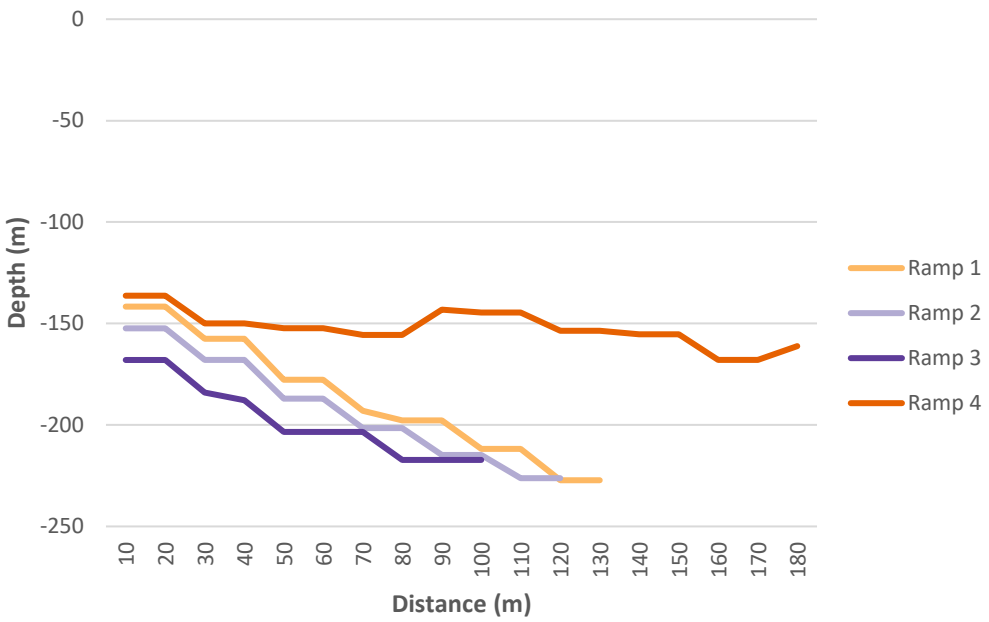

Figure 44: 2013 survey points were interpolated using nearest neighbour and display the mean depth. The orange lines note subaqueous ice ramps of various sizes.

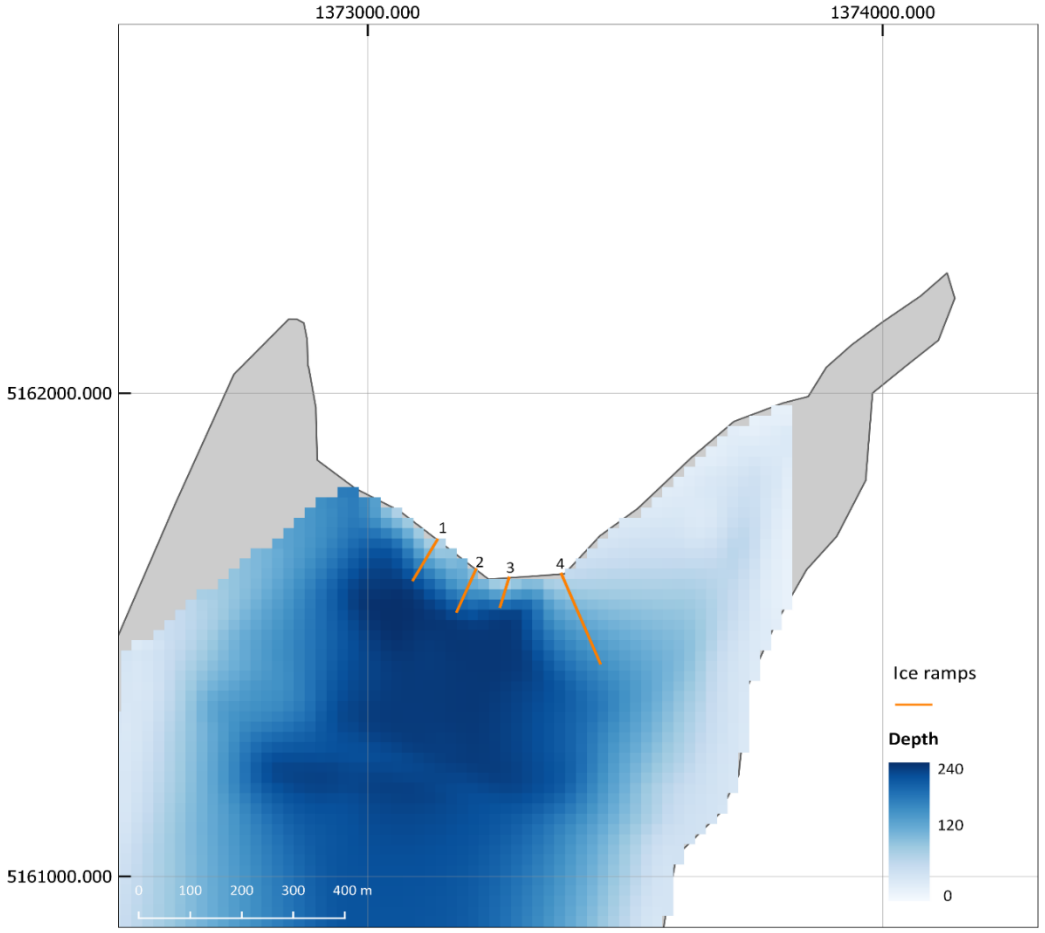

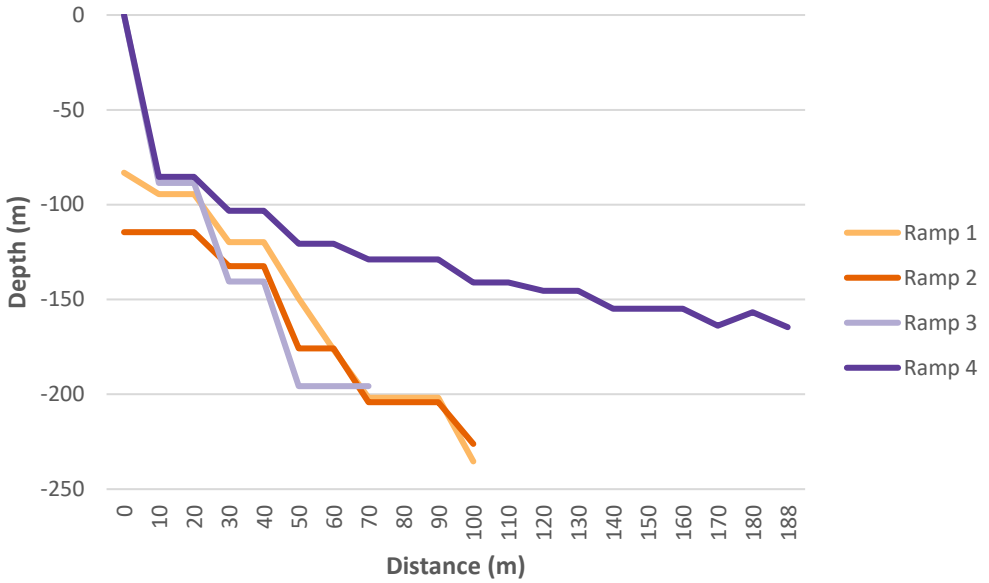

Figure 45: 2014 survey points were interpolated using nearest neighbour and display the mean depth. The orange lines note subaqueous ice ramps of various sizes

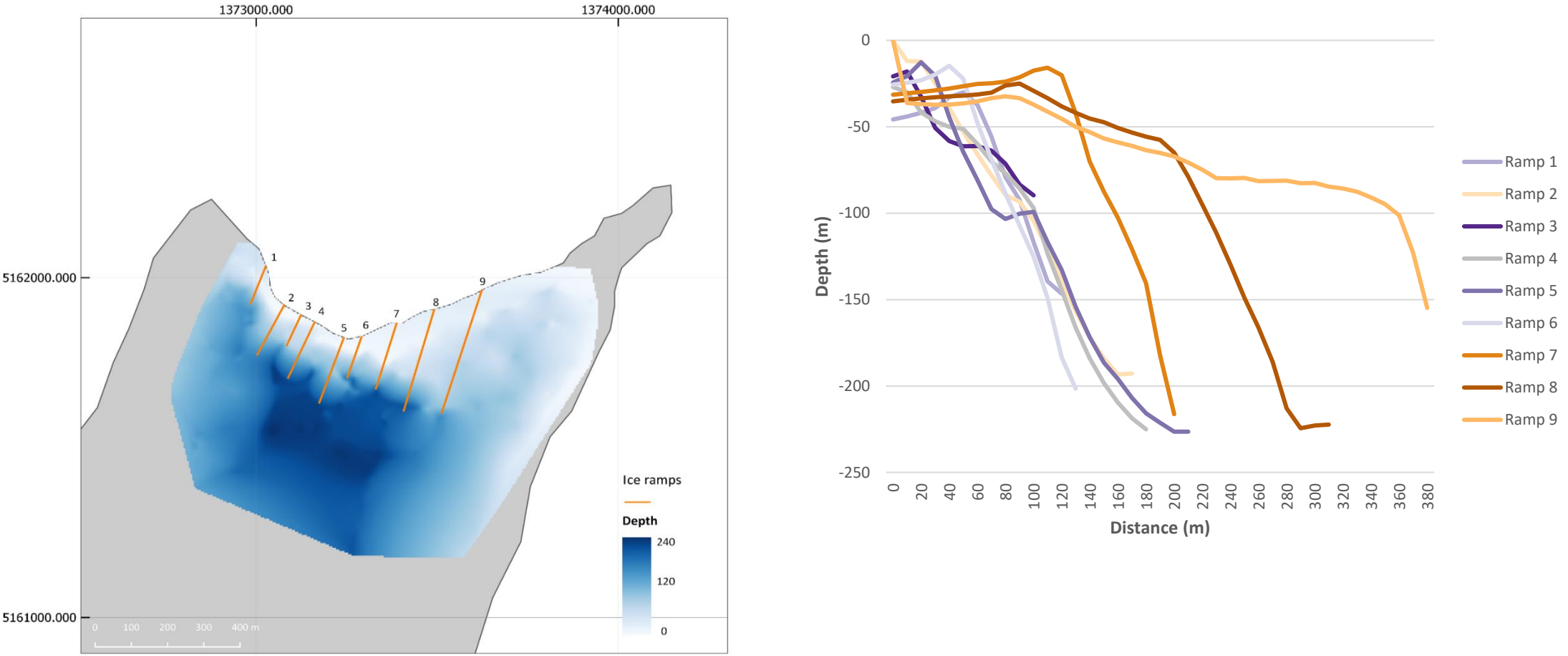

Figure 46: 2015 survey points were interpolated using nearest neighbour and display the mean depth. The orange lines note subaqueous ice ramps of various sizes and were used as the transect profiles.

5.3.1 Bathymetric data collected during this study

In 2016 there were 5 ramps recorded along the outer sides of the main ice front. Four ramps were identified on the western side of the main ice front, the maximum length of these ramps reached 120 m, ramp 6 was identified on the eastern side of the main ice front and reached 150 m in length. There was a large gap in the middle of the main ice front with no ice ramp development measuring 150 m across (Figure 47), a new lake depth was recorded in front of the terminus of 250 m. The 2018 survey 10 ice ramps identified the length of the subaqueous morphology across the main ice front. The longest ramp was on the eastern side up to 240 m long (Figure 48), this ramp formed in a similar location where the gap in subaqueous morphology was identified from 2016. The shortest ramp is on the western side of the main ice front at 80 m. Ice ramps 1, 3-8 and 10 are between 90 m and 150 m in length. Depth at the near terminus is 260 m.

The distribution of ramp lengths from 2013 – 2018 are commonly between 40 – 120 m in length (n=170) with the next largest group (n=12) between 120 – 200 m, only three ramps have been identified as greater than 200 m over the five-year survey time.

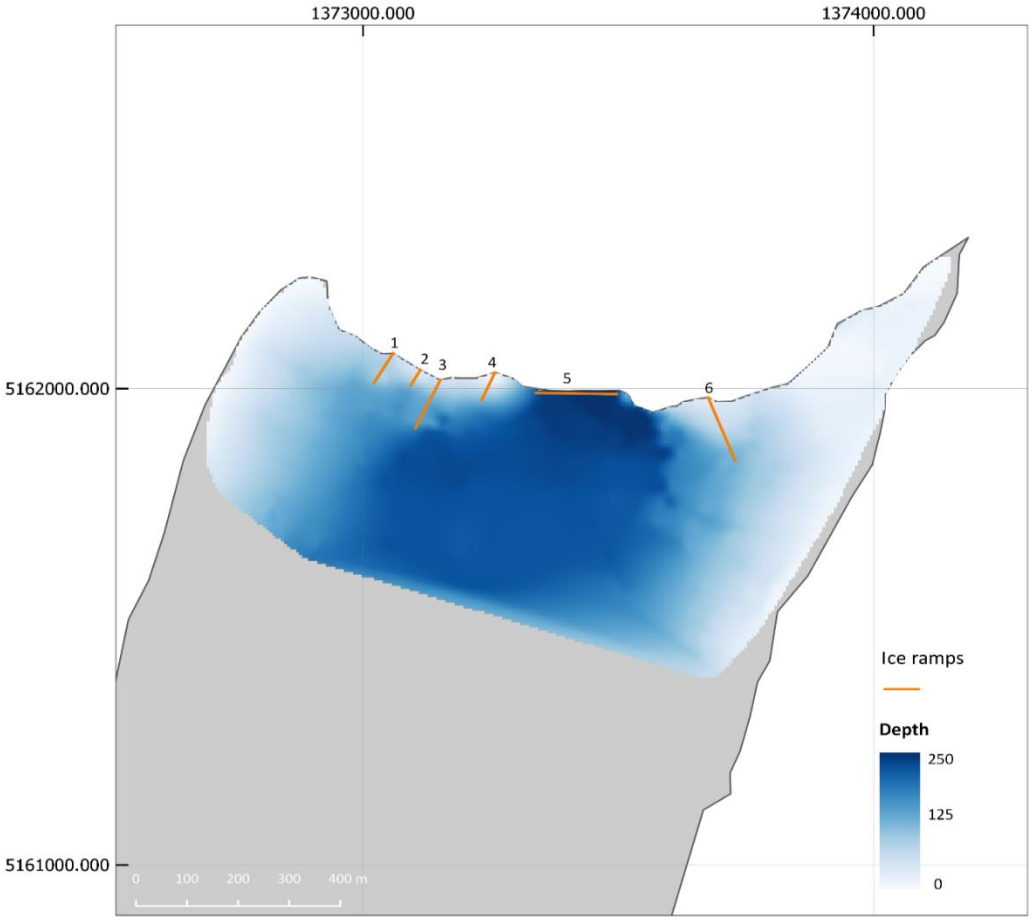

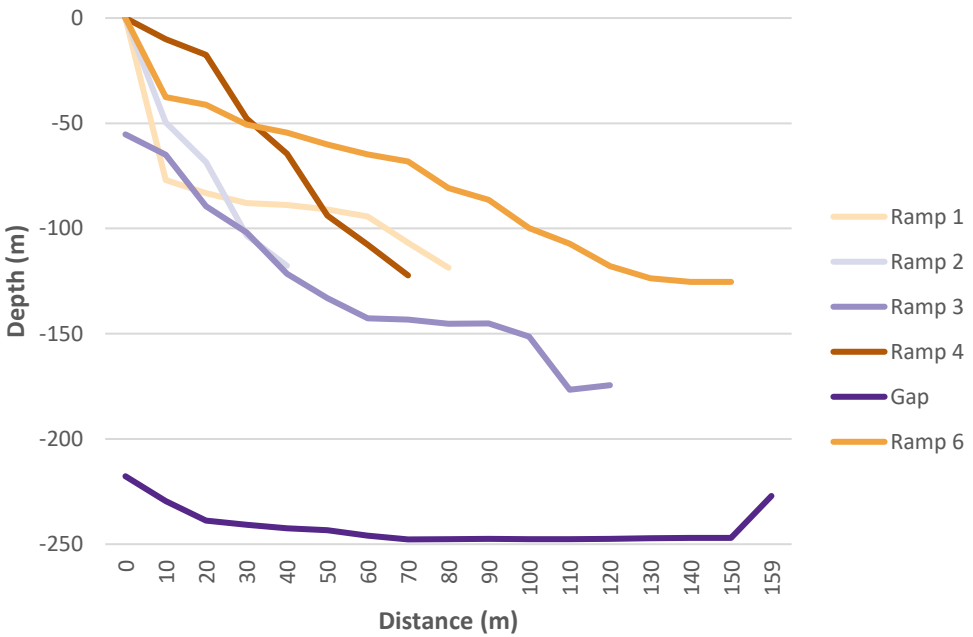

Figure 47: 2016 survey points were interpolated using nearest neighbour and display the mean depth. After the 2015 survey there was a large subaqueous calving, the survey shows a gap in subaqueous morphology of 150 m and, the depth of the lake at this gap is 250 m.

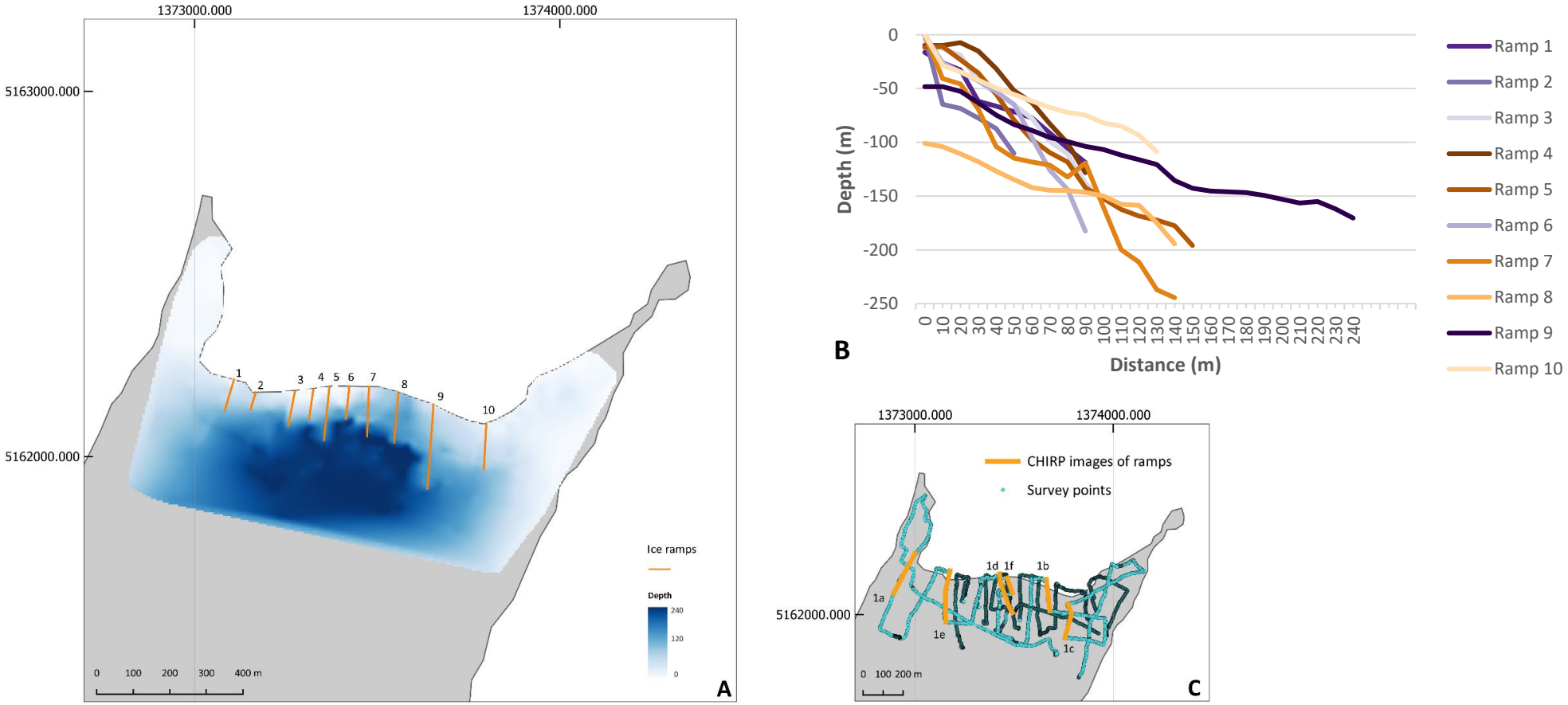

Figure 48: A: 2018 mean depth interpolated surface, orange lines denote ice ramps. B: Ice ramp profiles identified in A. C: Orange lines show where the CHIRP images of the subaqueous morphology are located. The blue dots are the 2018 bathymetry points. All CHIRP subaqueous morphology images were taken from transect leading towards the terminus, except 1a which is heading away from the terminus. The identification number by each orange line corresponds to CHIRP Figure 50.

5.3.2 Subaqueous ice ramps CHIRP sonar

The subaqueous ice ramps as revealed by the CHIRP sonar survey show a variety of ice ramp morphology. Ice ramps 1a, 1c in Figure 49 both have gentle ramp gradients, 1a drops gradually below 60 m. 1c starts off with a flat shelf at 60 m which then slopes gently to 180 m. Ice ramp 1d drops away quickly and gets wider at depth, ramp 1d is over 180 m deep. Distinctive shelf features, are displayed in 1b, 1e and 1f. Ice ramps 1e and 1f show 'step' like shelf features, compared with 1b which has a more gently gradient and drops down to 120 m.

During the 2018 survey and subaqueous and aerial calving took place. High resolution photos were taken of icebergs and detail melt features that are attributed to subaqueous processes. Image 2a in Figure 49 shows an iceberg with thermal melt/notch features, on the other side of this iceberg the was evidence of scalloping which can be seen in 2d. Melt features consistent with 'rills' were identified in 2b and 2c. All these features are consistent with circulation derived melting.

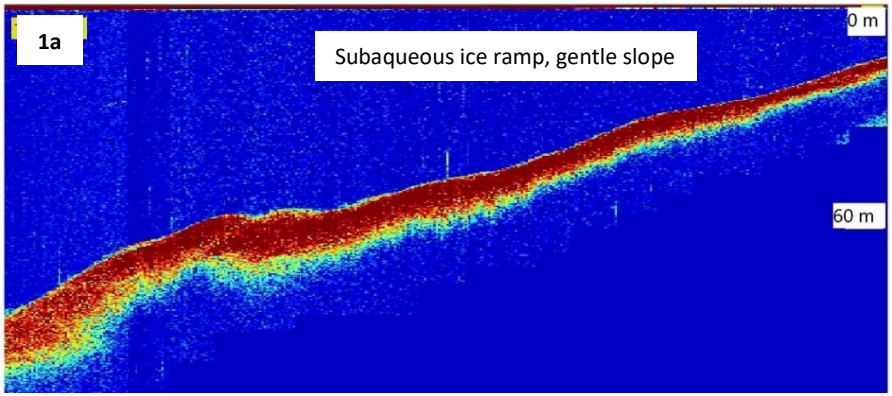
1a
Subaqueous ice ramp, gentle slope
0 m
60 m

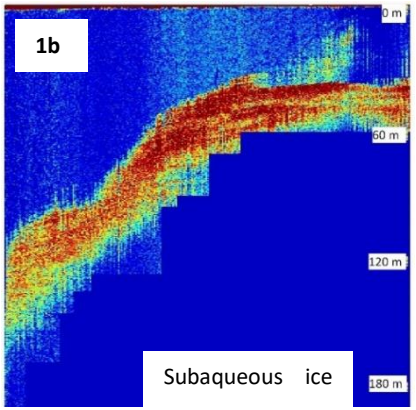
1b
0 m
60 m
120 m
Subaqueous ice
180 m

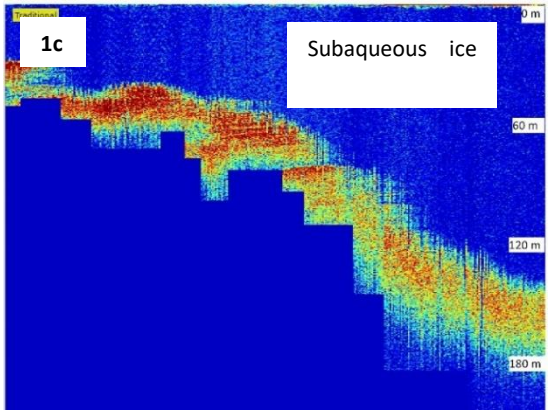
1c
Subaqueous ice
0 m
60 m
120 m
180 m

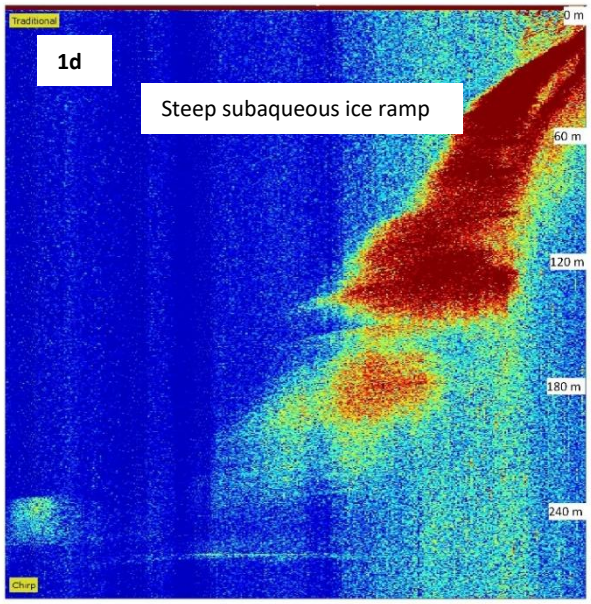
Traditional
1d
Steep subaqueous ice ramp
0 m
60 m
120 m
180 m
240 m
Chirp

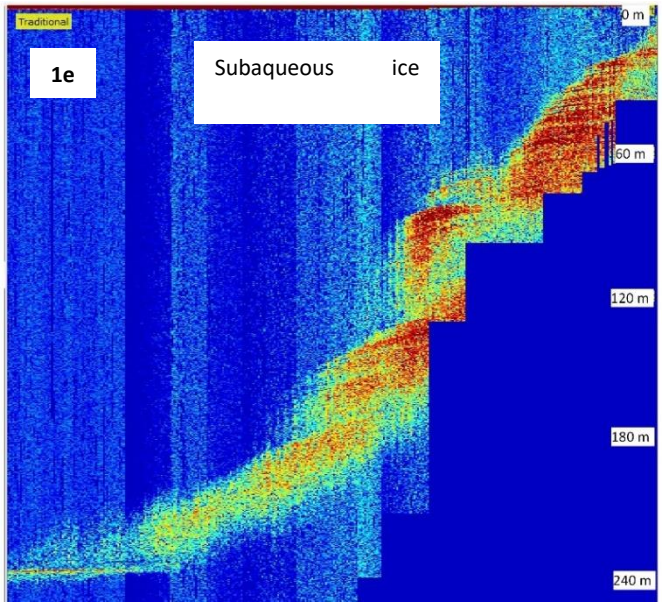
Traditional
1e
Subaqueous ice
0 m
60 m
120 m
180 m
240 m

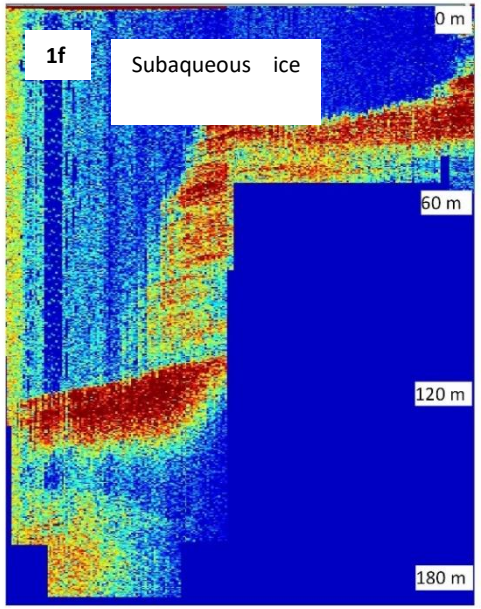
1f
Subaqueous ice
0 m
60 m
120 m
180 m

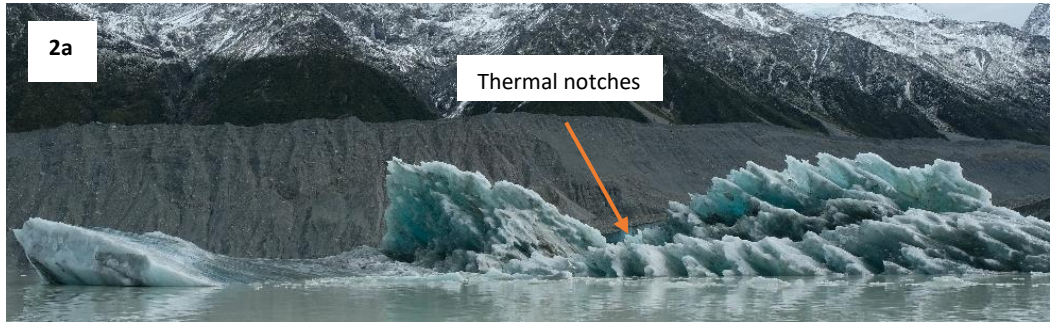

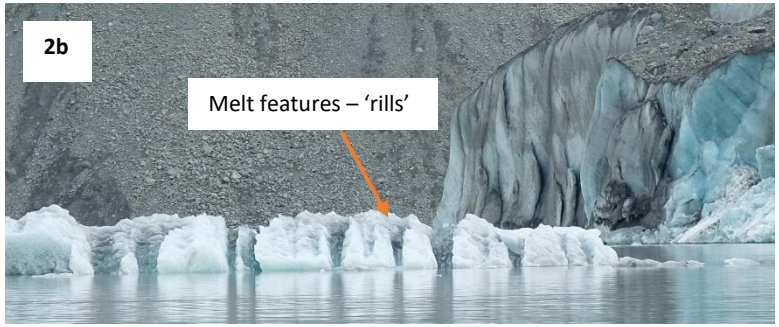

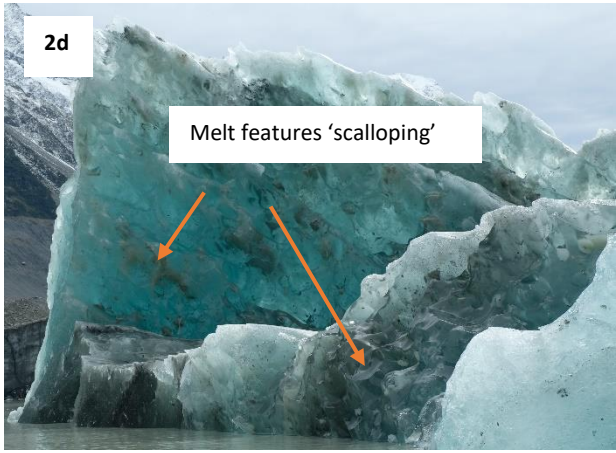

Figure 49: CHIRP sonar survey recordings,1a-1f, these are recorded with the jet boat heading towards the terminus, they show the ice ramp in the traditional view. Photos 2a-d show icebergs from a subaqueous calving event during the 2018 survey. Photos taken by Justin Harrison

5.3.3 Ice ramp length change of all bathymetry data from 2013 - 2018

If an assumption is made that in between surveys the ice ramps have not fully or partially calved, then an estimation can be made about the rate at which the size of the ramps change. This could be due to growth associated with subaerial melting and calving or a reduction in size due to subaqueous melting. It was found that ramp size between surveys 2013/2014 (Figure 50, A) and 2015/2016 (Figure 50, B) had decreased, and it was assumed that the 2018 ice ramps (Figure 50, C) were newly formed since the 2016 survey.

Ice ramps between the 2013/2014 and 2015/2016 survey were assumed to be the same ice ramps. The change in length was calculated in meters per day over a 397-day time interval for 2013/2014, 321-day interval for 2015/2016 and 576 days for 2018. Previous melt rates at Tasman Glacier by Purdie et al. (1999) and Rohl, (2006) were used to compare with the change in length of ice ramps identified in Table 8.

Purdie et al. (1999) used a melt rate of 0.007 m d^{-1} for debris covered (1.1 m thick) ice and 0.096 md^{-1} for bare ice. Applying this melt rate to the 397-day time interval 2013/2014, a change in length was up to 2.84 md^{-1} more than the length change calculated during this study. Using the debris melt rate the change in length was up to 38.14 md^{-1} greater than the length calculated for this study. Changes in length found using the subaqueous melt rate from Rohl, (2006), showed changes in length for a melt rate of 0.030 md^{-1} were 11.91 md^{-1}.

For 2018 with a 576-day interval 4.03 md^{-1} and 55.30 md^{-1} could be attributed to melt using the debris and bare ice melt rates from Purdie et al. (1999) and 17.28 md^{-1} change in length

could be attributed to melt using the melt rate from Rohl, (2006). Changes in length from the 2018 survey range from 0.24 -0.40 md^{-1}.

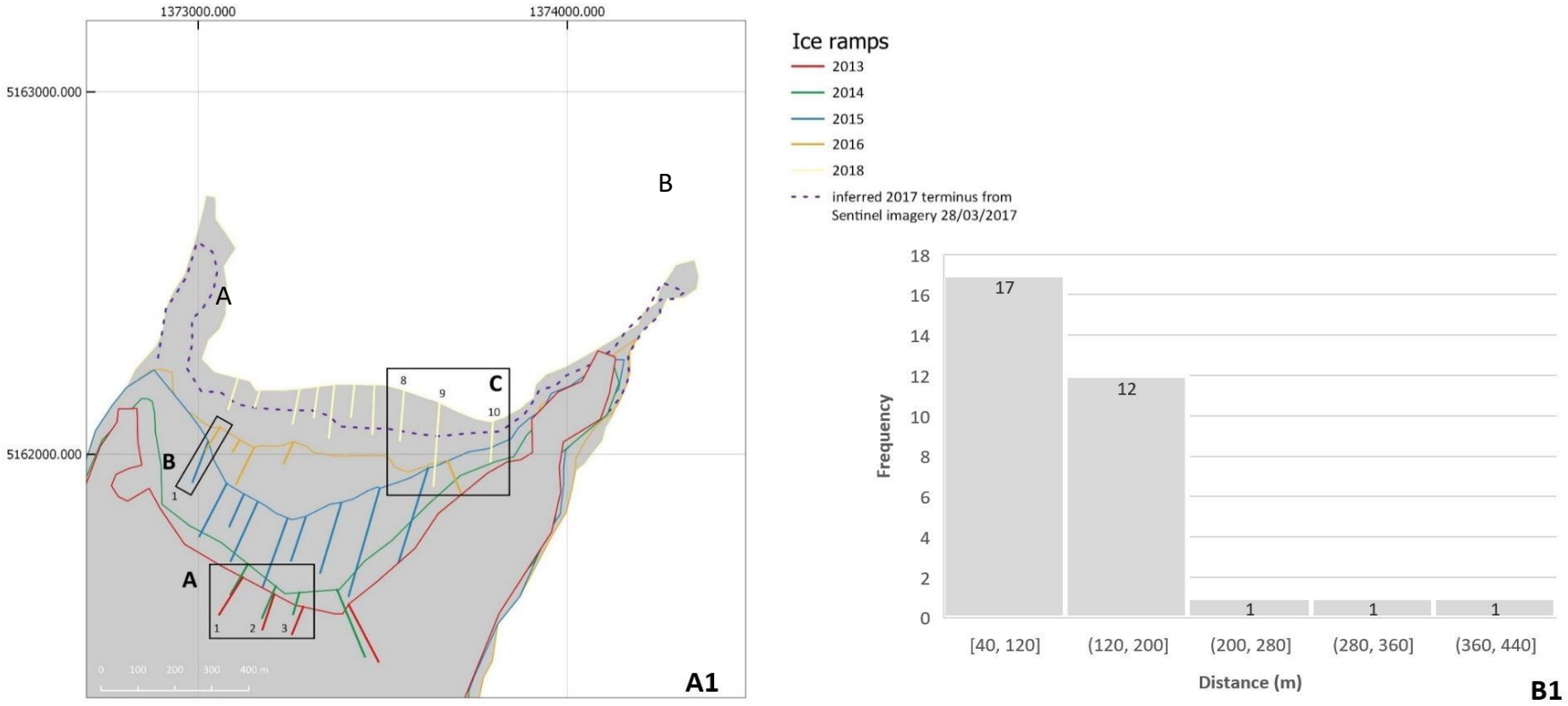

Figure 50: A1: Ice ramp development 2013 -2018, there was no survey in 2017 so a terminus outlined was inferred from Sentinel imagery. Ice ramps outlined in A,B and C were used to calculate rate of growth, it was assumed that 1) these ramps were the same ramps from previous years for A and B. 2) that ice ramps from the 2018 survey were new ramps that had formed since 2016 and 3) that no subaqueous calving or regrowth took place for these ramps. B1: A frequency distribution of ramp profile lengths shows that ice ramps do not often exceed 200 m.

Table 8: Changes in ice ramp length for 2013/2014, 2015/2016 and 2018 survey. An assumption is made that no subaqueous calving or regrowth took place for these ramps during the survey period. Changes in ramp length are compared with changes in length using bare ice and debris melt rates from Purdie et al. (1999) and a subaqueous ice melt rate from Rohl, (2006).

Survey	Ice ramp no.	T1 (m)	T2(m)	Difference (m)	Time interval (days)	Rohl (2005) Subaqueous ice melt (m) at given a melt rate of 0.030 md^{-1}	Length change (md^{-1}) Based on melt rate of 0.03 md^{-1}	Purdie et al (1999) Bare ice melt (m) at a given melt rate 0.096 md^{-1}	Length change (md^{-1}) Based on melt rate of 0.096 md^{-1}	Purdie et al (1999) Debris melt rate (1.1 m thick) 0.007 md^{-1}	Length change (md^{-1}) Based on melt rate of 0.007 md^{-1}
2013/2014	1	120.57	95.48	25.09	397	11.91	-0.22	38.12	-0.14	2.78	-0.23
2013/2014	2	102.43	94.43	8.00	397	11.91	-0.21	38.12	-0.14	2.78	-0.23
2013/2014	3	81.05	61.92	19.13	397	11.91	-0.13	38.12	-0.06	2.78	-0.15
2015/2016	1	163.18	95.24	67.94	321	9.63	-0.27	30.82	-0.18	2.25	-0.29
2016/2018	8	-	135.89	-	576	17.28	0.21	55.30	0.14	4.03	0.24
2016/2018	9	-	137.02	-	576	17.28	0.21	55.30	0.14	4.03	0.24
2016/2018	10	-	230.04	-	576	17.28	0.34	55.30	0.30	4.03	0.40

5.3.4 Terminus buoyancy

During the 2016 survey a series of 69 overlapping photos were taken across the terminus. These photos were processed using SfM (Figure 51). The RMS reprojection error was 0.14 m (0.74 pix) Several height estimates were taken across the terminus from the dense point cloud for comparison with the floatation thickness (H_F) for the 2016 survey. The floatation thickness (H_F) (Eq 2) for the 2016 survey was calculated at 273 m, in order for the terminus to prevent floatation the terminus height (H_T) must exceed 23 m. the area highlighted by the green box indicates areas of the terminus that do not exceed the floatation thickness (H_F).

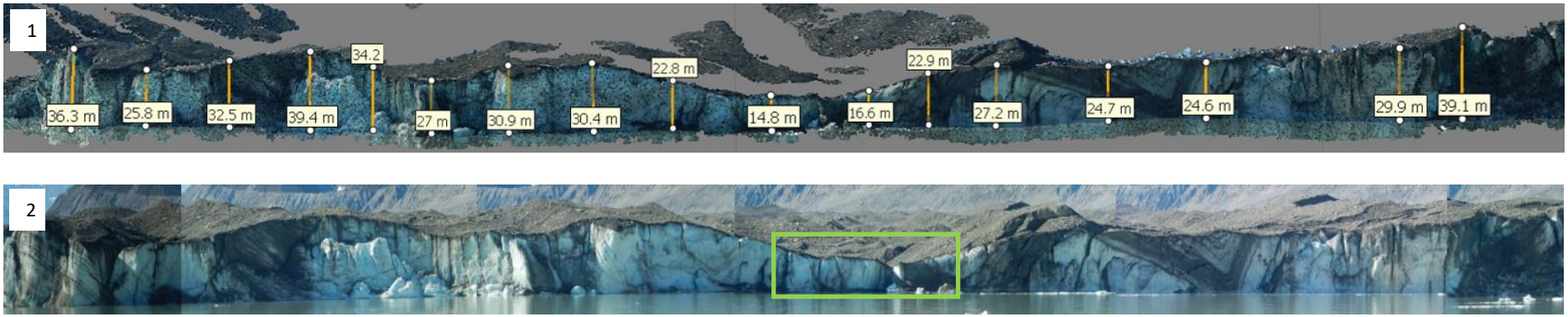

Figure 51: Terminus (1) dense point cloud generated from SfM using 69 photos from the 2016 survey. The dense point cloud was generated and heights were measured in Agisoft Metashape 1.5.0 using the measure tool. The terminus in (2) is made from overlapping photos taken from the 2016 survey and is provided for comparison purposes with the SfM model. The green box shows the portion of the terminus below the floatation thickness.

The floatation thickness (H_F) for the depth recorded from the 2018 survey is 283 m, meaning the terminus needs to exceed 24 m to prevent
floatation. No overlapping photos were taken for the 2018 survey.

Chapter 6 – Discussion

6.0 Are there relationships between near-terminus surface velocity, calving and subaqueous morphology?

One of the primary aims of this thesis was to find relationships between processes and feedbacks at Tasman/Haupapa Glacier; between calving, velocity and subaqueous morphology. The relationships between these processes are shown in Figure 52 and Table 9 where these relationships are indicated by a series of arrows whereby the direction of the arrow shows which variable is having an effect on the other.

Table 9: Matrix showing relationships found between calving, velocity and subaqueous morphology. Green boxes indicate a strong relationship, and red boxes indicate no relationship between variables.

	Calving	Velocity	Subaqueous morphology
Calving			
Velocity			
Subaqueous morphology			

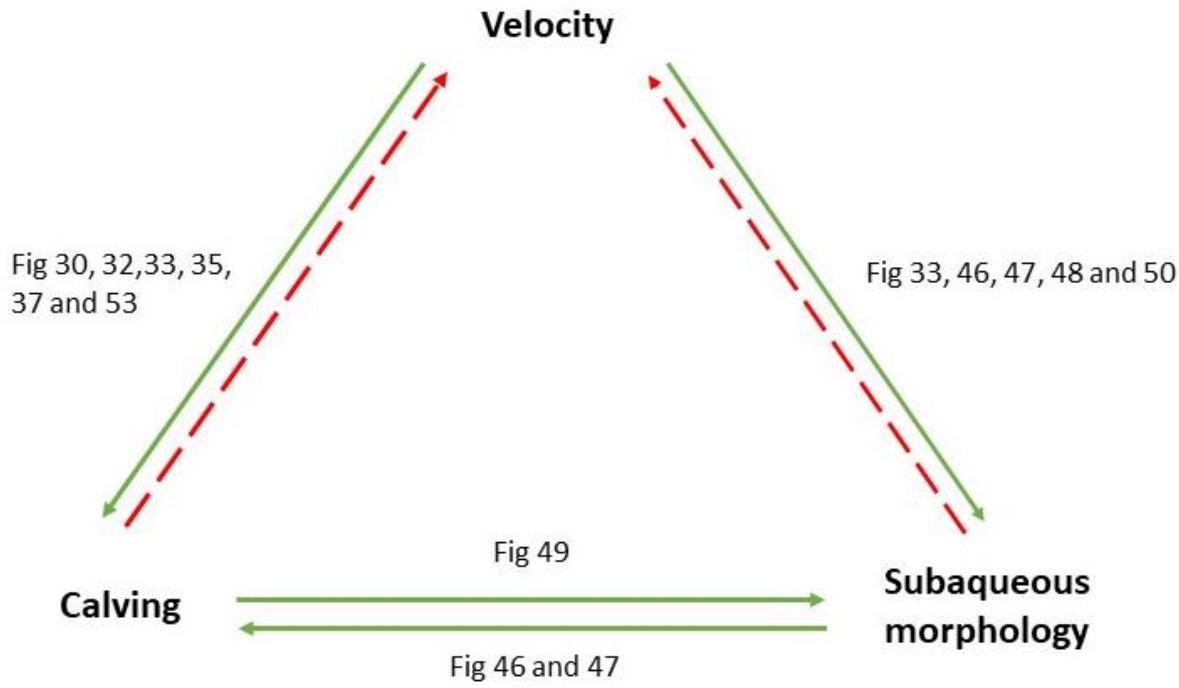

Figure 52: Diagram showing the relationships identified during this study. The green arrows show a strong relationship between the two variables and the red dotted lines indicate no relationship between the relevant variables. The direction of the arrows show which variable is affecting which. Figures listed beside the arrows reference the figures from the text which show the relationship between the variables in detail.

6.0.1 Velocity influencing calving

A spatial and temporal relationship was found between surface velocity and calving at Tasman/Haupapa Glacier. It was stated by Benn & Astrom (2018) that all iceberg calving is a function of the propagation and formation of crevasses, and that the location and depth of crevasses is determined by variations in velocity (Benn et al. 2007). At Tasman/Haupapa Glacier, surface velocity generally showed an increase during the spring and summer seasons, and deceleration during the autumn and winter seasons (Figure 30). Iceberg calving also showed seasonal variation, with a greater number of events recorded during the spring and summer compared to the autumn and winter (Figure 35, 37). The larger number of calving events during the spring and summer is attributed to the increase in surface velocity. An increase in velocity is required for an increase in calving, as without the velocity increase and

subsequent crevasse propagation, the rate of calving would be dependent on the rate of waterline melt (Kirkbride and Warren, 1999).

Surface velocity on Tasman/Haupapa Glacier decreased down glacier. This is consistent with findings from Redpath, (2013) who found that surface velocity decreased down glacier of the Hochstetter confluence, with surface velocity ~0.16 md^{-1} between 2009-2010, and 0.19 md^{-1} from 2010-2011. The highest surface velocity over a one-year time interval at the Ball Glacier confluence was 0.19 md^{-1}, which is similar to velocities recorded by Purdie et al. (2018) of 0.25 md^{-1} in a similar region. Surface velocities at the Upper near-terminus were generally lower than the surface velocity at the Lower near-terminus. Surface velocity at the Lower near-terminus was 0.13 md^{-1}, which is similar to Haritashya's et al. (2015) finding of 0.11 md^{-1} in 2014. An increase in surface velocity over a 20-day time interval near the Ball Glacier confluence was recorded during winter (Figure 28). Over this time interval there was >200 mm of rain (Table 07). Increases in surface velocity during the winter months at the Ball Glacier confluence may be associated with changes in basal water supply and storage reorganisation resulting from rainfall.

It was found by Horgan et al. (2015) that Tasman/Haupapa Glacier exhibited some of the fastest recorded short-term speed up events reported in the literature. Rain induced accelerations over the observed period could account for 11-14% of the glacier's displacement (Horgan et al. 2015). Rain induced accelerations identified by Horgan et al. (2015) were from a 3 hr and 24 hr observation period. The total time intervals over which surface velocity was analysed in this study ranged from 5 – 60 days. While total rainfall over

the time interval may have influenced the velocity measurements, short-term speed up events could not be isolated.

From this study, a decrease in surface velocity over the course of the melt season was observed in the summers of 2016 and 2017. As melt seasons progress, the velocity of glaciers decreas due to the increased efficiency of englacial and subglacial drainage systems (Nineow et al. 1998). When dye tracing techniques were used at the Haut Glacier d'Arolla to interrogate changes in englacial and subglacial drainage systems between 1990 – 1991, it was found by Nineow et al. (1998), from a series of breakthrough curve characteristics, that major channels had developed as the melt season progressed. While a decrease in surface velocity for 2016 and 2017 may be a result of greater hydrological connection through cavity growth at the bed of the glacier, it is likely due to the 60-day and 30-day time interval, which will have smoothed out any short-term variability.

Surface velocity before and during four major calving events was recorded from 2016 – 2018 (Figure 35,37). One event had a significant increase in velocity over a 10-day period prior to this event, recorded at 0.39 md^{-1} ± 0.04 md^{-1}. This was followed by a 58.97% decrease over the 20-day time interval during which the calving event occurred. Small increases were recorded in surface velocity for two other major calving events, on 18/02/2016 and 28/11/2017, and one large calving event during the 60-day time interval had a decrease in surface velocity. While three of the four major calving events show an increase in velocity prior to or during a large calving event, a velocity increase may not always be an indication that a large calving event is imminent.

Spring and summer show surface velocity increases throughout the season of 2016 and 2017 without producing large calving events, although multiple smaller calving events are recorded. Kirkbride and Warren (1997) found that short term velocity variations did not impact the rate of calving, but it can increase longitudinal stretching, which encourages crevasse development. The lack of large calving events after some surface velocity increases indicates that large calving events are likely a result of multiple processes.

It was suggested by Chinn (2014) that the expansion of Tasman/Haupapa lake had significant effects on the surface gradients of the glacier, initiating a drawdown, leading to an increase in calving. The surface velocity increases at Tasman/Haupapa Glacier are not reflective of drawdown processes (Figure 2). Variation and strength of surface velocity may be the first order of control for calving, but it does not mean that it is the only process operating across the terminus (Benn et al. 2007; Benn & Astrom 2018).

When analysing the spatial variation in surface velocity from the longitudinal velocity profiles, an acceleration of 50% at the terminus was seen. The acceleration extended from the terminus to 1.5 km up glacier (Figure 33). This was followed by a substantially slow area between 1.5-2.8 km up glacier. This pattern could be observed in the longitudinal velocity profiles from the 16/07/2017 – 04/10/2017 (Appendix B). A possible explanation for this region of reduced surface velocity is that there could be a topographic pinning point at the bed of the glacier in this region (Figure 32). Pinning points at the bed of the glacier can act as a stabilising feature for a calving terminus (Boyce et al. 2007). This is due to a high increase in resistance, resulting from basal and lateral drag around the pinning point area (Benn et al.

2007). Hart (2014) previously identified a pinning point at Tasman/Haupapa Glacier (gravity surveys were used to identify ice thickness and found a localised high area surrounded by lower bed elevations). This sudden increase in velocity past the substantially slow velocity area indicates this section of the terminus was buoyant over this time interval. Gravity surveys by Hart (2014) also indicate that a reverse slope bed profile is present at Tasman/Haupapa Glacier near the terminus. Given a reverse slope at the base of the glacier, water can permeate down the reverse slope resulting in an increase in water pressure. This reduces basal and lateral drag, thereby increasing velocity (Figure 55).

Surface velocity results from this study add to the previous but sporadic surface velocity record for Tasman Glacier (Purdie et al. 2018). The relationship between velocity and calving identified in this study may provide localised evidence that calving is the 'master' process over ice dynamics (the 'slave' process) (Benn et al. 2007). Previously at Tasman/Haupapa Glacier, an increase in crevasse development and propagation was observed from 1995-1997 by Kirkbride and Warren (1999) and attributed to flow acceleration. It was noted by Kirkbride and Warren (1999) that the increase in surface velocity preceded faster calving rates, suggesting that ice dynamics was the 'master' process and calving the 'slave' process. The results of this study align with the observations of Kirkbride and Warren (1999), in that a change in ice dynamics up glacier is needed to influence calving rates. However, care needs to be exercised when drawing conclusions on the patterns from surface velocity from this study due to the different time intervals over which velocity was calculated, dictated by the availability of satellite imagery.

6.0.2 Velocity and calving influencing subaqueous morphology

The differences in velocity at the terminus may explain the different retreat rates across the terminus and the subsequent formation of subaqueous morphology. It was suggested by Dykes et al. (2011) that multiple compounding factors and mechanisms may drive differences in retreat rates, and that changes in ice velocity across the lower terminus may partly explain these different retreat rates. Dykes et al. (2011) identified that the rate of retreat 2006-2008 was 166.67% faster compared to the retreat rate over the previous 6 years.

This study identified a relationship between surface velocity and subaqueous morphology from the longitudinal velocity profiles (Figure 33) and the length of subaqueous ice ramp lengths mapped by bathymetric survey (Figure 47, 48). As highlighted in section 5.0.2, the longitudinal velocity profiles showed an increase in surface velocity that extended ~1.5 km up from the glacier terminus (Figure 33). This velocity pattern was present in longitudinal profiles from the 16/07/2017 - 04/10/2017, suggesting this portion of the terminus would have been periodically buoyant during this period in 2017.

In contrast to findings by Rohl (2006), who found that surface velocity was higher at the eastern embayment ice cliff than the main ice cliff, surface velocity was greater from the middle of the glacier with velocity values up to 1.50 md^{-1} and slower surface velocity values were reported from the longitudinal profile on the outer margins with surface velocity up to 0.99 md^{-1}. Longer ice ramps on the eastern side of the terminus have consistently been identified from bathymetry surveys from 2013 – 2018), producing ice ramps up to 380 m in length (Figure 46,48,50). The slower velocity near the margins is due in part to the increase in lateral drag from the valley walls (Benn et al. 2007). This may produce a more stable setting

for ice ramp development, with a lower longitudinal strain rate resulting in less crevasse propagation (Figure 53)

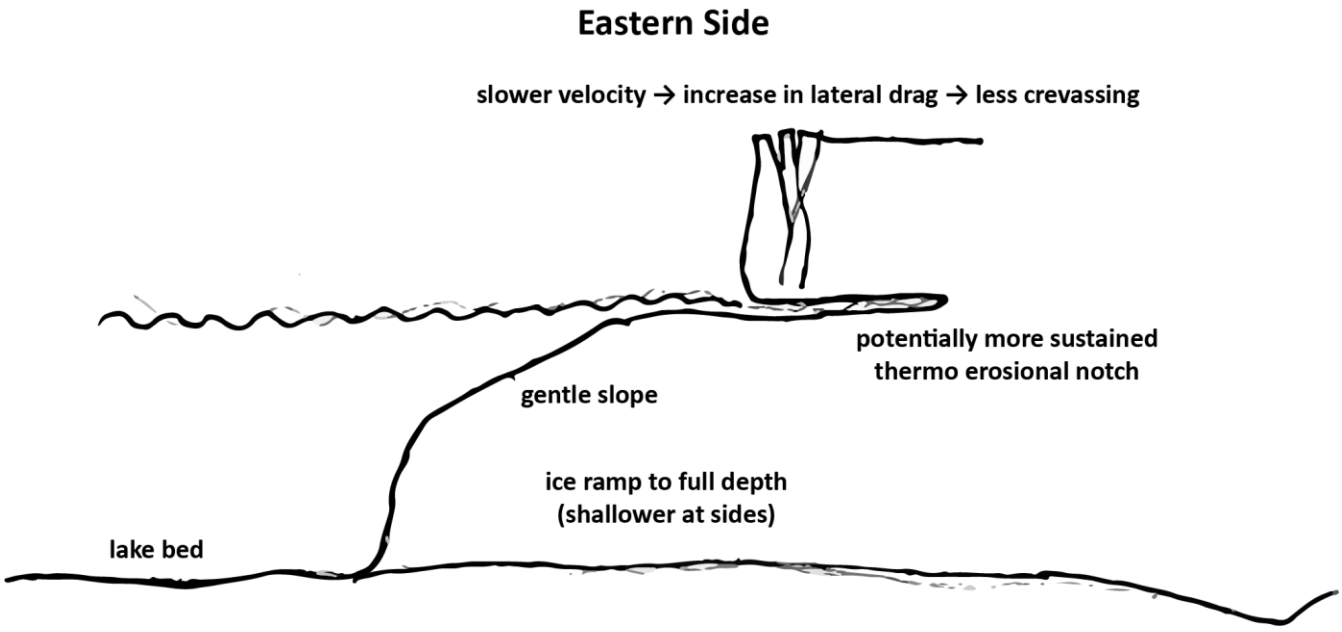

Figure 53: Sketch of processes in effect on the eastern side of the terminus that results in longer ice ramps

Utilising lake outlines from satellite imagery (Figure 50), the highest rate of terminus retreat was along the centre of the terminus. This was the region of the ice cliff where spatial variation in velocity along the terminus was linked to variation in subaqueous ice ramps. Higher velocity at the middle of the glacier can lead to an increase in longitudinal strain rate and the development and propagation of crevasse formation (Figure 2, 54) (Benn et al. 2007). Given the higher velocity and retreat rate of the middle of the glacier, with calving events not to depth, and combined with low melt rates, it would be expected that this area would produce the longest ice ramps. However, from the 2018 bathymetric survey (Figure 49), subaqueous ice ramps in the middle of the glacier with higher velocity rates were typically shorter and steeper in length than ice ramps identified on the eastern side of the terminus. This finding aligns with that of Robertson et al. (2012), who also found that terminus areas

with the fastest aerial retreat rates are not always the areas with the longest ice ramps. This difference suggests that processes other than just velocity and subaerial melt rates, such as subglacial hydrology, may also drive higher melt rates, affecting ice ramp development at the middle of the terminus (Figure 54). Although higher aerial calving rates and low melt rates are the primary driver of ice ramp development, they are not isolated from other processes.

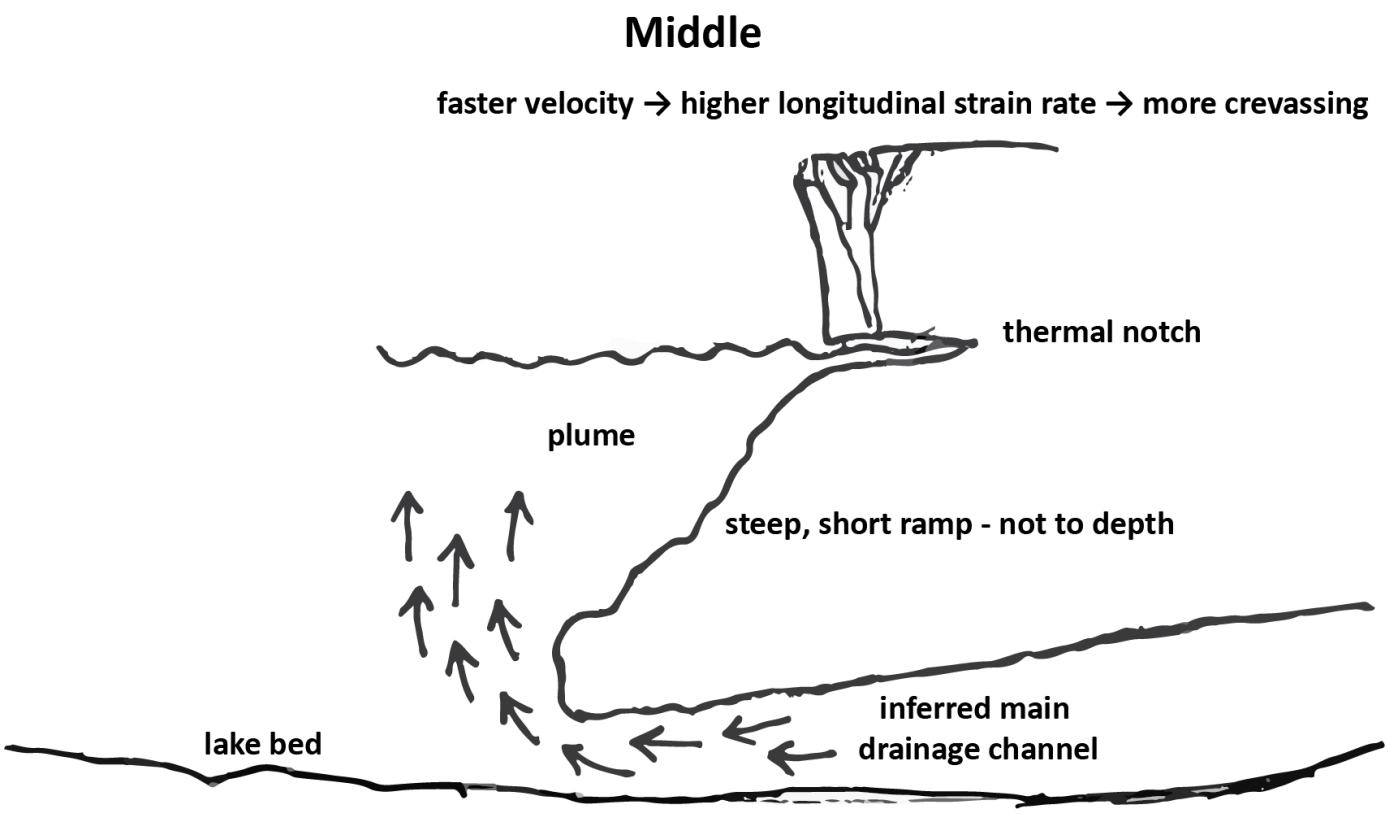

Figure 54: Sketch of processes at the central part of the terminus. Processes exhibit temporal variations and may not always be an active component of calving. This is an example of processes at the central section of the terminus.

Between 2013-2018 it was found that a combination of faster rates of aerial calving and subaerial melt rates appeared to be the primary control of ice ramp development. Aerial calving at Tasman/Haupapa Glacier is not calving the full depth of the glacier, resulting in extended subaqueous morphology across the width of the terminus (Figure 46,48). After the 2000-2008 survey it was proposed by Dykes et al. (2011) that the more stable, slower section

of the ice cliff would be subject to more vigorous thermal-erosional notching. This would increase the retreat rate by destabilising the ice cliff, eventually leading to large scale aerial calving. It was found by Rohl (2006) that spatial variation in thermal notch development was determined by water temperature, circulation, cliff geometry, debris supply and lake level fluctuations. Given the presence of thermal notches along the terminus from the 2018 survey and the slower velocities near the margins, large scale aerial calving arising from thermal-erosional notching may help explain the longer and larger ice ramps on the eastern side of the terminus, providing thermal notch development is not reset from changes in lake level.

6.0.3 Subaqueous morphology influencing calving

Although spatial and temporal variability of subaqueous morphology suggests multiple processes affect subaqueous morphology (Robertson et al. 2012), ice ramps develop at Tasman/Haupapa Glacier primarily through high aerial calving rates and low melt rates. While calving can act as a control on ice ramp development, it was found that calving can be influenced by subaqueous morphology through buoyant processes.

Calving at Tasman/Haupapa Glacier can be characterised by low frequency but high magnitude events (Dykes et al. 2011). During the 2015 survey (Figure 46) large, shelf-like ramps extending from the eastern side of the terminus measured up to 380 m, and at the end of 2015 a large subaqueous ice ramp buoyantly calved. The resulting iceberg contained basal debris, suggesting the ice ramp extended down to the bed of the glacier (Figure 9, Purdie et al. 2016). This large subaqueous calving event was followed by a large aerial calving event, supporting the theory that aerial calving can be triggered from an increase in the net upward

forces due to the sudden reduction in pressure from subaqueous calving (Benn & Evans, 2010).

Ice ramps will buoyantly calve once the ice exceeds the critical shear stress. The critical shear stress will vary depending on physical characteristics such as subglacial hydrology, weighting from debris and water temperatures (Hunter and Powell, 1998). The large subaqueous calving event at Tasman/Haupapa Glacier was likely the result of the ice ramp/shelf on the eastern side exceeding the critical shear stress and buoyantly calving. The 2016 survey (Figure 47) confirmed the eastern side had experienced a large calving event with an ice ramp extending only 150 m on the eastern side of the terminus. An area in the central part of the terminus that went to depth was recorded in the 2016 survey, with previous subaqueous calving events likely shearing off any ice ramp development. Out of 32 digitised ice ramps from bathymetric surveys between 2013-2018, only three protruded at least 200 m into the lake (Figure 47). The limited number of ice ramps that exceed 200 m length suggests that ice ramps greater that 200 m are highly prone to buoyant calving, given that no ice ramp has exceeded 380 m during the 6-year survey period. It may also indicate an upper limit to the length the ice ramps can grow to before they will buoyantly calve. Subaqueous ice ramps were identified in a 2008 survey of Tasman/Haupapa Glacier ~400 m in length by Robertson et al. (2012). The length of the ice ramps was attributed to a higher aerial calving rate over the subaqueous calving and melt rates, as well as thick debris cover on the ice ramps.

Ice ramps from the 2008 survey were found to have up to 10 m of debris cover. Debris cover can act as a weight, decreasing buoyant forces (Hunter & Powell, 1998). Debris falling from

the terminus onto ice ramps was initially observed by Warren & Kirkbride (1998). Robertson et al. (2012) identified potential sediment sources for the ice ramps that included supraglacial debris falling from the terminus, slumping from the lateral moraine and iceberg fallout. The debris cover of 5 – 10 m may have been enough to weight the ice ramp, reducing buoyant forces. This may partly explain how the ice ramp grew to ~400 m (Hunter & Powell 1998; Warren & Kirkbride 1998). During the 2018 survey there was a subaqueous calving event that produced several icebergs (Figure 49). The visible faces of the icebergs were not rich with englacial debris, indicating that the ramp length was not weighted by debris. While small amounts of debris may fall onto the ice ramps from the near terminus and lateral moraines, it is not thick enough to produce the weighted effects that was observed during the 2008 survey by Robertson et al. (2012).

6.1 Do the limnological characteristics of the lake influence subaqueous morphology?

Another aim of this study was to identify whether limnological processes at Tasman/Haupapa Glacier affect the formation and calving of subaqueous morphology. Subaqueous morphology is influenced by limnological characteristics and these characteristics vary spatially and temporally across the terminus creating variations in ice ramp length and style of calving. Key processes affecting subaqueous morphology are; lake level fluctuations, topography at the bed of the glacier, thermal notch development and water temperature variations (Figure 55).

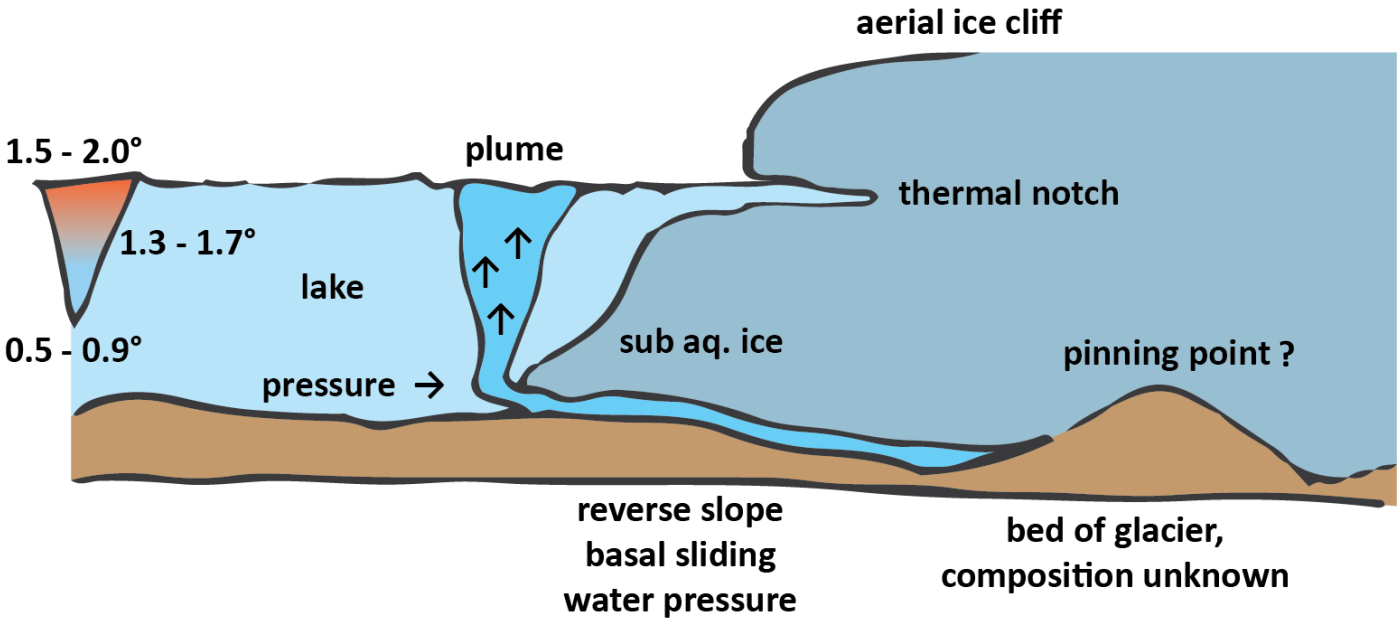

Figure 55: Key limnological processes affecting subaqueous morphology at Tasman/Haupapa Glacier. Results from this study indicate the presence of a reverse slope and a pinning point up glacier from the terminus, further work is needed to refine topographical relief at the base of the glacier. A reverse slope and an increase in water pressure can lead to an increase in basal sliding.

6.1.0 Water temperature at surface affects morphology

Results from this study indicate that lake conditions do influence subaqueous morphology. Surface water temperatures can affect the location of thermo-erosional notch development and influence the geometry of the glacier margin through thermo-erosion. It was noted by Kirkbride & Warren (1999) that the extended 'arm' of the lake on the eastern side of the terminus was influenced by ground water springs from the Murchison valley. Kirkbride and Warren (1999) suggested that water input from the moraine walls may increase the temperature of the lake water, which will enhance the melting at the terminus. From the 2018 survey, two lake 'arms' can be seen from the 2018 lake outline (Figure 48) on the eastern and western sides of the terminus, with the central ice cliff extending across the deepest part of the lake. Water seepage from the moraine walls was photographed during the 2018 survey (Figure 43), and the lake depth is shallower near the margins of the moraine walls. This

combined with the water seepage from the moraine walls may enhance thermo-erosional processes from higher water temperatures.

Thermal notches can develop where ice is exposed to water and exhibit seasonal variation as their development is inhibited during the winter months (Rohl 2006), as well as being enhanced by warm surface lake surface temperatures. During the 2016 and 2018 survey, thermal notches were recorded along the width of the glacier terminus. Strong seasonal variation was evident in the average surface lake temperatures from the Landsat-8 imagery (Figure 39), with surface temperatures during the spring and summer months ranging between 6 - 14 °C, which would have contributed to the development of thermal notches. Temperatures in the winter months showed negative temperatures due to the lake freezing during some winters, inhibiting thermo-erosional processes.

It was found by Rohl (2006) that the seasonal variation in thermal notch development was largely brought about by changes in water temperature, but that the spatial variability of the thermal notches was affected by multiple factors including water temperature, circulation, cliff geometry, debris supply and water level fluctuations. Thermal notch development along the terminus affects subaqueous morphology as it can control the rate of subaerial calving. The thermal notches destabilise the ice cliff, leading to greater rates of aerial calving (Figure 5). For example, because subaerial calving only involves ice above the water line, ice below the water remains attached (Figure 55). While thermal notches can affect the rate of aerial calving, the frequency and magnitude of the calving events is dependent on the pre-existing lines of weakness, such as crevasses at the terminus (Rohl, 2006).

Data collected during this study did not specifically target thermal notch development, but the presence of thermal notches along the terminal face will have affected aerial calving rates through undercutting of the ice cliff. Dykes (2013) found that 60% of all calving events between 2011 and 2012 were derived from thermal erosional processes, and that calving on the eastern margin was predominantly related to thermal erosional notch development. Calving from thermal notching explains the faster aerial calving rate over the slower subaqueous calving rate. Continual erosion at the thermal notch lengthens the extent of the undercutting, placing stress on a greater area of ice at the terminus (Figure 55). However, fluctuations in lake level can shift the location of water line melting and undercutting, slowing down thermal notch development, and in some cases resetting the thermal notch process (Rohl, 2006). It was found by Rohl (2006) that a 15 cm change in lake level within 24 hrs was enough to reset the thermal notch process. Lake level fluctuations from 2013-2018 showed seasonal variation, with lower lake levels during the winter and higher lake levels and greater lake level fluctuation in summer (Figure 34). Lake levels fluctuated from 2-3 m in the summer, frequently exceeding the 15 cm change in lake level needed to reset the thermal notch process within 24 hrs. This constant resetting of the thermal notch process will therefore have slowed down the extent of undercutting at the ice cliff.

It was found by Dykes (2013) that lake levels at Tasman/Haupapa Glacier can fluctuate up to 5 m within a 48-hr period. The fluctuation of the lake levels increases tensile stress through buoyant flexure, increasing the susceptibility to calving. Dykes (2013) found that while some calving events were associated with fluctuations in lakes levels, there were also multiple calving events that were not affected by lake levels. Findings from this study also found that

lake level fluctuations coincided with major calving events (Figure 36, 38), but it is noted that multiple calving events showed no association to lake level fluctuations between 2016-2017.

6.1.1 Water temperature below the surface affecting morphology

Melting of subaqueous ice in freshwater lakes is dependent on the lake's heat content and its ability to effectively transport heat to the terminus (Truffer & Motyka 2016b). Unlike tidewater glaciers, where meltwater circulation is driven by the density differences between subglacial fresh water and seawater, creating a density driven current (Motyka et al. 2003), the glacial meltwater entering a freshwater lake is controlled by the density differences in the glacial meltwater and the lake water. This in turn depends on water temperature, pressure and sediment concentration (Sugiyama, 2016). Sugiyama et al. (2016) found that thermal stratification of a freshwater lake could shape subaqueous morphology through preferential melting.

A series of vertical temperature profiles at Tasman/Haupapa Glacier indicate that the lake is largely isothermal between 10 – 110 m (Figure 39). A profile of water temperature taken close to the terminus and in the middle of the lake indicated an influx of cold water entering the lake from the base of the glacier. The decrease in temperature at depth is more rapid in the near-terminus profile than the more gradual decrease in temperature recorded in the middle of the lake. The effects of the cold subglacial meltwater will decrease with increasing distance from the terminus due to mixing, explaining the smaller decrease in temperature with depth recorded in the middle of the lake.

A study by Slater et al. (2015) indicated that subglacial hydrology in a tide water setting can influence the type and rate of calving as well as total melt. In a tide water setting, buoyant plumes of meltwater arising from subglacial melt water are considered an important component of subaqueous melting and thermal undercutting of the ice cliff (How et al. 2019). It was noted by How et al. (2019) that waterline calving events were the dominant calving type in regions where water plumes were identified along the terminus of the Tunabreen Glacier in Svalbard. It was also noted that while subaqueous calving events were rare, they often took place at sites of water plumes producing large debris-laden icebergs.

Although upwelling in freshwater lakes is rare due to the small density differences between subglacial meltwater and lake water, observations of upwelling have been made (Watson 1995; Rohl 2005; Boyce et al. 2007). A water plume in front of the central ice cliff was recorded from satellite imagery at Tasman/Haupapa Glacier (Figure 41). This water plume was identified in front of the central ice cliff. It was noted by Purdie et al. (2016) that subglacial hydrology and/or convection currents may affect subaqueous morphology along the terminus.

During the 6-year survey period this study found that the ice ramps at Tasman/Haupapa Glacier exhibit different profiles depending on their spatial location (Figure 44, 45, 46, 47, 48). Ice ramps on the eastern side of the terminus have predominantly longer, gentle slopes and shelf-like profiles. This is due to their development in a more stable area on the outer margins, with lower ice velocities and lack of upwelling in the lake; calving in this area is driven by buoyancy processes. Ice ramps in the middle of terminus have shorter and steeper profiles.

Water plumes at the centre of the central ice cliff are more frequent and produce an increased subaqueous melt rate indicative of a cavity at the base of glacier, which affects the length of any subaqueous morphology (Dykes, 2013).

Due to the closed system of freshwater lakes, density-driven circulation of their cold water can result in low subaqueous melt rates (Truffer & Motyka, 2016b). The changing length and location of ice ramps from 2013-2018 (Figure 50) indicates that ramps calve and melt at sub-annual time scales. The total change in the length of the ice ramps was identified in 2013/2014 using the subaqueous melt rate of 0.03 md^{-1} based on a lake temperature of 1.5°C (Rohl, 2005). The total change in length over 397 days, assuming no calving took place, was 11.91 m (0.03 md^{-1}). Water temperature at the surface on average was 2°C warmer during the spring and summer months than temperatures recorded during the autumn and winter months. Water temperature at depth during spring and summer of 2015 were found to be ~0.3°C warmer than temperatures in the autumn and winter months of 2016 (Figure 39).

Due to the gap in ice ramps identified from the 2016 survey, ice ramps surveyed in 2018 were assumed to be new ramps that had developed since the previous survey. The change in length of the ice ramps based on Rohl's, (2005) melt rate was 17.28 m (0.03 md^{-1}). Lake temperatures near the terminus from the temperature profile in 2015 were 1.6 - 1.7°C at 10 – 175 m depth, which are comparable to the lake temperature of 1.5°C and 0.03 md^{-1} melt rate derived by Rohl (2005). For greater certainty that no calving events took place, time series photos were used to identify calving events.

Time series photos from 2016-2018 showed few subaqueous calving events, indicating the change in ice ramp growth for 2016-2018 was not subject to a change in length from subaqueous calving. How et al. (2019) used a time lapse camera to record calving events at the Tunabreen Glacier. The camera took 3 images every three seconds for a 28 hr period during summer. Using this method, they captured 358 calving events and were able to identify submarine melt rates as the main driver of ablation at the terminus. Given that many processes in a freshwater lake setting are an order of magnitude lower than in a marine environment (Warren & Kirkbride 2003; Truffer and Motyka 2016), a similar process could be set up at Tasman/Haupapa Glacier during the spring and summer, but with a longer time interval capture between images. Currently a time lapse camera is set up that records 14 images per day at the terminus, but this can miss the location of subaqueous calving events due to the time intervals between photos.

A series of vertical water temperature profiles across the terminus could be used to provide information on the spatial variation in temperature across the terminus. If temperature varies spatially across the terminus, ice ramps may be subject to different melt rates, thereby affecting ice ramp development. Melt rates may be a key process in triggering large changes in the behaviour of the glacier such as rapid retreat, but once the process of rapid retreat has commenced, mechanical instabilities of the ice will be the dominant process over melting (Truffer and Motyka 2016).

6.1.2 Effects of terminus buoyancy and subaqueous morphology

A buoyant terminus can be maintained as part of a stable setting in a freshwater environment, as processes in a freshwater setting are generally an order of magnitude lower (Truffer and

Motyka 2016; Boyce et al. 2007; Benn & Astrom 2018). Long floating ice-tongues in a freshwater setting can accommodate slow perturbations resulting in viscoelastic deformation instead of a calving event (Boyce et al. 2006; Chernos et al. 2016). When the terminus can no longer accommodate the bending stresses, high magnitude calving events will occur until the terminus can reach a stable position where the terminus height exceeds the floatation thickness (van der Veen 2002).

The terminus profile constructed from the 2016 survey had the lowest ice cliff heights and deepest depths of 250 m in the middle of the terminus (Figure 51). Given the low ice cliff heights and deep water it is expected that buoyancy forces will be focused on this region (Boyce et al. 2007; Purdie et al. 2016). In order for the terminus to prevent flotation, the height of the terminus needs to exceed 23 m ± 5 m. However, it is noted by Purdie et al. (2016) that Eq (2) will overestimate H_F on debris covered glaciers if the weight added by the debris layer is not accounted for, as debris thickness may be enough keep the terminus grounded. Estimates of debris thickness at the terminus range between 0.5 - 2.0 m (Kirkbride & Warren 1999; Purdie & Fitzharris 1999), using a debris thickness of 2 m would reduce Ho by 1.3 m (Purdie et al. 2016).

The central part of the terminus had subaerial cliff heights between 14.8 m ± 5 m and 16.6 m ± 5 m. Although these heights were below the floatation thickness, it is unlikely that the entire terminus was buoyant due to cliff height exceeding the floatation thickness at each margin. Buoyancy was also reduced due to shallow lake depths and lateral drag at the glacier margins, and therefore greater water depth and thinning of the terminus would have been needed

before full floatation was achieved (Dykes 2013). The Tasman/Haupapa Glacier is characterised as undergoing low frequency, high magnitude calving events (Dykes 2013). Currently, these large events are the result of subaqueous ice ramps buoyantly calving, rather than the disintegration of a floating terminus (Dykes et al. 2013).

While the terminus was not fully buoyant, there was spatial variation in the longitudinal velocity profiles where the terminus was partially buoyant ~1.5 km up glacier (Figure 33), from 16/07/2017 – 04/10/2017. This indicated that part of the terminus may be buoyant, buoyancy may have been the result of a reverse slope, meaning that lake water could penetrate further up glacier, decreasing effective pressure and increasing basal sliding (Figure 56). Buoyancy of parts of the terminus could be looked at as further areas of study, pinning points and buoyant sections could be refined using high resolution surface elevation data. As mentioned in section 5.0.1, above the region of higher surface velocities there was a region where surface velocity was 50% slower than that recorded close to the terminus. This may have been an area of stick slip, which could have been acting as a stabilising point for the ice as the terminus retreated to this point. Evidence of a reverse slope was identified by Hart (2014) using gravity surveys. Hart (2014) found the bed gradually deepened up glacier from the terminus with lower ice thickness measured at the terminus and greater ice thickness adjacent to Ball Glacier.

6.1.3 Lake level fluctuations influencing subaqueous morphology

A hydrological connection was found by Boyce et al. (2007) between lake level increases and a corresponding decrease in water temperature at the Mendenhall Glacier. It was noted by

Boyce et al. (2007) that thinning rates and elevated lake levels could increase buoyancy forces at the terminus. Tasman/Haupapa lake levels fluctuate up to 4.5 m seasonally, with the greatest fluctuations during the main melt season between September-February (Figure 36, 38).

Major calving events at Tasman/Haupapa glacier between 2016-2018 coincided with lake level fluctuations. The calving event on 21/01/2016 was associated with a lake level increase > 2.0 m, with the two other large calving events associated with smaller increases < 1.0 m. The lake temperatures at the time of the major calving events are unknown, the elevated lake levels increased buoyancy forces at the terminus that could not be accommodated by viscoelastic deformation, resulting in large calving events.

While the lake level fluctuations are consistent with observation from the Mendenhall Glacier, the correlation with a decrease in water temperature cannot be compared. It is noted that smaller calving events took place throughout 2016-2018 that also coincided with lake level increases at Tasman/Haupapa Glacier. From this analysis, the magnitude of the calving events cannot be defined solely through lake level fluctuations. Future research could refine the relationship between lake level fluctuations, rainfall and calving events by incorporating continuous vertical temperature profiles to help refine the conditions required to trigger calving through buoyant processes.

Conclusion

This thesis identified the relationships between processes and feedbacks at Tasman/Haupapa Glacier between calving, velocity and subaqueous morphology. Ice dynamics were compared with calving rates to test the theory of the 'master' and 'slave' theory outlined by (Benn et al. 2007). Velocity was found to influence calving whereby an increase in surface velocity would result in higher longitudinal strain rates and crevasse propagation that would lead to calving. Surface velocity also influenced subaqueous morphology across the width of the terminus. The margins of the terminus with slower surface velocity and high lateral drag, had less crevasse propagation and were considered a more stable, these areas typically had the longest ice ramps. The central part of the ice cliff with higher surface velocity was more prone to crevassing and was not stabilised by the outer margins. Ice ramps in these areas were typically steeper and shorter.

Subaqueous morphology influenced the rate of calving at Tasman/Haupapa Glacier through buoyant calving processes. Ice ramps that developed in more stable areas could grow in length until the weight of the ice ramp buoyantly calved. Calving was also found to affect the formation of subaqueous morphology. Higher aerial calving rates compared to subaqueous calving rates lead to ice ramp development across the terminus. Results from this study could not conclusively say that calving had a direct effect on velocity or that subaqueous morphology had an effect on surface velocity. It is acknowledged that no one single process can explain calving, velocity and subaqueous morphology, it is likely to involve a combination of processes at different spatial and temporal scales that may include relationships where calving and subaqueous morphology affect surface velocity, of which, was not identified in

this study.

Temporal patterns exist between surface velocity and calving, with the higher surface velocities and number of calving events taking place during the spring and summer months, including four major calving events. Three out of four major calving events had a velocity increase prior to the calving event, indicating that velocity is not always an indication that a large calving event is imminent, and that other processes may also contribute to triggering large calving events.

At the terminus an acceleration in surface velocity was seen on the longitudinal velocity profiles. This was followed by a substantially slow area between 1.5-2.8 km up glacier. The location of a possible pinning point was identified from longitudinal velocity profiles. The pinning point may act as a stabilising feature as the terminus retreats back to this point.

Velocity and calving have a strong relationship with subaqueous morphology. Velocity varies spatially across the terminus with lower velocities on the eastern side of the terminus. The slower velocity combined with the increase in lateral drag at the margins of the glacier means that calving events are less frequent resulting in a more stable setting for long, gently sloping ice ramps to form. The velocity in the central part of the terminus is faster with higher longitudinal strain rate and more crevassing. Shorter, steeper ice ramps are more typical in this area. Thermal notches exist across the terminus which can cause large calving events and a higher aerial calving rate.

Ice ramps develop at Tasman/Haupapa Glacier primarily through high aerial calving rates and low melt rates. The dominant processes affecting subaqueous morphology are buoyant processes. The changing length and location of ice ramps indicates that ramps calve and melt at sub-annual time scales. Of the ice ramps digitised from bathymetric surveys, only three protruded at least 200 m into the lake. The limited number of ice ramps that exceed 200 m length suggests that ice ramps greater that 200 m are highly prone to buoyant calving. It may also indicate an upper limit to the length ice ramps can grow before they will buoyantly calve.

This study also identified limnological processes at Tasman/Haupapa Glacier that affected the formation and calving of subaqueous morphology. Subaqueous morphology is influenced by limnological characteristics and these characteristics vary spatially and temporally across the terminus creating variation in ice ramp length and style of calving.

Surface water temperatures can affect the location of thermo-erosional notch development and influence the geometry of the glacier margin through thermo-erosion. Strong seasonal variation was evident in the average surface lake temperatures, with surface temperature increases during the spring and summer months contributing to the development of thermal notches. Temperatures in the winter months showed negative temperatures due to the lake freezing during some winters, inhibiting thermo-erosional processes. Fluctuations in lake level can shift notches by changing the location of water line melting and undercutting, slowing down thermal notch development. Lake level fluctuations showed seasonal variation, with lower lake levels during the winter and higher lake levels and greater lake level fluctuation in summer. Lake level fluctuations coincided with major calving events, but it is noted that

multiple calving events showed no association to lake level fluctuations.

A series of vertical temperature profiles at Tasman/Haupapa Glacier indicate that the lake is largely isothermal. A profile of water temperature taken close to the terminus and in the middle of the lake indicated an influx of cold water entering the lake from the base of the glacier. The water plume was identified in front of the central ice cliff. It was noted that subglacial hydrology and/or convection currents may affect subaqueous morphology along the terminus.

Terminus cliff heights at the centre of the glacier are below the floatation thickness, but it is unlikely that the entire terminus is buoyant due to cliff height exceeding the floatation thickness at each margin. Currently, large calving events are the result of subaqueous ice ramps buoyantly calving, rather than the disintegration of a floating terminus (Dykes et al. 2013).

This thesis has provided an outline of how multiple processes interact at the terminus to influence calving and subaqueous morphology by identifying relationships between velocity, calving and subaqueous morphology, and by identifying the limnological characteristics that affect subaqueous morphology

References

Anderton, P. (1975). Tasman glacier 1971-1973. *Hydrological research: annual report No. 33. Wellington: Ministry of Works and Development for the National Water and Soil Conservation Organisation.*

Barsi, J. A., Schott, J. R., Hook, S. J., Raqueno, N. G., Markham, B. L., & Radocinski, R. G. (2014). Landsat-8 thermal infrared sensor (TIRS) vicarious radiometric calibration. *REMOTE SENSING, 6*(11), 11607-11626. doi:10.3390/rs61111607

Benn, D. I., & Åström, J. A. (2018). Calving glaciers and ice shelves. *Advances in Physics: X, 3*(1), 1513819. doi:10.1080/23746149.2018.1513819

Benn, D. I., Bolch, T., Hands, K., Gulley, J., Luckman, A., Nicholson, L. I., . . . Wiseman, S. (2012). Response of debris-covered glaciers in the Mount Everest region to recent warming, and implications for outburst flood hazards. *Earth-Science Reviews, 114*(1-2), 156-174. doi:10.1016/j.earscirev.2012.03.008

Benn, D. I., & Evans, D. J. A. (2010). *Glaciers & glaciation* (2nd ed.). London: Hodder Education.

Benn, D. I., Warren, C. R., & Mottram, R. H. (2007). Calving processes and the dynamics of calving glaciers. *Earth Science Reviews, 82*(3), 143-179. doi:10.1016/j.earscirev.2007.02.002

Berthier, E., Vadon, H., Baratoux, D., Arnaud, Y., Vincent, C., Feigl, K. L., . . . Legrésy, B. (2005). Surface motion of mountain glaciers derived from satellite optical imagery. *Remote Sensing of Environment, 95*(1), 14-28. doi:10.1016/j.rse.2004.11.005

Brown, C.S., Meier, M.F., & Post, A. (1982). Calving speed of Alaska tidewater glaciers, with application to Columbia Glacier. *U.S. Geological Survey Professional Paper 1258-C,* 13 pp.

Bowen, A. D., Yoerger, D. R., German, C. C., Kinsey, J. C., Jakuba, M. V., Gomez-Ibanez, D., . . . Mayer, L. (2014). *Design of Nereid-UI: A remotely operated underwater vehicle for oceanographic access under ice*.

Boyce, E. S., Motyka, R. J., & Truffer, M. (2007). Flotation and retreat of a lake-calving terminus, Mendenhall Glacier, southeast Alaska, USA. *Journal of Glaciology, 53*(181), 211-224.

Brodrick, T.N. (1891). Report on the Tasman Glacier. *Appendix J House Rep NZ. 1(C-1A):*39–43.

Carrivick, J. L., & Tweed, F. S. (2013). Proglacial lakes: character, behaviour and geological importance. *Quaternary Science Reviews, 78*, 34-52. doi:10.1016/j.quascirev.2013.07.028

Chernos, M., Koppes, M., & Moore, R. D. (2016). Ablation from calving and surface melt at lake-terminating Bridge Glacier, British Columbia, 1984-2013. *CRYOSPHERE, 10*(1), 87-102. doi:10.5194/tc-10-87-2016

Chikita, K.A., & T. Yamada., (2005). The expansion of Himalayan glacial lakes due to global warming: field observations and numerical simulation. *IAHS Publ. 295 (Symposium at Foz do Iguac¸u 2005 – Regional Hydrological Impacts of Climatic Change – Impact Assessment and Decision Making)*, 111–119.

Chinn, T. J. (2001). Distribution of the glacial water resources of New Zealand. *Journal of Hydrology (New Zealand), 40*(2), 139-187.

Chinn, T.J., Kargel, J.S., Leonard, G.J., Haritashya, U.K., & Plesants, M. (2014). New Zealand's Glaciers*. Kargel J. S., Leonard G. J., Bishop M. P., Kaab A., Raup B., editor. Global land ice measurements from space. Berlin: Springer Praxis.* 675–715.

Cuffey, K., & Paterson, W. S. B. (2010). *The physics of glaciers* (4th ed.). Burlington, MA: Butterworth-Heinemann/Elsevier.

Dykes, R. C. (2013). *A multi-parameter study of iceberg calving and the retreat of Haupapa/Tasman Glacier, South Island, New Zealand: a thesis presented in partial fulfilment of the requirements for the degree of Doctor of Philosophy in Geography at Massey University, Palmerston North, New Zealand.* Massey University,

Dykes, R. C., Brook, M. S., Robertson, C. M., & Fuller, I. C. (2011). Twenty-First Century Calving Retreat of Tasman Glacier, Southern Alps, New Zealand. *Arctic, Antarctic, and Alpine Research, 43*(1), 1-10. doi:10.1657/1938-4246-43.1.1

Funk, M., & Röthlisberger, H. (1989). Forecasting the Effects of a Planned Reservoir which will Partially Flood the Tongue of Unteraargletscher in Switzerland. *ANNALS OF GLACIOLOGY, 13*, 76-81. doi:10.3189/S0260305500007679

Gardner, A. S., Moholdt, G., Cogley, J. G., Wouters, B., Arendt, A. A., Wahr, J., . . . Institutionen för, g. (2013). A reconciled estimate of glacier contributions to sea level rise: 2003 to 2009. *Science (New York, N.Y.), 340*(6134), 852-857. doi:10.1126/science.1234532

Gulley, J. D., Benn, D. I., Screaton, E., & Martin, J. (2009). Mechanisms of englacial conduit formation and their implications for subglacial recharge. *Quaternary Science Reviews, 28*(19), 1984-1999. doi:10.1016/j.quascirev.2009.04.002

Hart,R. (2014). The Ice Thickness Distribution of a Debris-Covered Glacier : Tasman Glacier, New Zealand. *MSc thesis Victoria University of Wellington*.

Haritashya, U. K., Pleasants, M. S., & Copland, L. (2015). Assessment of the Evolution in Velocity of Two Debris-Covered Valley Glaciers in Nepal and New Zealand. *Geografiska Annaler: Series A, Physical Geography, 97*(4), 737-751. doi:10.1111/geoa.12112

Herman, F., Anderson, B., & Leprince, S. (2011). Mountain glacier velocity variation during a retreat/advance cycle quantified using sub-pixel analysis of aster images. *Journal of Glaciology, 57*(202), 197-207. doi:10.3189/002214311796405942

Hoffman, M., & Price, S. (2014). Feedbacks between coupled subglacial hydrology and glacier dynamics. *Journal of Geophysical Research: Earth Surface, 119*(3), 414-436. doi:10.1002/2013JF002943

Horgan, H. J., Anderson, B., Alley, R. B., Chamberlain, C. J., Dykes, R., Kehrl, L. M., & Townend, J. (2015). Glacier velocity variability due to rain-induced sliding and cavity formation. *EARTH AND PLANETARY SCIENCE LETTERS, 432*, 273-282. doi:10.1016/j.epsl.2015.10.016

How, P., Schild, K. M., Benn, D. I., Noormets, R., Kirchner, N., Luckman, A., . . . Borstad, C. (2019). Calving controlled by melt-under-cutting: Detailed calving styles revealed through time-lapse observations. *ANNALS OF GLACIOLOGY*, 1-12. doi:10.1017/aog.2018.28

Hunter, L. E., & Powell, R. D. (1998). Ice foot development at temperate tidewater margins in Alaska. *Geophysical Research Letters, 25*(11), 1923-1926. doi:10.1029/98GL01403

Immerzeel, W. W., Kraaijenbrink, P. D. A., Shea, J. M., Shrestha, A. B., Pellicciotti, F., Bierkens, M. F. P., & De Jong, S. M. (2014). High-resolution monitoring of Himalayan glacier dynamics using unmanned aerial vehicles. *Remote Sensing of Environment, 150*, 93-103. doi:10.1016/j.rse.2014.04.025

Immerzeel, W. W., Pelliciotti, F., & Bierkens, M. F. P. (2013). Rising river flows throughout the twenty-first century in two Himalayan glacierized watersheds. *Nature Geoscience, 6*(9), 742. doi:10.1038/ngeo1896

Javernick, L., Brasington, J., & Caruso, B. (2014). Modelling the topography of shallow braided rivers using Structure-from-Motion photogrammetry. *Geomorphology 213*, 166–182.

Kaab, A., Berthier, E., Nuth, C., Gardelle, J., & Arnaud, Y. (2012). Contrasting patterns of early twenty-first-century glacier mass change in the Himalayas. *Nature, 488*(7412), 495-498. doi:http://www.nature.com/nature/journal/v488/n7412/abs/nature11324.html#supplementary-information

Kääb, A., Bolch, T., Casey, K., Heid, T., Kargel, J., J Leonard, G., . . . Raup, B. (2014). Glacier Mapping and Monitoring Using Multispectral Data. doi:10.5167/uzh-102068

Kääb, A., Winsvold, S. H., Altena, B., Nuth, C., Nagler, T., & Wuite, J. (2016). Glacier Remote Sensing Using Sentinel-2. Part I: Radiometric and Geometric Performance, and Application to Ice Velocity. *REMOTE SENSING, 8*(7), 598. doi:10.3390/rs8070598

Kirkbride, M. P., & Warren, C. R. (1999). Tasman Glacier, New Zealand: 20th-century thinning and predicted calving retreat. *Global and Planetary Change, 22*(1), 11-28. doi:10.1016/S0921-8181(99)00021-1

Kirkbride, M., &Warren,C. (1997). Calving processes at a grounded ice cliff. *Ann.Glaciol.24*, 116–121.

Kraaijenbrink, P. D. A., Shea, J. M., Pellicciotti, F., Jong, S. M. d., & Immerzeel, W. W. (2016). Object-based analysis of unmanned aerial vehicle imagery to map and characterise surface features on a debris-covered glacier. *Remote Sensing of Environment, 186*, 581-595. doi:10.1016/j.rse.2016.09.013

Larsen, C. F., Burgess, E., Arendt, A. A., O'Neel, S., Johnson, A. J., & Kienholz, C. (2015). Surface melt dominates Alaska glacier mass balance. *Geophysical Research Letters, 42*(14), 5902-5908. doi:10.1002/2015GL064349

Leprince, S., Barbot, S., Ayoub, F., & Avouac, J. P. (2007). Automatic and Precise Orthorectification, Coregistration, and Subpixel Correlation of Satellite Images, Application to Ground Deformation Measurements. *IEEE Transactions on Geoscience and Remote Sensing, 45*(6), 1529-1558. doi:10.1109/TGRS.2006.888937

Liu, Y. C., Wu, J., Liu, Y., Hu, B. X., Hao, Y. H., Huo, X. L., . . . Wang, Z. L. (2015). Analyzing effects of climate change on streamflow in a glacier mountain catchment using an ARMA model. *QUATERNARY INTERNATIONAL, 358*, 137-145. doi:10.1016/j.quaint.2014.10.001

Luckman, A., Benn, D. I., Cottier, F., Bevan, S., Nilsen, F., & Inall, M. (2015). Calving rates at tidewater glaciers vary strongly with ocean temperature. *NATURE COMMUNICATIONS, 6*, 8566. doi:10.1038/ncomms9566

Mair, D., Nienow, P., Sharp, M., Wohlleben, T., & Willis, I. (2002). Influence of subglacial drainage system evolution on glacier surface motion: Haut Glacier d'Arolla, Switzerland. *Journal of Geophysical Research: Solid Earth, 107*(B8).

Meier, M. F., Dyurgerov, M. B., Rick, U. K., O'Neel, S., Pfeffer, W. T., Anderson, R. S., . . . Glazovsky, A. F. (2007). Glaciers Dominate Eustatic Sea-Level Rise in the 21st Century. *Science, 317*(5841), 1064-1067. doi:10.1126/science.1143906

Meier, M.F., & Reeh, N. (1994). Columbia Glacier during rapid retreat: interaction between glacier flow and iceberg calving dynamics. *Report of a workshop on 'The calving rate of the West Greenland glaciers in response to climate change', Copenhagen, 13–15 September, 1993. Copenhagen: Danish Polar Center,* 63–83.

Miles, E. S., Willis, I. C., Arnold, N. S., Steiner, J., & Pellicciotti, F. (2017). Spatial, seasonal and interannual variability of supraglacial ponds in the Langtang Valley of Nepal, 1999–2013. *Journal of Glaciology, 63*(237), 88-105. doi:10.1017/jog.2016.120

Motyka, R. J., Hunter, L., Echelmeyer, K. A., & Connor, C. (2003). Submarine melting at the terminus of a temperate tidewater glacier, LeConte Glacier, Alaska, USA. *ANNALS OF GLACIOLOGY, 36*(1), 57-65.

Naito, N., M. Nakawo, T. Kadota, & C.F. Raymond. (2000).Numerical simulation of recent shrinkage of Khumbu Glacier, Nepal Himalayas. *IAHS Publ. 264 (Symposium at Seattle 2000 –Debris-Covered Glaciers),* 245–254.

Narama, C., Daiyrov, M., Tadono, T., Yamamoto, M., Kääb, A., Morita, R., & Ukita, J. (2017). Seasonal drainage of supraglacial lakes on debris-covered glaciers in the Tien Shan Mountains, Central Asia. *GEOMORPHOLOGY, 286*, 133-142. doi:10.1016/j.geomorph.2017.03.002

Neal, M., Blanchard, T., Hubbard, A., Chauché, N., Bates, R., & Woodward, J. (2012). A hardware proof of concept for a remote-controlled glacier-surveying boat. *Journal of Field Robotics, 29*(6), 880-890. doi:10.1002/rob.21420

Nienow, P., Sharp, M., & Willis, I. (1998). Seasonal changes in the morphology of the subglacial drainage system, Haut Glacier d'Arolla, Switzerland. *Earth Surface Processes and Landforms, 23*(9), 825-843. doi:10.1002/(SICI)1096-9837(199809)23:9<825::AID-ESP893>3.0.CO;2-2

Purdie, H., Bealing, P., Tidey, E., Gomez, C., & Harrison, J. (2016). Bathymetric evolution of Tasman Glacier terminal lake, New Zealand, as determined by remote surveying techniques. *Global and Planetary Change, 147*, 1-11. doi:10.1016/j.gloplacha.2016.10.010

Purdie H., Anderson B., Mackintosh A. and Lawson W. (2018). *Revisiting glaciological measurements on Haupapa/Tasman Glacier, New Zealand, in a contemporary context.* Geografiska Annaler, Series A: Physical Geography 100(4): 351-369. http://dx.doi.org/10.1080/04353676.2018.1522958.

Purdie J.M. (1996). Ice loss at the terminus of the Tasman Glacier. Unpublished MSc thesis, lodged in the *Library, University of Otago*. 191 p.

Purdie, J., & Fitzharris, B. (1999). Processes and rates of ice loss at the terminus of Tasman Glacier, New Zealand. *Global and Planetary Change, 22*(1), 79-91. doi:10.1016/S0921-8181(99)00027-2

Quincey, D. J., & Glasser, N. F. (2009). Morphological and ice-dynamical changes on the Tasman Glacier, New Zealand, 1990–2007. *Global and Planetary Change, 68*(3), 185-197. doi:10.1016/j.gloplacha.2009.05.003

Radic, V., & Hock, R. (2014). Glaciers in the Earth's Hydrological Cycle: Assessments of Glacier Mass and Runoff Changes on Global and Regional Scales. *Surveys in Geophysics, 35*(3), 813. doi:10.1007/s10712-013-9262-y

Radic, V., Hock, R., Bliss, A., Beedlow, A. C., Miles, E., & Cogley, G. (2013). Regional and global projections of 21st century glacier mass changes in response to climate scenarios from global climate models. *Climate Dynamics, 42*(1-2), 37.

Radic, V., Hock, R., Oerlemans, J., Uppsala, u., Miljö- och, l., Geovetenskapliga, s., . . . Institutionen för, g. (2008). Analysis of scaling methods in deriving future volume evolutions of valley glaciers. *Journal of Glaciology, 54*(187), 601-612. doi:10.3189/002214308786570809

Redpath, T. A. N., Sirguey, P., Fitzsimons, S. J., & Kääb, A. (2013). Accuracy assessment for mapping glacier flow velocity and detecting flow dynamics from ASTER satellite imagery: Tasman Glacier, New Zealand. *Remote Sensing of Environment, 133*, 90-101. doi:10.1016/j.rse.2013.02.008

Rignot, E., Fenty, I., Xu, Y., Cai, C., & Kemp, C. (2015). Undercutting of marine-terminating glaciers in West Greenland. *Geophysical Research Letters, 42*(14), 5909-5917. doi:10.1002/2015GL064236

Robertson, C. M., Benn, D. I., Brook, M. S., Fuller, I. C., & Holt, K. A. (2012). Subaqueous calving margin morphology at Mueller, Hooker and Tasman glaciers in Aoraki/Mount Cook National Park, New Zealand. *Journal of Glaciology, 58*(212), 1037-1046. doi:10.3189/2012JoG12J048

Röhl,K. (2005).Terminus Disintegration of Debris-Covered , Lake-Calving Glaciers. *PhD thesis Department of Geography, University of Otago, Dunedin.*

Rohl, K. (2006). Thermo-erosional notch development at fresh-water-calving Tasman Glacier, New Zealand. *Journal of Glaciology, 52*(177), 203-213. doi:10.3189/172756506781828773

Rohl, K. (2008). Characteristics and evolution of supraglacial ponds on debris-covered Tasman Glacier, New Zealand. *Journal of Glaciology, 54*(188), 867-880. doi:10.3189/002214308787779861

Sakai, A., Takeuchi, N., Fujita, K., & Nakawo, M., (2000). Role of supraglacial pond in the ablation process of a debris-covered glacier in the Nepal Himalayas. *Debris-Covered Glaciers: Proceeding ofan International Workshop at the University Washington in Seattle. TAHS Publication, 264:* 119-130.

Sakai, A., Takeuchi, N., Fujita, K., & Nakawo, M. (2000). Role of supraglacial pond in the ablation process of a debris-cov- ered glacier in the Nepal Himalayas. *Debris-Covered Glaciers: Proceeding of an Internation- al Workshop at the University Washington in Seattle. IAHS Publication, 264:* 119-130.

Scambos, T. A., Dutkiewicz, M. J., Wilson, J. C., & Bindschadler, R. A. (1992). Application of image cross-correlation to the measurement of glacier velocity using satellite image data. *Remote Sensing of Environment, 42*(3), 177-186. doi:10.1016/0034-4257(92)90101-O

Scherler, D., Leprince, S., & Strecker, M. R. (2008). Glacier-surface velocities in alpine terrain from optical satellite imagery—Accuracy improvement and quality assessment. *Remote Sensing of Environment, 112*(10), 3806-3819. doi:10.1016/j.rse.2008.05.018

Slater, D. A., Nienow, P. W., Cowton, T. R., Goldberg, D. N., & Sole, A. J. (2015). Effect of near-terminus subglacial hydrology on tidewater glacier submarine melt rates. *Geophysical Research Letters, 42*(8), 2861-2868. doi:10.1002/2014GL062494

Song, C., Ke, L., Huang, B., & Richards, K. S. (2015). Can mountain glacier melting explains the GRACE-observed mass loss in the southeast Tibetan Plateau: From a climate perspective? *Global and Planetary Change, 124*, 1-9. doi:10.1016/j.gloplacha.2014.11.001

Song, C., Sheng, Y., Ke, L., Nie, Y., & Wang, J. (2016). Glacial lake evolution in the southeastern Tibetan Plateau and the cause of rapid expansion of proglacial lakes linked to glacial-hydrogeomorphic processes. *Journal of Hydrology, 540*, 504-514. doi:10.1016/j.jhydrol.2016.06.054

Sugiyama, S., Minowa, M., Sakakibara, D., Skvarca, P., Sawagaki, T., Ohashi, Y., . . . Chikita, K. (2016). Thermal structure of proglacial lakes in Patagonia. *Journal of Geophysical Research: Earth Surface, 121*(12), 2270-2286. doi:10.1002/2016JF004084

Truffer, M., & Motyka, R. J. (2016a). Where glaciers meet water: Subaqueous melt and its relevance to glaciers in various settings. *Reviews of Geophysics, 54*(1), 220-239. doi:10.1002/2015RG000494

Truffer, M., & Motyka, R. J. (2016b). Where glaciers meet water: Subaqueous melt and its relevance to glaciers in various settings: SUBAQUEOUS GLACIER MELT. *Reviews of Geophysics, 54*(1), 220-239. doi:10.1002/2015RG000494

Trussel, B. L., Motyka, R. J., Truffer, M., & Larsen, C. F. (2013). Rapid thinning of lake-calving Yakutat Glacier and the collapse of the Yakutat Icefield, southeast Alaska, USA. *Journal of Glaciology, 59*(213), 149-161. doi:10.3189/2013JoG12J081

van der Veen, C. J. (2002). Calving glaciers. *Progress in Physical Geography, 26*(1), 96-122. doi:10.1191/0309133302pp327ra

van der Veen, C.J. (1996). The iceberg discharge process: observations and inferences drawn from the study of Columbia Glacier*. Calving glaciers: report of a workshop, February 28–March 2, 1996. BPRC Report No. 15, Byrd Polar Research Center, Columbus, Ohio: The Ohio State University,* 109–14.

Venteris, E. R. (1999). Rapid tidewater glacier retreat: a comparison between Columbia Glacier, Alaska and Patagonian calving glaciers. *Global and Planetary Change, 22*(1), 131-138. doi:10.1016/S0921-8181(99)00031-4

Warren,C., Greene, D., & Glasser,N.F. (1995). Glaciar Upsala, Patagonia: rapid calving retreat in fresh water*. Ann. Glaciol. 21*, 311–316.

Warren, C., & Aniya, M. (1999). The calving glaciers of southern South America. *Global and Planetary Change, 22*(1), 59-77. doi:10.1016/S0921-8181(99)00026-0

Warren, C., Benn, D., Winchester, V., & Harrison, S. (2001). Buoyancy-driven lacustrine calving, Glaciar Nef, Chilean Patagonia. *Journal of Glaciology, 47*(156), 135-146. doi:10.3189/172756501781832403

Watson, M. (1995). Geophysical and Glaciological Studies of the Tasman*. Mueller Glaciers MSc thesis University of Auckland, Auckland.*

Watson, C. S., Quincey, D. J., Carrivick, J. L., & Smith, M. W. (2016). The dynamics of supraglacial ponds in the Everest region, central Himalaya. *Global and Planetary Change, 142*, 14-27. doi:10.1016/j.gloplacha.2016.04.008

Wright, G. F., 1892: Man and the Glacial Period. Worthington, Ohio: Werner Company.

Yan, S., Li, Y., Li, Z., Liu, G., Ruan, Z., & Li, Z. (2018). An insight into the surface velocity of Inylchek Glacier and its effect on Lake Merzbacher during 2006–2016 with Landsat time-series imagery. *Environmental Earth Sciences, 77*(23), 1-10. doi:10.1007/s12665-018-7964-7

Zemp, M., Frey, H., Gartner-Roer, I., Nussbaumer, S. U., Hoelzle, M., Paul, F., . . . Institutionen för, n. (2015). Historically unprecedented global glacier decline in the early 21st century. *Journal of Glaciology, 61*(228), 745-745. doi:10.3189/2015JoG15J017

Appendix A: Longitudinal velocity profiles

To explore how surface velocity varies spatially, velocity was determined along six longitudinal transects. The velocity of each transect, for each individual velocity surface was plotted against the mean of all 36 velocity values for that transect. The length of the transects was adjusted to account for terminus retreat.

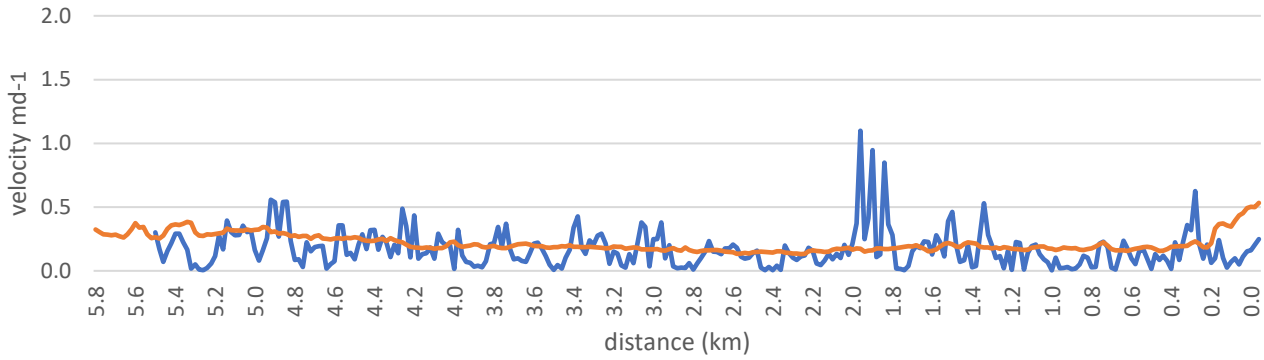

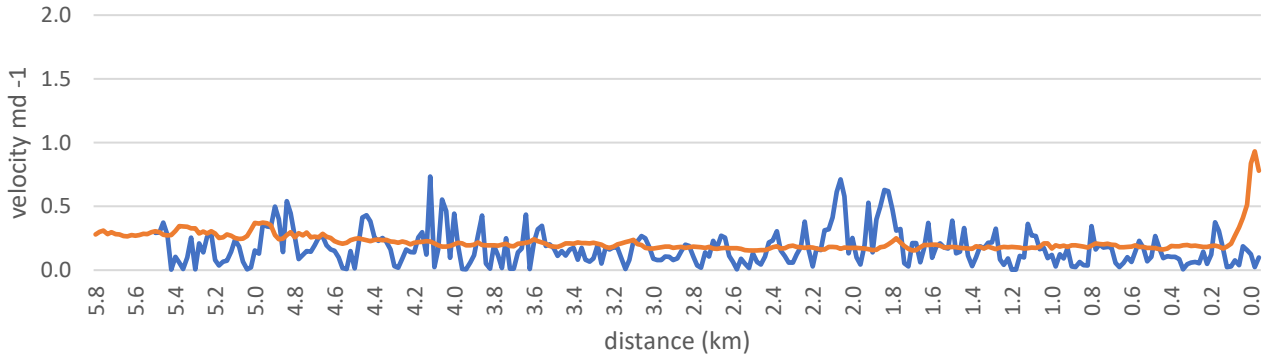

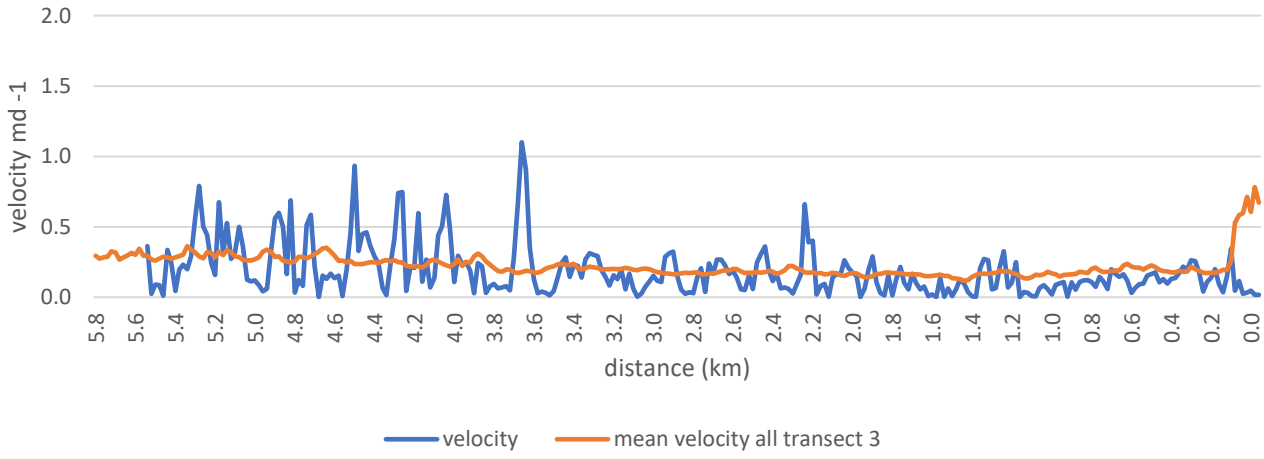

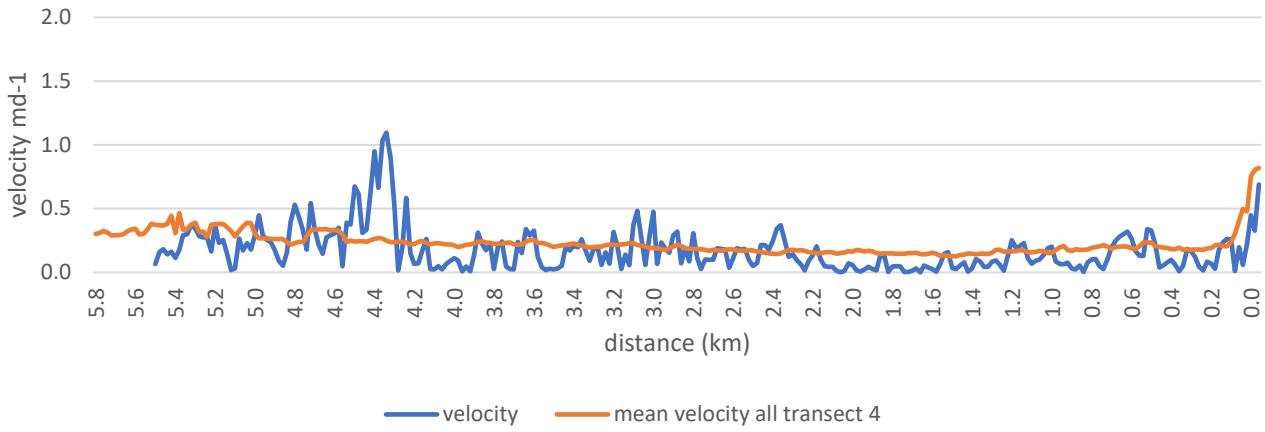
velocity md-1
2.0
1.5
1.0
0.5
0.0
5.8 5.6 5.4 5.2 5.0 4.8 4.6 4.4 4.2 4.0 3.8 3.6 3.4 3.2 3.0 2.8 2.6 2.4 2.2 2.0 1.8 1.6 1.4 1.2 1.0 0.8 0.6 0.4 0.2 0.0
distance (km)
velocity
mean velocity all transect 4

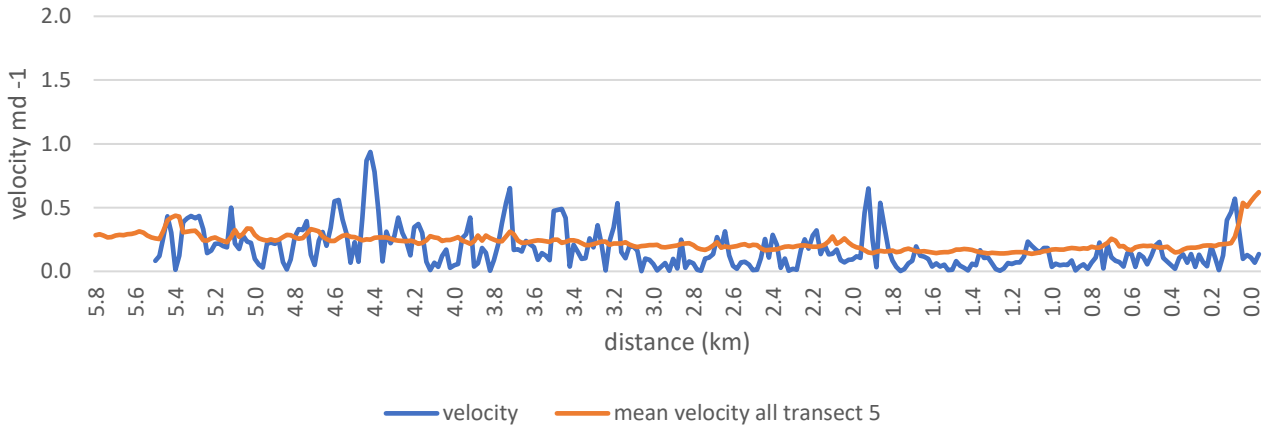
velocity md -1
2.0
1.5
1.0
0.5
0.0
5.8 5.6 5.4 5.2 5.0 4.8 4.6 4.4 4.2 4.0 3.8 3.6 3.4 3.2 3.0 2.8 2.6 2.4 2.2 2.0 1.8 1.6 1.4 1.2 1.0 0.8 0.6 0.4 0.2 0.0
distance (km)
velocity
mean velocity all transect 5

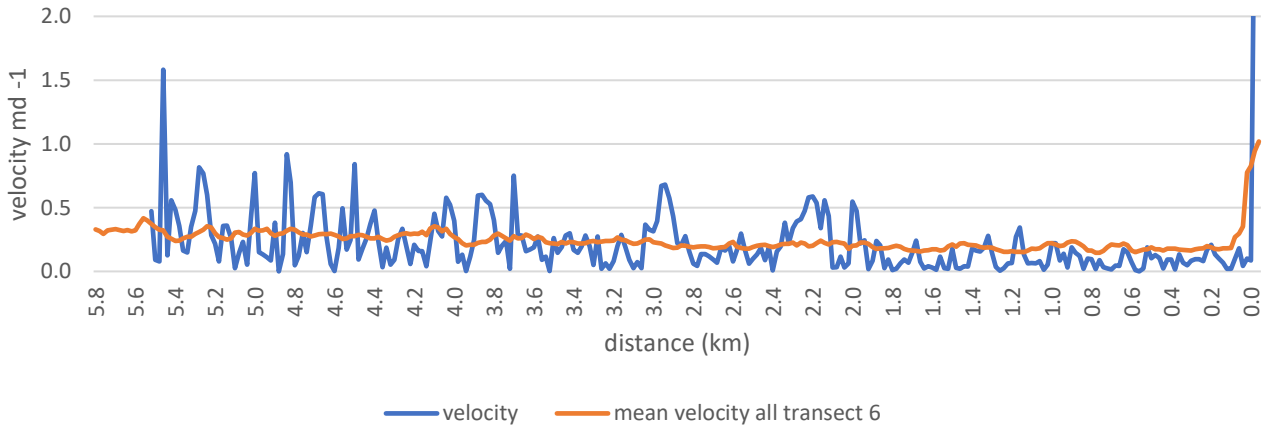
velocity md -1
2.0
1.5
1.0
0.5
0.0
5.8 5.6 5.4 5.2 5.0 4.8 4.6 4.4 4.2 4.0 3.8 3.6 3.4 3.2 3.0 2.8 2.6 2.4 2.2 2.0 1.8 1.6 1.4 1.2 1.0 0.8 0.6 0.4 0.2 0.0
distance (km)
velocity
mean velocity all transect 6

Appendix 1A: Longitudinal velocity profiles from 24/12/2015 – 03/01/2016 (time period of 10 days) The orange line indicates the surface velocity values extracted from all surface velocity images. The blue line is the surface velocity values extracted from each profile. Profiles run from A near the Ball Glacier confluence down to B at the terminus.

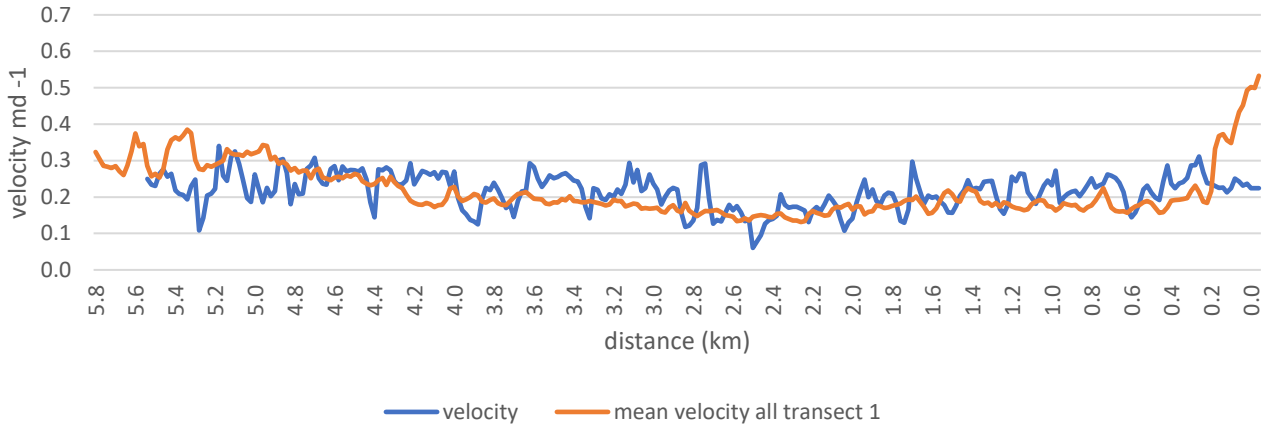

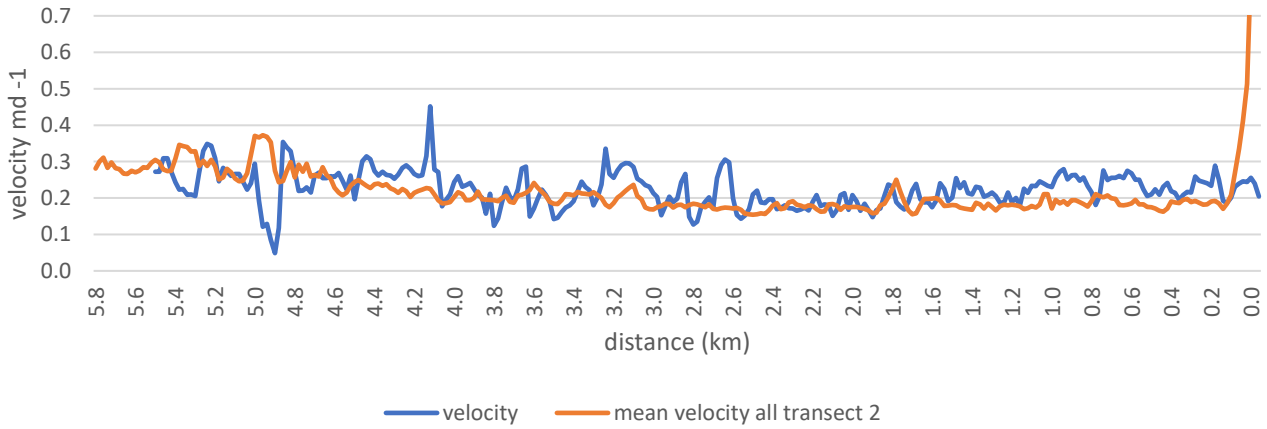

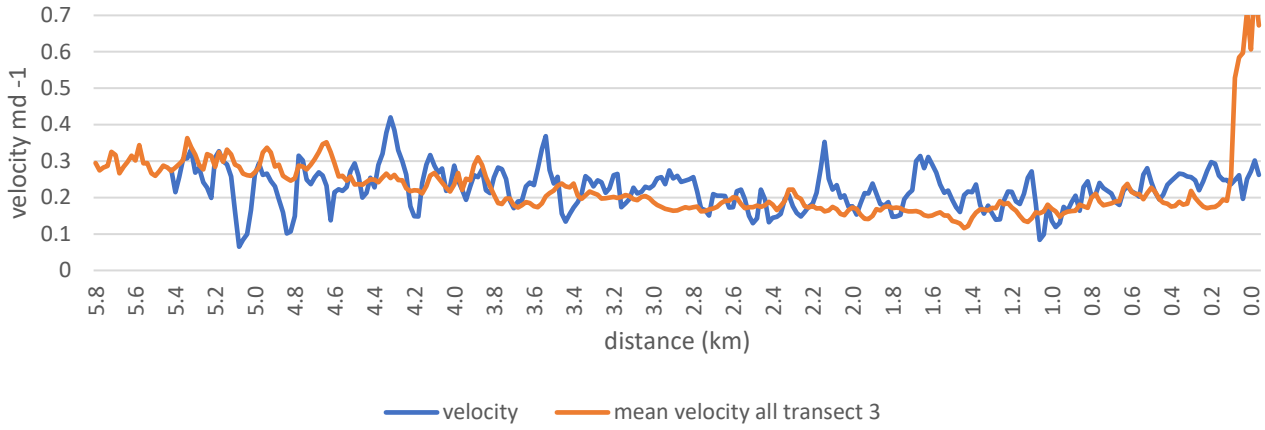
velocity md -1
0.7
0.6
0.5
0.4
0.3
0.2
0.1
0
5.8 5.6 5.4 5.2 5.0 4.8 4.6 4.4 4.2 4.0 3.8 3.6 3.4 3.2 3.0 2.8 2.6 2.4 2.2 2.0 1.8 1.6 1.4 1.2 1.0 0.8 0.6 0.4 0.2 0.0
distance (km)
velocity
mean velocity all transect 3

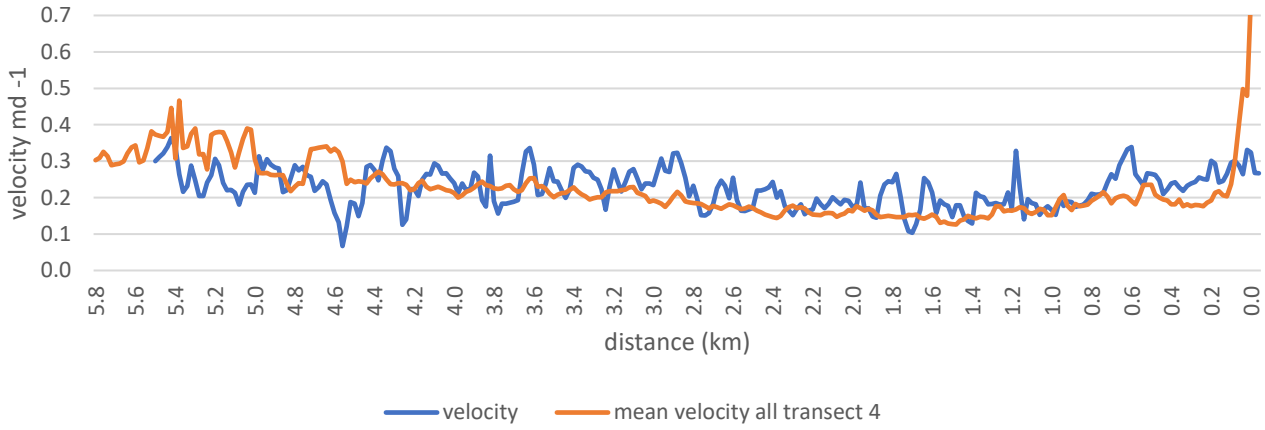
velocity md -1
0.7
0.6
0.5
0.4
0.3
0.2
0.1
0.0
5.8 5.6 5.4 5.2 5.0 4.8 4.6 4.4 4.2 4.0 3.8 3.6 3.4 3.2 3.0 2.8 2.6 2.4 2.2 2.0 1.8 1.6 1.4 1.2 1.0 0.8 0.6 0.4 0.2 0.0
distance (km)
velocity
mean velocity all transect 4

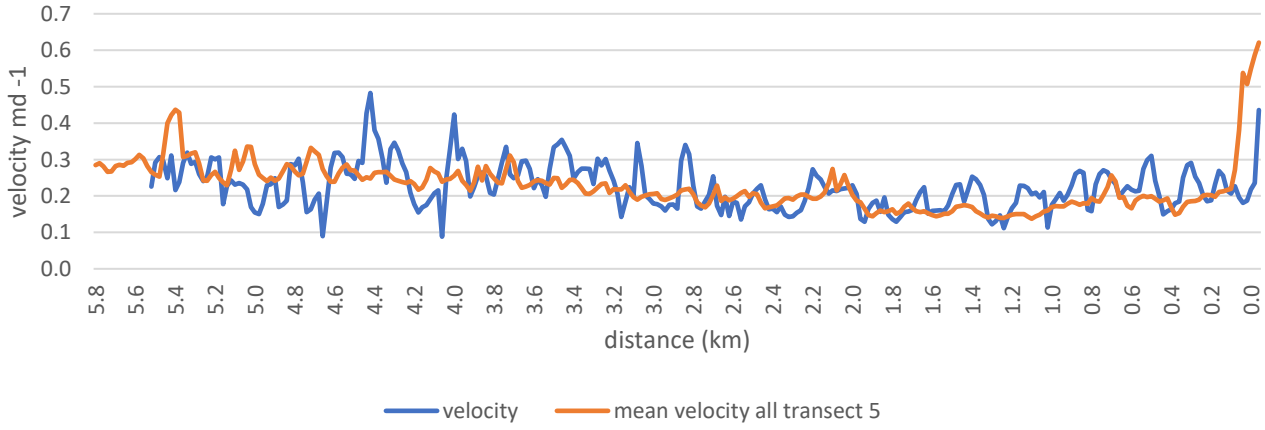
velocity md -1
0.7
0.6
0.5
0.4
0.3
0.2
0.1
0.0
5.8 5.6 5.4 5.2 5.0 4.8 4.6 4.4 4.2 4.0 3.8 3.6 3.4 3.2 3.0 2.8 2.6 2.4 2.2 2.0 1.8 1.6 1.4 1.2 1.0 0.8 0.6 0.4 0.2 0.0
distance (km)
velocity
mean velocity all transect 5

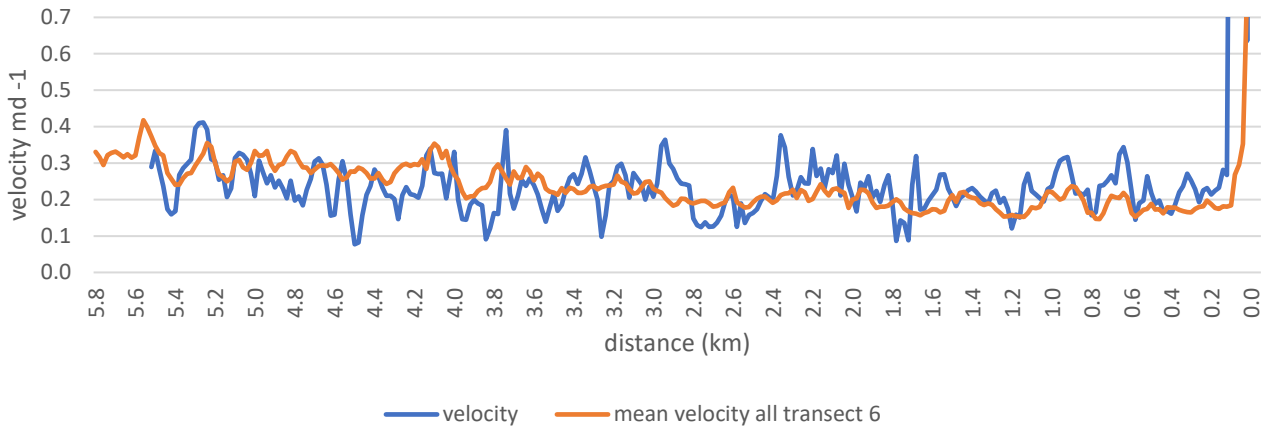

Appendix 2A: Longitudinal velocity profiles from 24/12/2015 – 02/02/2016 (time period of 40 days) The orange line indicates the surface velocity values extracted from all surface velocity images. The blue line is the surface velocity values extracted from each profile. Profiles run from A near the Ball Glacier confluence down to B at the terminus.

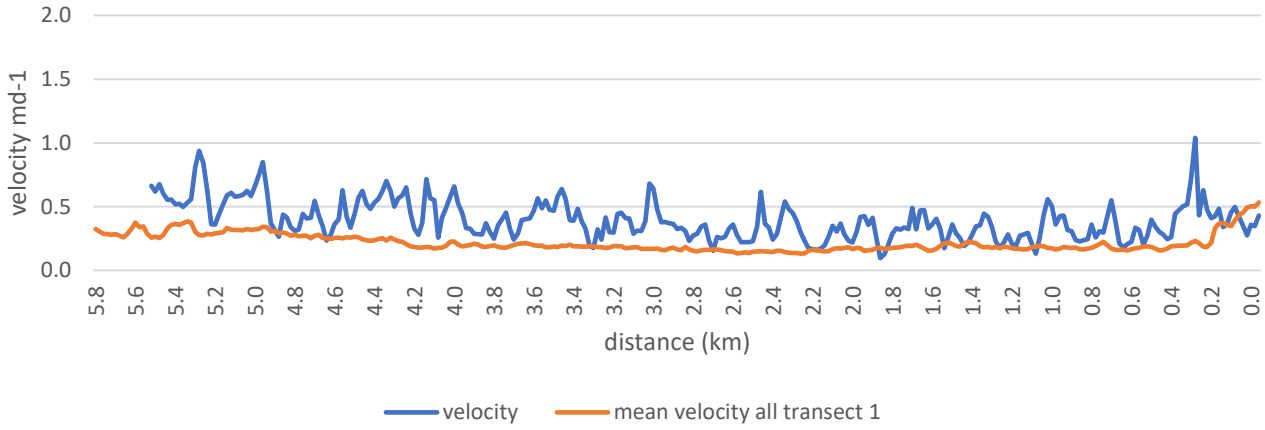

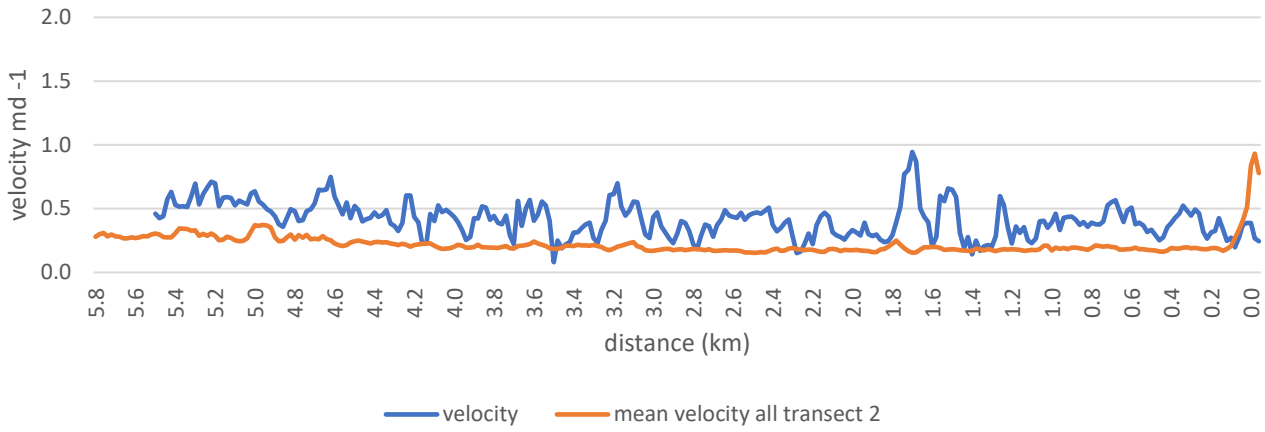
velocity md -1
2.0
1.5
1.0
0.5
0.0
5.8 5.6 5.4 5.2 5.0 4.8 4.6 4.4 4.2 4.0 3.8 3.6 3.4 3.2 3.0 2.8 2.6 2.4 2.2 2.0 1.8 1.6 1.4 1.2 1.0 0.8 0.6 0.4 0.2 0.0
distance (km)
velocity
mean velocity all transect 2

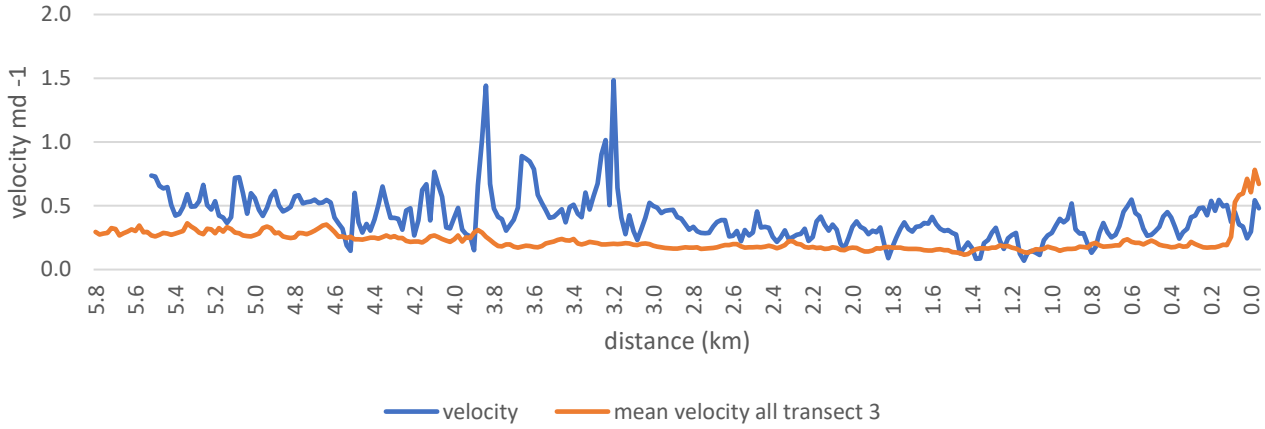
velocity md -1
2.0
1.5
1.0
0.5
0.0
5.8 5.6 5.4 5.2 5.0 4.8 4.6 4.4 4.2 4.0 3.8 3.6 3.4 3.2 3.0 2.8 2.6 2.4 2.2 2.0 1.8 1.6 1.4 1.2 1.0 0.8 0.6 0.4 0.2 0.0
distance (km)
velocity
mean velocity all transect 3

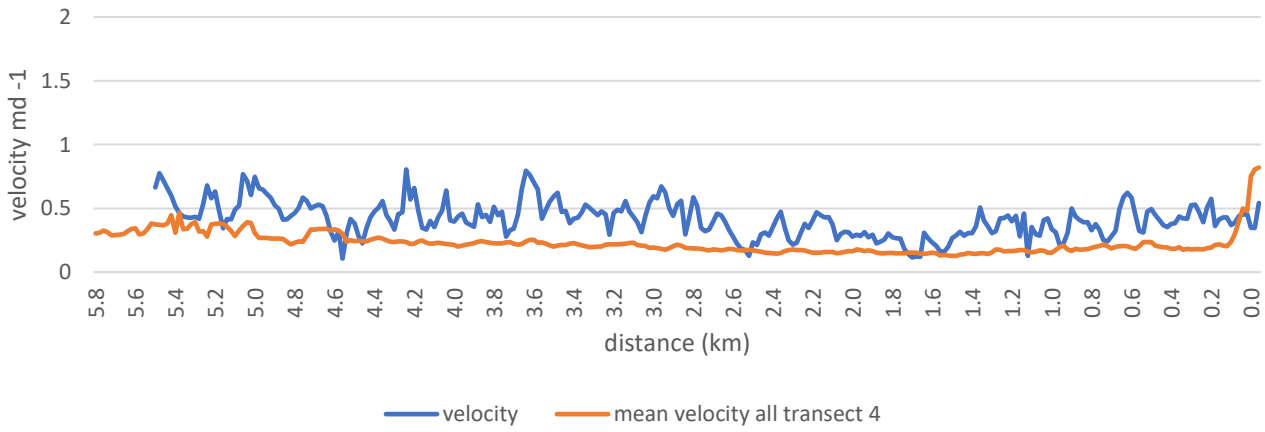
velocity md -1
2
1.5
1
0.5
0
5.8 5.6 5.4 5.2 5.0 4.8 4.6 4.4 4.2 4.0 3.8 3.6 3.4 3.2 3.0 2.8 2.6 2.4 2.2 2.0 1.8 1.6 1.4 1.2 1.0 0.8 0.6 0.4 0.2 0.0
distance (km)
velocity
mean velocity all transect 4

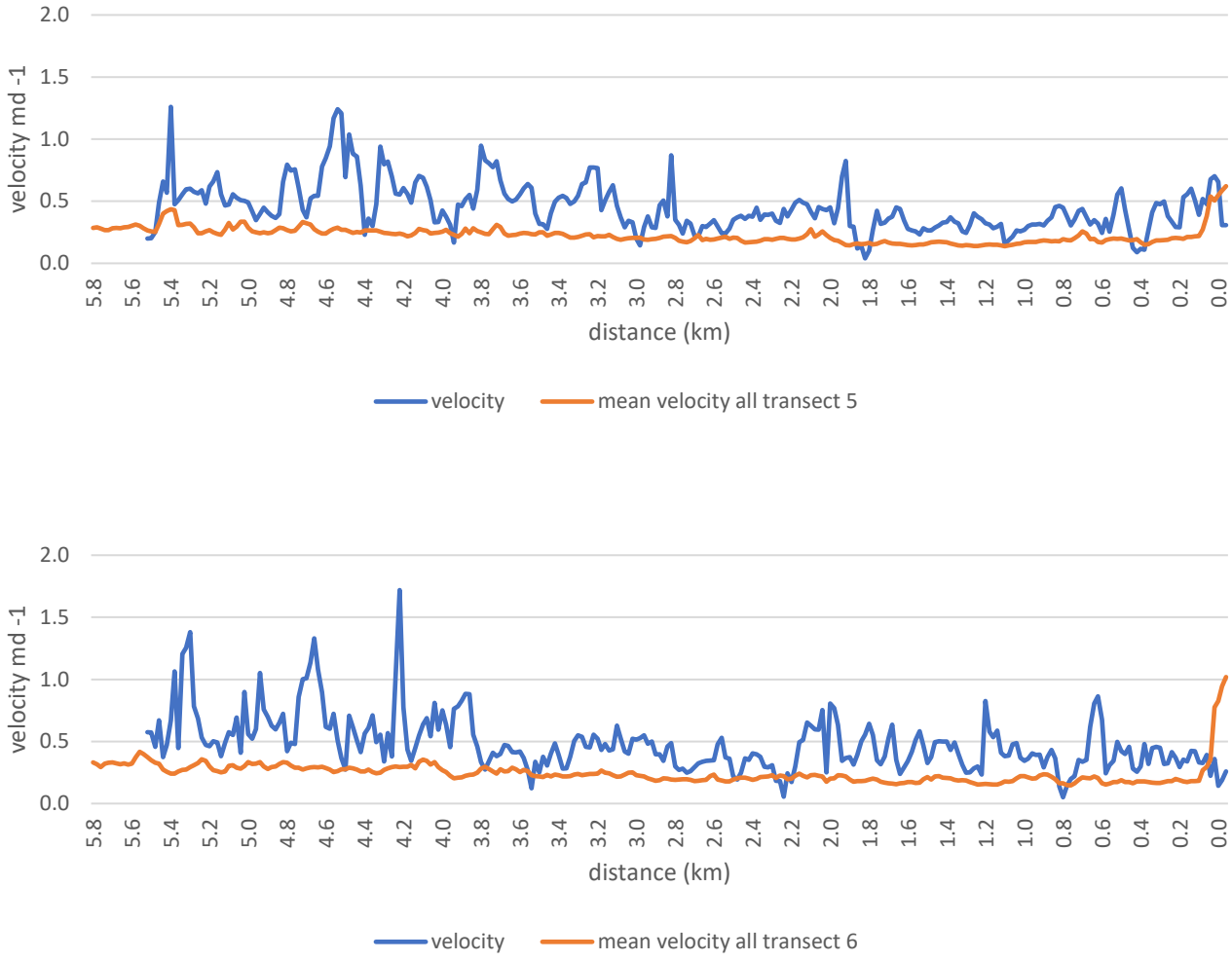

Appendix 3A: Longitudinal velocity profiles from 03/01/2016 – 13/01/2016 (time period of 10 days) The orange line indicates the surface velocity values extracted from all surface velocity images. The blue line is the surface velocity values extracted from each profile. Profiles run from A near the Ball Glacier confluence down to B at the terminus.

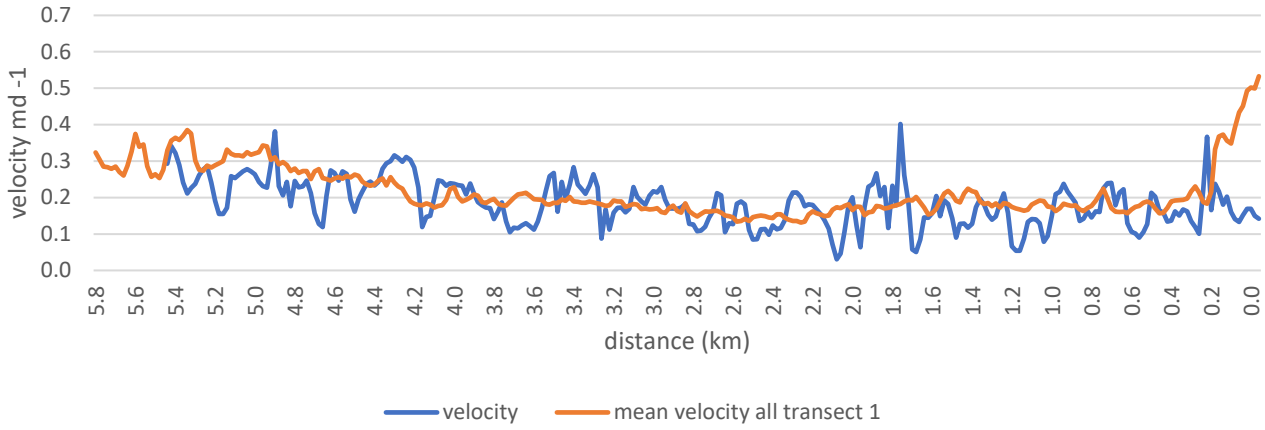
velocity md -1
0.7
0.6
0.5
0.4
0.3
0.2
0.1
0.0
5.8 5.6 5.4 5.2 5.0 4.8 4.6 4.4 4.2 4.0 3.8 3.6 3.4 3.2 3.0 2.8 2.6 2.4 2.2 2.0 1.8 1.6 1.4 1.2 1.0 0.8 0.6 0.4 0.2 0.0
distance (km)
velocity
mean velocity all transect 1

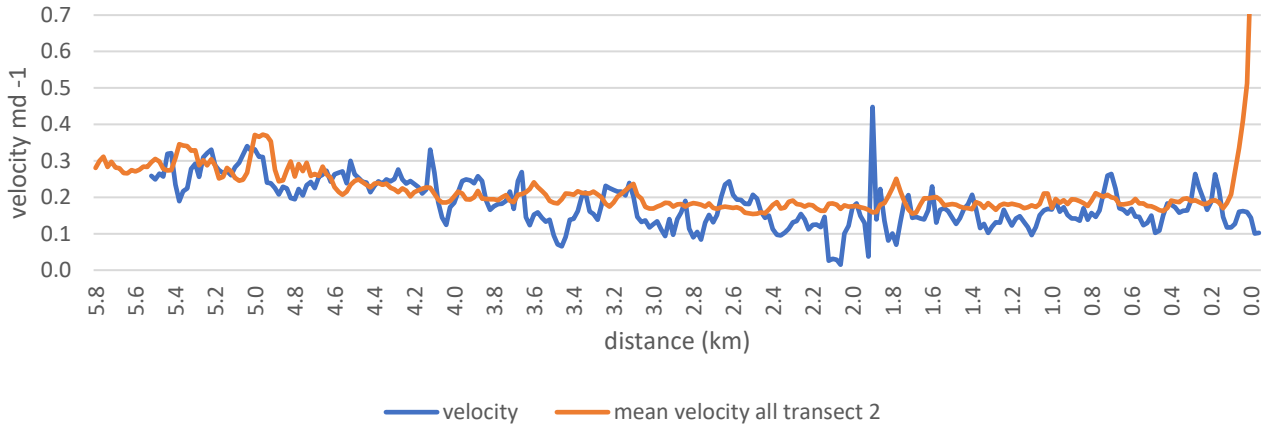
velocity md -1
0.7
0.6
0.5
0.4
0.3
0.2
0.1
0.0
5.8 5.6 5.4 5.2 5.0 4.8 4.6 4.4 4.2 4.0 3.8 3.6 3.4 3.2 3.0 2.8 2.6 2.4 2.2 2.0 1.8 1.6 1.4 1.2 1.0 0.8 0.6 0.4 0.2 0.0
distance (km)
velocity
mean velocity all transect 2

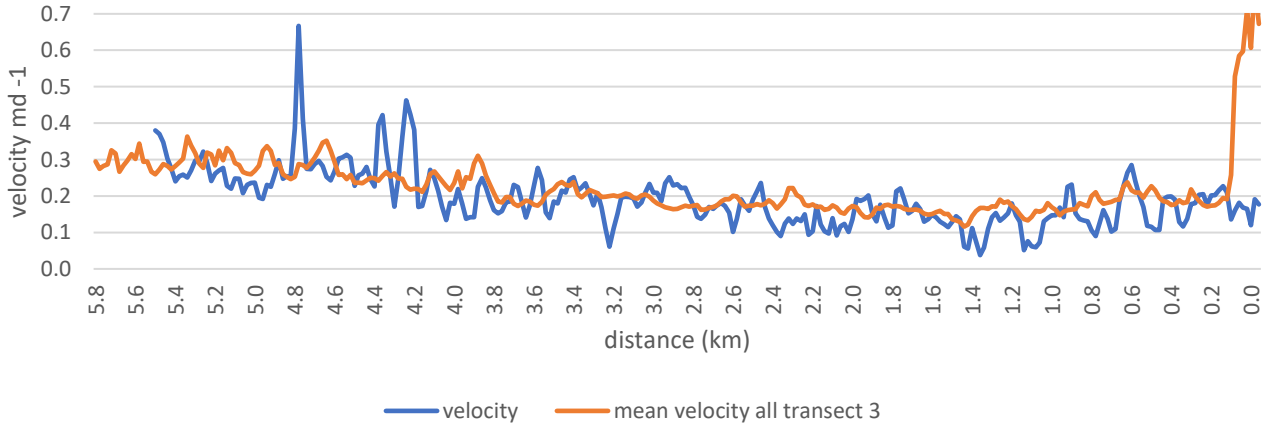
velocity md -1
0.7
0.6
0.5
0.4
0.3
0.2
0.1
0.0
5.8 5.6 5.4 5.2 5.0 4.8 4.6 4.4 4.2 4.0 3.8 3.6 3.4 3.2 3.0 2.8 2.6 2.4 2.2 2.0 1.8 1.6 1.4 1.2 1.0 0.8 0.6 0.4 0.2 0.0
distance (km)
velocity
mean velocity all transect 3

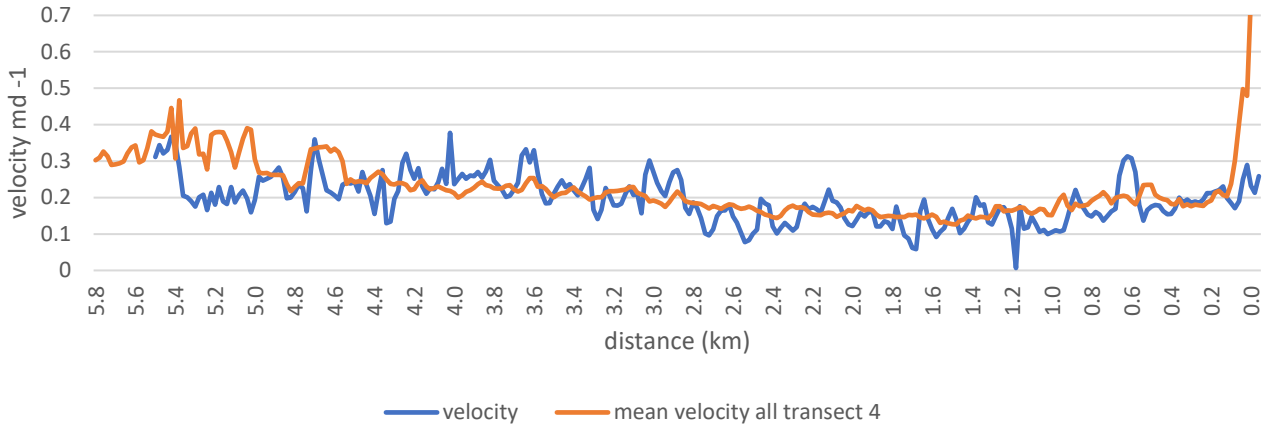

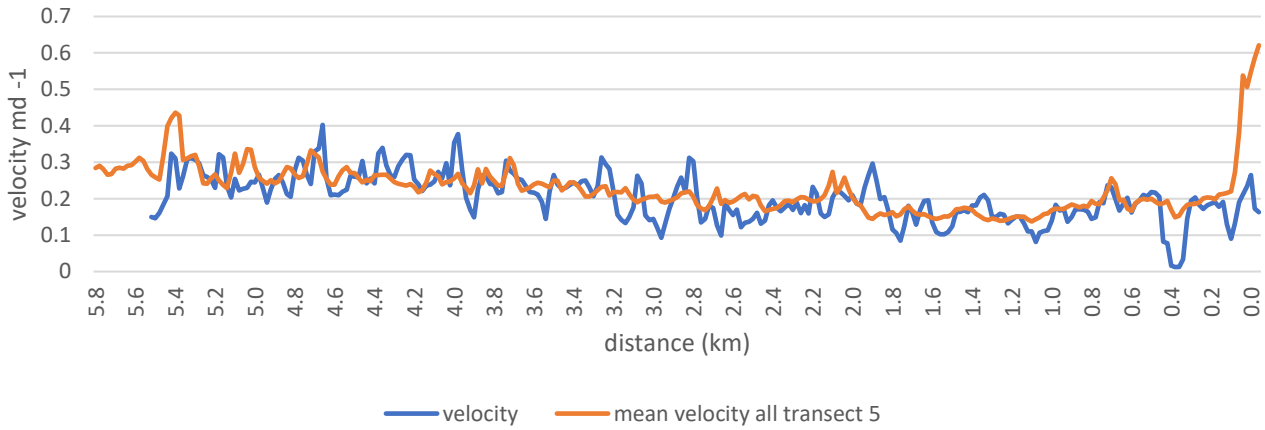

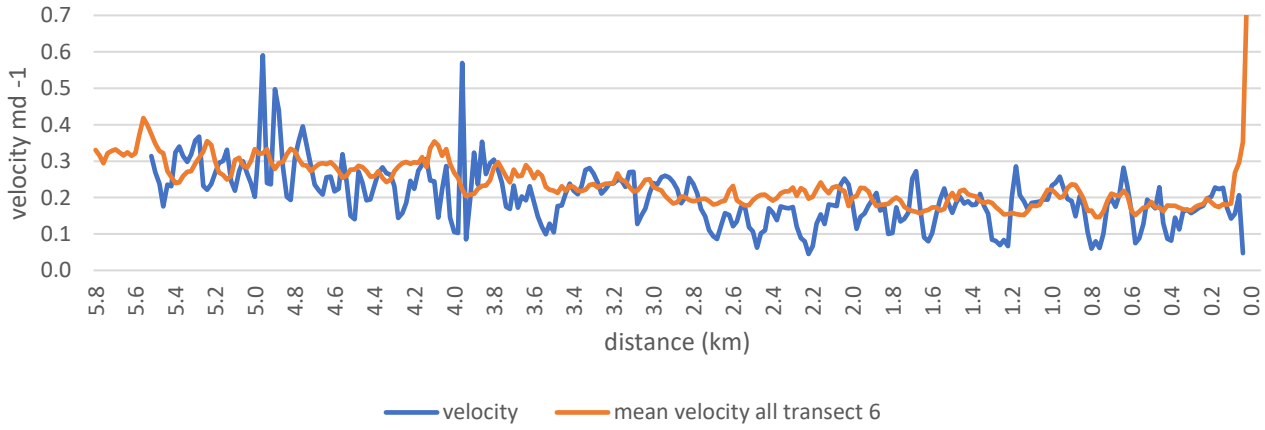

Appendix 4A: Longitudinal velocity profiles from 03/01/2016 – 13/01/2016 (time period of 40 days) The orange line indicates the surface velocity values extracted from all surface velocity images. The blue line is the surface velocity values extracted from each profile. Profiles run from A near the Ball Glacier confluence down to B at the terminus.

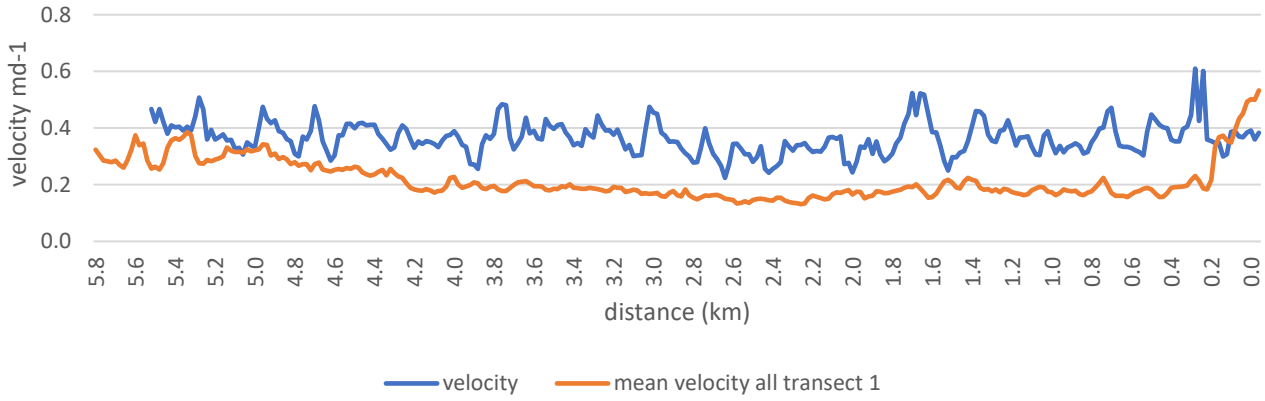
velocity md-1
0.8
0.6
0.4
0.2
0.0
5.8 5.6 5.4 5.2 5.0 4.8 4.6 4.4 4.2 4.0 3.8 3.6 3.4 3.2 3.0 2.8 2.6 2.4 2.2 2.0 1.8 1.6 1.4 1.2 1.0 0.8 0.6 0.4 0.2 0.0
distance (km)
velocity
mean velocity all transect 1

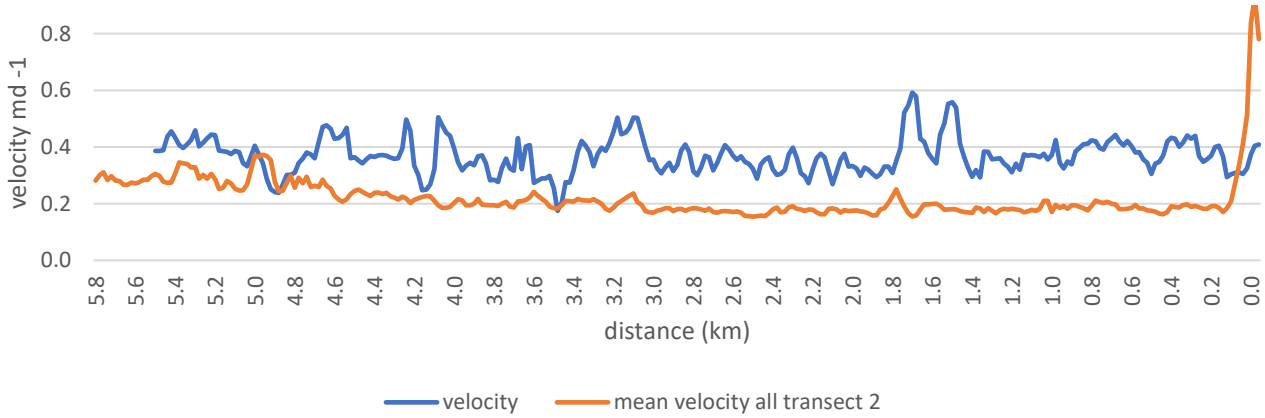
velocity md -1
0.8
0.6
0.4
0.2
0.0
5.8 5.6 5.4 5.2 5.0 4.8 4.6 4.4 4.2 4.0 3.8 3.6 3.4 3.2 3.0 2.8 2.6 2.4 2.2 2.0 1.8 1.6 1.4 1.2 1.0 0.8 0.6 0.4 0.2 0.0
distance (km)
velocity
mean velocity all transect 2

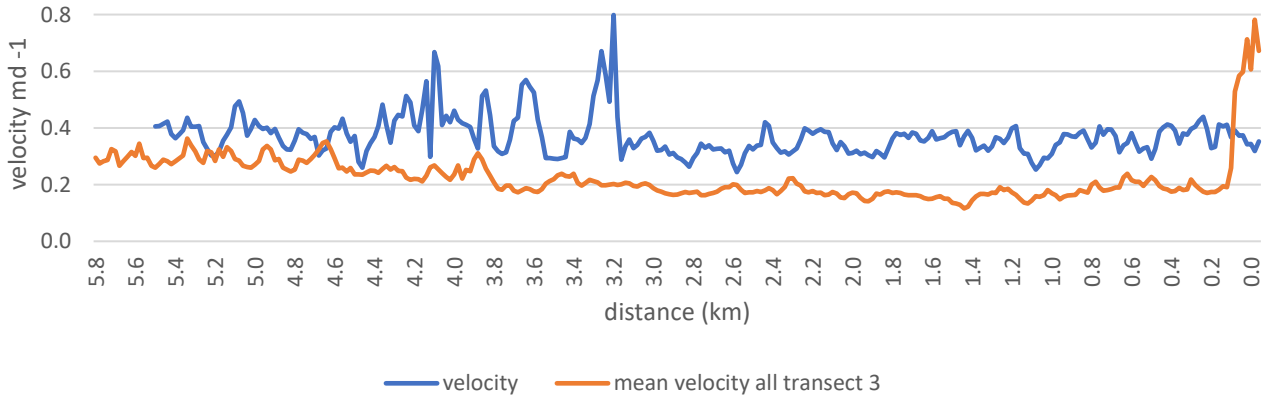
velocity md -1
0.8
0.6
0.4
0.2
0.0
5.8 5.6 5.4 5.2 5.0 4.8 4.6 4.4 4.2 4.0 3.8 3.6 3.4 3.2 3.0 2.8 2.6 2.4 2.2 2.0 1.8 1.6 1.4 1.2 1.0 0.8 0.6 0.4 0.2 0.0
distance (km)
velocity
mean velocity all transect 3

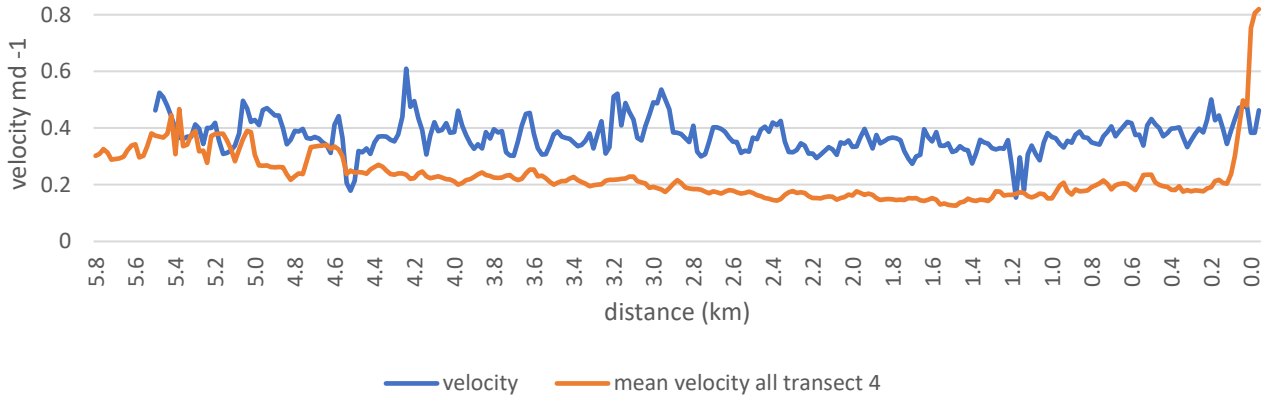

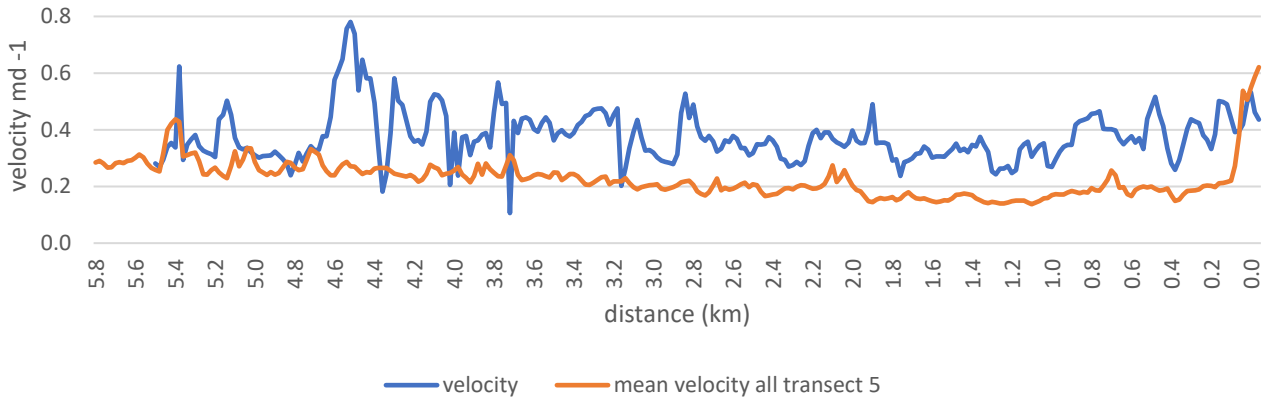

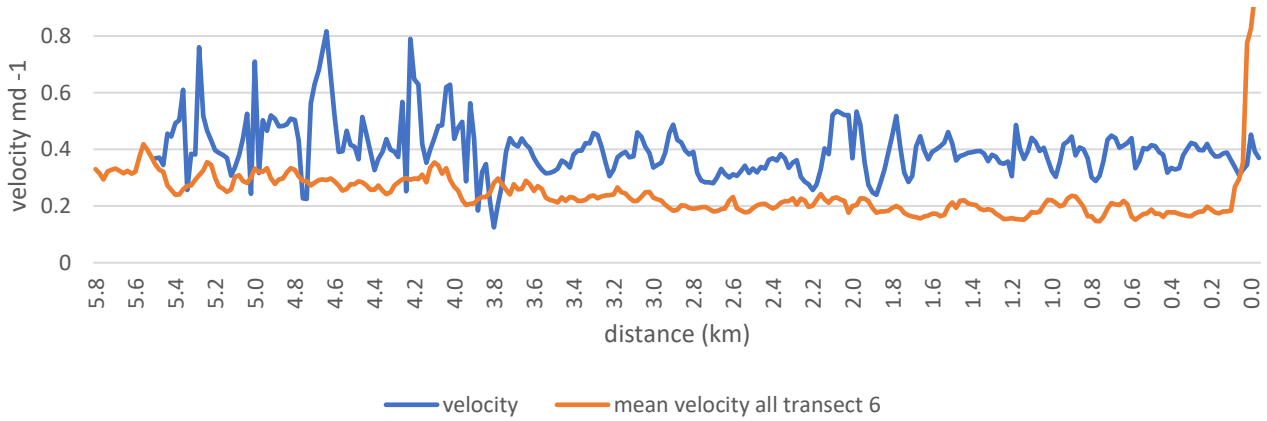

Appendix 5A: Longitudinal velocity profiles from 03/01/2016 – 13/01/2016 (time period of 20 days) The orange line indicates the surface velocity values extracted from all surface velocity images. The blue line is the surface velocity values extracted from each profile. Profiles run from A near the Ball Glacier confluence down to B at the terminus.

187

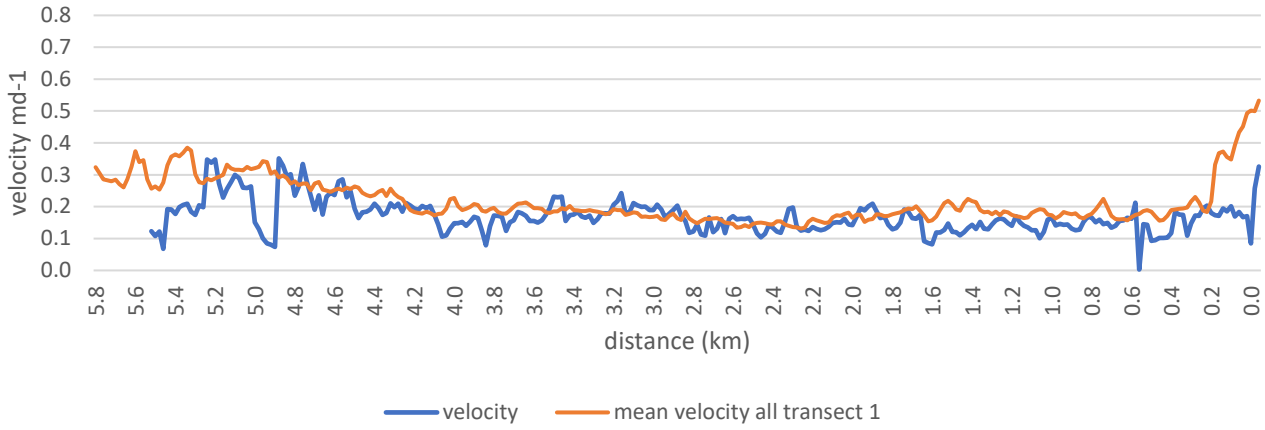
velocity md-1
0.8
0.7
0.6
0.5
0.4
0.3
0.2
0.1
0.0
5.8 5.6 5.4 5.2 5.0 4.8 4.6 4.4 4.2 4.0 3.8 3.6 3.4 3.2 3.0 2.8 2.6 2.4 2.2 2.0 1.8 1.6 1.4 1.2 1.0 0.8 0.6 0.4 0.2 0.0
distance (km)
velocity
mean velocity all transect 1

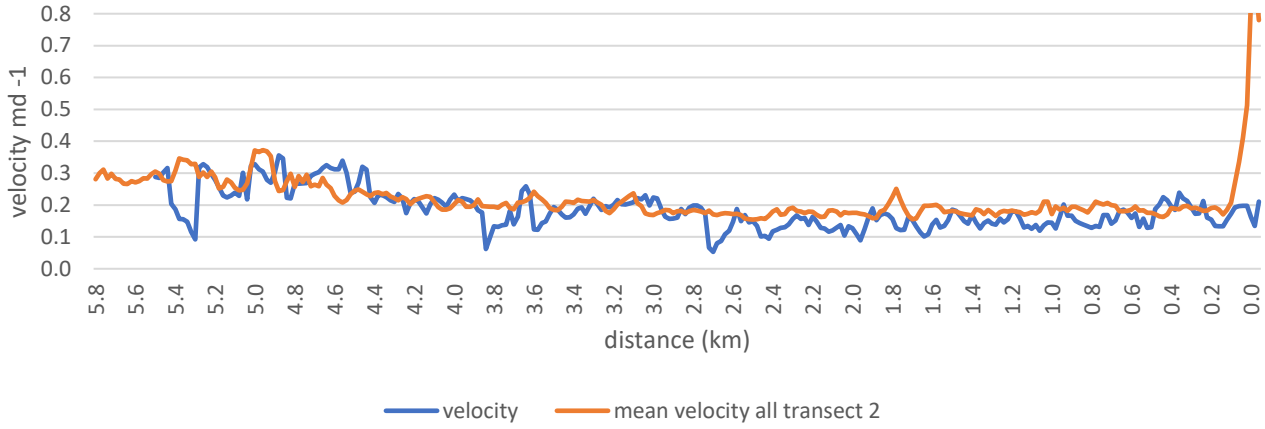
velocity md -1
0.8
0.7
0.6
0.5
0.4
0.3
0.2
0.1
0.0
5.8 5.6 5.4 5.2 5.0 4.8 4.6 4.4 4.2 4.0 3.8 3.6 3.4 3.2 3.0 2.8 2.6 2.4 2.2 2.0 1.8 1.6 1.4 1.2 1.0 0.8 0.6 0.4 0.2 0.0
distance (km)
velocity
mean velocity all transect 2

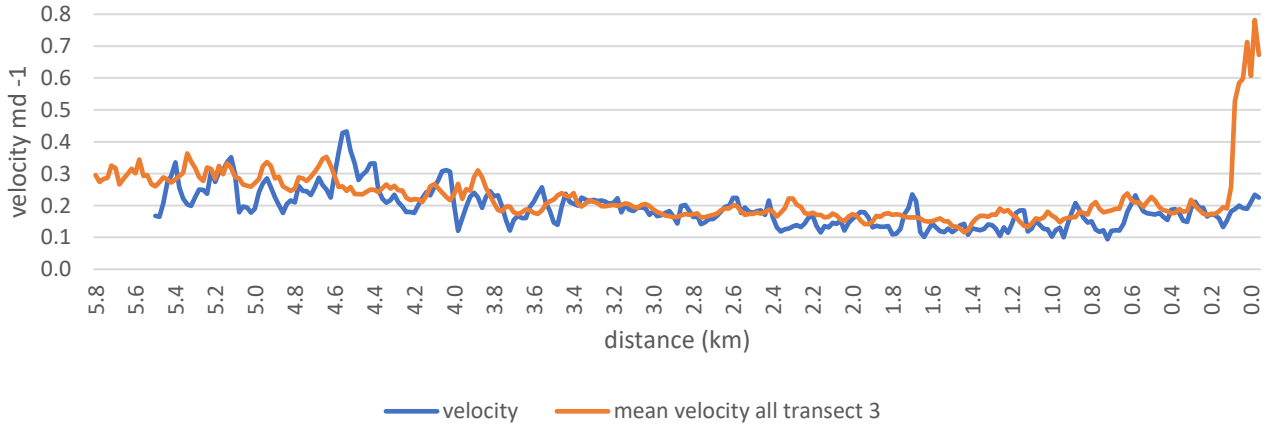
velocity md -1
0.8
0.7
0.6
0.5
0.4
0.3
0.2
0.1
0.0
5.8 5.6 5.4 5.2 5.0 4.8 4.6 4.4 4.2 4.0 3.8 3.6 3.4 3.2 3.0 2.8 2.6 2.4 2.2 2.0 1.8 1.6 1.4 1.2 1.0 0.8 0.6 0.4 0.2 0.0
distance (km)
velocity
mean velocity all transect 3

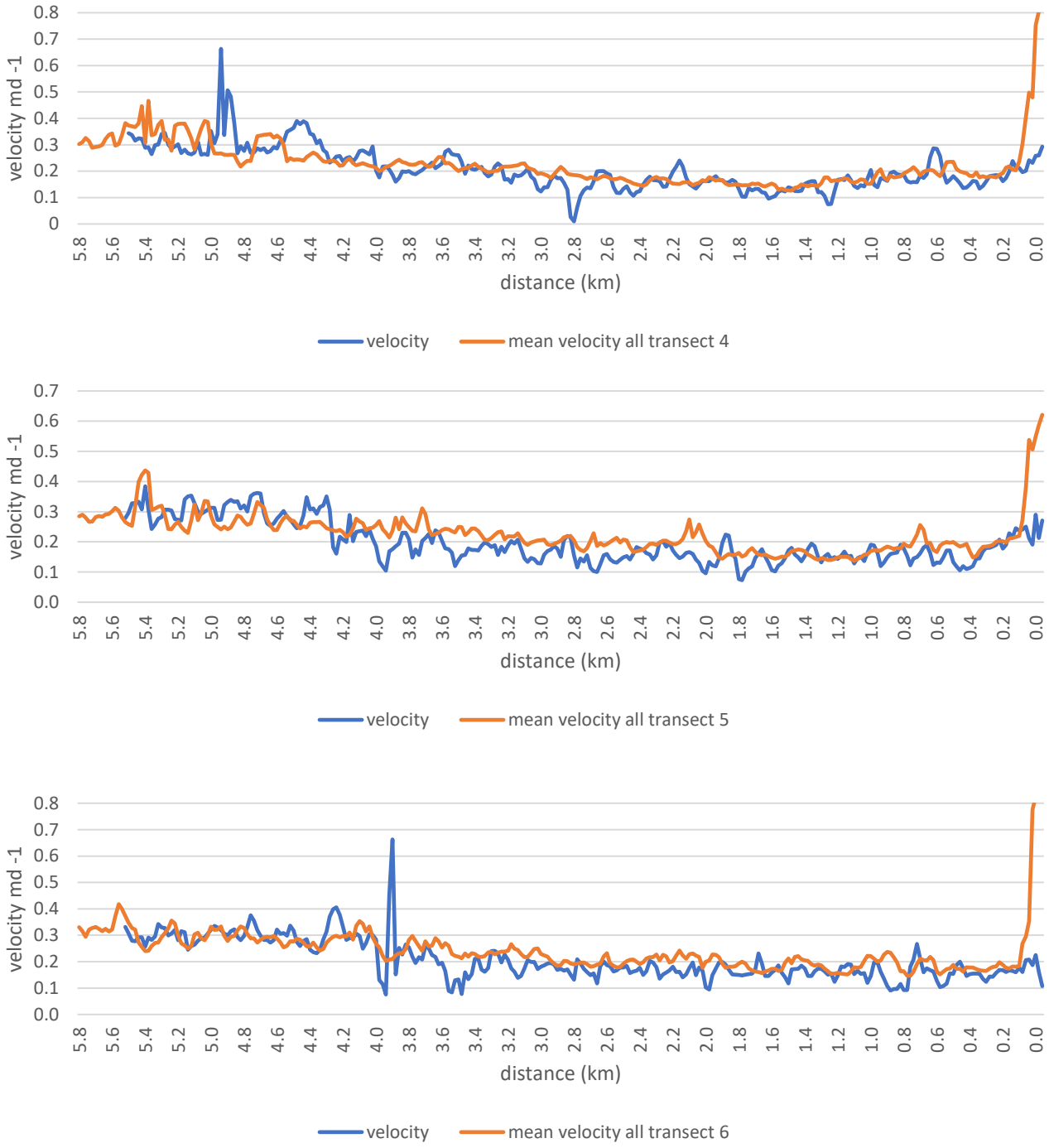

Appendix 6A: Longitudinal velocity profiles from 02/02/2016 – 13/03/2016 (time period of 20 days) The orange line indicates the surface velocity values extracted from all surface velocity images. The blue line is the surface velocity values extracted from each profile. Profiles run from A near the Ball Glacier confluence down to B at the terminus.

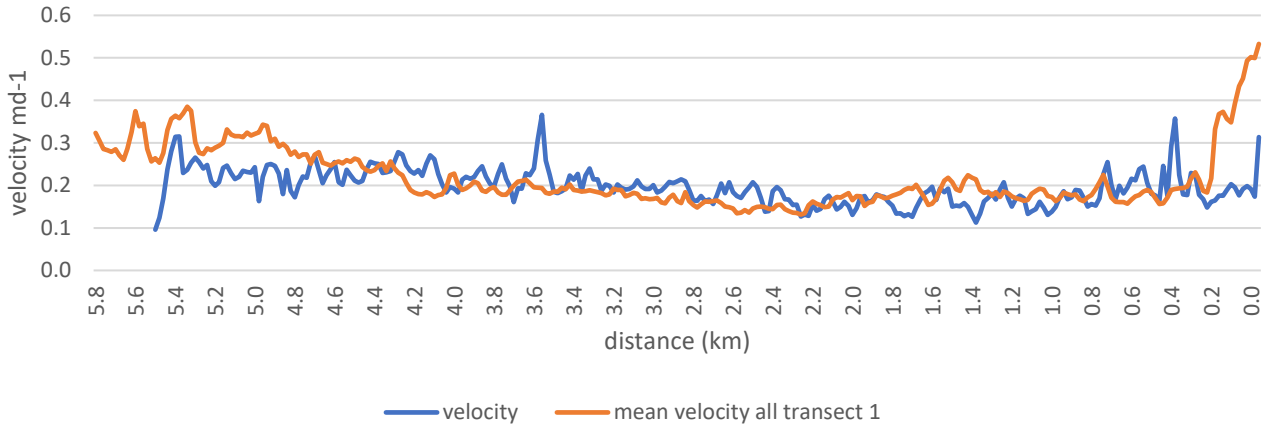
velocity md-1
0.6
0.5
0.4
0.3
0.2
0.1
0.0
5.8 5.6 5.4 5.2 5.0 4.8 4.6 4.4 4.2 4.0 3.8 3.6 3.4 3.2 3.0 2.8 2.6 2.4 2.2 2.0 1.8 1.6 1.4 1.2 1.0 0.8 0.6 0.4 0.2 0.0
distance (km)
velocity
mean velocity all transect 1

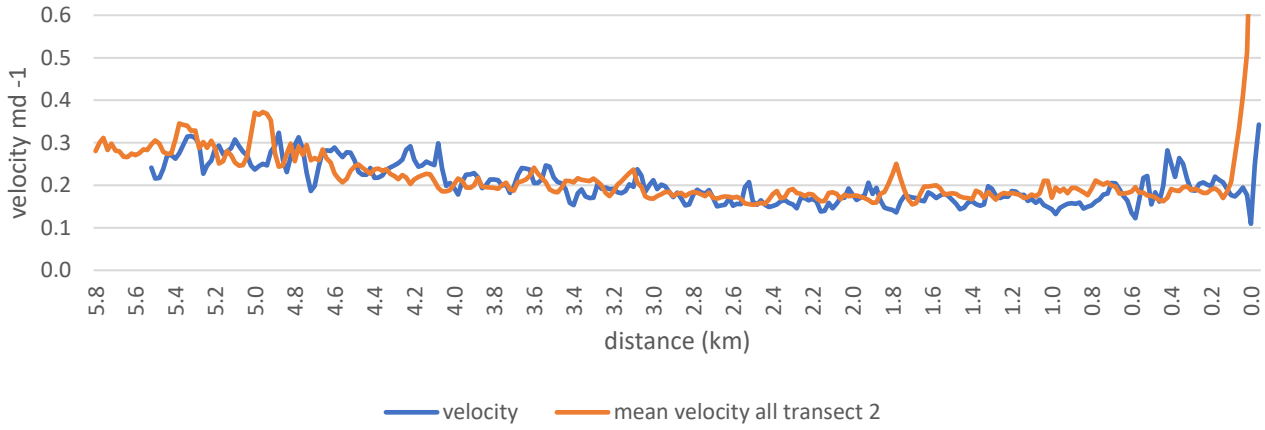
velocity md -1
0.6
0.5
0.4
0.3
0.2
0.1
0.0
5.8 5.6 5.4 5.2 5.0 4.8 4.6 4.4 4.2 4.0 3.8 3.6 3.4 3.2 3.0 2.8 2.6 2.4 2.2 2.0 1.8 1.6 1.4 1.2 1.0 0.8 0.6 0.4 0.2 0.0
distance (km)
velocity
mean velocity all transect 2

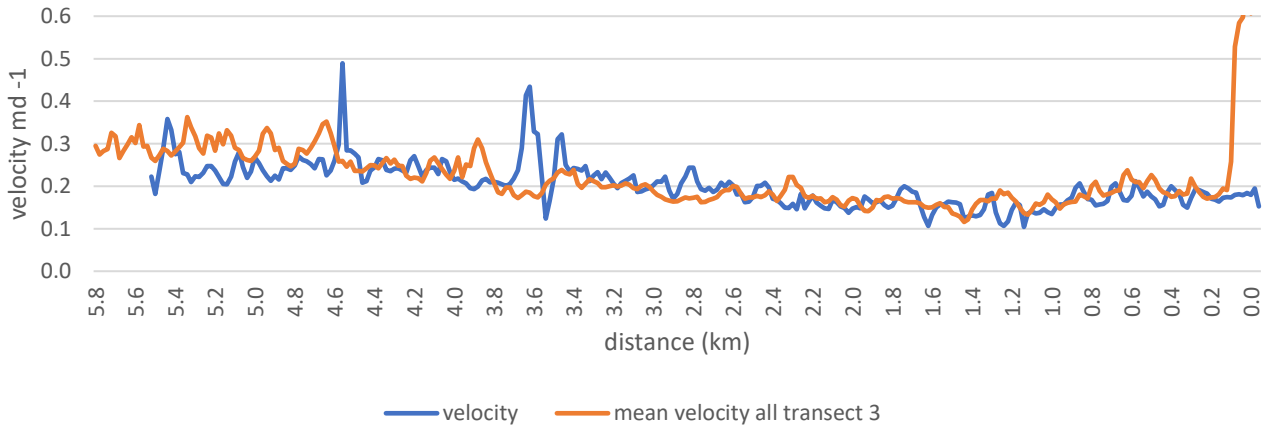
velocity md -1
0.6
0.5
0.4
0.3
0.2
0.1
0.0
5.8 5.6 5.4 5.2 5.0 4.8 4.6 4.4 4.2 4.0 3.8 3.6 3.4 3.2 3.0 2.8 2.6 2.4 2.2 2.0 1.8 1.6 1.4 1.2 1.0 0.8 0.6 0.4 0.2 0.0
distance (km)
velocity
mean velocity all transect 3

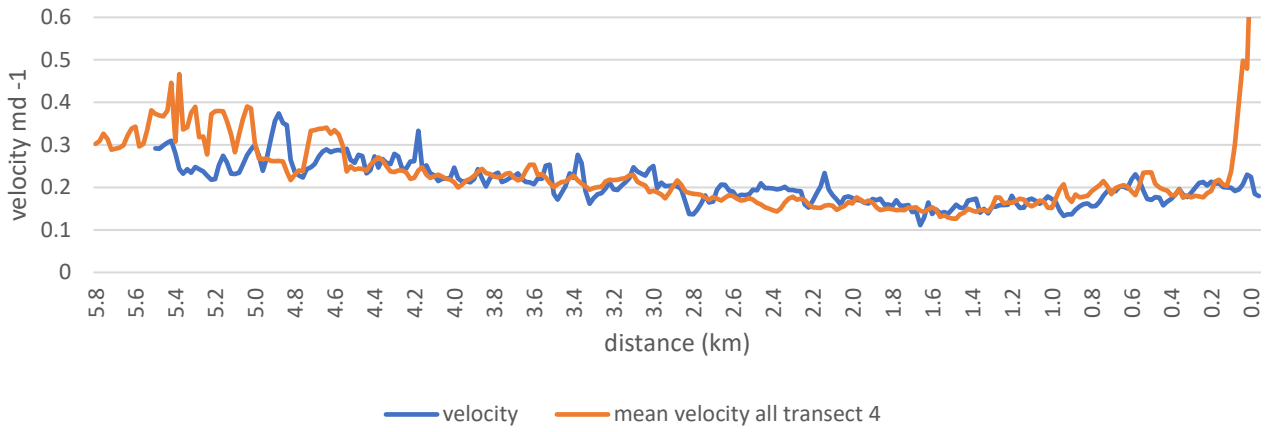
velocity md -1
0.6
0.5
0.4
0.3
0.2
0.1
0
5.8 5.6 5.4 5.2 5.0 4.8 4.6 4.4 4.2 4.0 3.8 3.6 3.4 3.2 3.0 2.8 2.6 2.4 2.2 2.0 1.8 1.6 1.4 1.2 1.0 0.8 0.6 0.4 0.2 0.0
distance (km)
velocity
mean velocity all transect 4

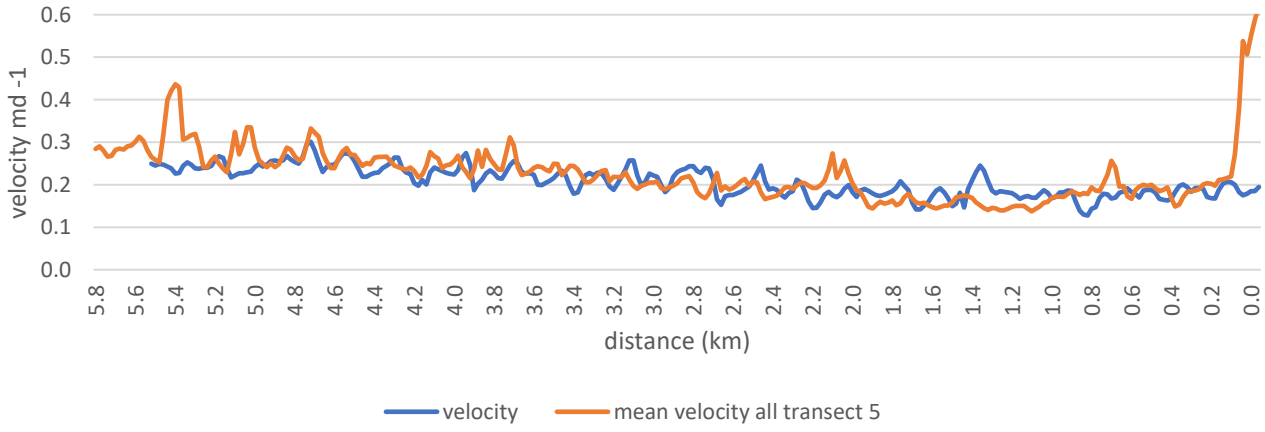
velocity md -1
0.6
0.5
0.4
0.3
0.2
0.1
0.0
5.8 5.6 5.4 5.2 5.0 4.8 4.6 4.4 4.2 4.0 3.8 3.6 3.4 3.2 3.0 2.8 2.6 2.4 2.2 2.0 1.8 1.6 1.4 1.2 1.0 0.8 0.6 0.4 0.2 0.0
distance (km)
velocity
mean velocity all transect 5

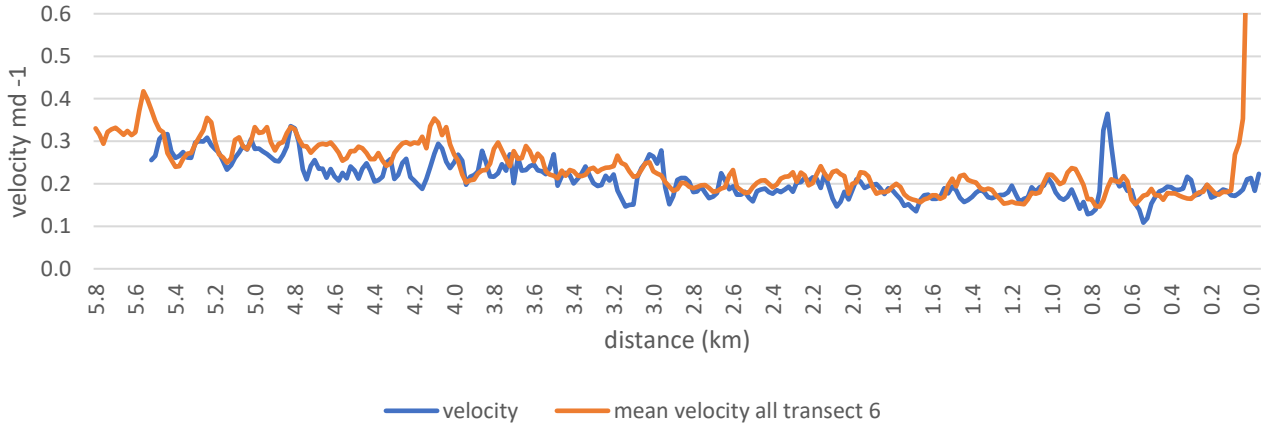
velocity md -1
0.6
0.5
0.4
0.3
0.2
0.1
0.0
5.8 5.6 5.4 5.2 5.0 4.8 4.6 4.4 4.2 4.0 3.8 3.6 3.4 3.2 3.0 2.8 2.6 2.4 2.2 2.0 1.8 1.6 1.4 1.2 1.0 0.8 0.6 0.4 0.2 0.0
distance (km)
velocity
mean velocity all transect 6

Appendix 7A: Longitudinal velocity profiles from 13/03/2016 – 12/04/2016 (time period of 30 days) The orange line indicates the surface velocity values extracted from all surface velocity images. The blue line is the surface velocity values extracted from each profile. Profiles run from A near the Ball Glacier confluence down to B at the terminus.

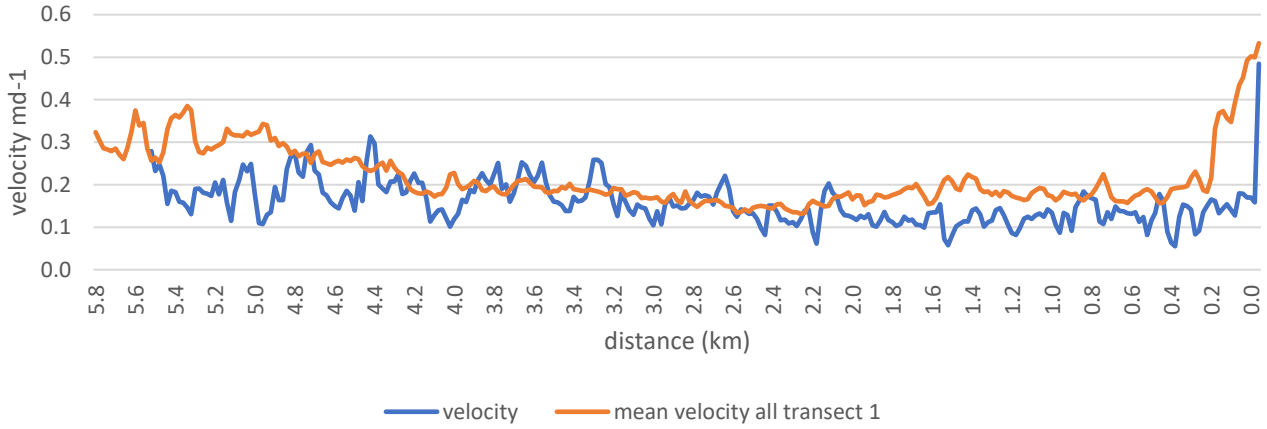

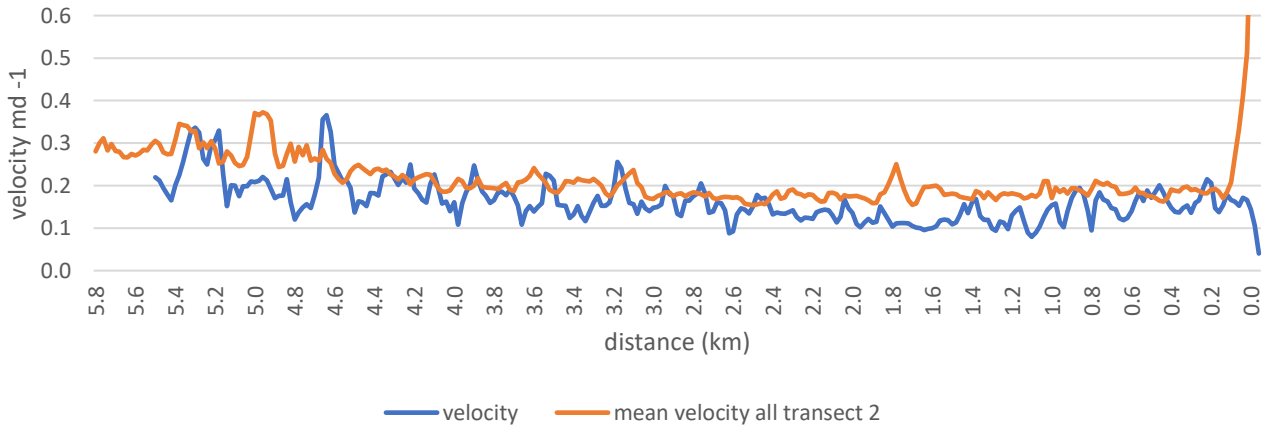

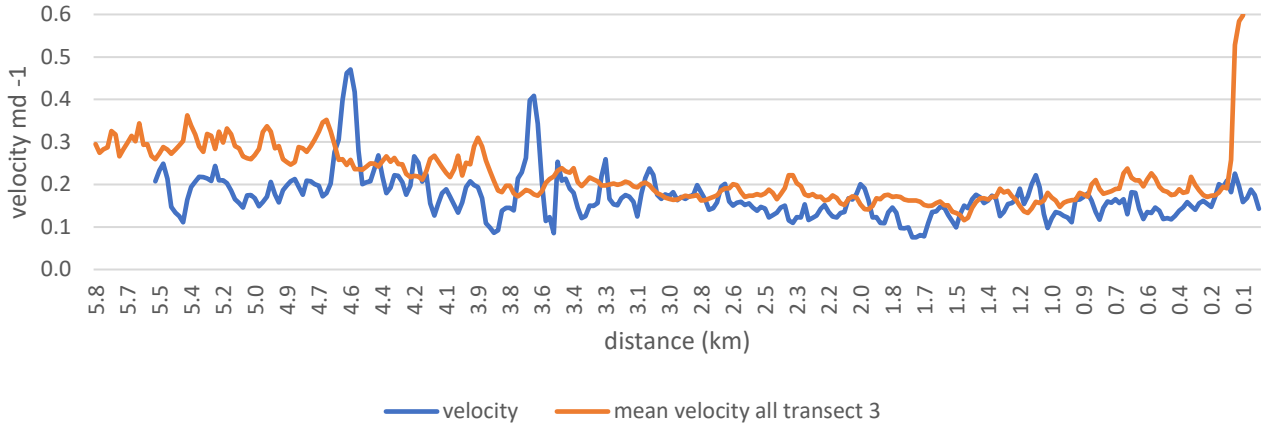
velocity md -1
0.6
0.5
0.4
0.3
0.2
0.1
0.0
5.8 5.7 5.5 5.4 5.2 5.0 4.9 4.7 4.6 4.4 4.2 4.1 3.9 3.8 3.6 3.4 3.3 3.1 3.0 2.8 2.6 2.5 2.3 2.2 2.0 1.8 1.7 1.5 1.4 1.2 1.0 0.9 0.7 0.6 0.4 0.2 0.1
distance (km)
velocity
mean velocity all transect 3

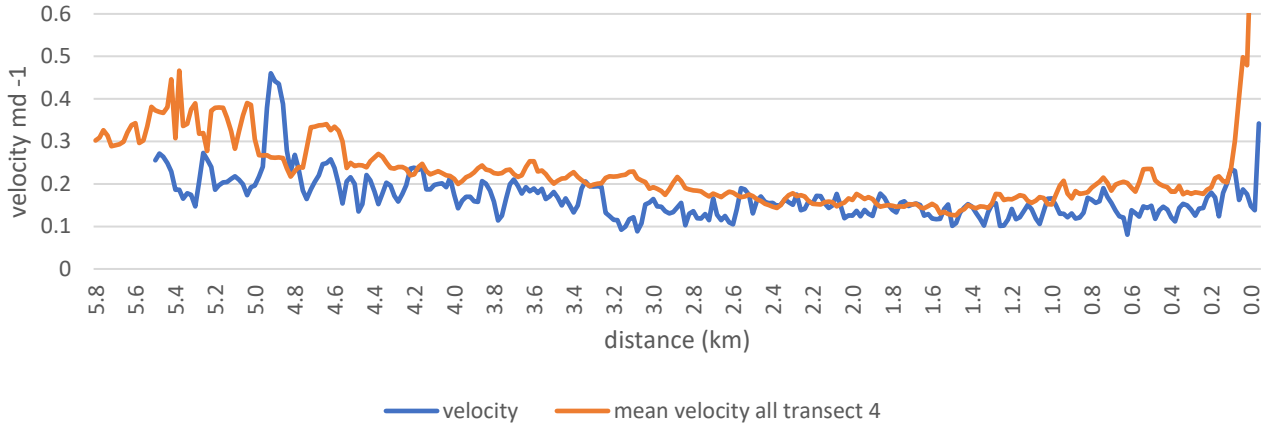
velocity md -1
0.6
0.5
0.4
0.3
0.2
0.1
0
5.8 5.6 5.4 5.2 5.0 4.8 4.6 4.4 4.2 4.0 3.8 3.6 3.4 3.2 3.0 2.8 2.6 2.4 2.2 2.0 1.8 1.6 1.4 1.2 1.0 0.8 0.6 0.4 0.2 0.0
distance (km)
velocity
mean velocity all transect 4

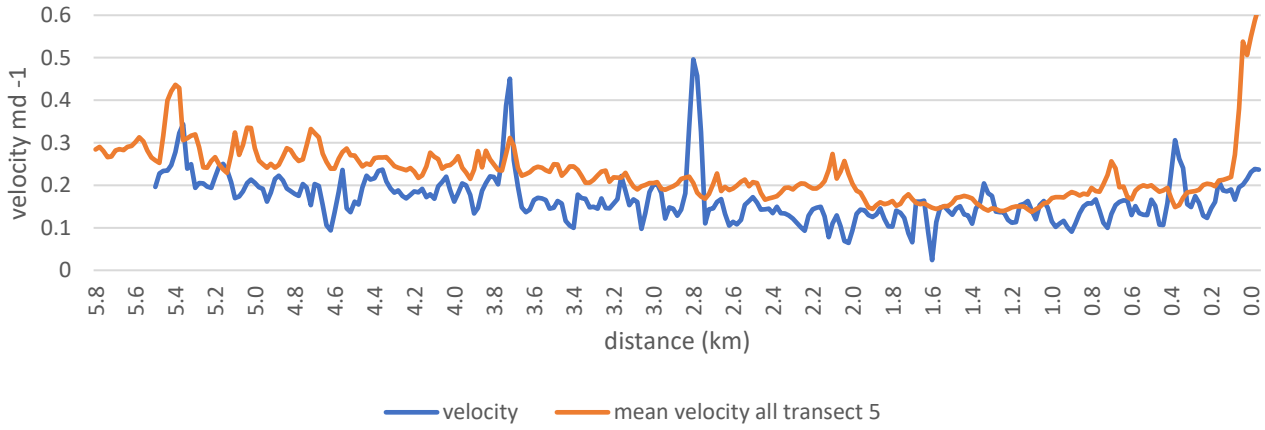
velocity md -1
0.6
0.5
0.4
0.3
0.2
0.1
0
5.8 5.6 5.4 5.2 5.0 4.8 4.6 4.4 4.2 4.0 3.8 3.6 3.4 3.2 3.0 2.8 2.6 2.4 2.2 2.0 1.8 1.6 1.4 1.2 1.0 0.8 0.6 0.4 0.2 0.0
distance (km)
velocity
mean velocity all transect 5

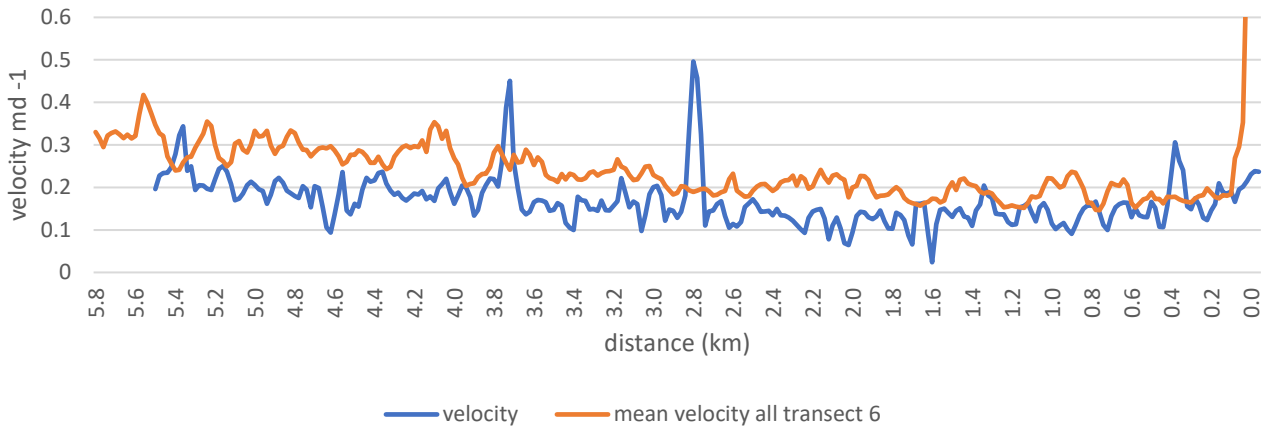

Appendix 8A: Longitudinal velocity profiles from 12/04/2016 – 02/05/2016 (time period of 20 days) The orange line indicates the surface velocity values extracted from all surface velocity images. The blue line is the surface velocity values extracted from each profile. Profiles run from A near the Ball Glacier confluence down to B at the terminus.

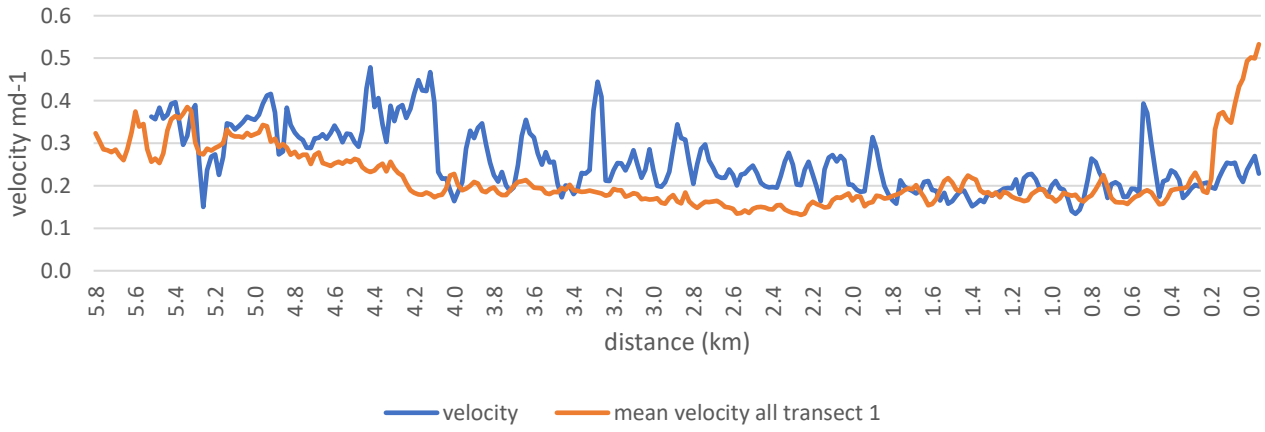

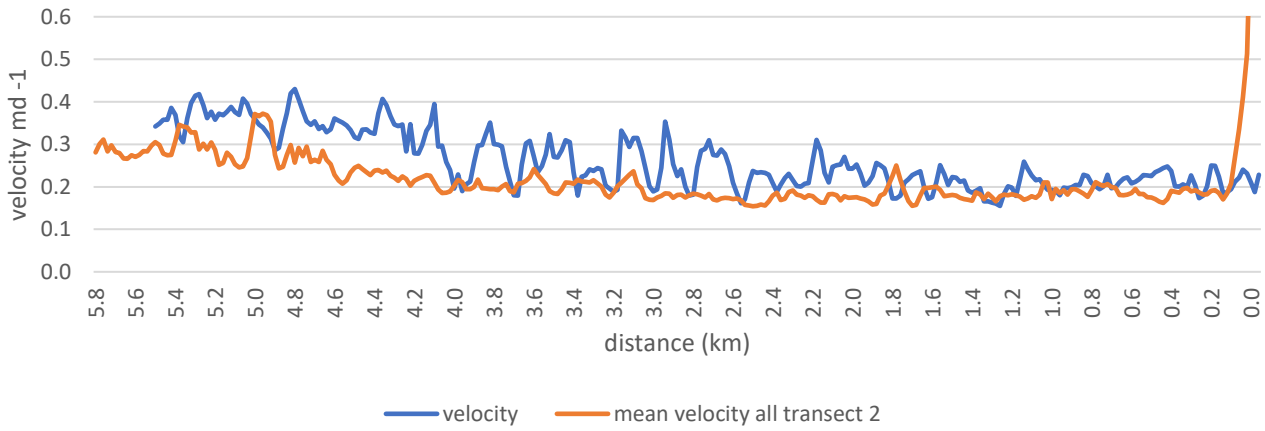

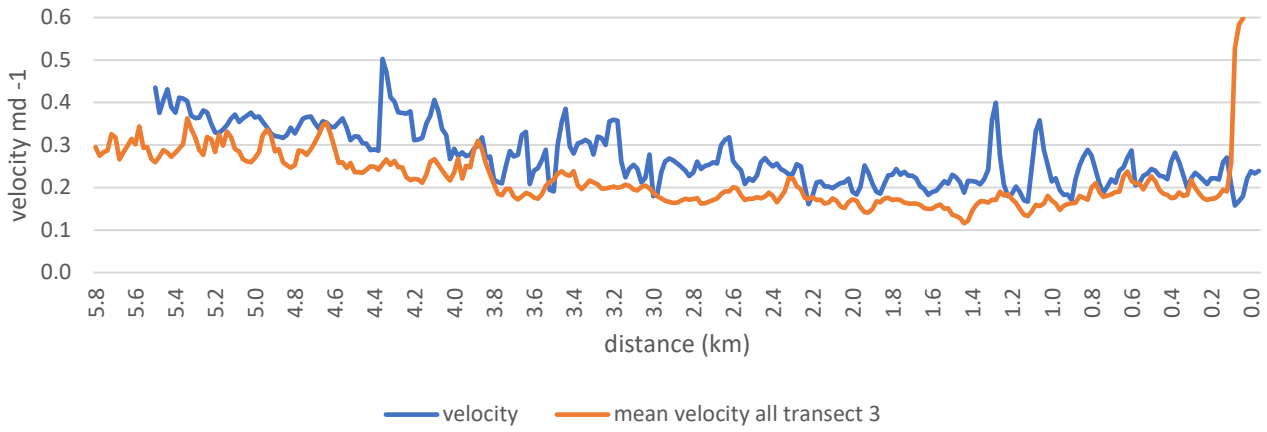
velocity md -1
0.6
0.5
0.4
0.3
0.2
0.1
0.0
5.8 5.6 5.4 5.2 5.0 4.8 4.6 4.4 4.2 4.0 3.8 3.6 3.4 3.2 3.0 2.8 2.6 2.4 2.2 2.0 1.8 1.6 1.4 1.2 1.0 0.8 0.6 0.4 0.2 0.0
distance (km)
velocity
mean velocity all transect 3

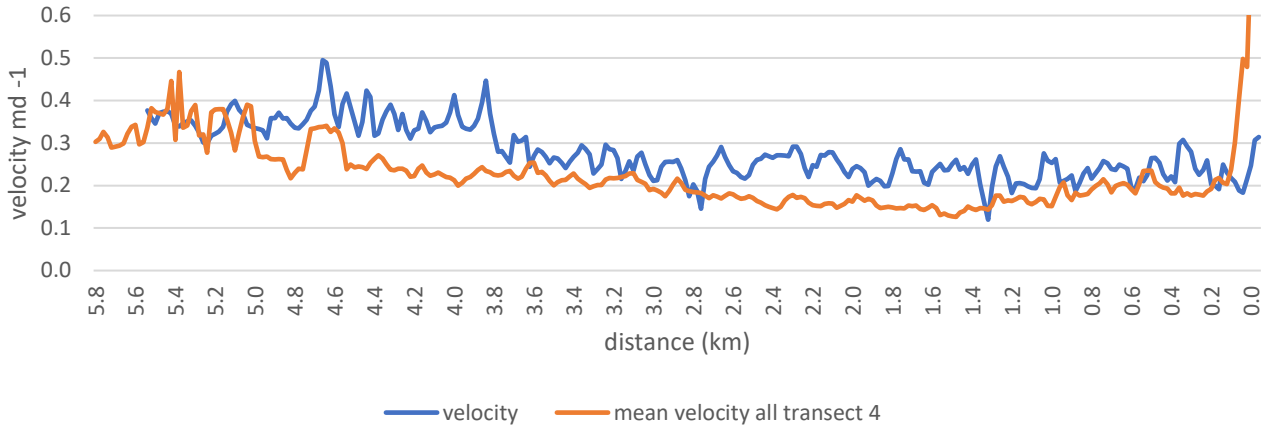
velocity md -1
0.6
0.5
0.4
0.3
0.2
0.1
0.0
5.8 5.6 5.4 5.2 5.0 4.8 4.6 4.4 4.2 4.0 3.8 3.6 3.4 3.2 3.0 2.8 2.6 2.4 2.2 2.0 1.8 1.6 1.4 1.2 1.0 0.8 0.6 0.4 0.2 0.0
distance (km)
velocity
mean velocity all transect 4

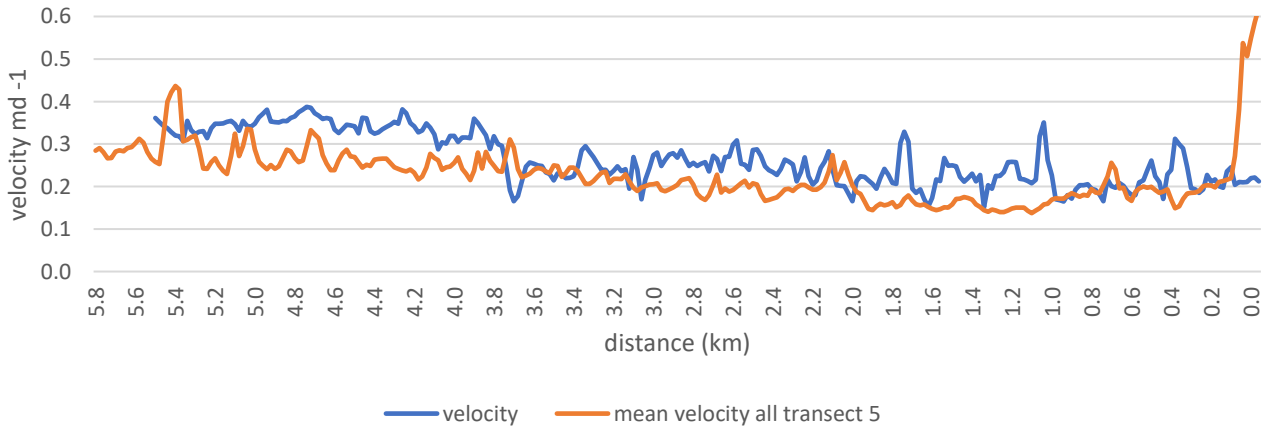
velocity md -1
0.6
0.5
0.4
0.3
0.2
0.1
0.0
5.8 5.6 5.4 5.2 5.0 4.8 4.6 4.4 4.2 4.0 3.8 3.6 3.4 3.2 3.0 2.8 2.6 2.4 2.2 2.0 1.8 1.6 1.4 1.2 1.0 0.8 0.6 0.4 0.2 0.0
distance (km)
velocity
mean velocity all transect 5

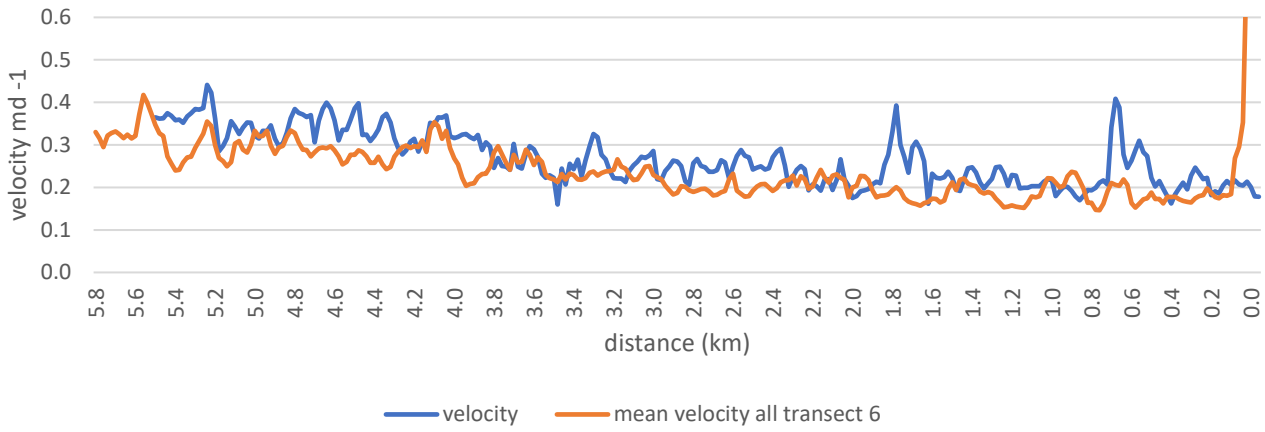

Appendix 9A: Longitudinal velocity profiles from 02/05/2016 – 01/06/2016 (time period of 20 days) The orange line indicates the surface velocity values extracted from all surface velocity images. The blue line is the surface velocity values extracted from each profile. Profiles run from A near the Ball Glacier confluence down to B at the terminus.

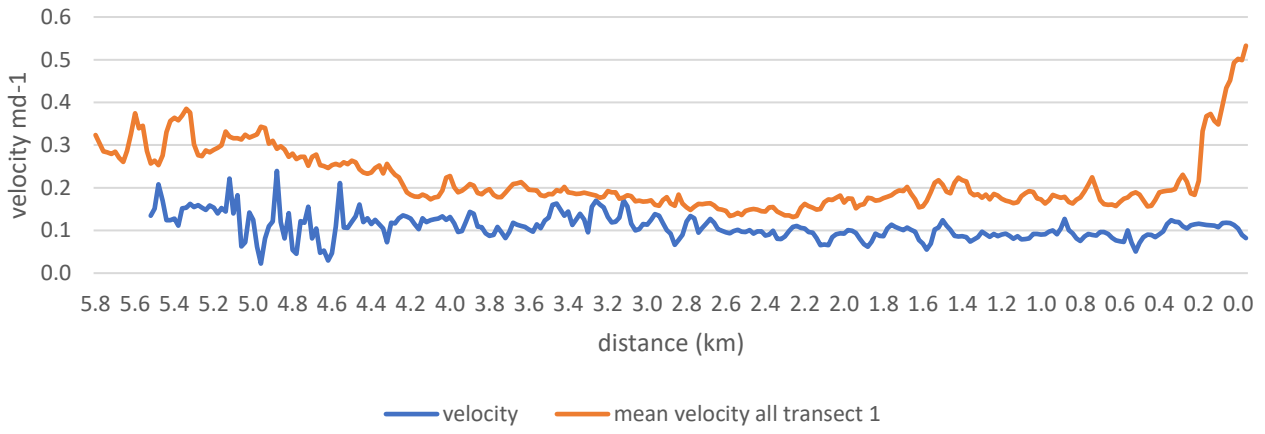

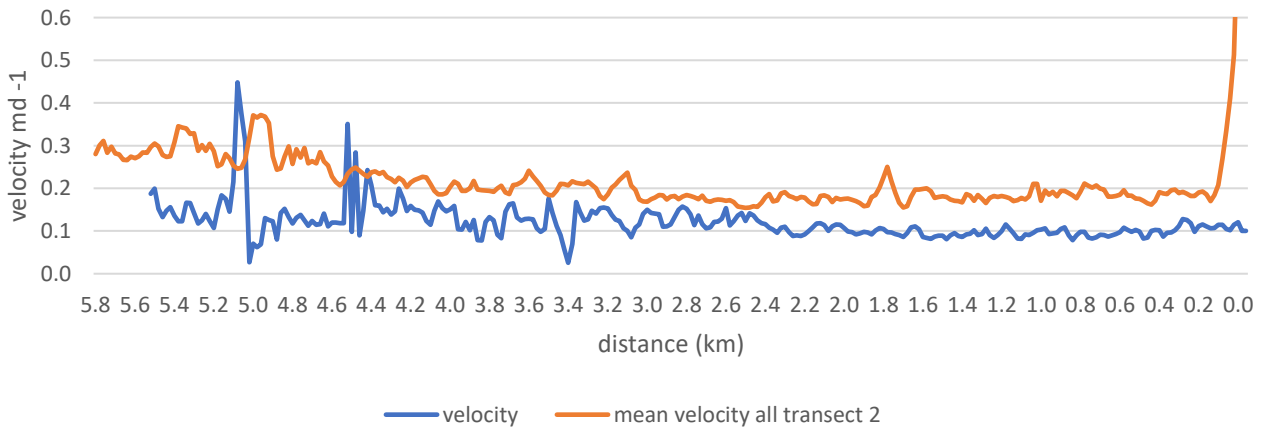

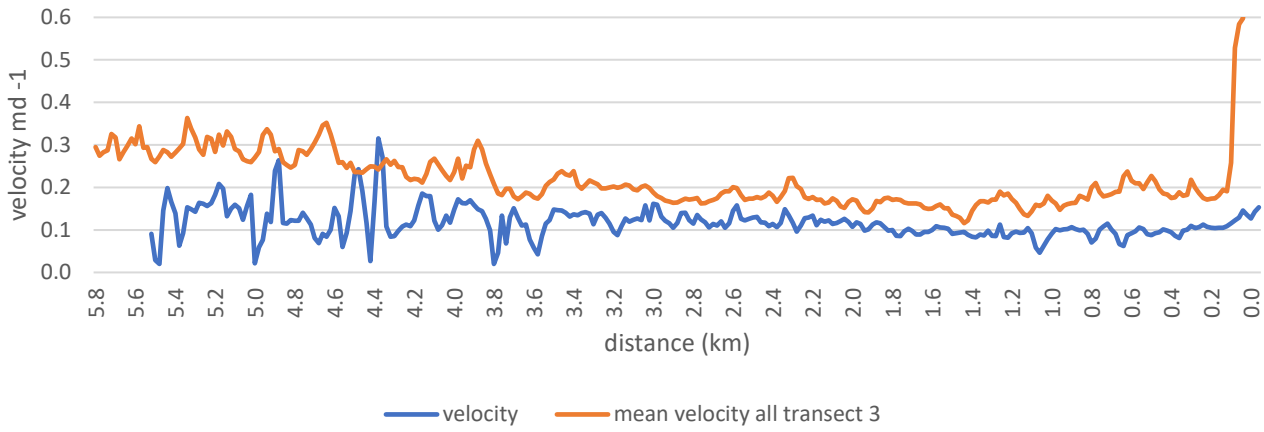
velocity md -1
0.6
0.5
0.4
0.3
0.2
0.1
0.0
5.8 5.6 5.4 5.2 5.0 4.8 4.6 4.4 4.2 4.0 3.8 3.6 3.4 3.2 3.0 2.8 2.6 2.4 2.2 2.0 1.8 1.6 1.4 1.2 1.0 0.8 0.6 0.4 0.2 0.0
distance (km)
velocity
mean velocity all transect 3

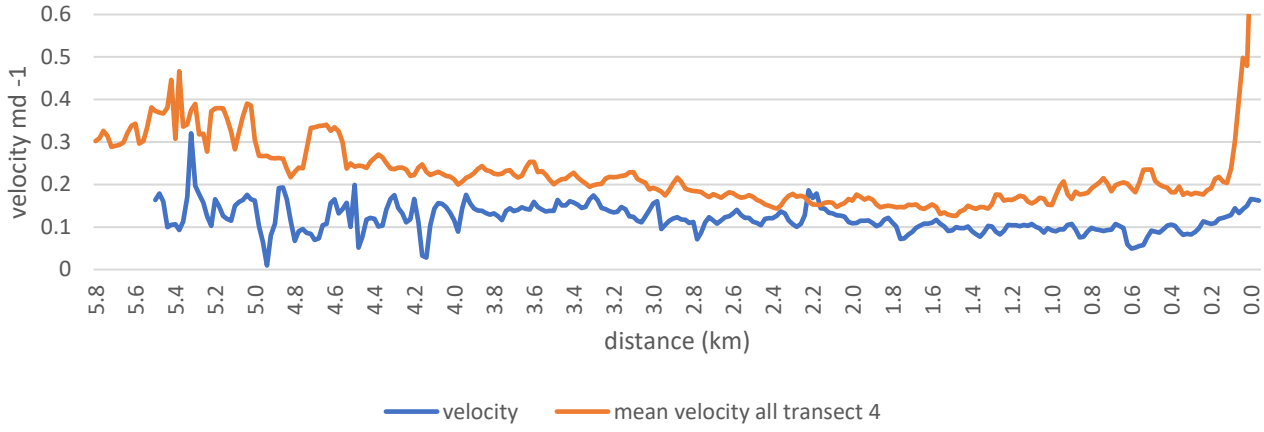
velocity md -1
0.6
0.5
0.4
0.3
0.2
0.1
0
5.8 5.6 5.4 5.2 5.0 4.8 4.6 4.4 4.2 4.0 3.8 3.6 3.4 3.2 3.0 2.8 2.6 2.4 2.2 2.0 1.8 1.6 1.4 1.2 1.0 0.8 0.6 0.4 0.2 0.0
distance (km)
velocity
mean velocity all transect 4

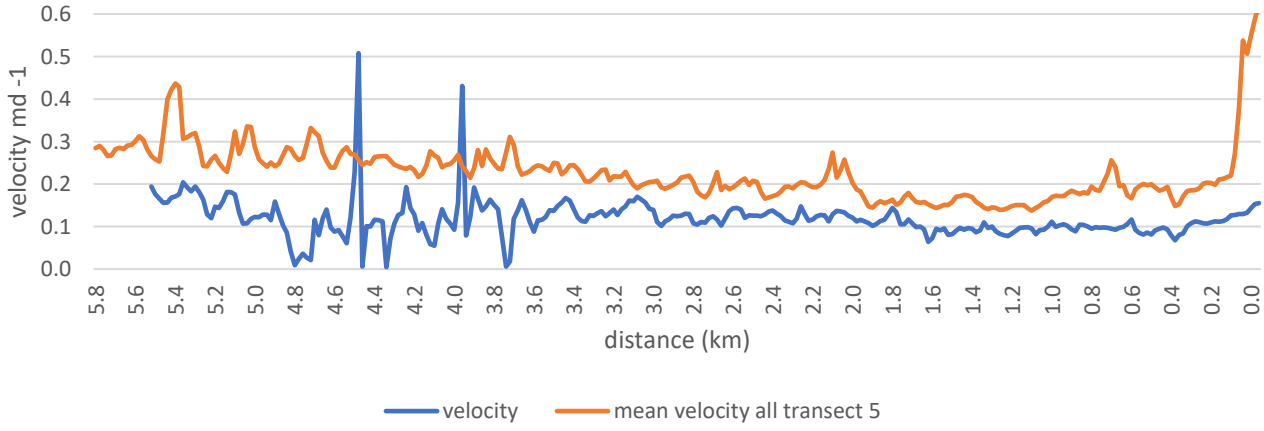
velocity md -1
0.6
0.5
0.4
0.3
0.2
0.1
0.0
5.8 5.6 5.4 5.2 5.0 4.8 4.6 4.4 4.2 4.0 3.8 3.6 3.4 3.2 3.0 2.8 2.6 2.4 2.2 2.0 1.8 1.6 1.4 1.2 1.0 0.8 0.6 0.4 0.2 0.0
distance (km)
velocity
mean velocity all transect 5

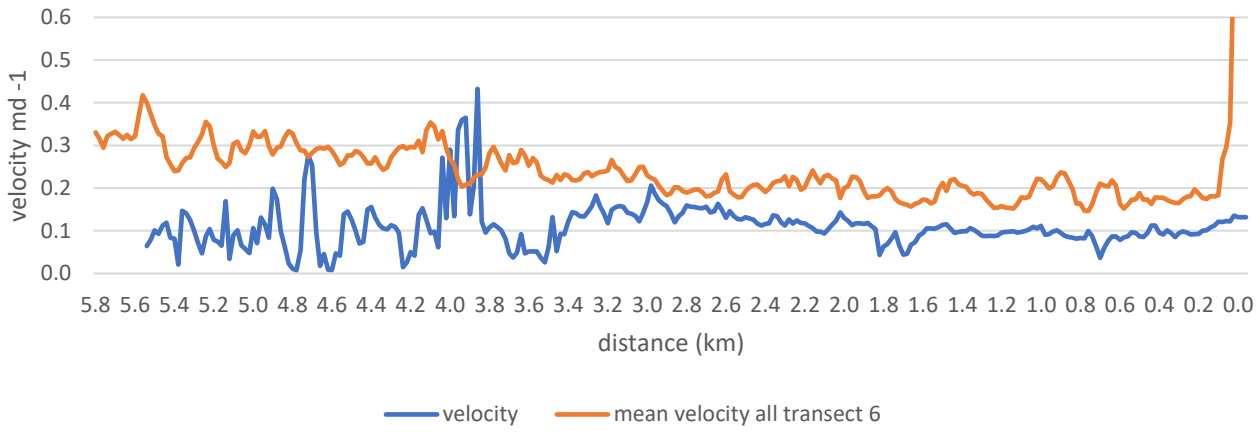

Appendix 10A: Longitudinal velocity profiles from 01/06/2016 – 21/07/2016 (time period of 50 days) The orange line indicates the surface velocity values extracted from all surface velocity images. The blue line is the surface velocity values extracted from each profile. Profiles run from A near the Ball Glacier confluence down to B at the terminus.

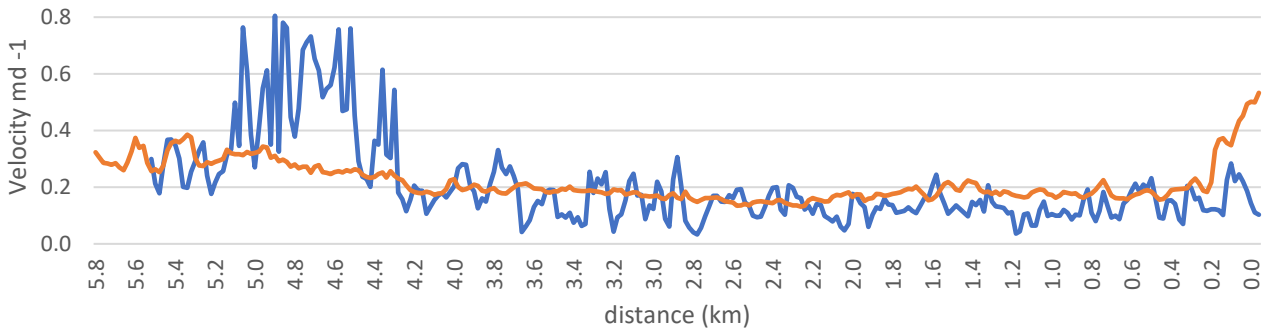

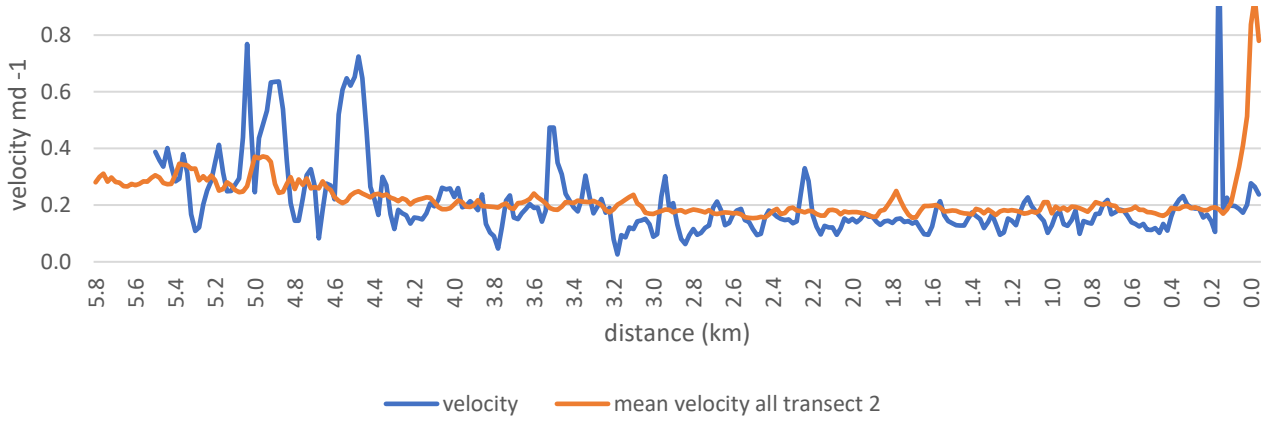

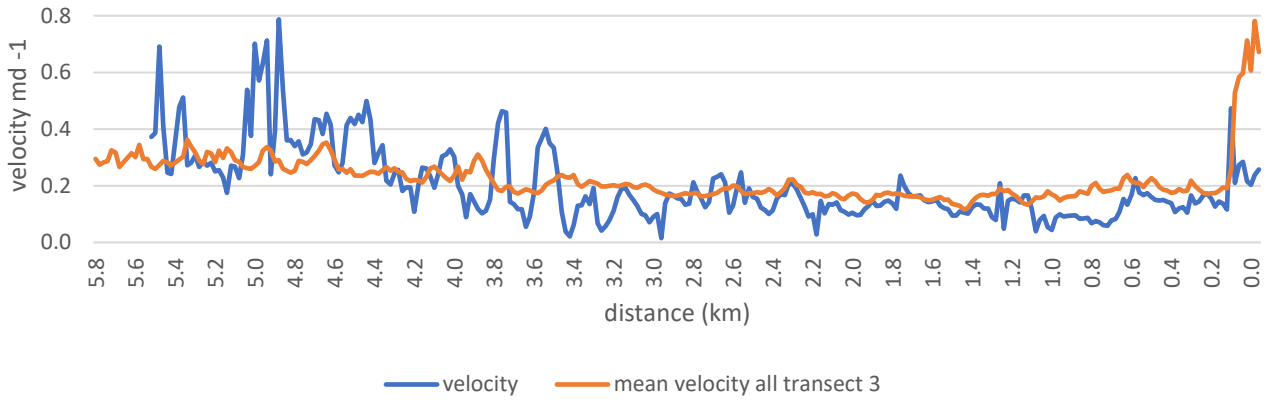
velocity md -1
0.8
0.6
0.4
0.2
0.0
5.8 5.6 5.4 5.2 5.0 4.8 4.6 4.4 4.2 4.0 3.8 3.6 3.4 3.2 3.0 2.8 2.6 2.4 2.2 2.0 1.8 1.6 1.4 1.2 1.0 0.8 0.6 0.4 0.2 0.0
distance (km)
velocity
mean velocity all transect 3

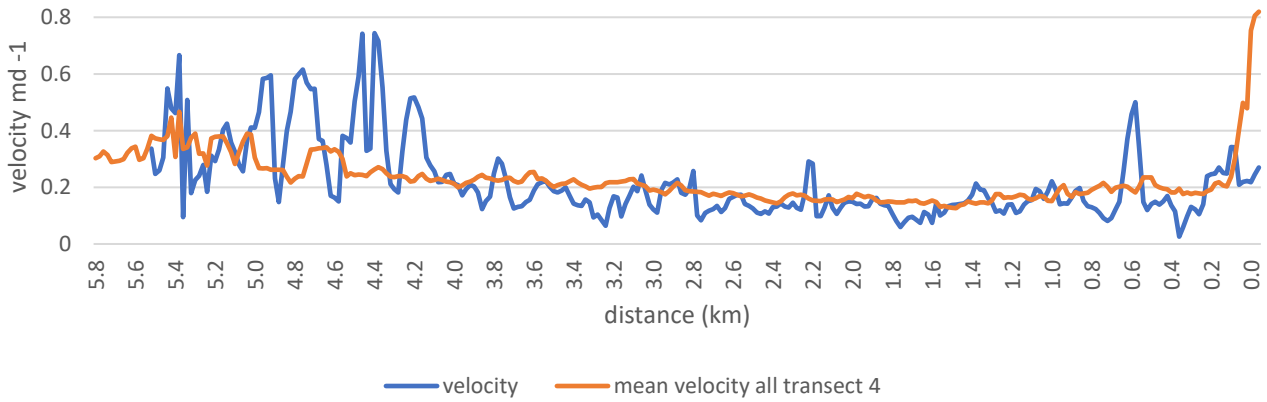
velocity md -1
0.8
0.6
0.4
0.2
0
5.8 5.6 5.4 5.2 5.0 4.8 4.6 4.4 4.2 4.0 3.8 3.6 3.4 3.2 3.0 2.8 2.6 2.4 2.2 2.0 1.8 1.6 1.4 1.2 1.0 0.8 0.6 0.4 0.2 0.0
distance (km)
velocity
mean velocity all transect 4

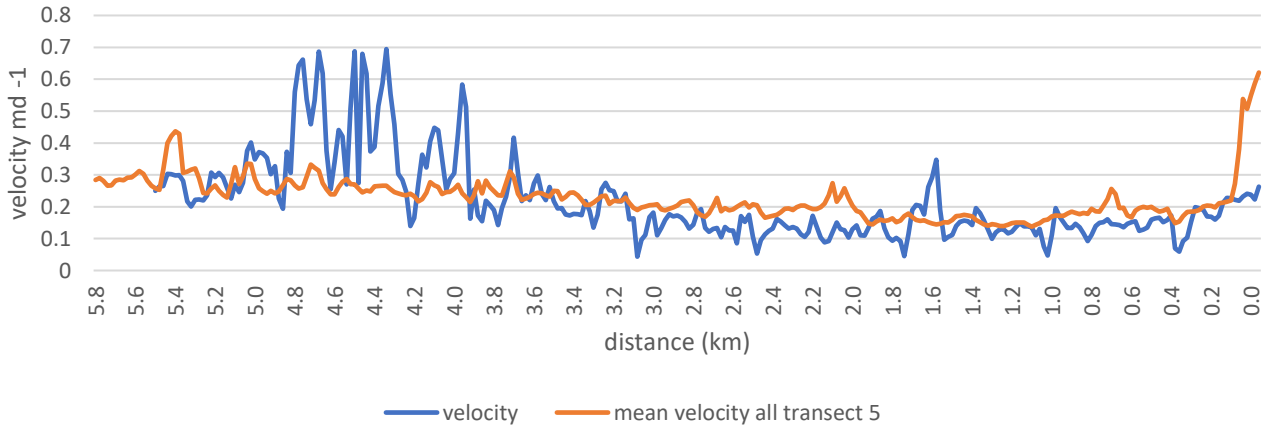
velocity md -1
0.8
0.7
0.6
0.5
0.4
0.3
0.2
0.1
0
5.8 5.6 5.4 5.2 5.0 4.8 4.6 4.4 4.2 4.0 3.8 3.6 3.4 3.2 3.0 2.8 2.6 2.4 2.2 2.0 1.8 1.6 1.4 1.2 1.0 0.8 0.6 0.4 0.2 0.0
distance (km)
velocity
mean velocity all transect 5

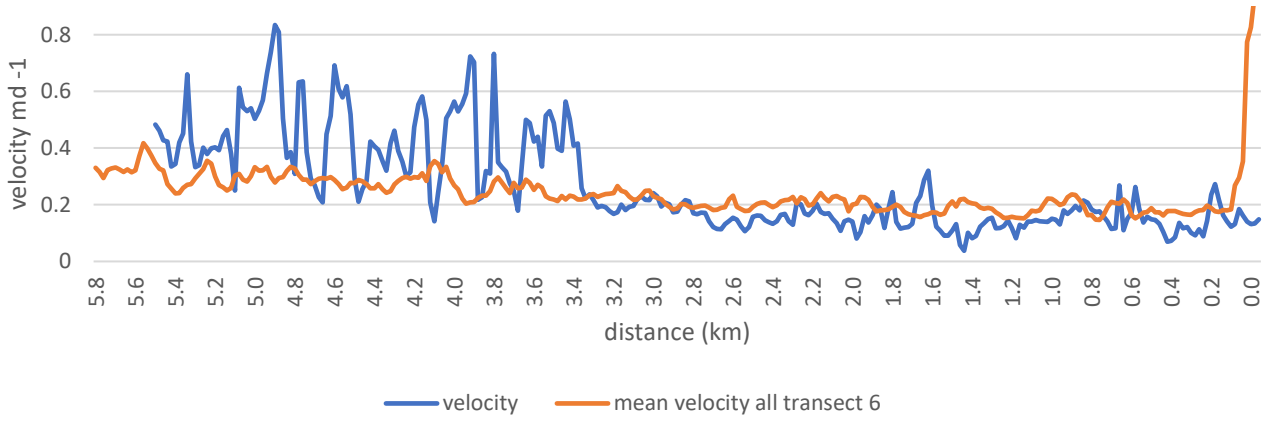

Appendix 11A: Longitudinal velocity profiles from 21/07/2016 – 10/08/2016 (time period of 20 days) The orange line indicates the surface velocity values extracted from all surface velocity images. The blue line is the surface velocity values extracted from each profile. Profiles run from A near the Ball Glacier confluence down to B at the terminus.

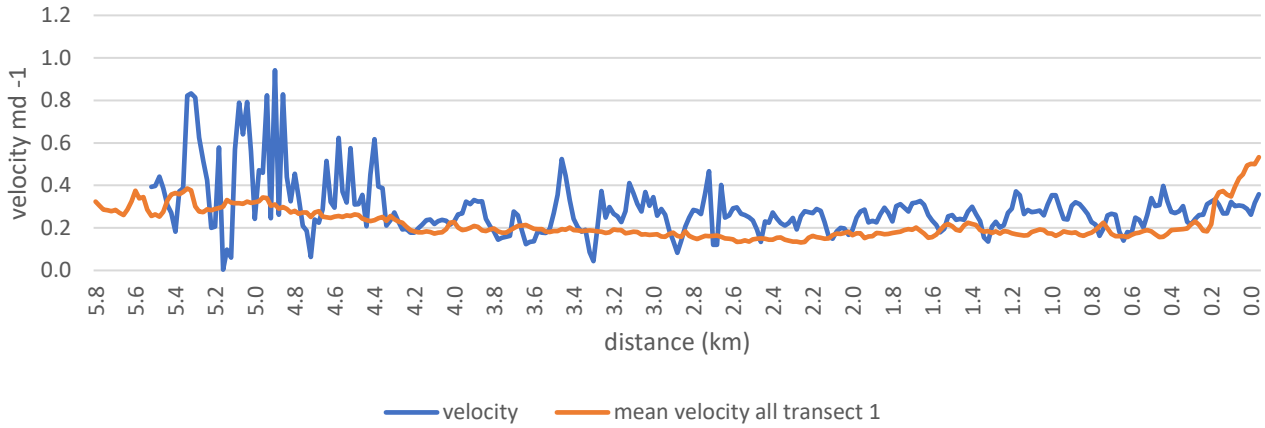

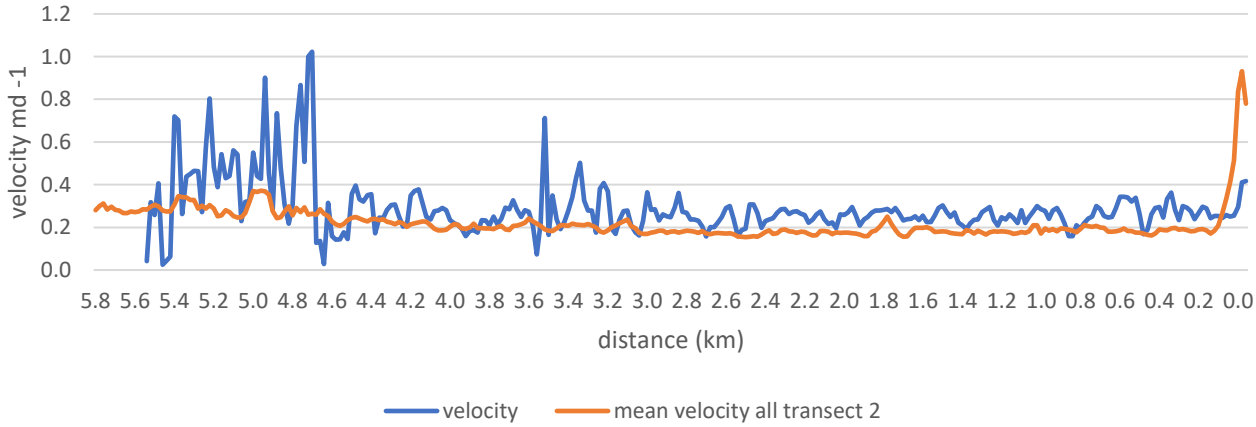

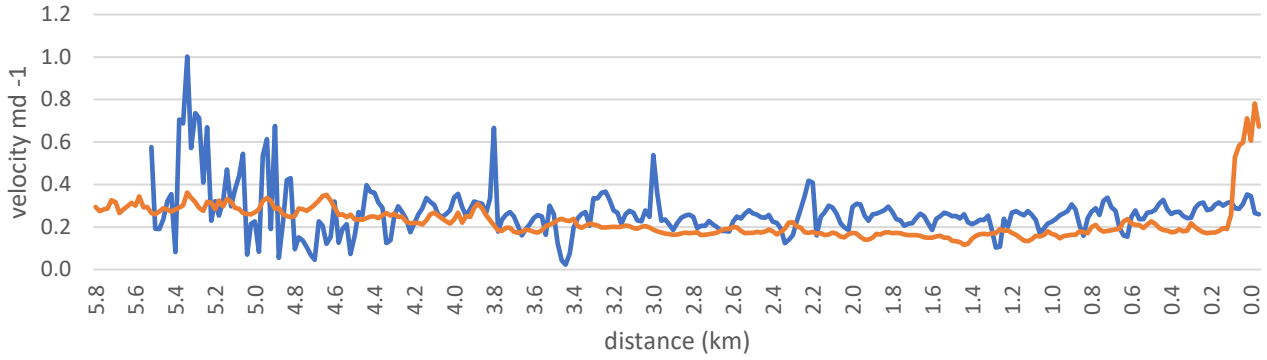
velocity md -1
1.2
1.0
0.8
0.6
0.4
0.2
0.0
5.8 5.6 5.4 5.2 5.0 4.8 4.6 4.4 4.2 4.0 3.8 3.6 3.4 3.2 3.0 2.8 2.6 2.4 2.2 2.0 1.8 1.6 1.4 1.2 1.0 0.8 0.6 0.4 0.2 0.0
distance (km)
velocity
mean velocity all transect 3

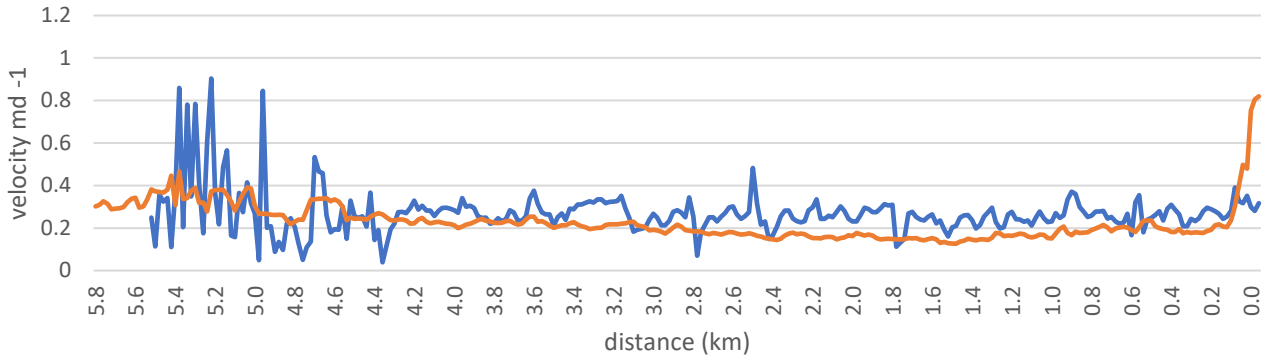
velocity md -1
1.2
1
0.8
0.6
0.4
0.2
0
5.8 5.6 5.4 5.2 5.0 4.8 4.6 4.4 4.2 4.0 3.8 3.6 3.4 3.2 3.0 2.8 2.6 2.4 2.2 2.0 1.8 1.6 1.4 1.2 1.0 0.8 0.6 0.4 0.2 0.0
distance (km)
velocity
mean velocity all transect 4

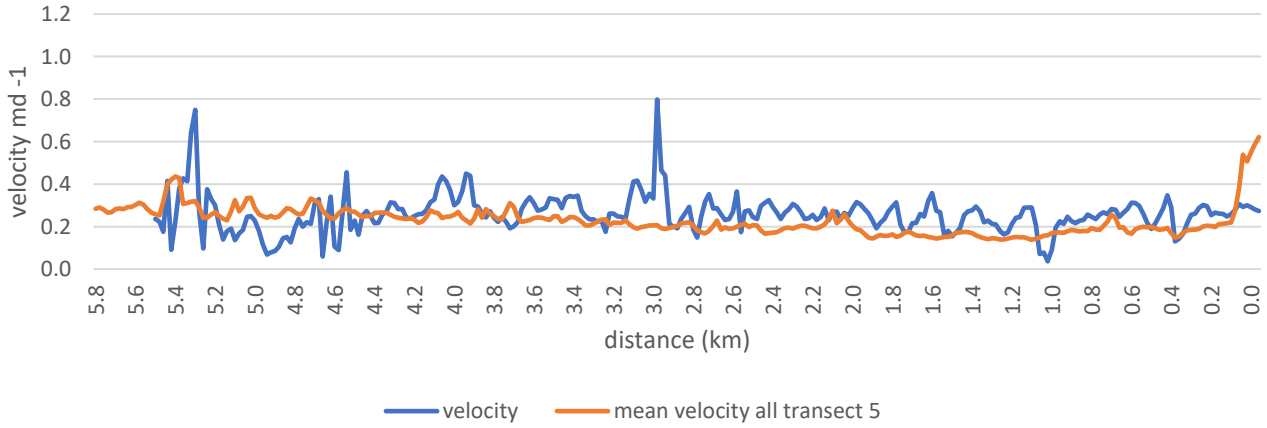
velocity md -1
1.2
1.0
0.8
0.6
0.4
0.2
0.0
5.8 5.6 5.4 5.2 5.0 4.8 4.6 4.4 4.2 4.0 3.8 3.6 3.4 3.2 3.0 2.8 2.6 2.4 2.2 2.0 1.8 1.6 1.4 1.2 1.0 0.8 0.6 0.4 0.2 0.0
distance (km)
velocity
mean velocity all transect 5

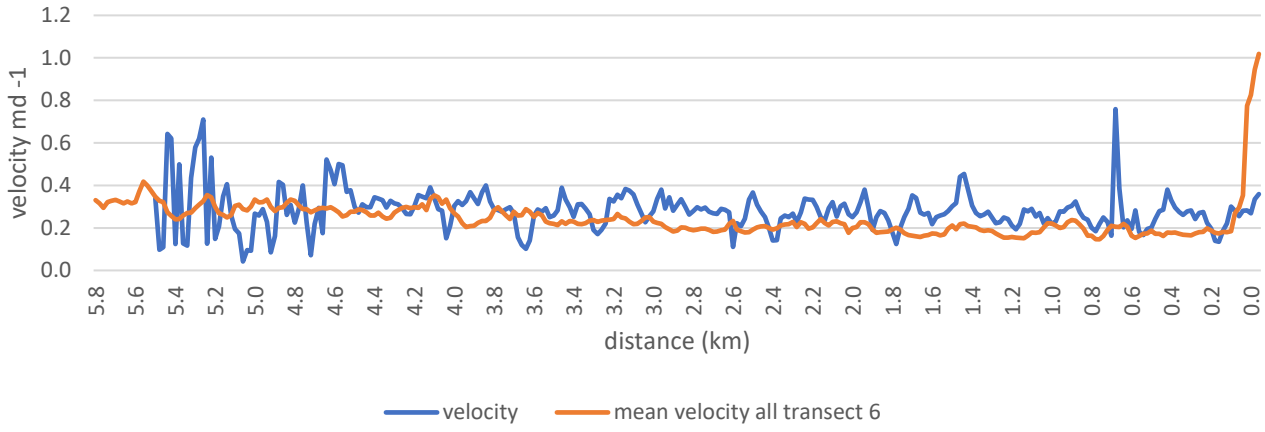

Appendix 12A: Longitudinal velocity profiles from 10/08/2016 – 30/08/2016 (time period of 20 days) The orange line indicates the surface velocity values extracted from all surface velocity images. The blue line is the surface velocity values extracted from each profile. Profiles run from A near the Ball Glacier confluence down to B at the terminus.

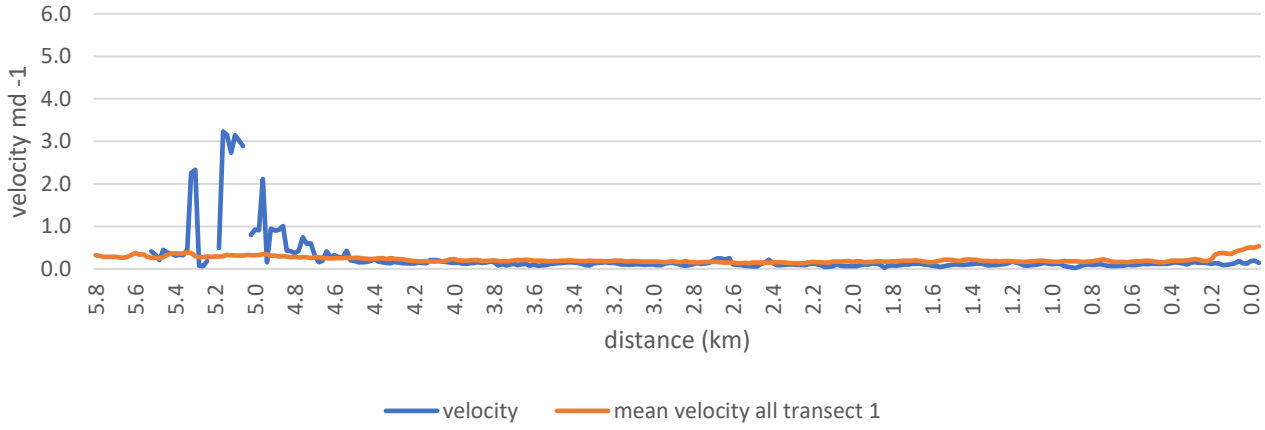

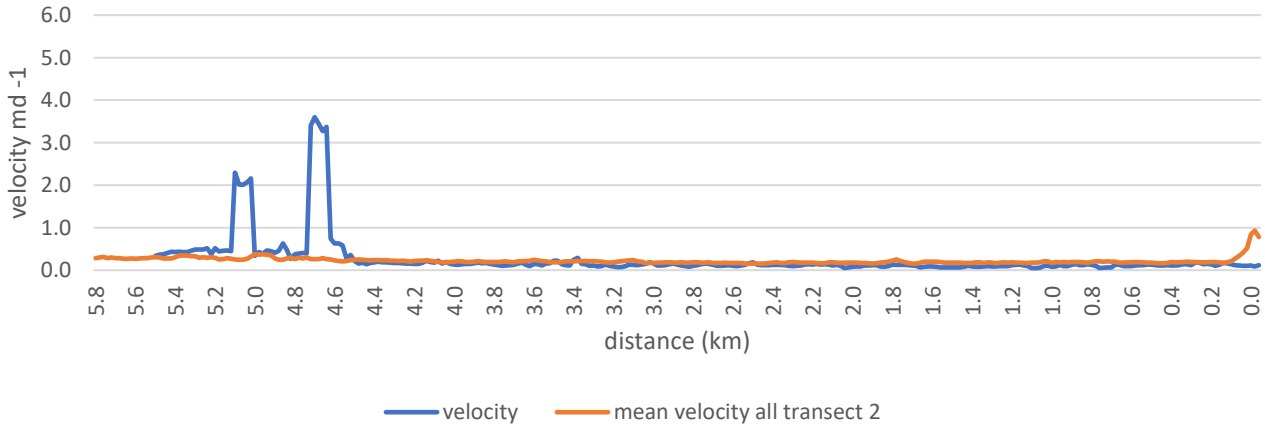

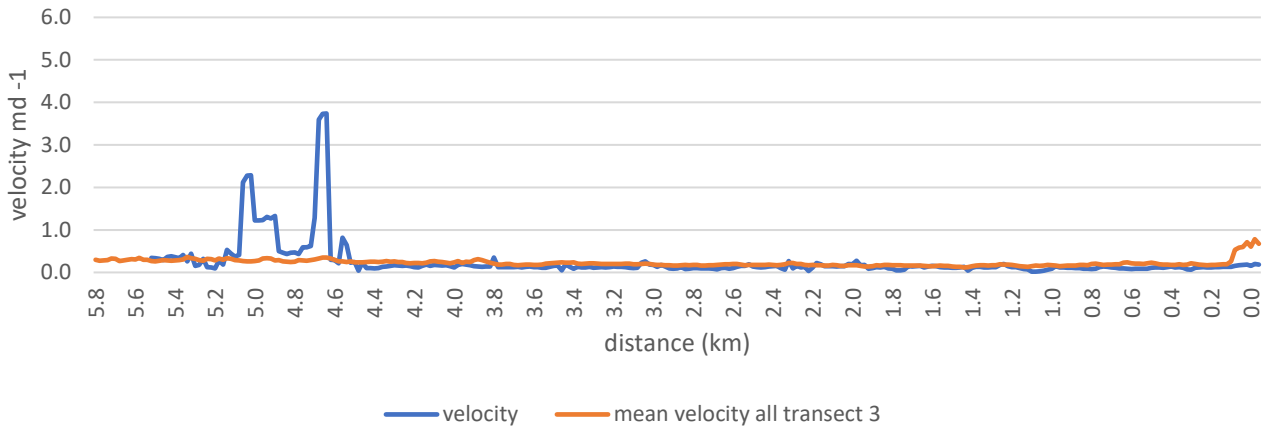
velocity md -1
6.0
5.0
4.0
3.0
2.0
1.0
0.0
5.8 5.6 5.4 5.2 5.0 4.8 4.6 4.4 4.2 4.0 3.8 3.6 3.4 3.2 3.0 2.8 2.6 2.4 2.2 2.0 1.8 1.6 1.4 1.2 1.0 0.8 0.6 0.4 0.2 0.0
distance (km)
velocity
mean velocity all transect 3

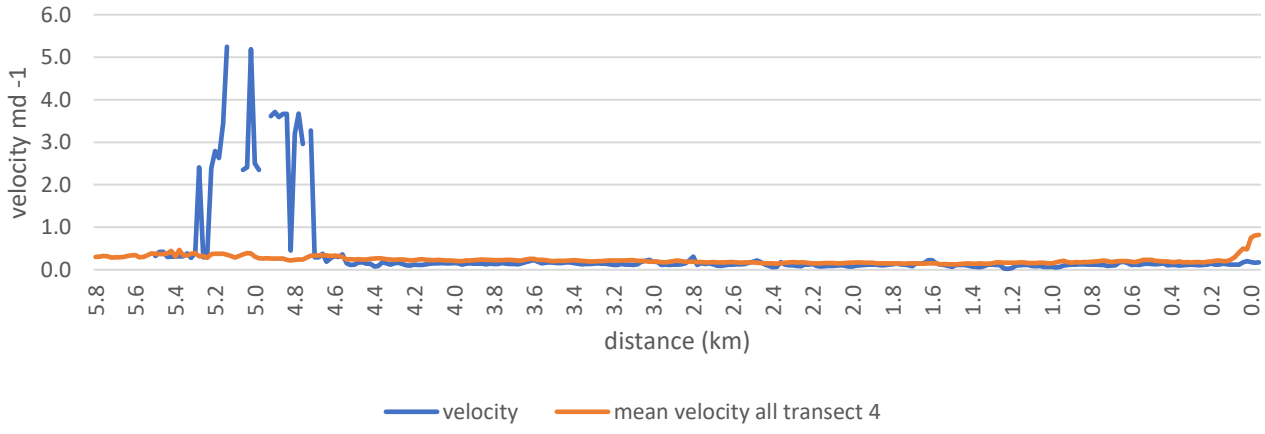
velocity md -1
6.0
5.0
4.0
3.0
2.0
1.0
0.0
5.8 5.6 5.4 5.2 5.0 4.8 4.6 4.4 4.2 4.0 3.8 3.6 3.4 3.2 3.0 2.8 2.6 2.4 2.2 2.0 1.8 1.6 1.4 1.2 1.0 0.8 0.6 0.4 0.2 0.0
distance (km)
velocity
mean velocity all transect 4

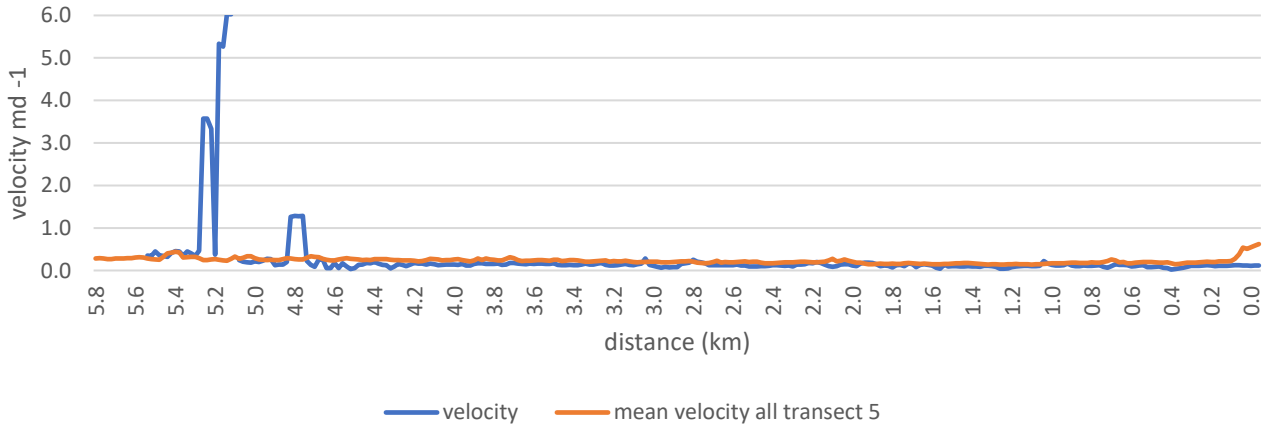
velocity md -1
6.0
5.0
4.0
3.0
2.0
1.0
0.0
5.8 5.6 5.4 5.2 5.0 4.8 4.6 4.4 4.2 4.0 3.8 3.6 3.4 3.2 3.0 2.8 2.6 2.4 2.2 2.0 1.8 1.6 1.4 1.2 1.0 0.8 0.6 0.4 0.2 0.0
distance (km)
velocity
mean velocity all transect 5

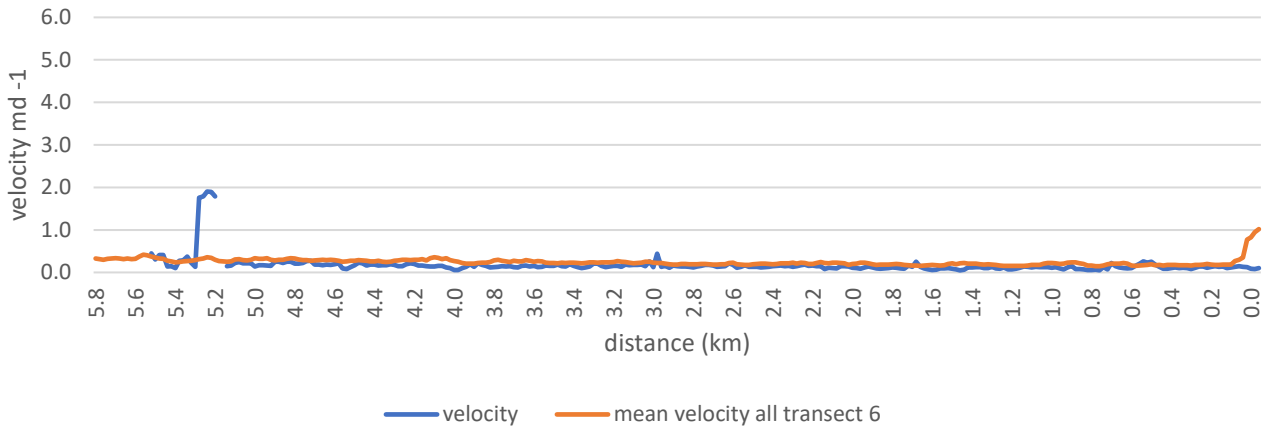

Appendix 13A: Longitudinal velocity profiles from 30/08/2016 – 29/10/2016 (time period of 60 days) The orange line indicates the surface velocity values extracted from all surface velocity images. The blue line is the surface velocity values extracted from each profile. Profiles run from A near the Ball Glacier confluence down to B at the terminus.

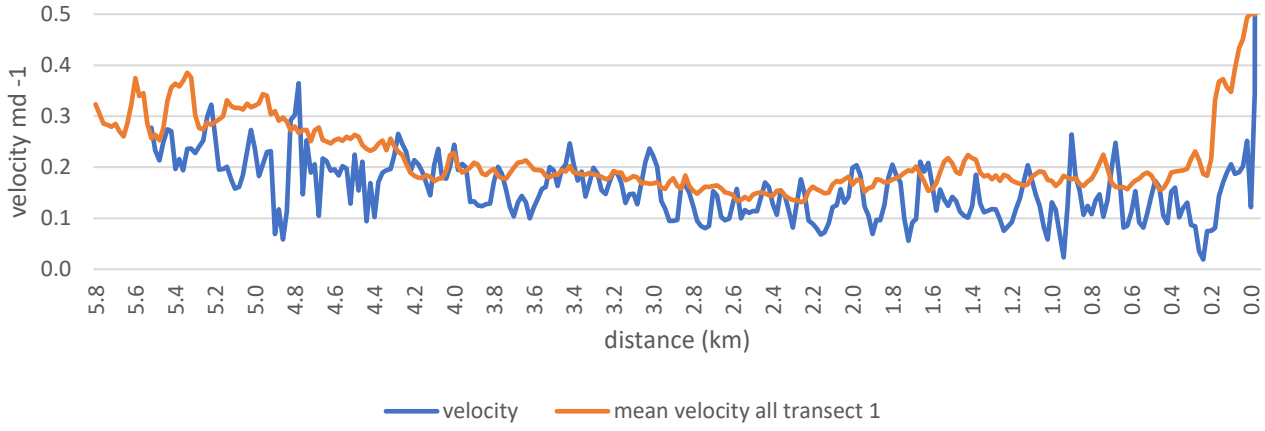

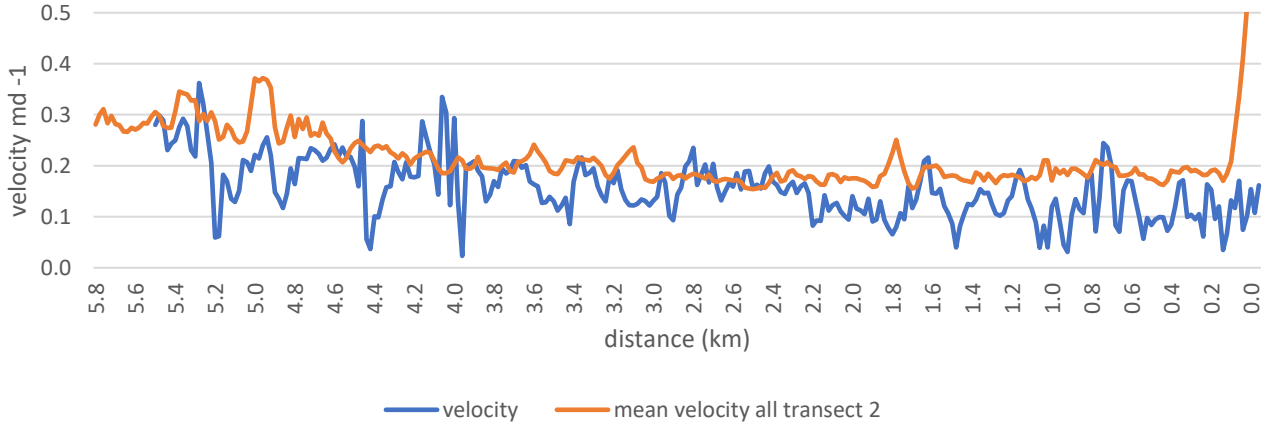

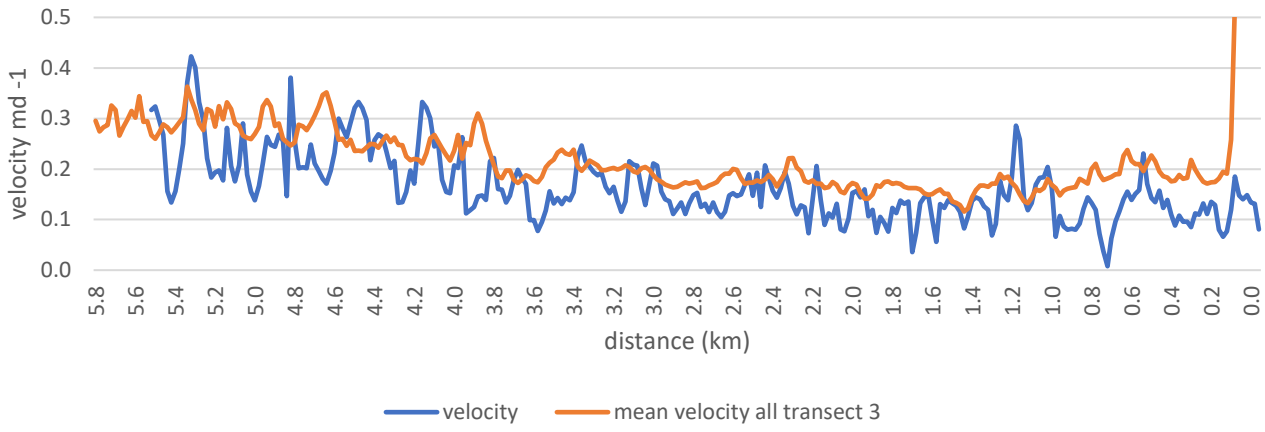
velocity md -1
0.5
0.4
0.3
0.2
0.1
0.0
5.8 5.6 5.4 5.2 5.0 4.8 4.6 4.4 4.2 4.0 3.8 3.6 3.4 3.2 3.0 2.8 2.6 2.4 2.2 2.0 1.8 1.6 1.4 1.2 1.0 0.8 0.6 0.4 0.2 0.0
distance (km)
velocity
mean velocity all transect 3

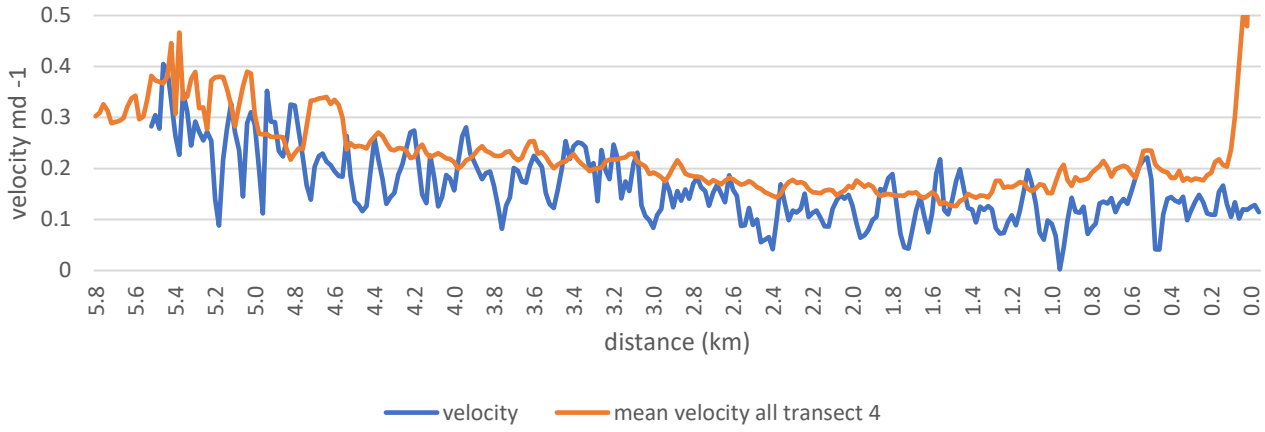
velocity md -1
0.5
0.4
0.3
0.2
0.1
0
5.8 5.6 5.4 5.2 5.0 4.8 4.6 4.4 4.2 4.0 3.8 3.6 3.4 3.2 3.0 2.8 2.6 2.4 2.2 2.0 1.8 1.6 1.4 1.2 1.0 0.8 0.6 0.4 0.2 0.0
distance (km)
velocity
mean velocity all transect 4

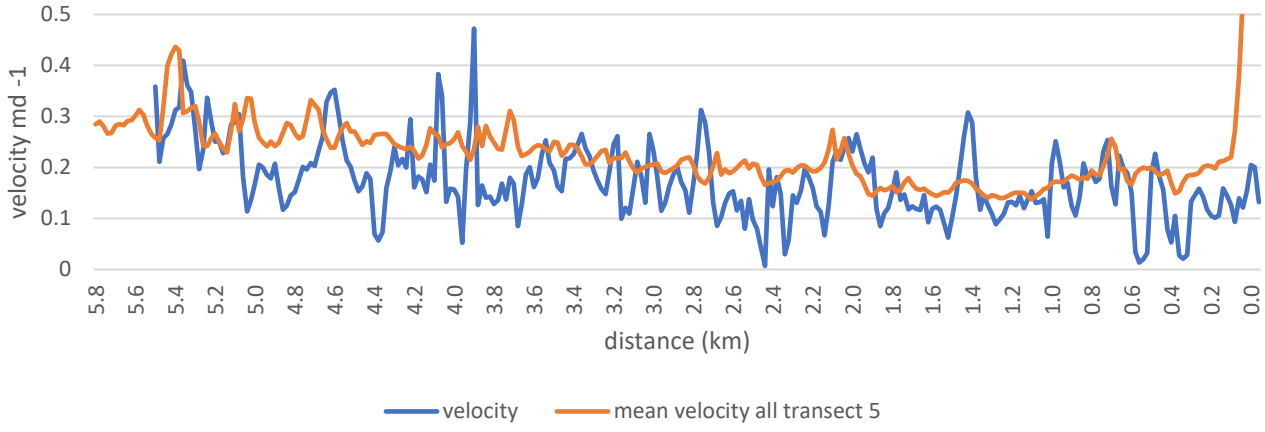
velocity md -1
0.5
0.4
0.3
0.2
0.1
0
5.8 5.6 5.4 5.2 5.0 4.8 4.6 4.4 4.2 4.0 3.8 3.6 3.4 3.2 3.0 2.8 2.6 2.4 2.2 2.0 1.8 1.6 1.4 1.2 1.0 0.8 0.6 0.4 0.2 0.0
distance (km)
velocity
mean velocity all transect 5

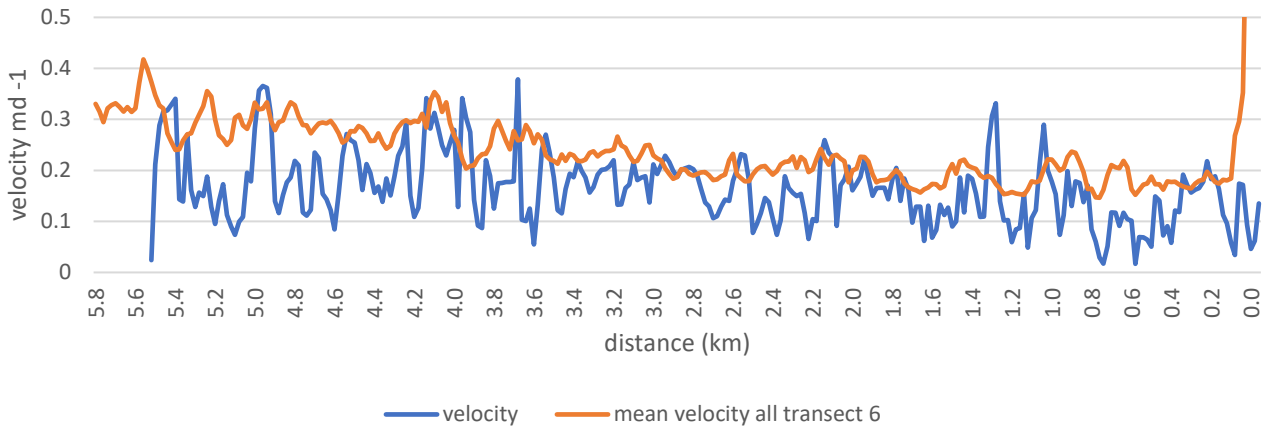

Appendix 14A: Longitudinal velocity profiles from 29/10/2016 – 08/12/2016 (time period of 40 days) The orange line indicates the surface velocity values extracted from all surface velocity images. The blue line is the surface velocity values extracted from each profile. Profiles run from A near the Ball Glacier confluence down to B at the terminus.

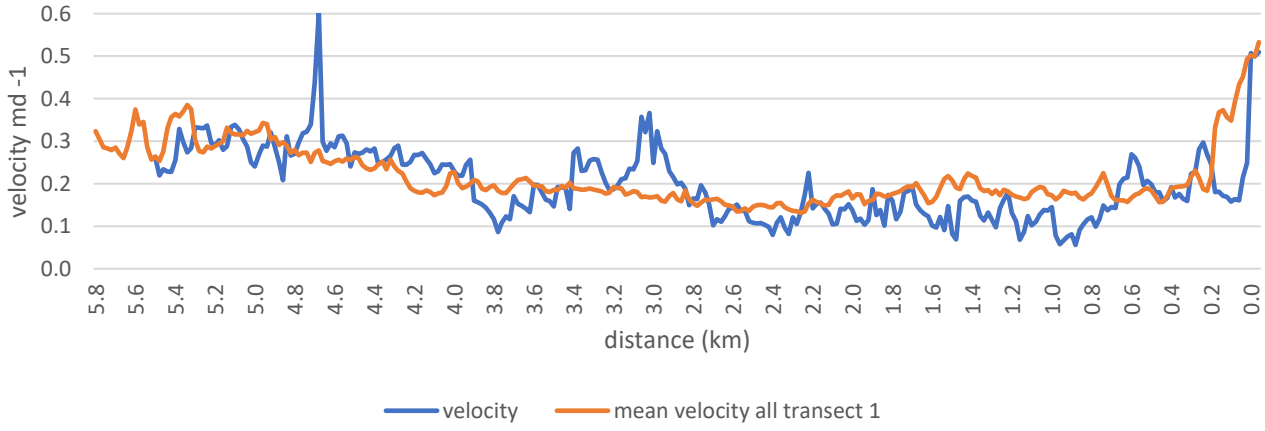

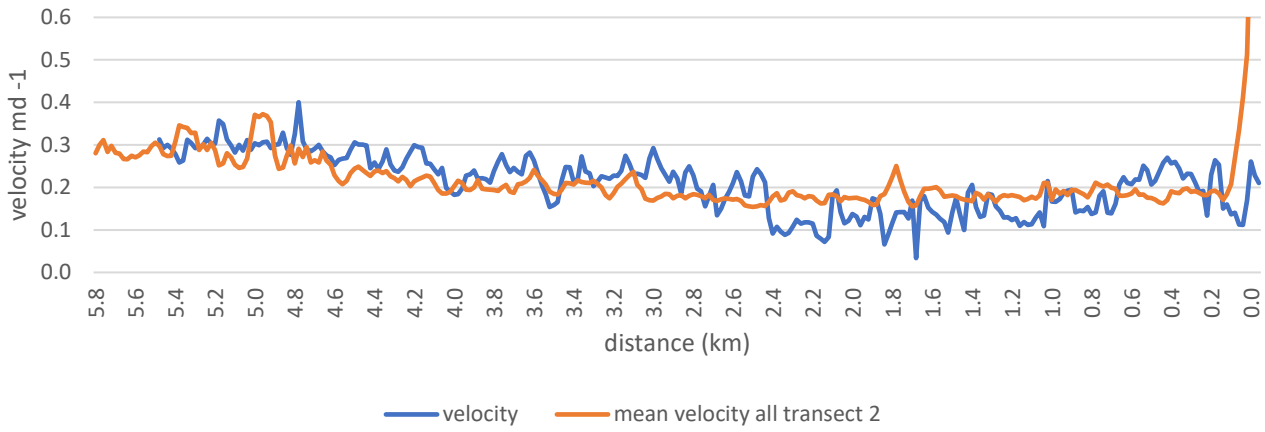
velocity md -1
0.6
0.5
0.4
0.3
0.2
0.1
0.0
5.8 5.6 5.4 5.2 5.0 4.8 4.6 4.4 4.2 4.0 3.8 3.6 3.4 3.2 3.0 2.8 2.6 2.4 2.2 2.0 1.8 1.6 1.4 1.2 1.0 0.8 0.6 0.4 0.2 0.0
distance (km)
velocity
mean velocity all transect 2

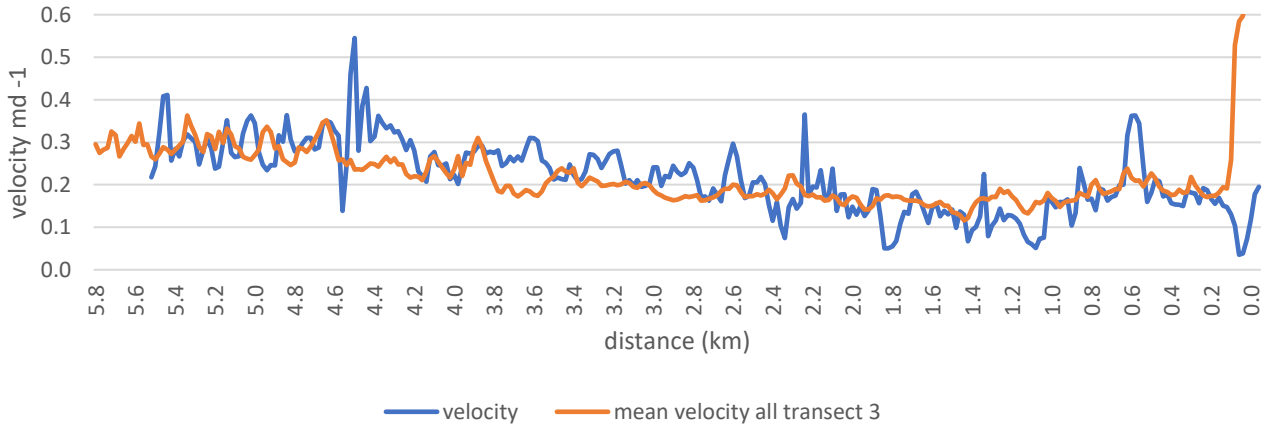
velocity md -1
0.6
0.5
0.4
0.3
0.2
0.1
0.0
5.8 5.6 5.4 5.2 5.0 4.8 4.6 4.4 4.2 4.0 3.8 3.6 3.4 3.2 3.0 2.8 2.6 2.4 2.2 2.0 1.8 1.6 1.4 1.2 1.0 0.8 0.6 0.4 0.2 0.0
distance (km)
velocity
mean velocity all transect 3

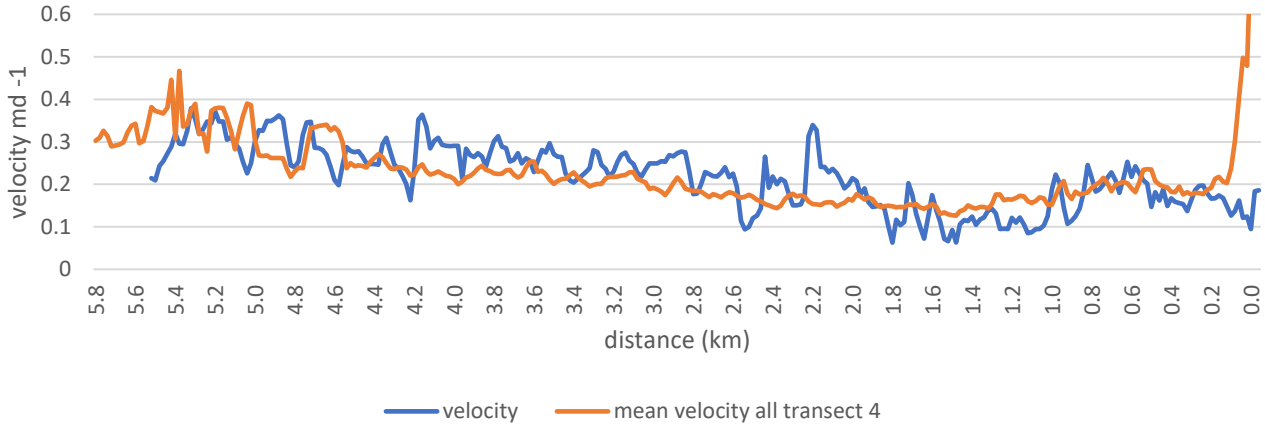
velocity md -1
0.6
0.5
0.4
0.3
0.2
0.1
0
5.8 5.6 5.4 5.2 5.0 4.8 4.6 4.4 4.2 4.0 3.8 3.6 3.4 3.2 3.0 2.8 2.6 2.4 2.2 2.0 1.8 1.6 1.4 1.2 1.0 0.8 0.6 0.4 0.2 0.0
distance (km)
velocity
mean velocity all transect 4

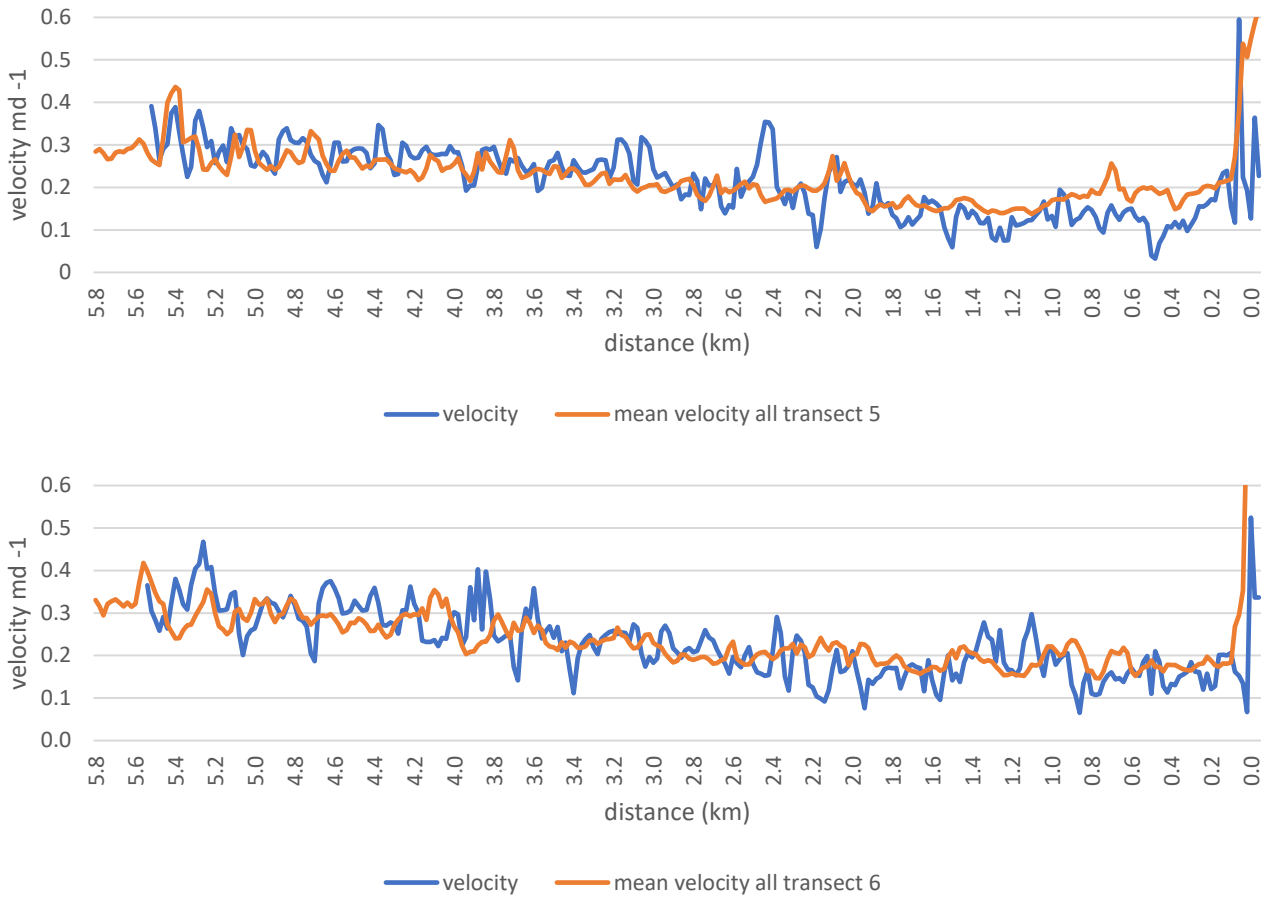

Appendix 15A: Longitudinal velocity profiles from 08/12/2016 – 27/01/2017 (time period of 50 days) The orange line indicates the surface velocity values extracted from all surface velocity images. The blue line is the surface velocity values extracted from each profile. Profiles run from A near the Ball Glacier confluence down to B at the terminus.

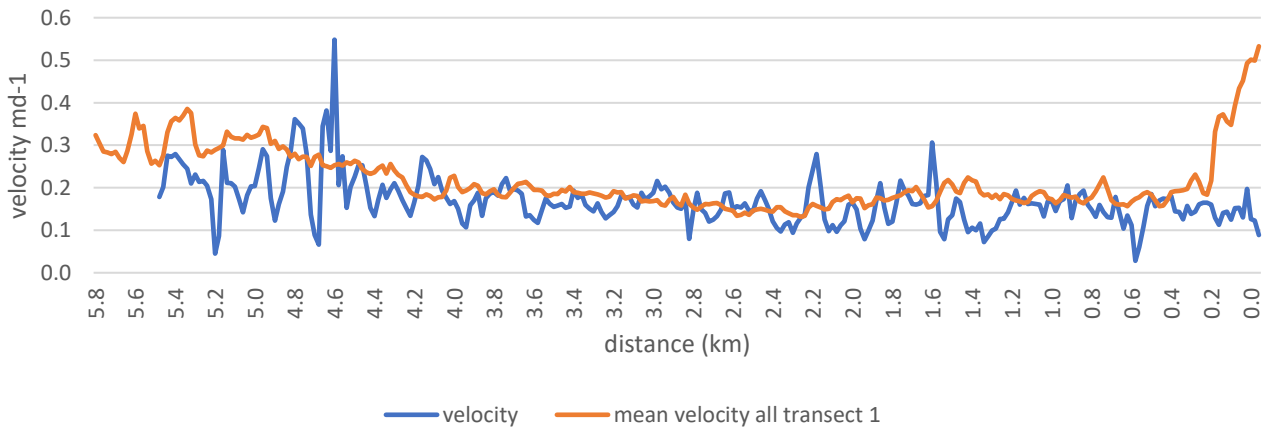

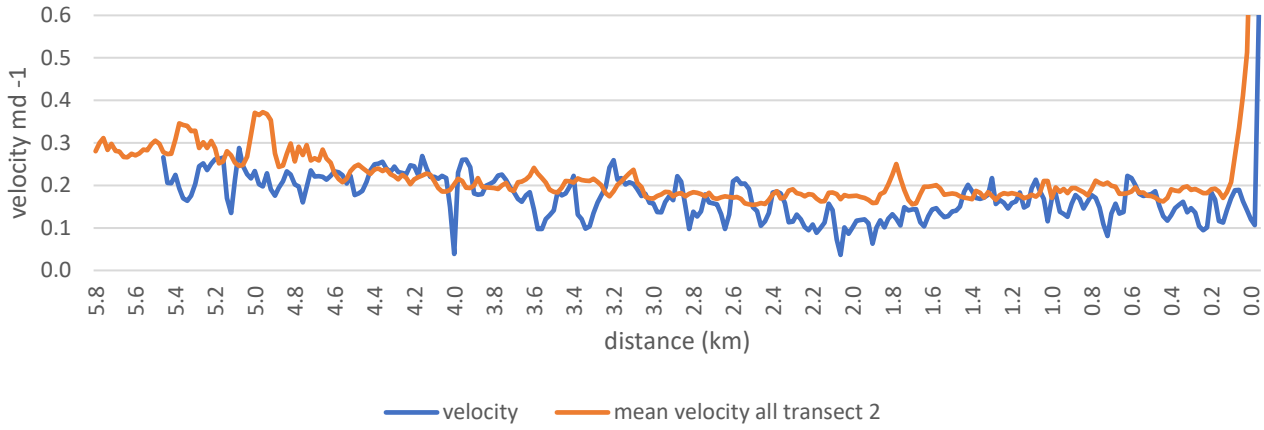
velocity md -1
0.6
0.5
0.4
0.3
0.2
0.1
0.0
5.8 5.6 5.4 5.2 5.0 4.8 4.6 4.4 4.2 4.0 3.8 3.6 3.4 3.2 3.0 2.8 2.6 2.4 2.2 2.0 1.8 1.6 1.4 1.2 1.0 0.8 0.6 0.4 0.2 0.0
distance (km)
velocity
mean velocity all transect 2

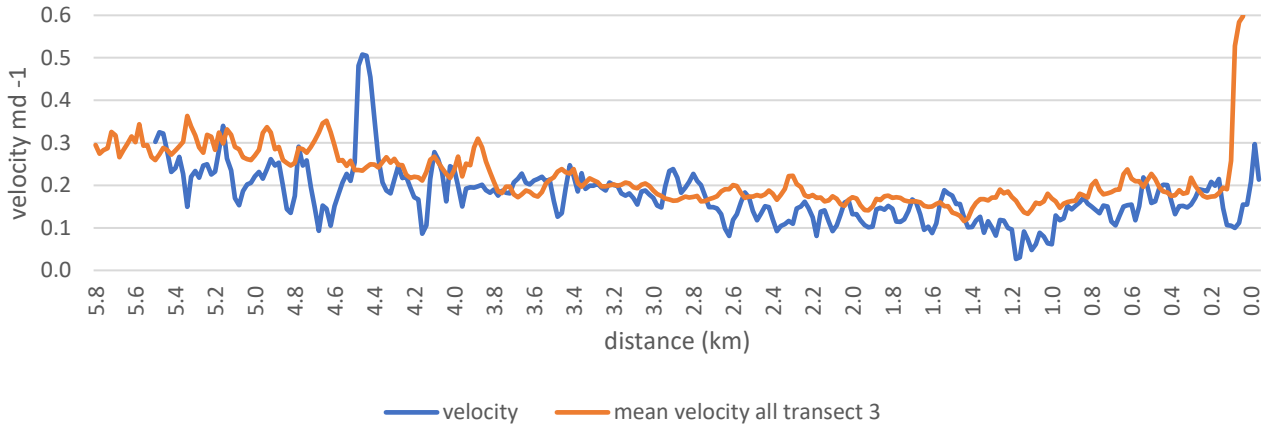
velocity md -1
0.6
0.5
0.4
0.3
0.2
0.1
0.0
5.8 5.6 5.4 5.2 5.0 4.8 4.6 4.4 4.2 4.0 3.8 3.6 3.4 3.2 3.0 2.8 2.6 2.4 2.2 2.0 1.8 1.6 1.4 1.2 1.0 0.8 0.6 0.4 0.2 0.0
distance (km)
velocity
mean velocity all transect 3

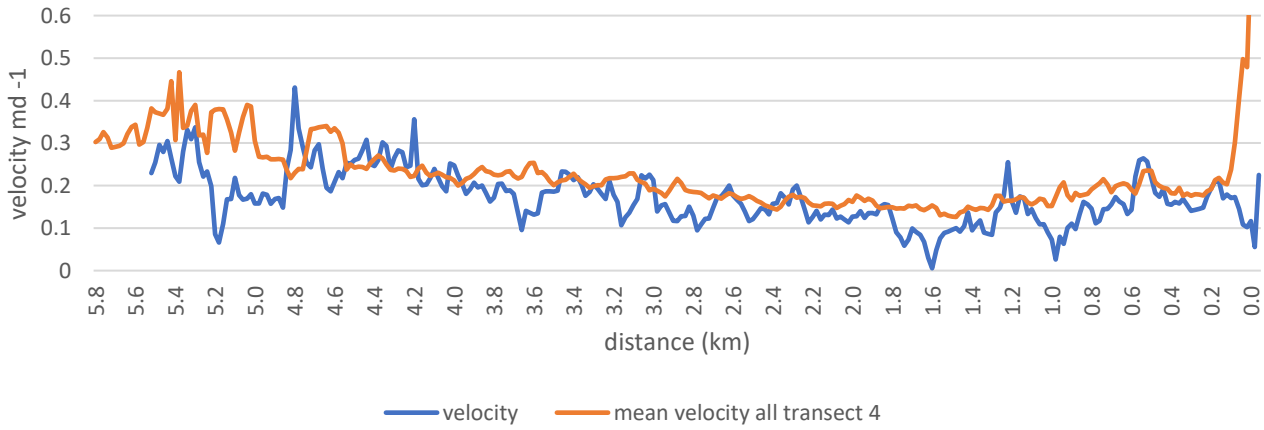
velocity md -1
0.6
0.5
0.4
0.3
0.2
0.1
0
5.8 5.6 5.4 5.2 5.0 4.8 4.6 4.4 4.2 4.0 3.8 3.6 3.4 3.2 3.0 2.8 2.6 2.4 2.2 2.0 1.8 1.6 1.4 1.2 1.0 0.8 0.6 0.4 0.2 0.0
distance (km)
velocity
mean velocity all transect 4

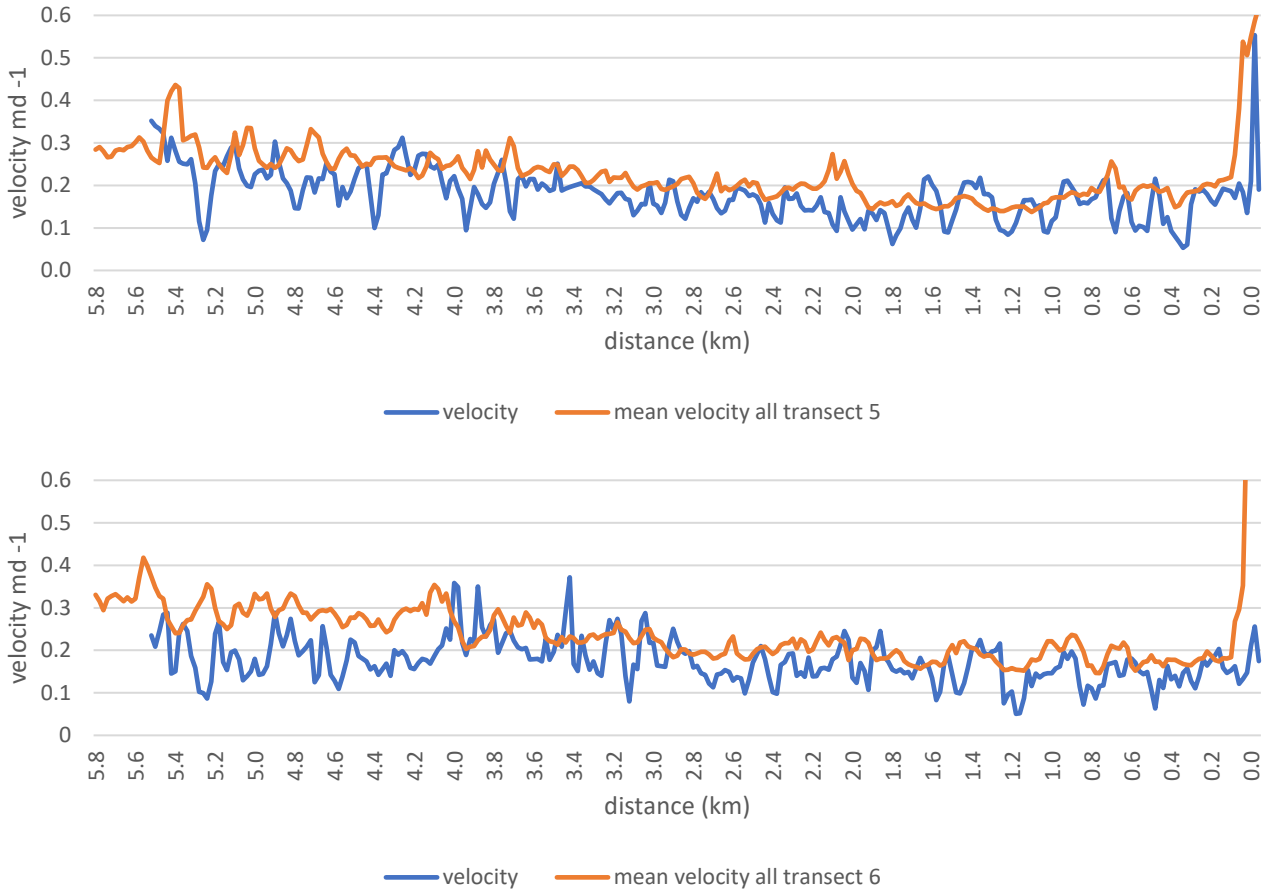

Appendix 16A: Longitudinal velocity profiles from 27/01/2017 – 26/02/2017 (time period of 50 days) The orange line indicates the surface velocity values extracted from all surface velocity images. The blue line is the surface velocity values extracted from each profile. Profiles run from A near the Ball Glacier confluence down to B at the terminus.

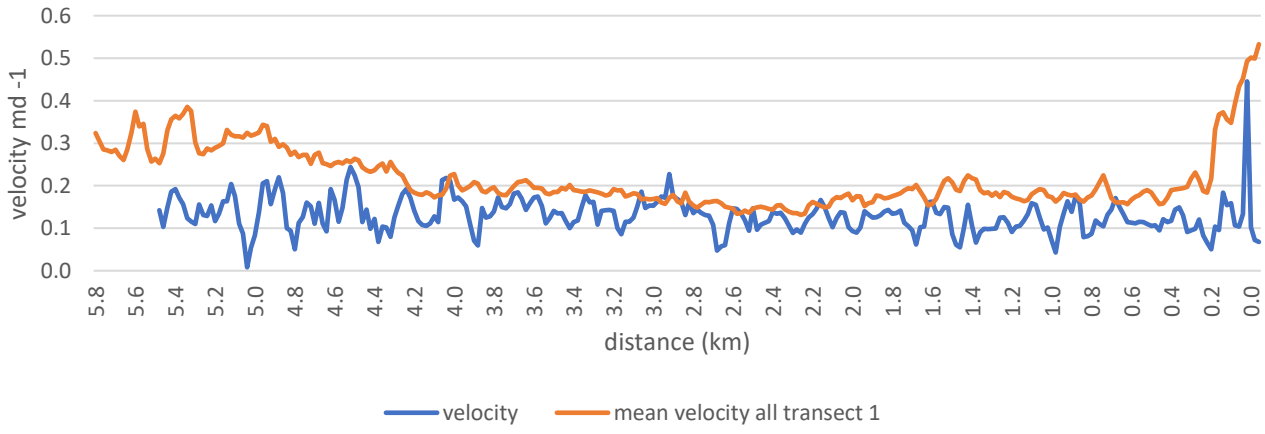

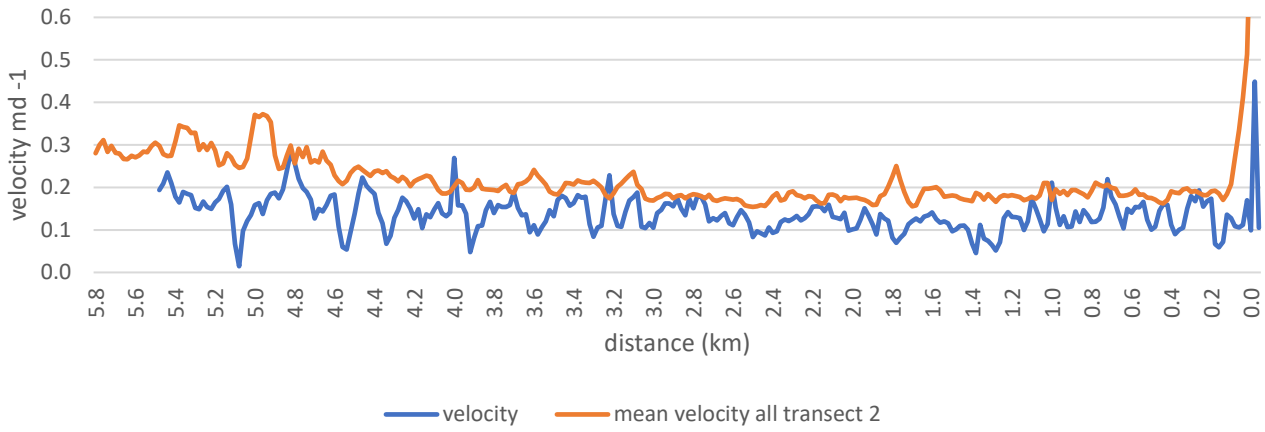
velocity md -1
0.6
0.5
0.4
0.3
0.2
0.1
0.0
5.8 5.6 5.4 5.2 5.0 4.8 4.6 4.4 4.2 4.0 3.8 3.6 3.4 3.2 3.0 2.8 2.6 2.4 2.2 2.0 1.8 1.6 1.4 1.2 1.0 0.8 0.6 0.4 0.2 0.0
distance (km)
velocity
mean velocity all transect 2

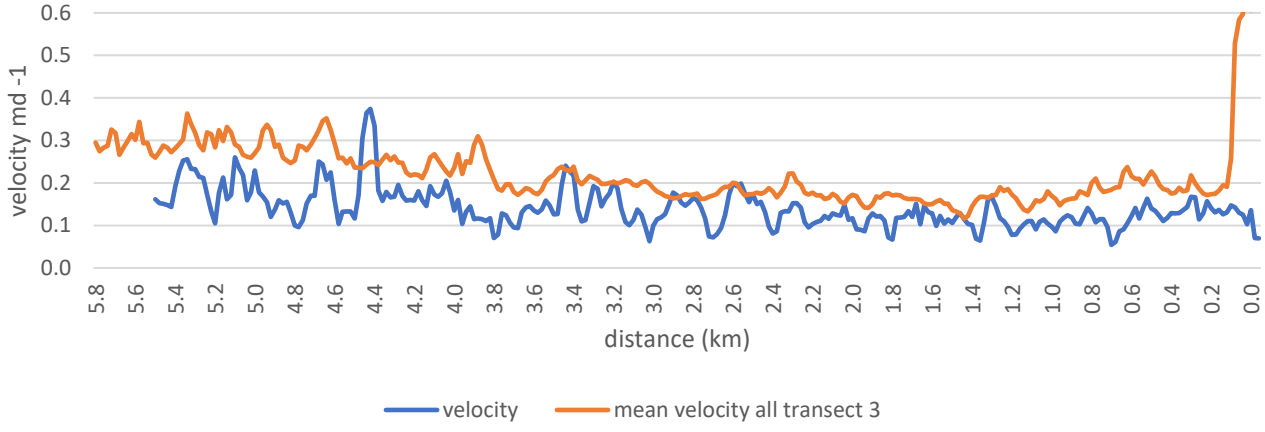
velocity md -1
0.6
0.5
0.4
0.3
0.2
0.1
0.0
5.8 5.6 5.4 5.2 5.0 4.8 4.6 4.4 4.2 4.0 3.8 3.6 3.4 3.2 3.0 2.8 2.6 2.4 2.2 2.0 1.8 1.6 1.4 1.2 1.0 0.8 0.6 0.4 0.2 0.0
distance (km)
velocity
mean velocity all transect 3

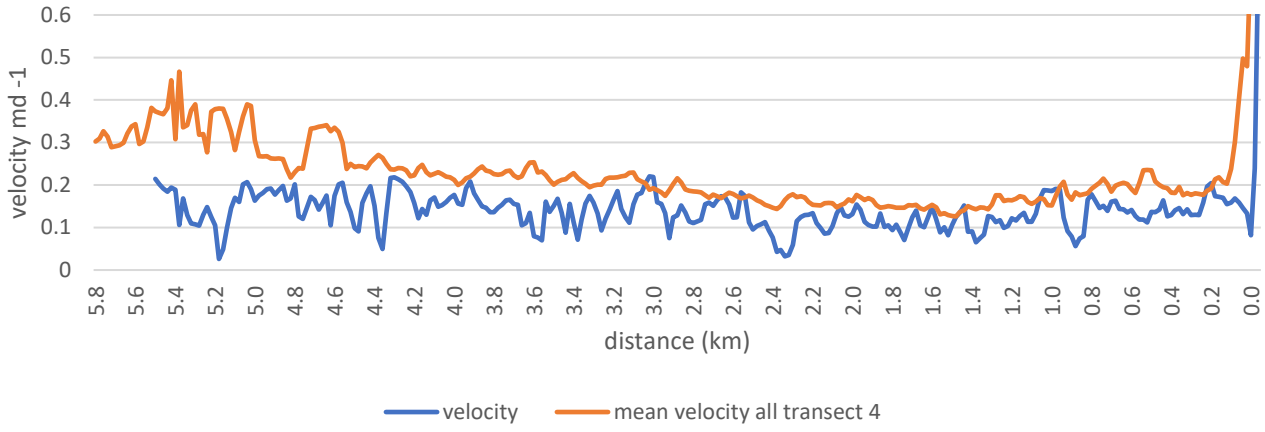
velocity md -1
0.6
0.5
0.4
0.3
0.2
0.1
0
5.8 5.6 5.4 5.2 5.0 4.8 4.6 4.4 4.2 4.0 3.8 3.6 3.4 3.2 3.0 2.8 2.6 2.4 2.2 2.0 1.8 1.6 1.4 1.2 1.0 0.8 0.6 0.4 0.2 0.0
distance (km)
velocity
mean velocity all transect 4

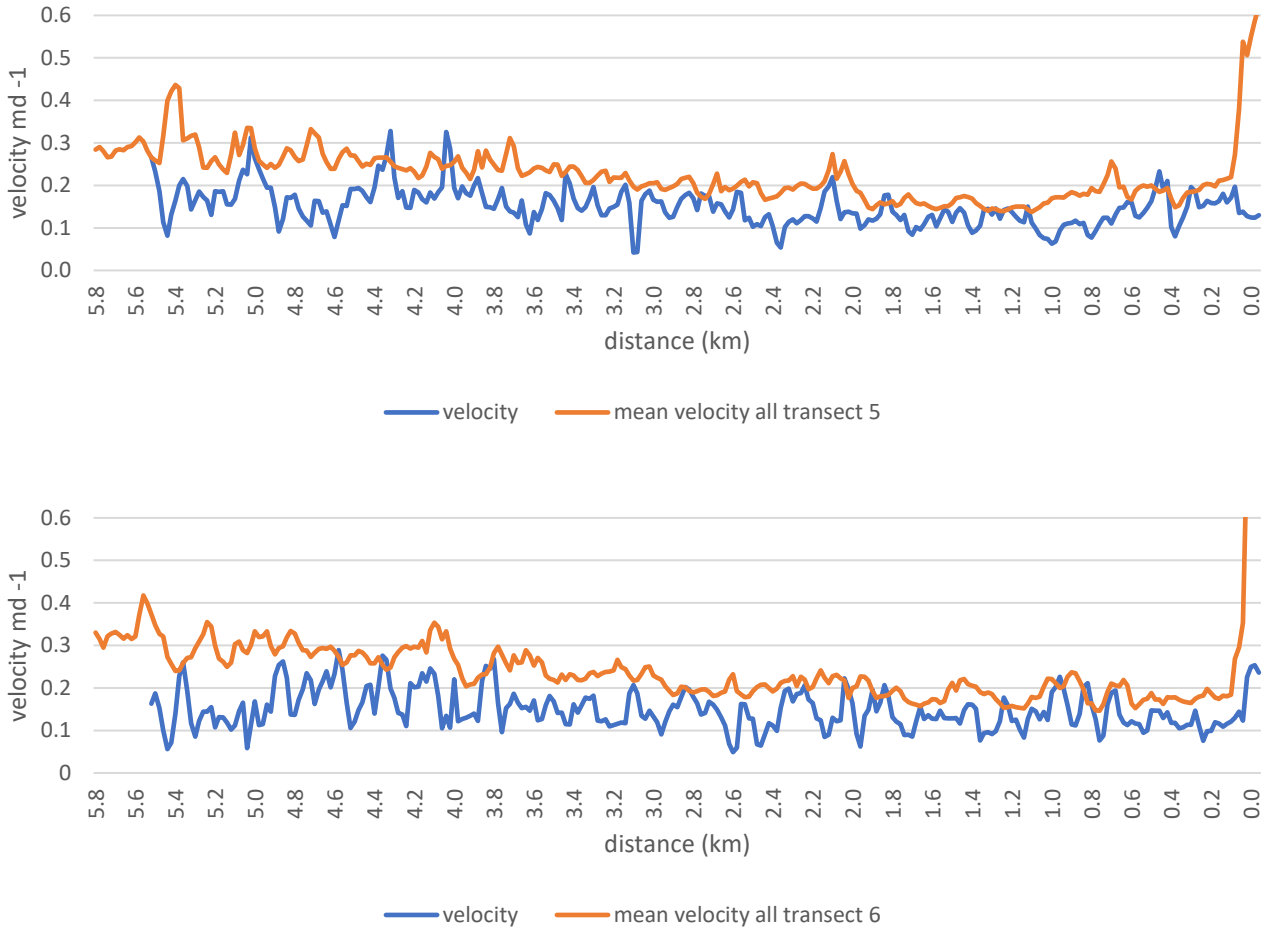

Appendix 17A: Longitudinal velocity profiles from 26/06/2017 – 18/03/2017 (time period of 50 days) The orange line indicates the surface velocity values extracted from all surface velocity images. The blue line is the surface velocity values extracted from each profile. Profiles run from A near the Ball Glacier confluence down to B at the terminus.

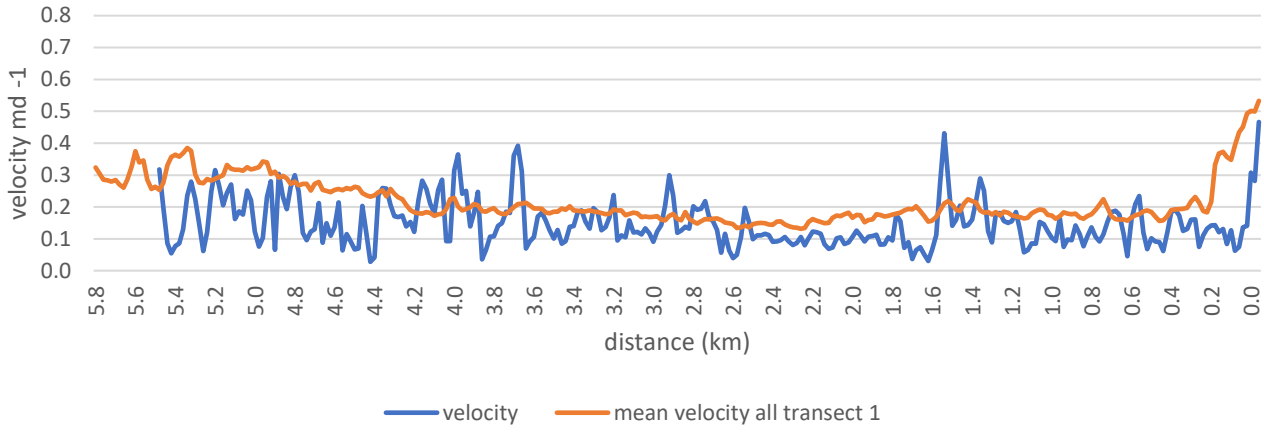
velocity md -1
0.8
0.7
0.6
0.5
0.4
0.3
0.2
0.1
0.0
5.8 5.6 5.4 5.2 5.0 4.8 4.6 4.4 4.2 4.0 3.8 3.6 3.4 3.2 3.0 2.8 2.6 2.4 2.2 2.0 1.8 1.6 1.4 1.2 1.0 0.8 0.6 0.4 0.2 0.0
distance (km)
velocity
mean velocity all transect 1

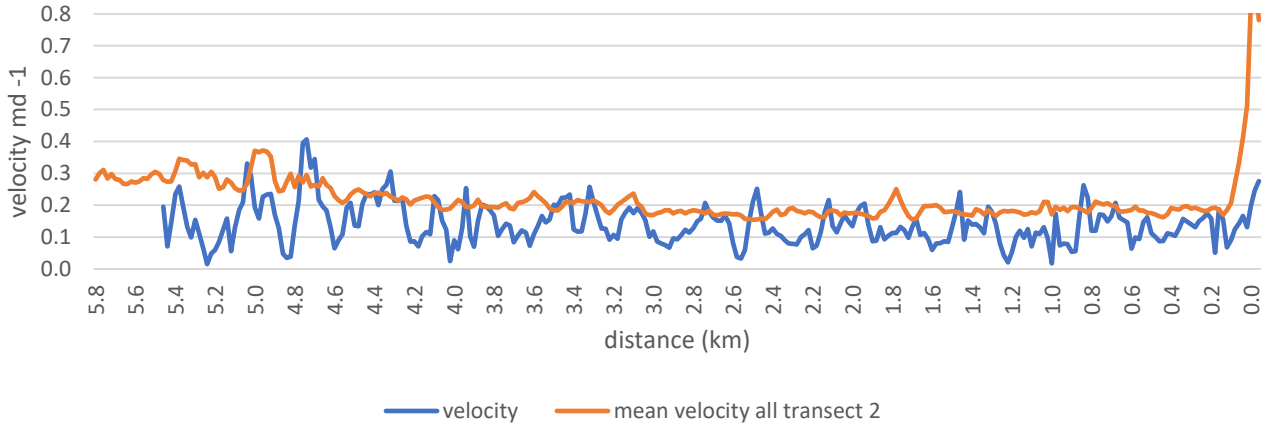
velocity md -1
0.8
0.7
0.6
0.5
0.4
0.3
0.2
0.1
0.0
5.8 5.6 5.4 5.2 5.0 4.8 4.6 4.4 4.2 4.0 3.8 3.6 3.4 3.2 3.0 2.8 2.6 2.4 2.2 2.0 1.8 1.6 1.4 1.2 1.0 0.8 0.6 0.4 0.2 0.0
distance (km)
velocity
mean velocity all transect 2

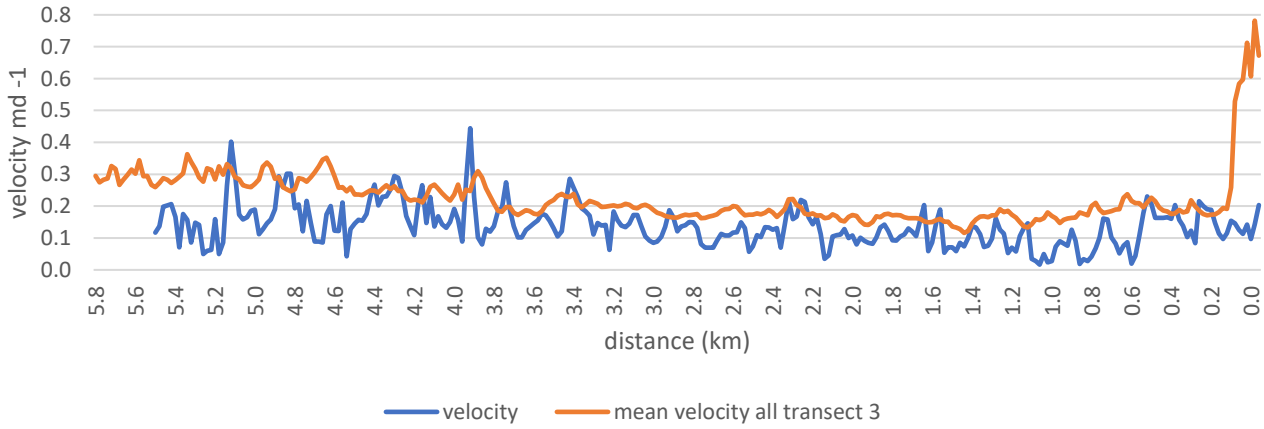
velocity md -1
0.8
0.7
0.6
0.5
0.4
0.3
0.2
0.1
0.0
5.8 5.6 5.4 5.2 5.0 4.8 4.6 4.4 4.2 4.0 3.8 3.6 3.4 3.2 3.0 2.8 2.6 2.4 2.2 2.0 1.8 1.6 1.4 1.2 1.0 0.8 0.6 0.4 0.2 0.0
distance (km)
velocity
mean velocity all transect 3

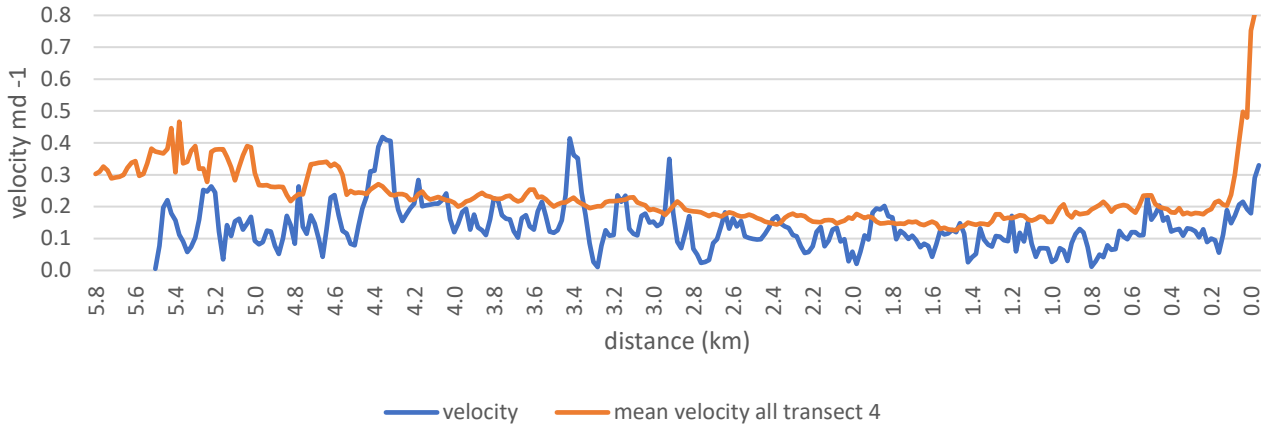

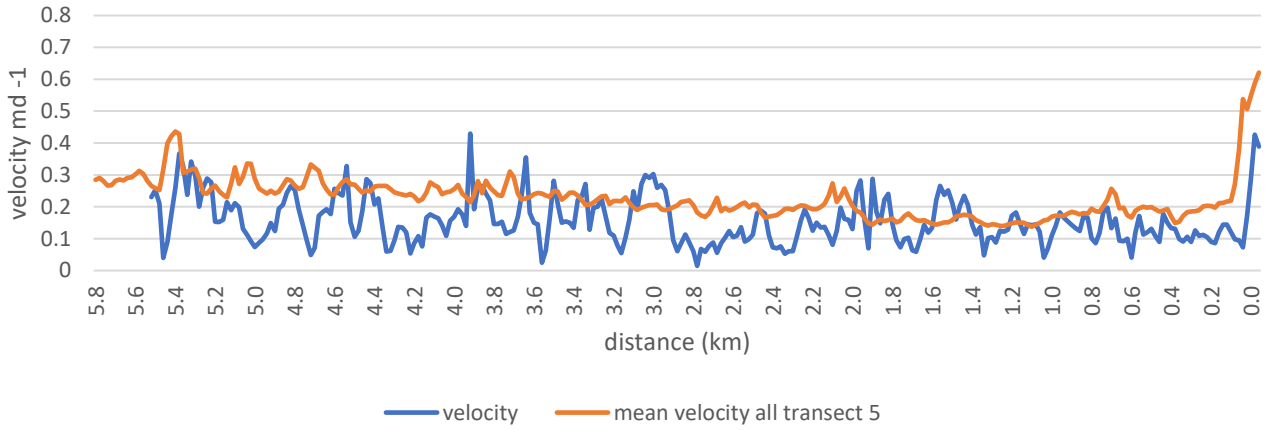

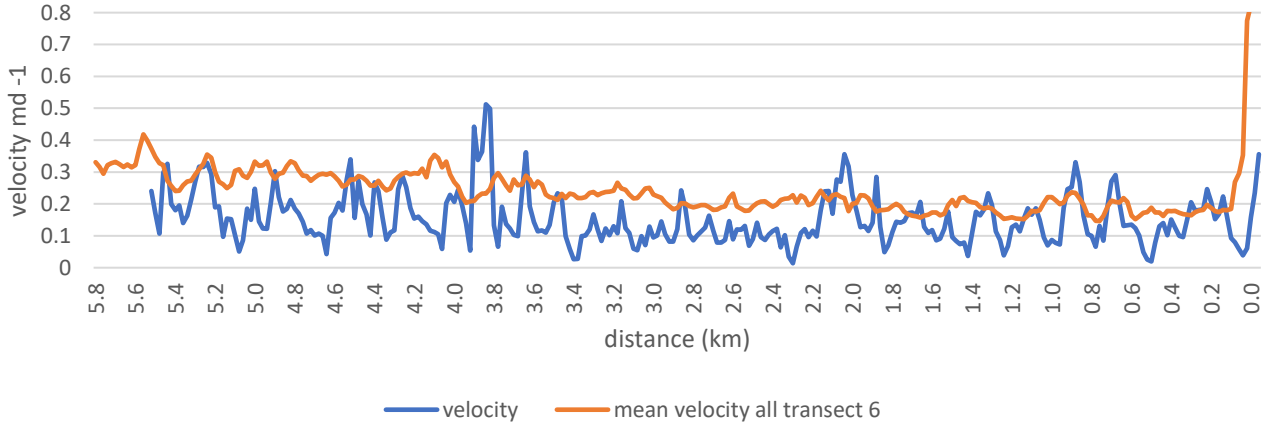

Appendix 18A: Longitudinal velocity profiles from 18/03/2017 – 28/03/2017 (time period of 10 days) The orange line indicates the surface velocity values extracted from all surface velocity images. The blue line is the surface velocity values extracted from each profile. Profiles run from A near the Ball Glacier confluence down to B at the terminus.

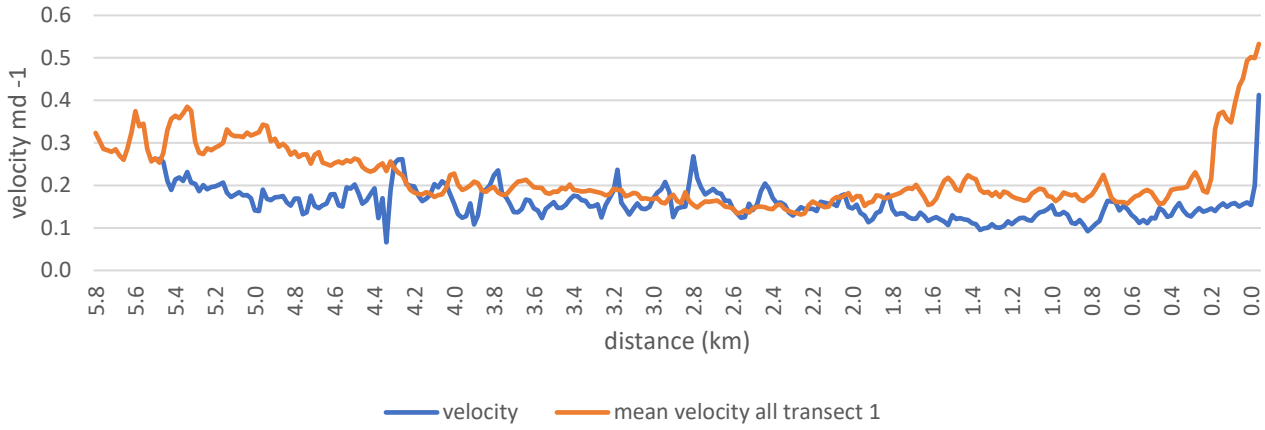
velocity md -1
0.6
0.5
0.4
0.3
0.2
0.1
0.0
5.8 5.6 5.4 5.2 5.0 4.8 4.6 4.4 4.2 4.0 3.8 3.6 3.4 3.2 3.0 2.8 2.6 2.4 2.2 2.0 1.8 1.6 1.4 1.2 1.0 0.8 0.6 0.4 0.2 0.0
distance (km)
velocity
mean velocity all transect 1

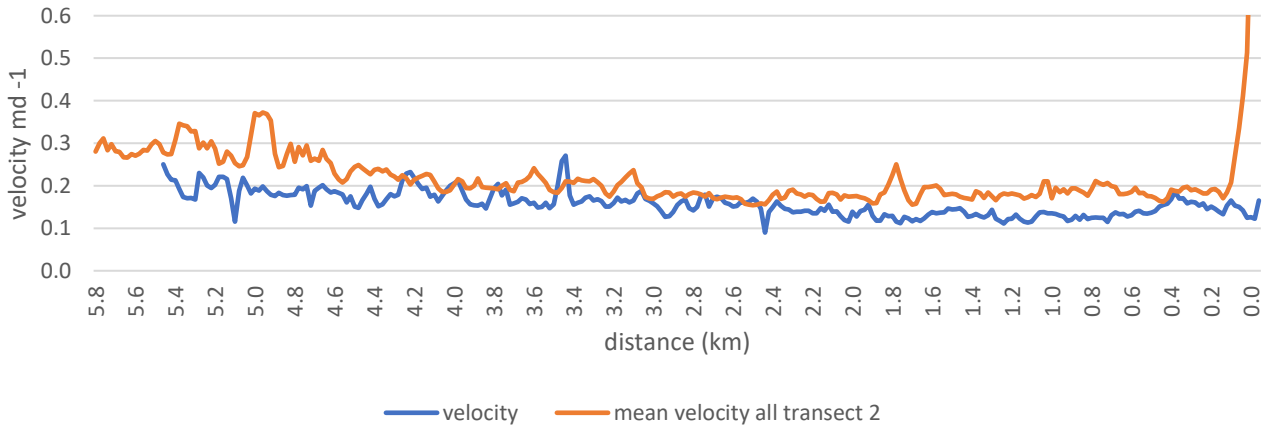
velocity md -1
0.6
0.5
0.4
0.3
0.2
0.1
0.0
5.8 5.6 5.4 5.2 5.0 4.8 4.6 4.4 4.2 4.0 3.8 3.6 3.4 3.2 3.0 2.8 2.6 2.4 2.2 2.0 1.8 1.6 1.4 1.2 1.0 0.8 0.6 0.4 0.2 0.0
distance (km)
velocity
mean velocity all transect 2

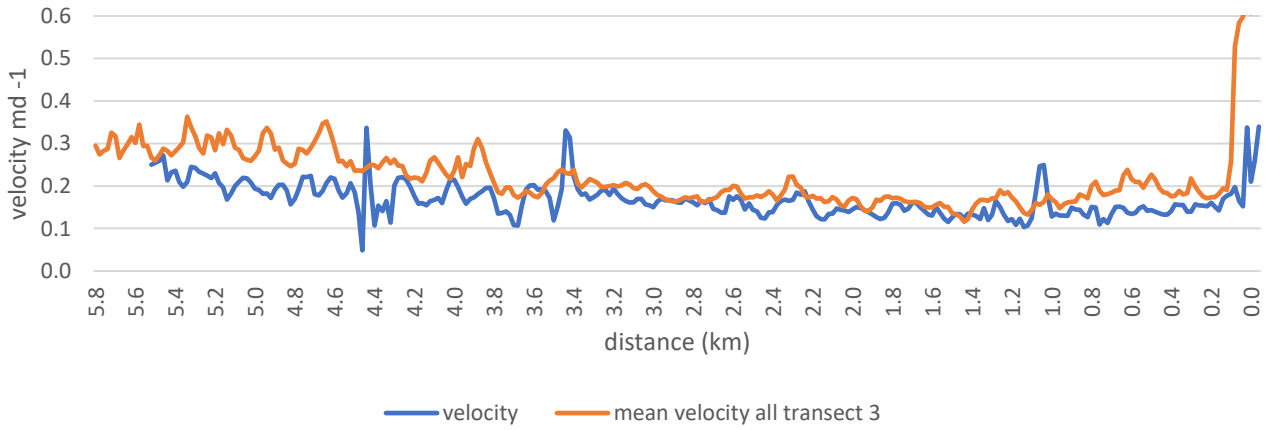
velocity md -1
0.6
0.5
0.4
0.3
0.2
0.1
0.0
5.8 5.6 5.4 5.2 5.0 4.8 4.6 4.4 4.2 4.0 3.8 3.6 3.4 3.2 3.0 2.8 2.6 2.4 2.2 2.0 1.8 1.6 1.4 1.2 1.0 0.8 0.6 0.4 0.2 0.0
distance (km)
velocity
mean velocity all transect 3

Appendix 19A: Longitudinal velocity profiles from 28/03/2017 – 17/05/2017 (time period of 50 days) The orange line indicates the surface velocity values extracted from all surface velocity images. The blue line is the surface velocity values extracted from each profile. Profiles run from A near the Ball Glacier confluence down to B at the terminus.

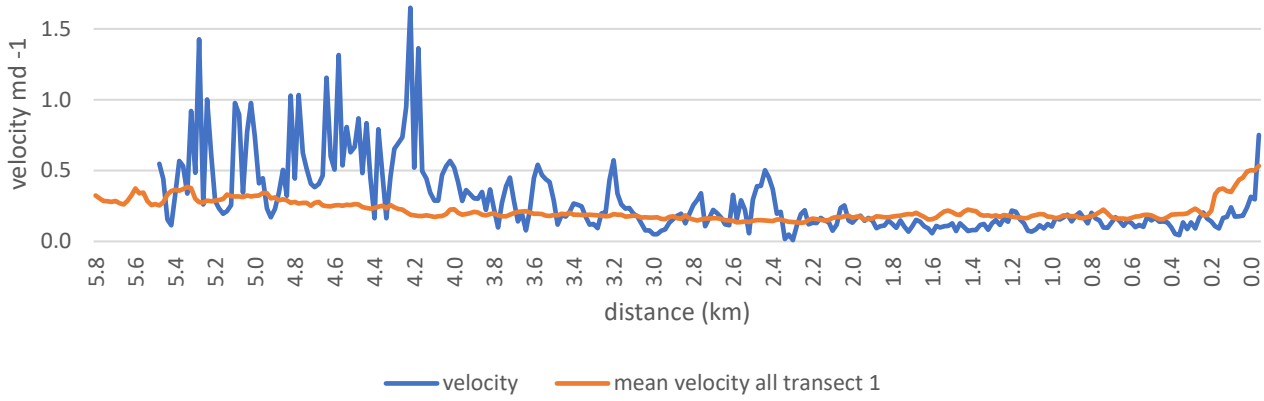
velocity md -1
1.5
1.0
0.5
0.0
5.8 5.6 5.4 5.2 5.0 4.8 4.6 4.4 4.2 4.0 3.8 3.6 3.4 3.2 3.0 2.8 2.6 2.4 2.2 2.0 1.8 1.6 1.4 1.2 1.0 0.8 0.6 0.4 0.2 0.0
distance (km)
velocity
mean velocity all transect 1

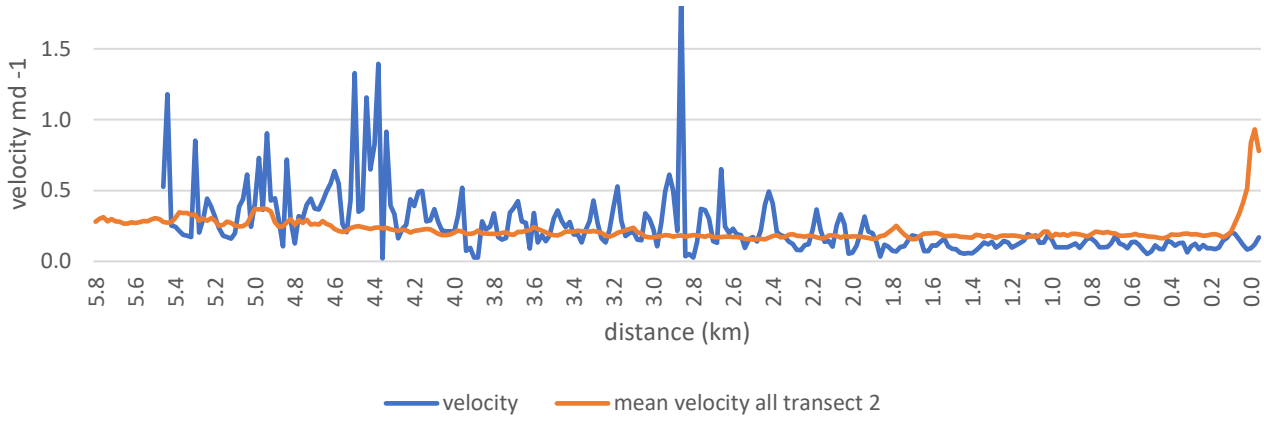
velocity md -1
1.5
1.0
0.5
0.0
5.8 5.6 5.4 5.2 5.0 4.8 4.6 4.4 4.2 4.0 3.8 3.6 3.4 3.2 3.0 2.8 2.6 2.4 2.2 2.0 1.8 1.6 1.4 1.2 1.0 0.8 0.6 0.4 0.2 0.0
distance (km)
velocity
mean velocity all transect 2

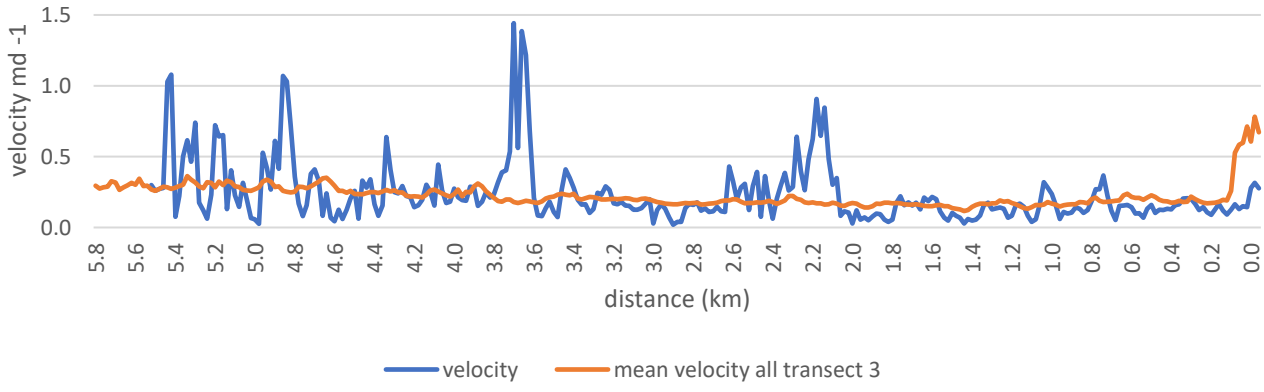
velocity md -1
1.5
1.0
0.5
0.0
5.8 5.6 5.4 5.2 5.0 4.8 4.6 4.4 4.2 4.0 3.8 3.6 3.4 3.2 3.0 2.8 2.6 2.4 2.2 2.0 1.8 1.6 1.4 1.2 1.0 0.8 0.6 0.4 0.2 0.0
distance (km)
velocity
mean velocity all transect 3

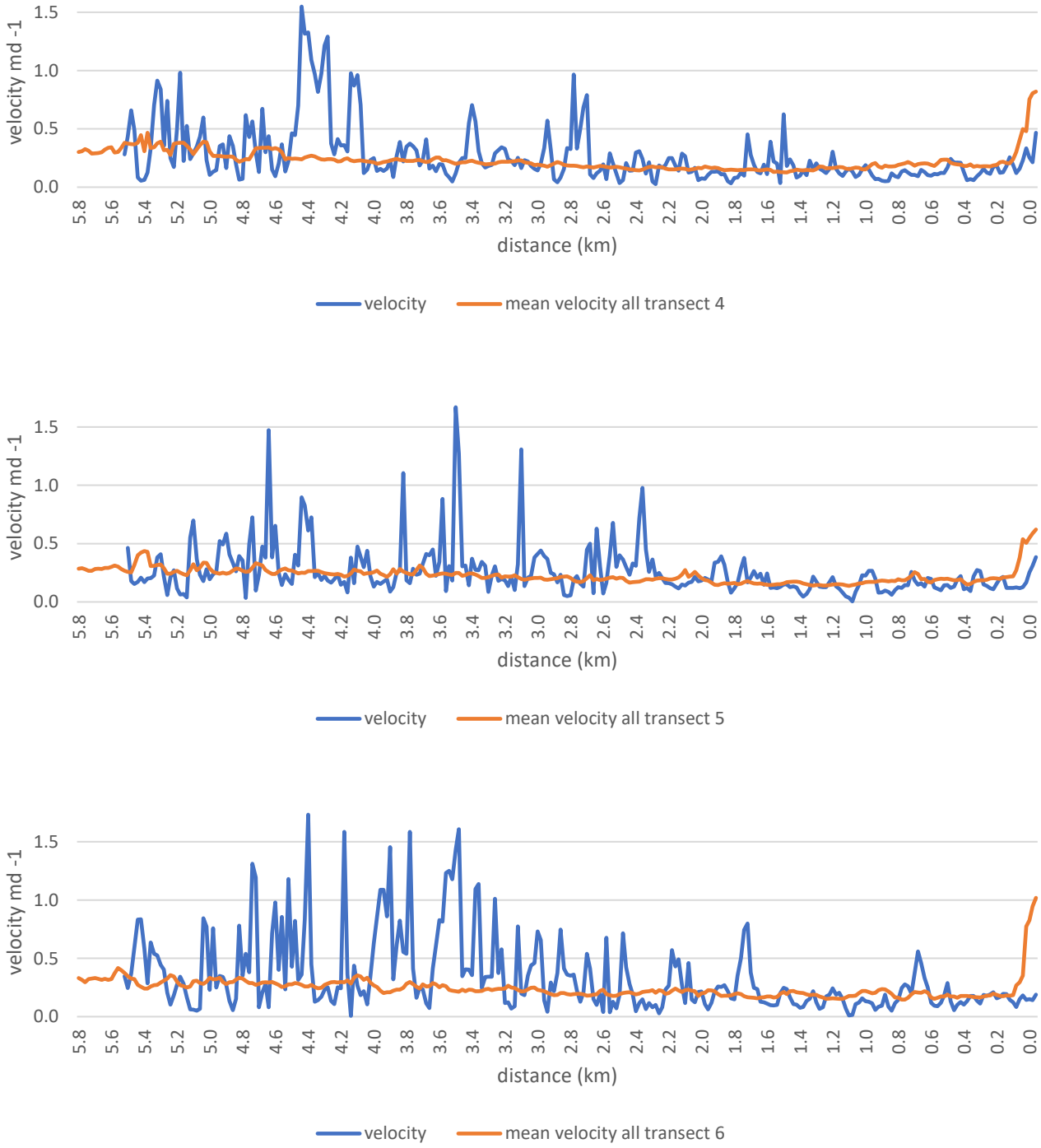

Appendix 20A: Longitudinal velocity profiles from 17/05/2017 – 27/05/2017 (time period of 10 days) The orange line indicates the surface velocity values extracted from all surface velocity images. The blue line is the surface velocity values extracted from each profile. Profiles run from A near the Ball Glacier confluence down to B at the terminus.

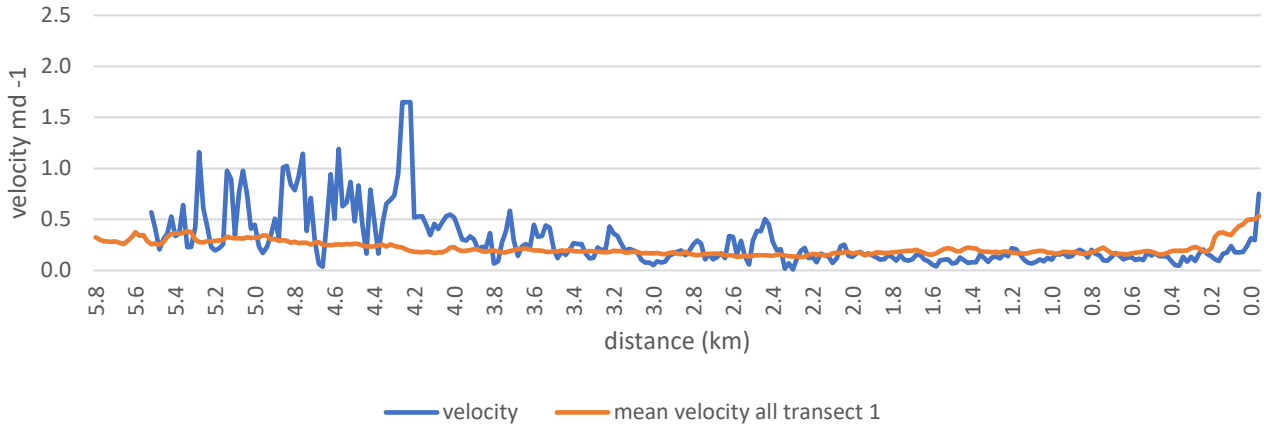
velocity md -1
2.5
2.0
1.5
1.0
0.5
0.0
5.8 5.6 5.4 5.2 5.0 4.8 4.6 4.4 4.2 4.0 3.8 3.6 3.4 3.2 3.0 2.8 2.6 2.4 2.2 2.0 1.8 1.6 1.4 1.2 1.0 0.8 0.6 0.4 0.2 0.0
distance (km)
velocity
mean velocity all transect 1

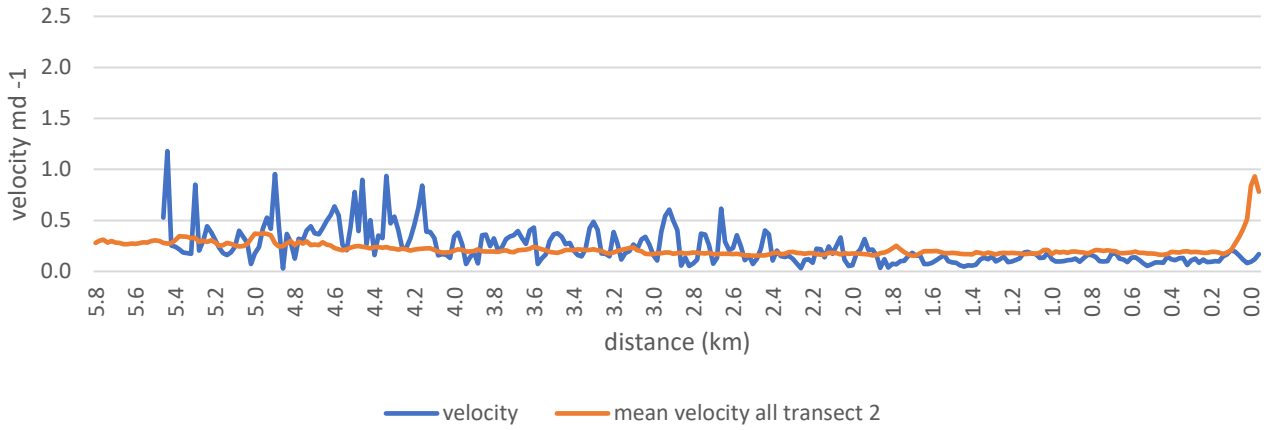
velocity md -1
2.5
2.0
1.5
1.0
0.5
0.0
5.8 5.6 5.4 5.2 5.0 4.8 4.6 4.4 4.2 4.0 3.8 3.6 3.4 3.2 3.0 2.8 2.6 2.4 2.2 2.0 1.8 1.6 1.4 1.2 1.0 0.8 0.6 0.4 0.2 0.0
distance (km)
velocity
mean velocity all transect 2

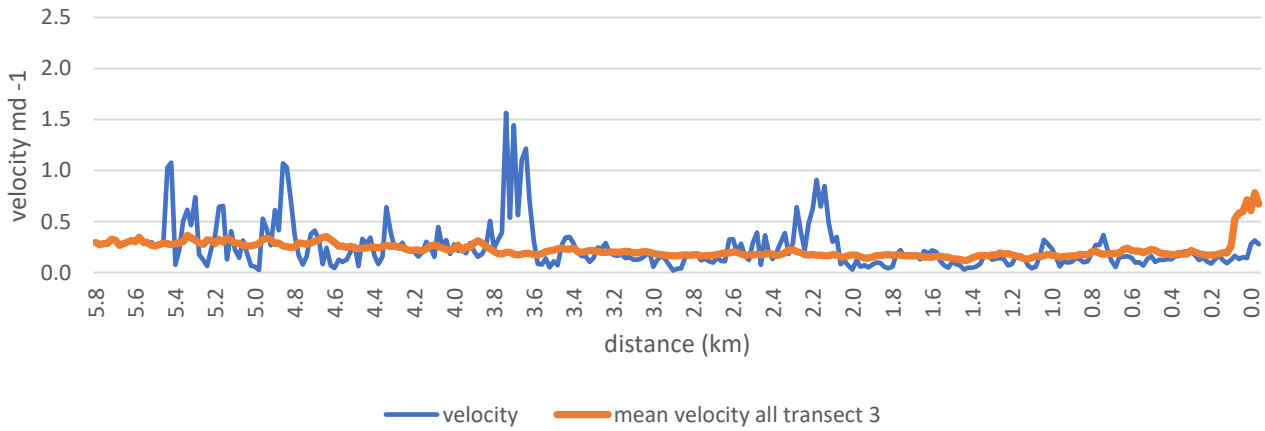
velocity md -1
2.5
2.0
1.5
1.0
0.5
0.0
5.8 5.6 5.4 5.2 5.0 4.8 4.6 4.4 4.2 4.0 3.8 3.6 3.4 3.2 3.0 2.8 2.6 2.4 2.2 2.0 1.8 1.6 1.4 1.2 1.0 0.8 0.6 0.4 0.2 0.0
distance (km)
velocity
mean velocity all transect 3

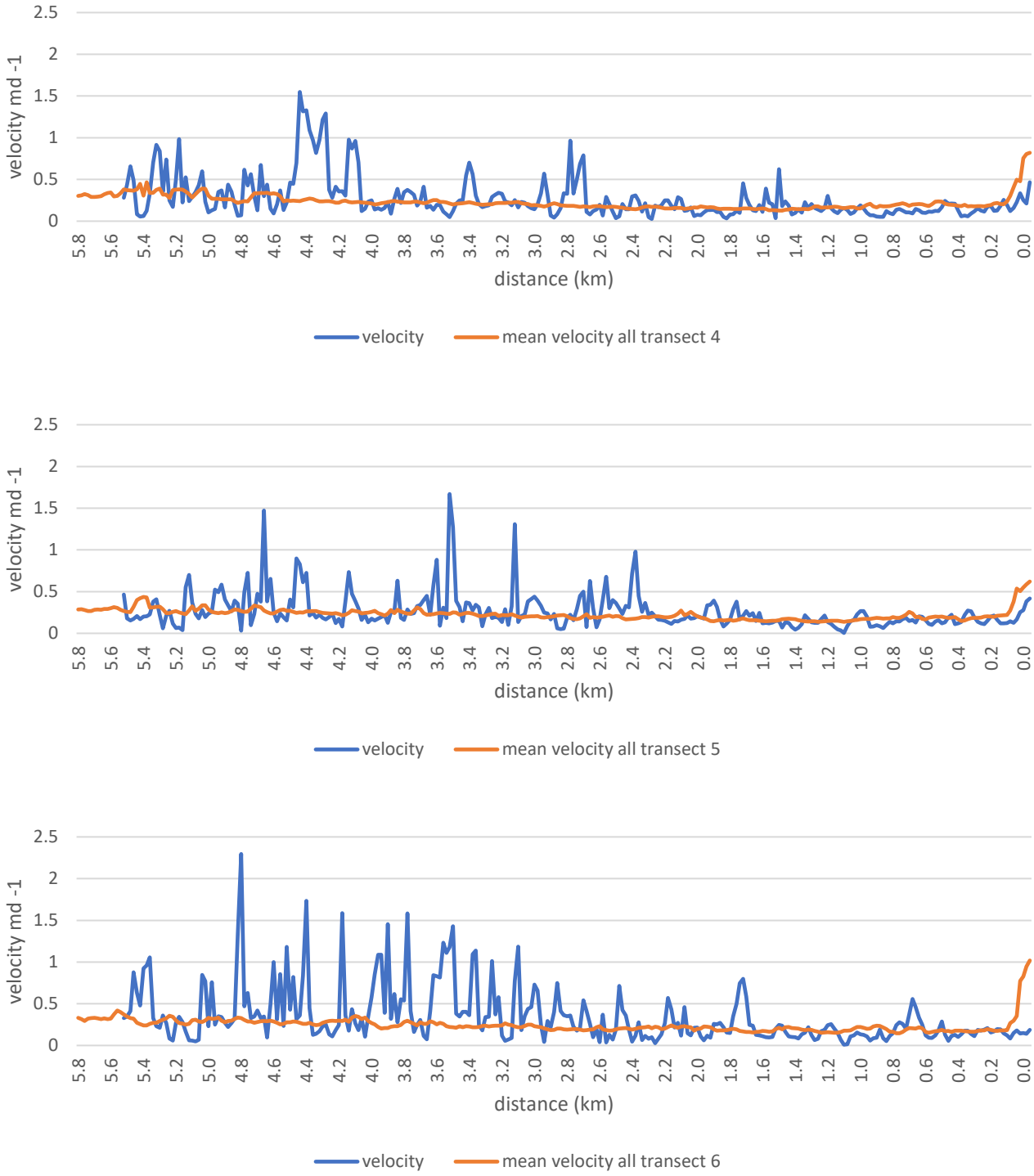

Appendix 21A: Longitudinal velocity profiles from 27/05/2017 – 06/06/2017 (time period of 30 days) The orange line indicates the surface velocity values extracted from all surface velocity images. The blue line is the surface velocity values extracted from each profile. Profiles run from A near the Ball Glacier confluence down to B at the terminus.

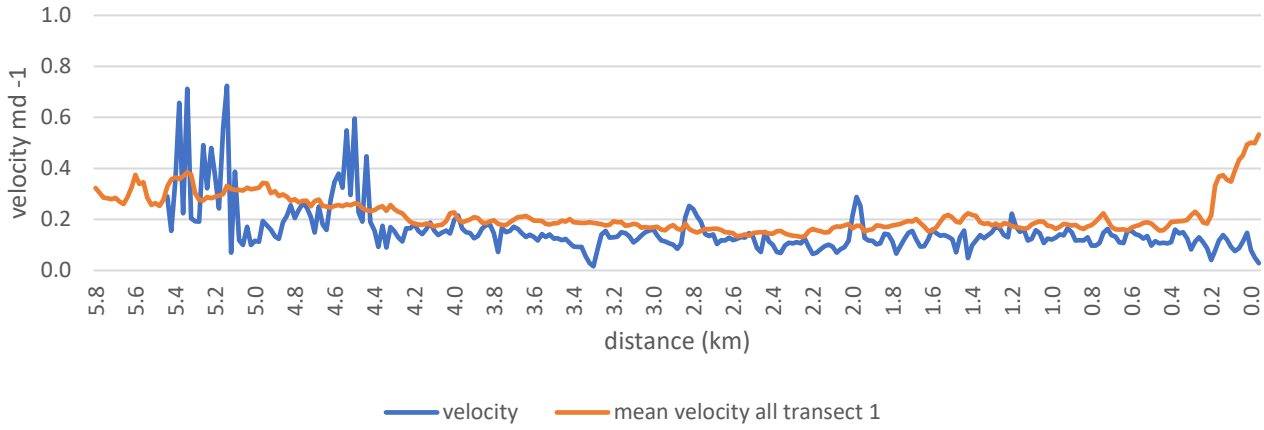
velocity md -1
1.0
0.8
0.6
0.4
0.2
0.0
5.8 5.6 5.4 5.2 5.0 4.8 4.6 4.4 4.2 4.0 3.8 3.6 3.4 3.2 3.0 2.8 2.6 2.4 2.2 2.0 1.8 1.6 1.4 1.2 1.0 0.8 0.6 0.4 0.2 0.0
distance (km)
velocity
mean velocity all transect 1

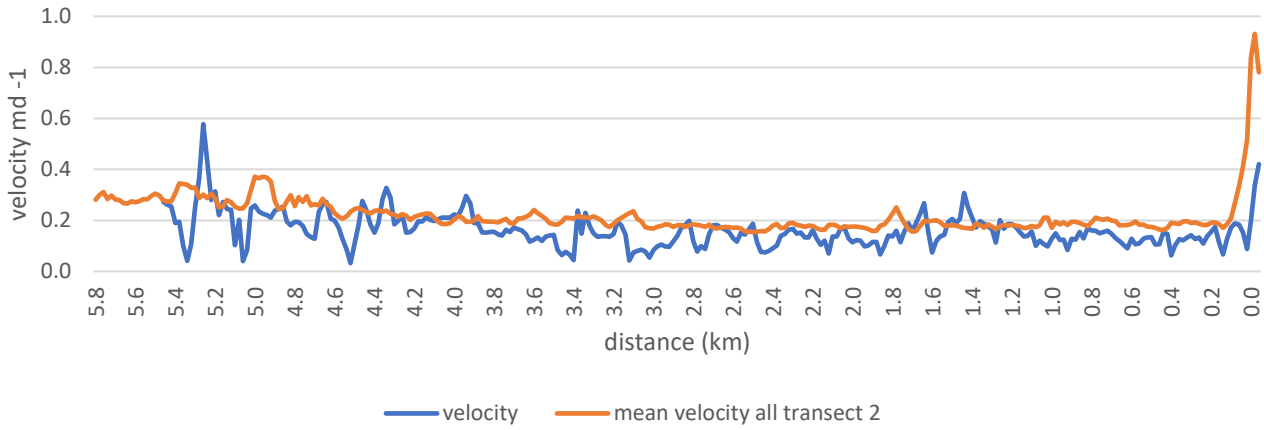
velocity md -1
1.0
0.8
0.6
0.4
0.2
0.0
5.8 5.6 5.4 5.2 5.0 4.8 4.6 4.4 4.2 4.0 3.8 3.6 3.4 3.2 3.0 2.8 2.6 2.4 2.2 2.0 1.8 1.6 1.4 1.2 1.0 0.8 0.6 0.4 0.2 0.0
distance (km)
velocity
mean velocity all transect 2

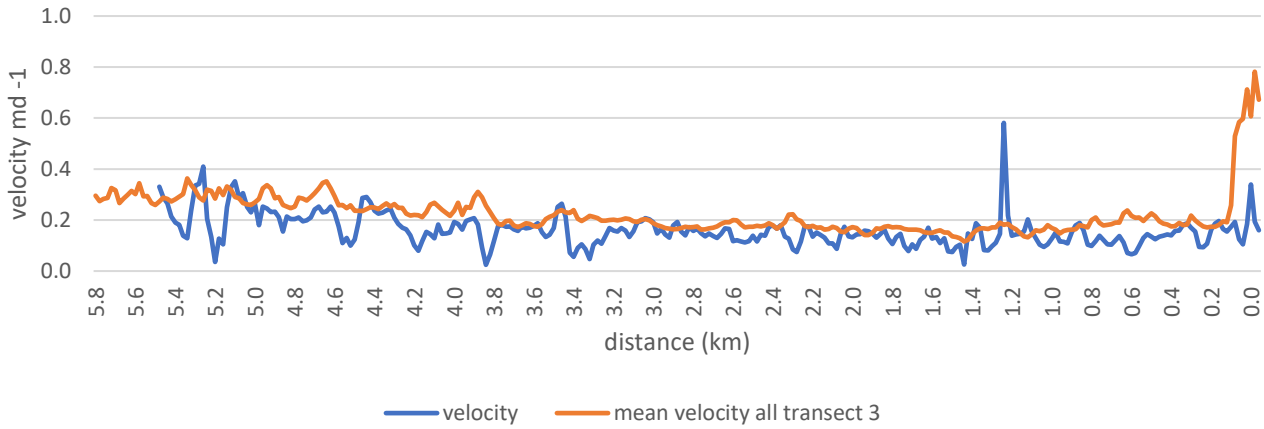
velocity md -1
1.0
0.8
0.6
0.4
0.2
0.0
5.8 5.6 5.4 5.2 5.0 4.8 4.6 4.4 4.2 4.0 3.8 3.6 3.4 3.2 3.0 2.8 2.6 2.4 2.2 2.0 1.8 1.6 1.4 1.2 1.0 0.8 0.6 0.4 0.2 0.0
distance (km)
velocity
mean velocity all transect 3

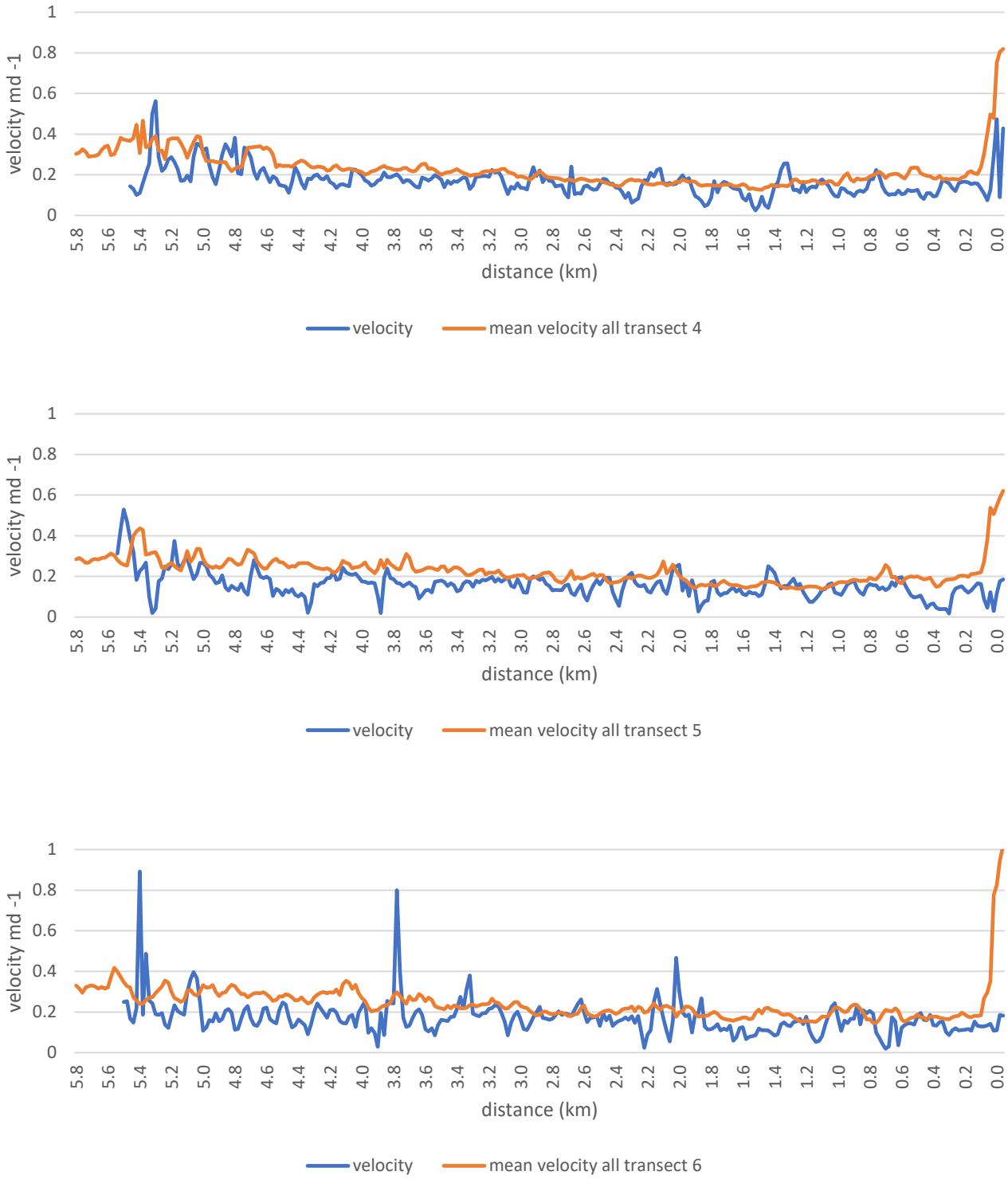

Appendix 21A: Longitudinal velocity profiles from 04/10/2017 – 29/10/2017 (time period of 25 days) The orange line indicates the surface velocity values extracted from all surface velocity images. The blue line is the surface velocity values extracted from each profile. Profiles run from A near the Ball Glacier confluence down to B at the terminus.

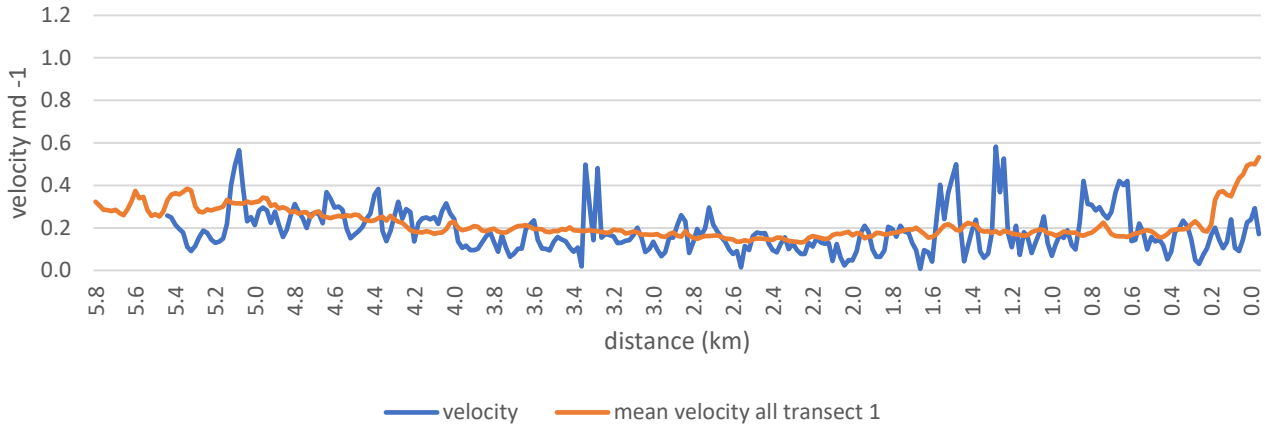
velocity md -1
1.2
1.0
0.8
0.6
0.4
0.2
0.0
5.8 5.6 5.4 5.2 5.0 4.8 4.6 4.4 4.2 4.0 3.8 3.6 3.4 3.2 3.0 2.8 2.6 2.4 2.2 2.0 1.8 1.6 1.4 1.2 1.0 0.8 0.6 0.4 0.2 0.0
distance (km)
velocity
mean velocity all transect 1

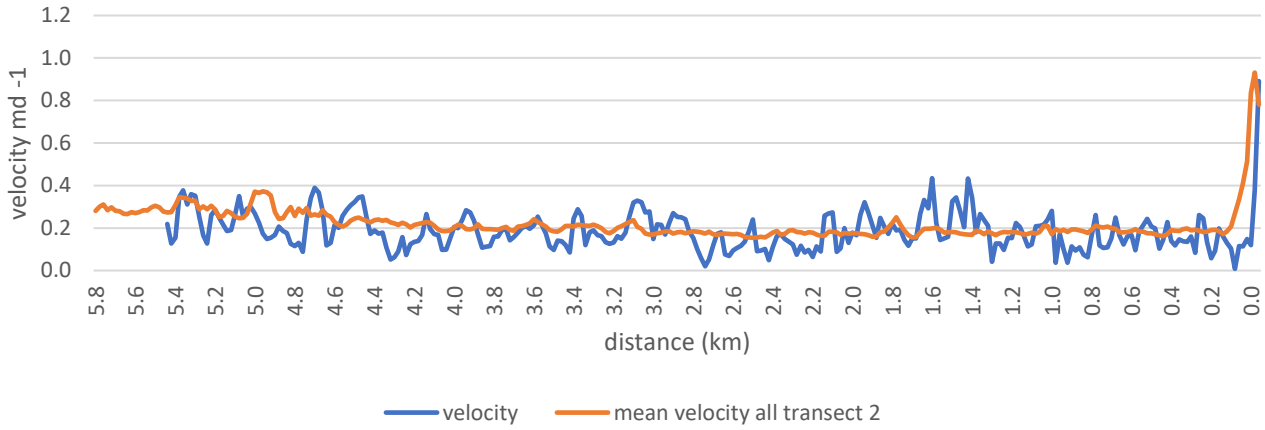
velocity md -1
1.2
1.0
0.8
0.6
0.4
0.2
0.0
5.8 5.6 5.4 5.2 5.0 4.8 4.6 4.4 4.2 4.0 3.8 3.6 3.4 3.2 3.0 2.8 2.6 2.4 2.2 2.0 1.8 1.6 1.4 1.2 1.0 0.8 0.6 0.4 0.2 0.0
distance (km)
velocity
mean velocity all transect 2

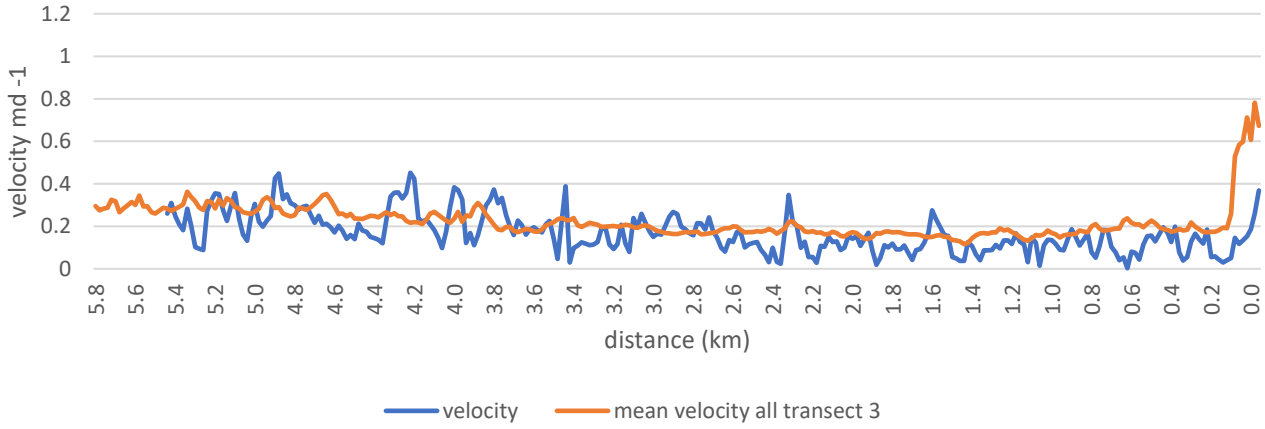
velocity md -1
1.2
1
0.8
0.6
0.4
0.2
0
5.8 5.6 5.4 5.2 5.0 4.8 4.6 4.4 4.2 4.0 3.8 3.6 3.4 3.2 3.0 2.8 2.6 2.4 2.2 2.0 1.8 1.6 1.4 1.2 1.0 0.8 0.6 0.4 0.2 0.0
distance (km)
velocity
mean velocity all transect 3

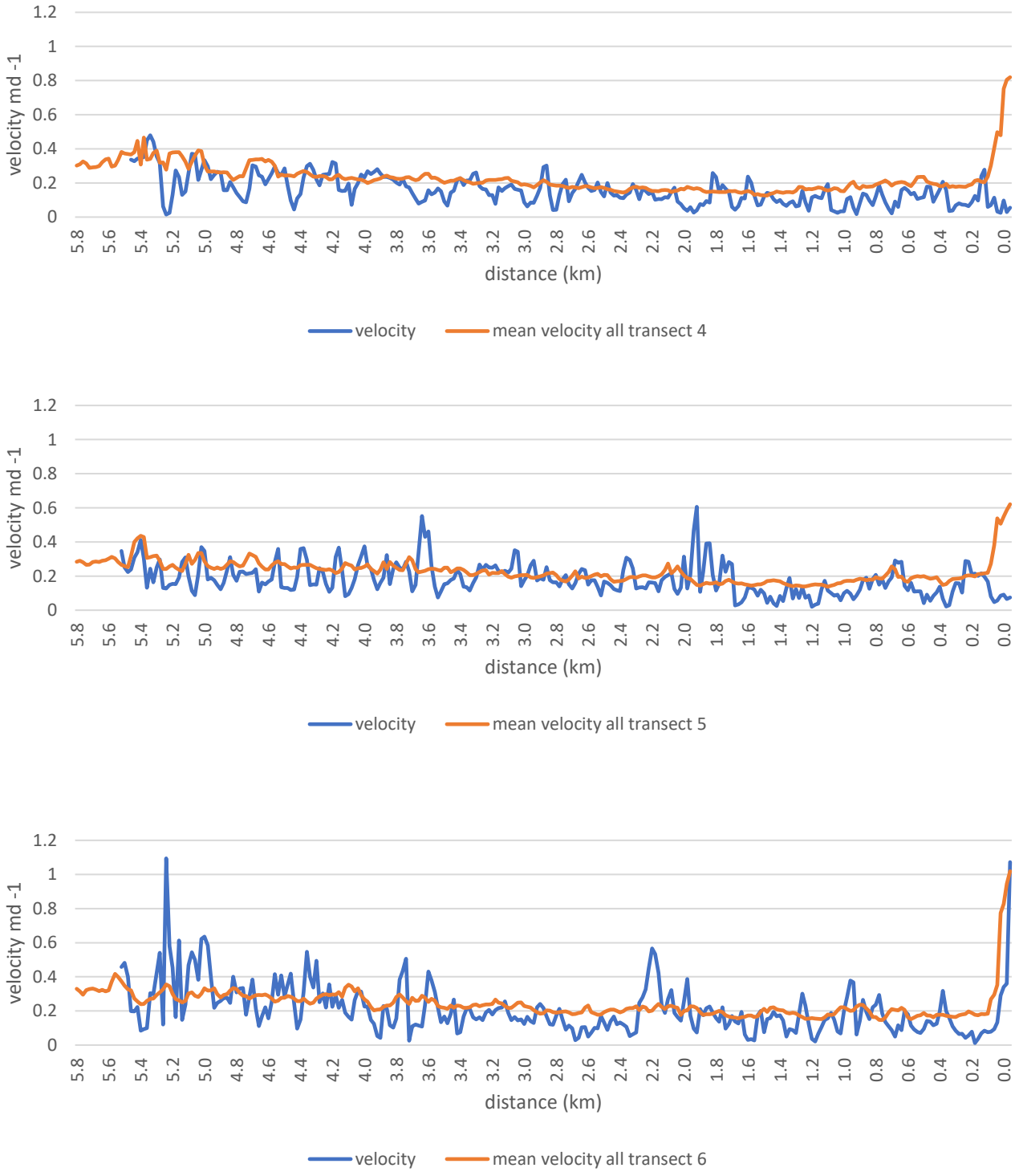

Appendix 22A: Longitudinal velocity profiles from 29/10/2017 – 13/11/2017 (time period of 15 days) The orange line indicates the surface velocity values extracted from all surface velocity images. The blue line is the surface velocity values extracted from each profile. Profiles run from A near the Ball Glacier confluence down to B at the terminus.

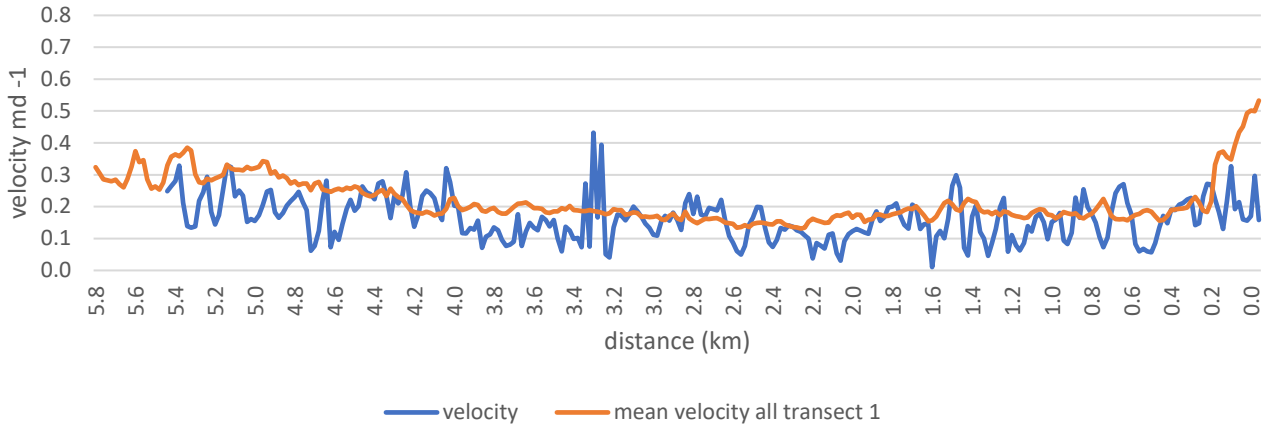
velocity md -1
0.8
0.7
0.6
0.5
0.4
0.3
0.2
0.1
0.0
5.8 5.6 5.4 5.2 5.0 4.8 4.6 4.4 4.2 4.0 3.8 3.6 3.4 3.2 3.0 2.8 2.6 2.4 2.2 2.0 1.8 1.6 1.4 1.2 1.0 0.8 0.6 0.4 0.2 0.0
distance (km)
velocity
mean velocity all transect 1

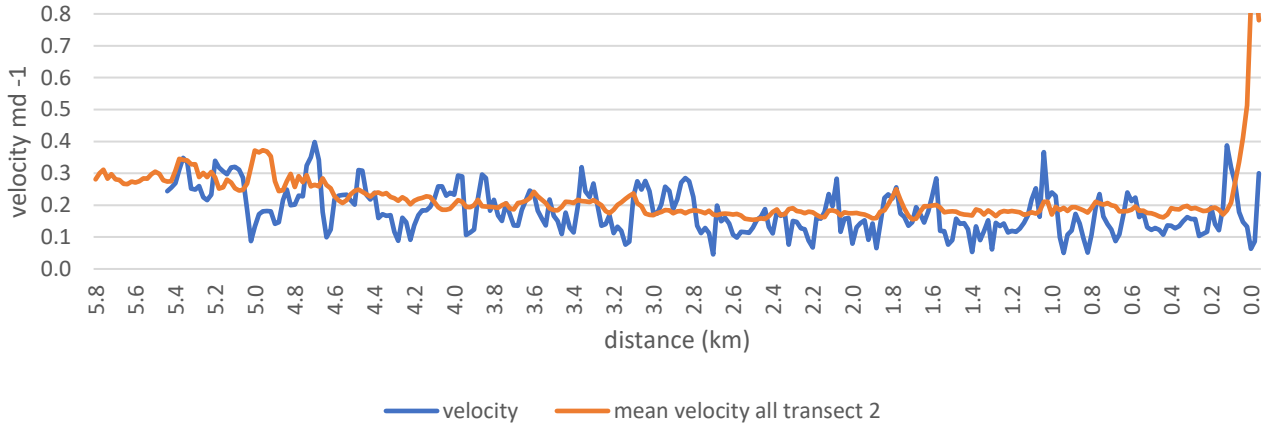
velocity md -1
0.8
0.7
0.6
0.5
0.4
0.3
0.2
0.1
0.0
5.8 5.6 5.4 5.2 5.0 4.8 4.6 4.4 4.2 4.0 3.8 3.6 3.4 3.2 3.0 2.8 2.6 2.4 2.2 2.0 1.8 1.6 1.4 1.2 1.0 0.8 0.6 0.4 0.2 0.0
distance (km)
velocity
mean velocity all transect 2

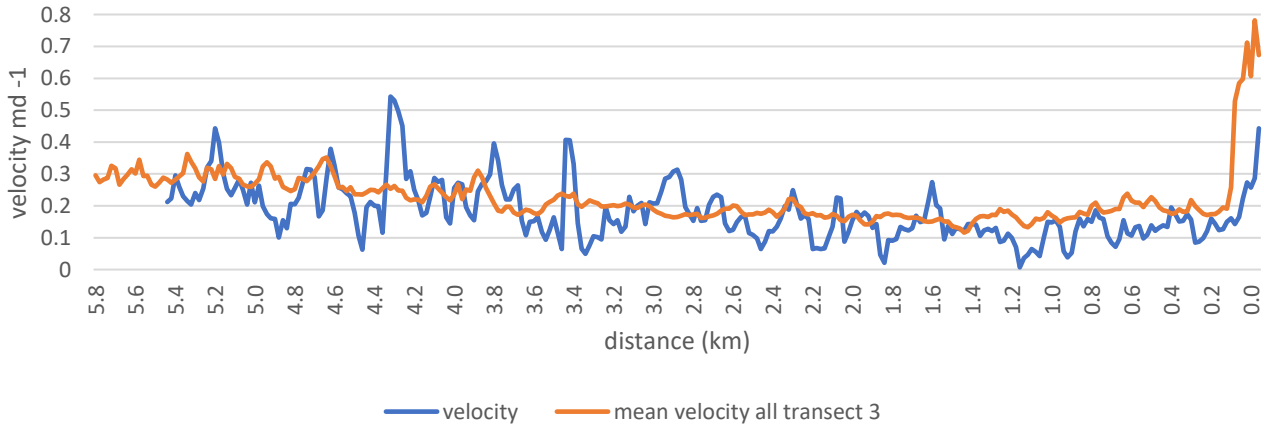
velocity md -1
0.8
0.7
0.6
0.5
0.4
0.3
0.2
0.1
0
5.8 5.6 5.4 5.2 5.0 4.8 4.6 4.4 4.2 4.0 3.8 3.6 3.4 3.2 3.0 2.8 2.6 2.4 2.2 2.0 1.8 1.6 1.4 1.2 1.0 0.8 0.6 0.4 0.2 0.0
distance (km)
velocity
mean velocity all transect 3

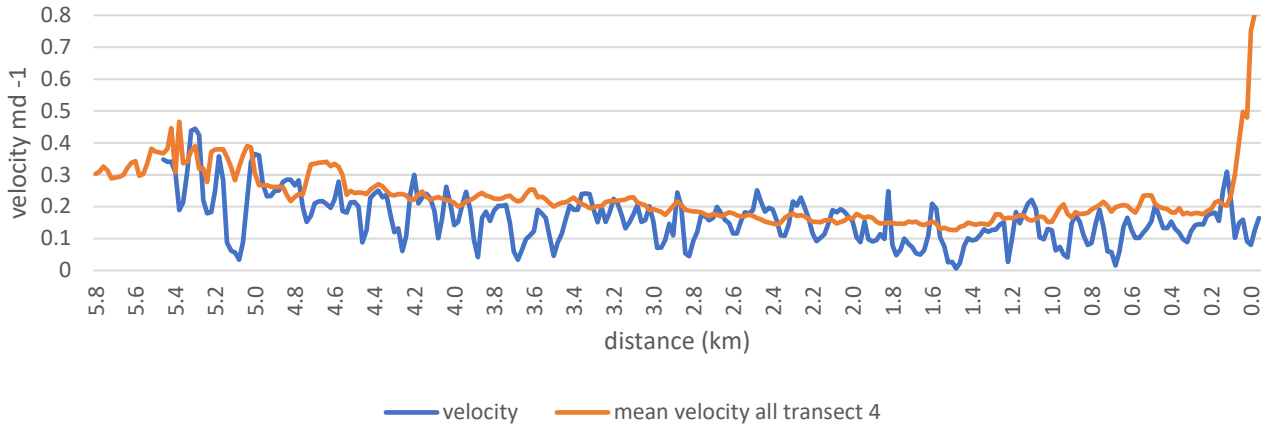

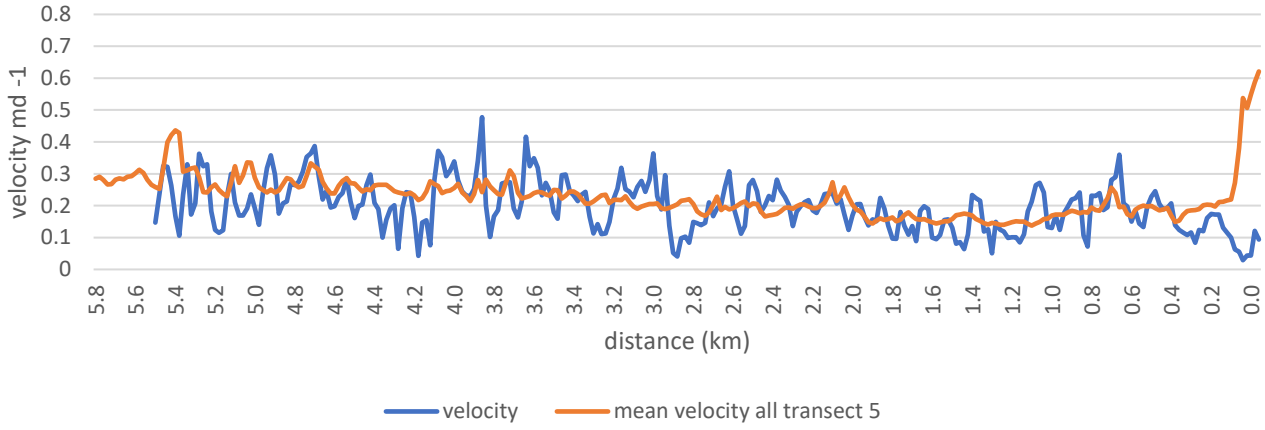

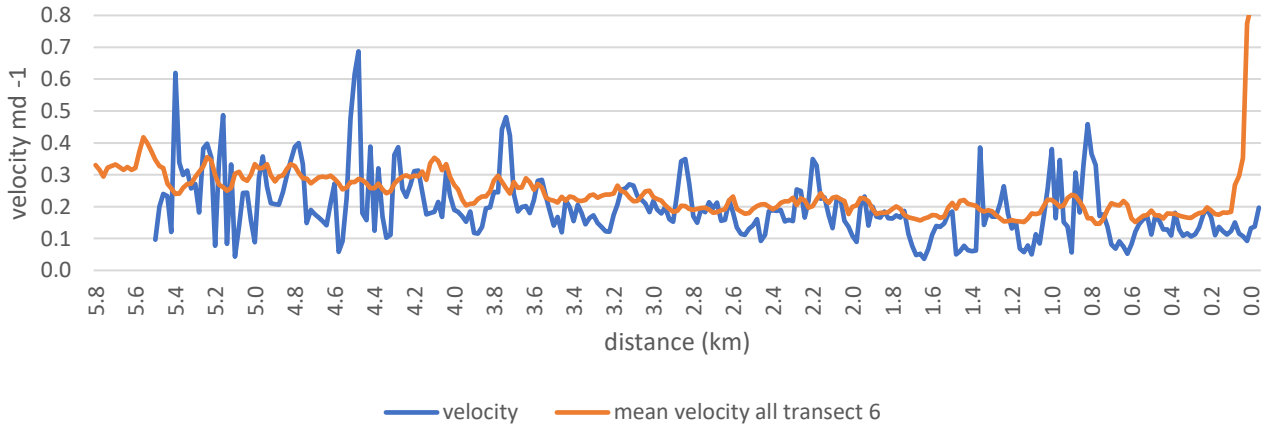

Appendix 23A: Longitudinal velocity profiles from 29/10/2017 – 18/11/2017 (time period of 20 days) The orange line indicates the surface velocity values extracted from all surface velocity images. The blue line is the surface velocity values extracted from each profile. Profiles run from A near the Ball Glacier confluence down to B at the terminus.

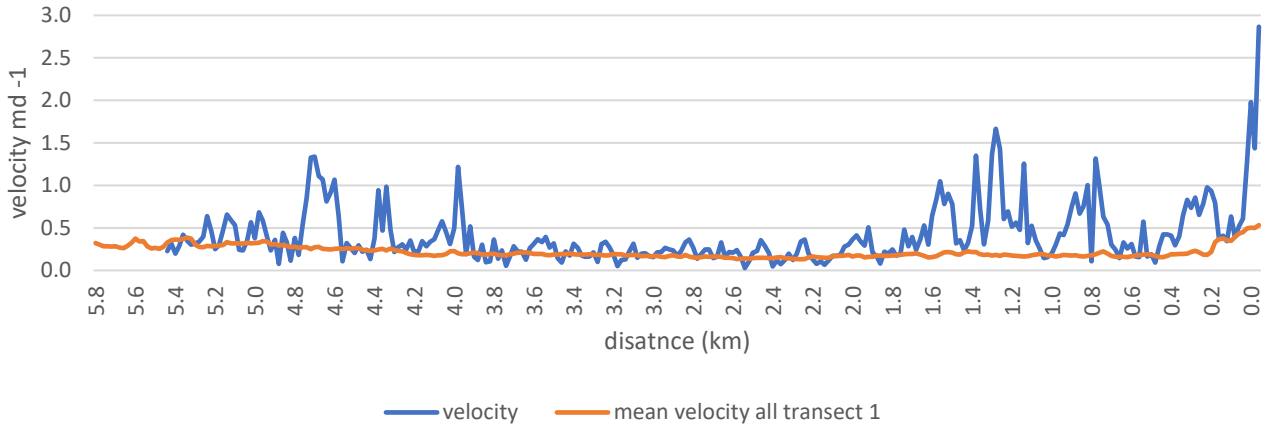
velocity md -1
3.0
2.5
2.0
1.5
1.0
0.5
0.0
5.8 5.6 5.4 5.2 5.0 4.8 4.6 4.4 4.2 4.0 3.8 3.6 3.4 3.2 3.0 2.8 2.6 2.4 2.2 2.0 1.8 1.6 1.4 1.2 1.0 0.8 0.6 0.4 0.2 0.0
disatnce (km)
velocity
mean velocity all transect 1

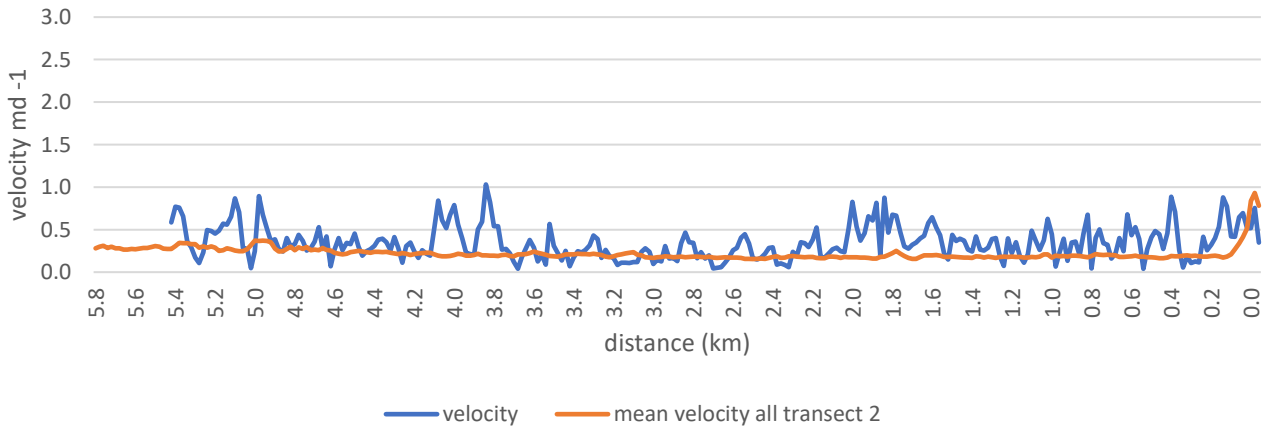
velocity md -1
3.0
2.5
2.0
1.5
1.0
0.5
0.0
5.8 5.6 5.4 5.2 5.0 4.8 4.6 4.4 4.2 4.0 3.8 3.6 3.4 3.2 3.0 2.8 2.6 2.4 2.2 2.0 1.8 1.6 1.4 1.2 1.0 0.8 0.6 0.4 0.2 0.0
distance (km)
velocity
mean velocity all transect 2

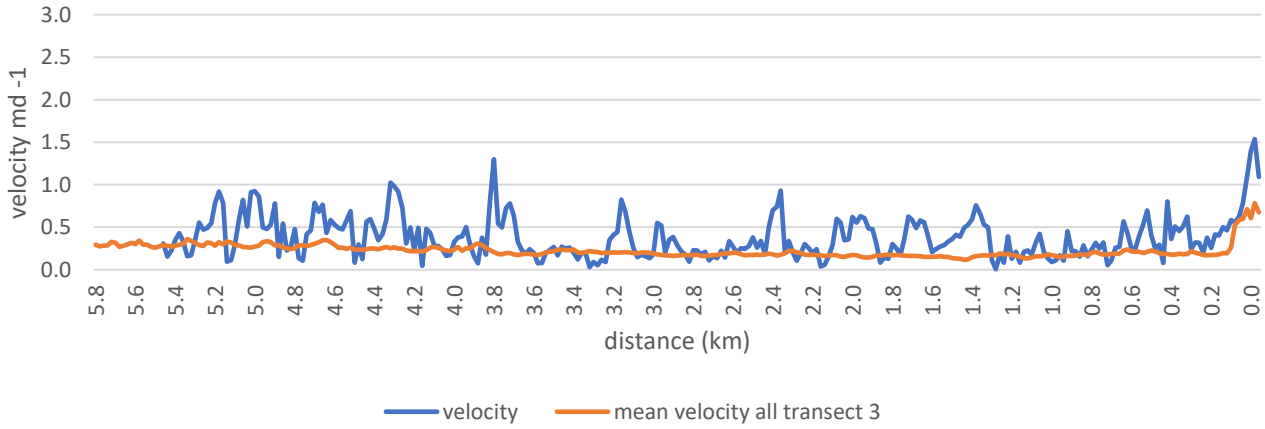
velocity md -1
3.0
2.5
2.0
1.5
1.0
0.5
0.0
5.8 5.6 5.4 5.2 5.0 4.8 4.6 4.4 4.2 4.0 3.8 3.6 3.4 3.2 3.0 2.8 2.6 2.4 2.2 2.0 1.8 1.6 1.4 1.2 1.0 0.8 0.6 0.4 0.2 0.0
distance (km)
velocity
mean velocity all transect 3

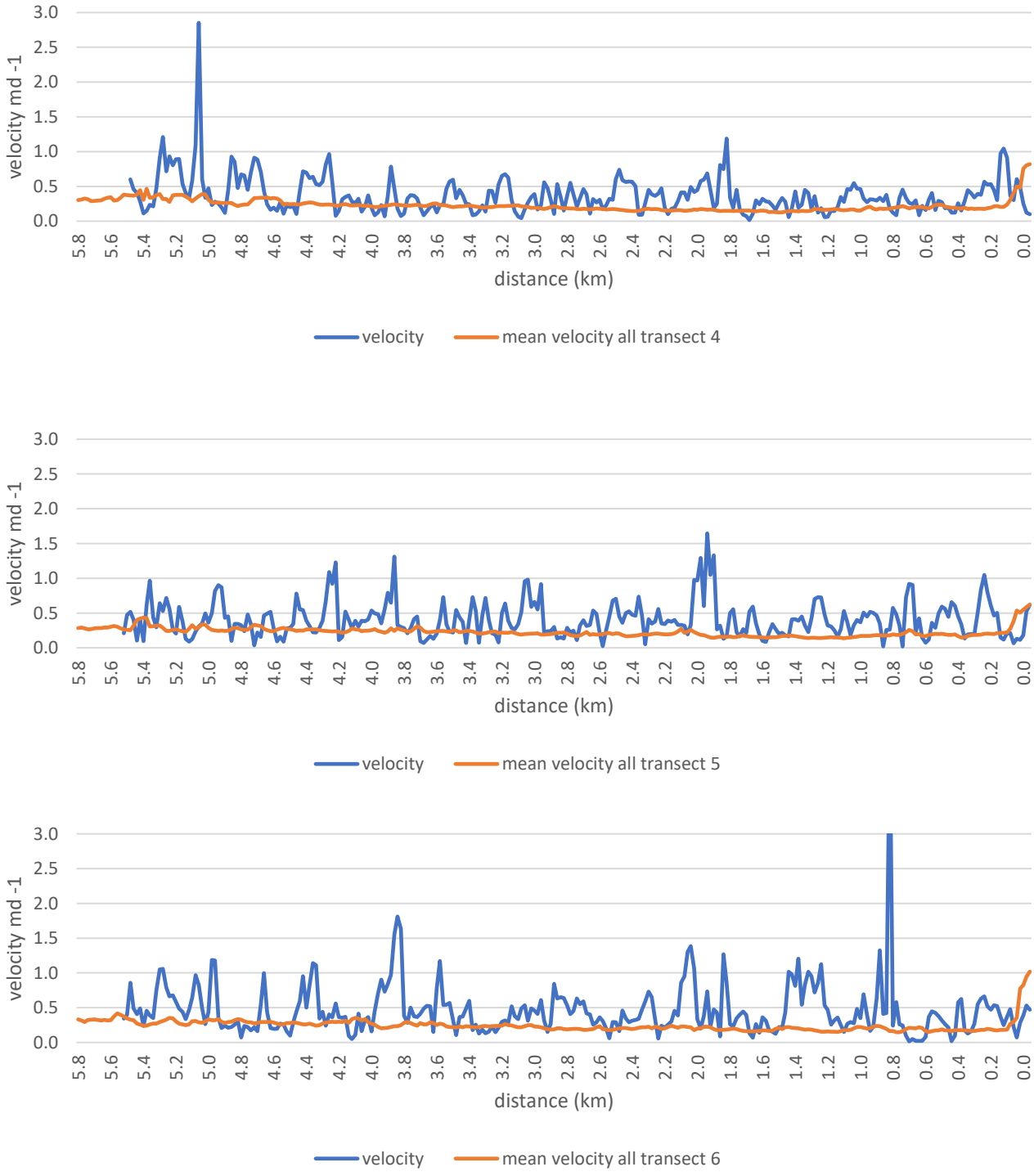

Appendix 24A: Longitudinal velocity profiles from 13/11/2017 – 18/11/2017 (time period of 20 days) The orange line indicates the surface velocity values extracted from all surface velocity images. The blue line is the surface velocity values extracted from each profile. Profiles run from A near the Ball Glacier confluence down to B at the terminus.

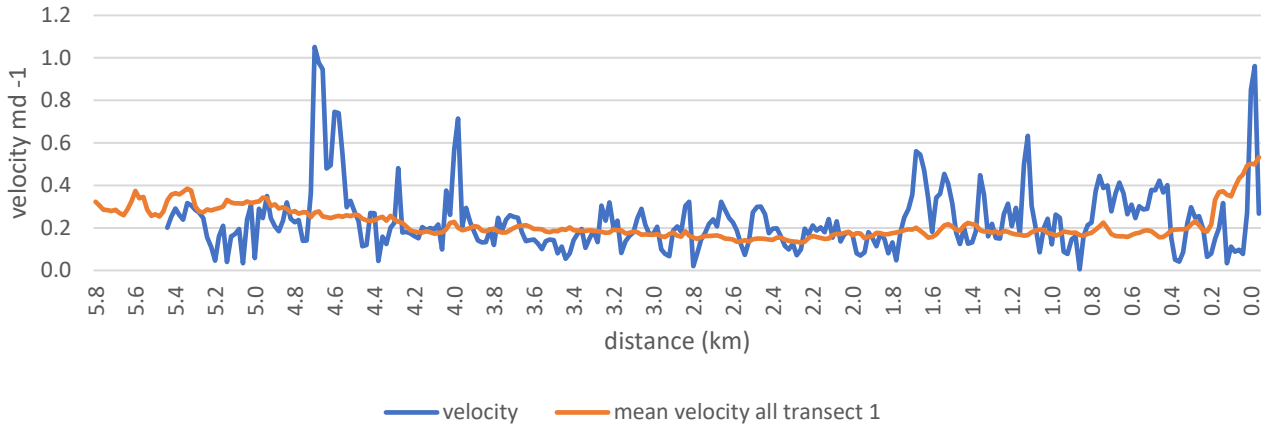
velocity md -1
1.2
1.0
0.8
0.6
0.4
0.2
0.0
5.8 5.6 5.4 5.2 5.0 4.8 4.6 4.4 4.2 4.0 3.8 3.6 3.4 3.2 3.0 2.8 2.6 2.4 2.2 2.0 1.8 1.6 1.4 1.2 1.0 0.8 0.6 0.4 0.2 0.0
distance (km)
velocity
mean velocity all transect 1

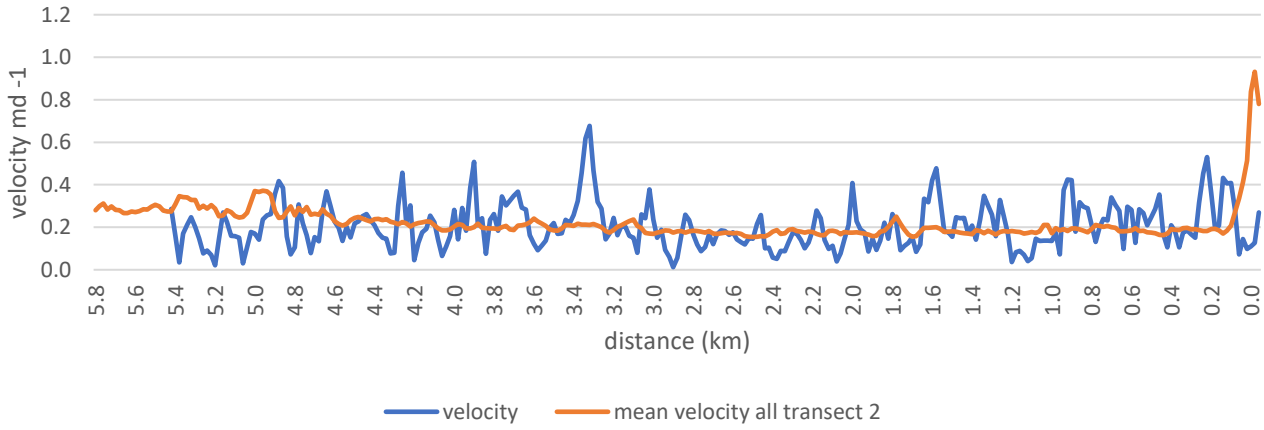
velocity md -1
1.2
1.0
0.8
0.6
0.4
0.2
0.0
5.8 5.6 5.4 5.2 5.0 4.8 4.6 4.4 4.2 4.0 3.8 3.6 3.4 3.2 3.0 2.8 2.6 2.4 2.2 2.0 1.8 1.6 1.4 1.2 1.0 0.8 0.6 0.4 0.2 0.0
distance (km)
velocity
mean velocity all transect 2

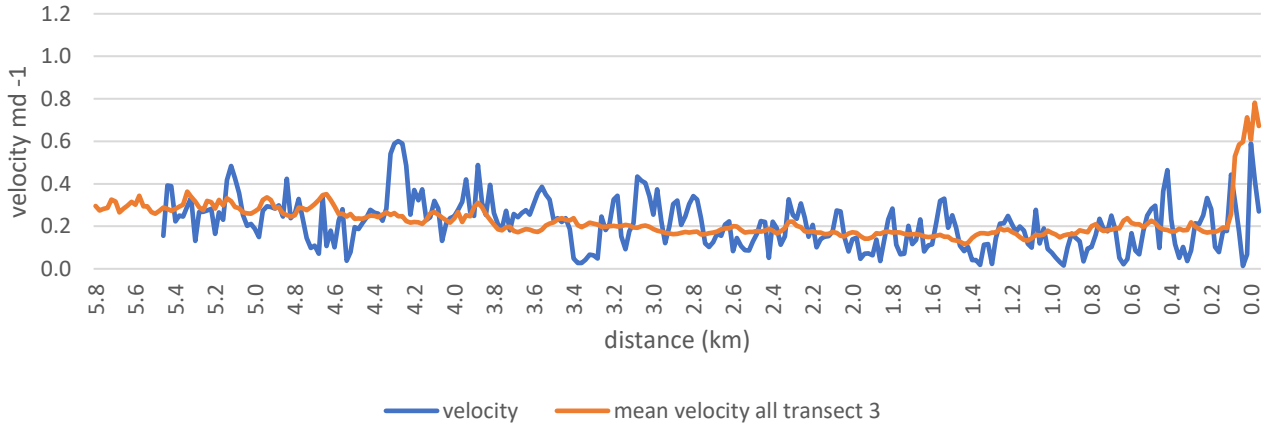
velocity md -1
1.2
1.0
0.8
0.6
0.4
0.2
0.0
5.8 5.6 5.4 5.2 5.0 4.8 4.6 4.4 4.2 4.0 3.8 3.6 3.4 3.2 3.0 2.8 2.6 2.4 2.2 2.0 1.8 1.6 1.4 1.2 1.0 0.8 0.6 0.4 0.2 0.0
distance (km)
velocity
mean velocity all transect 3

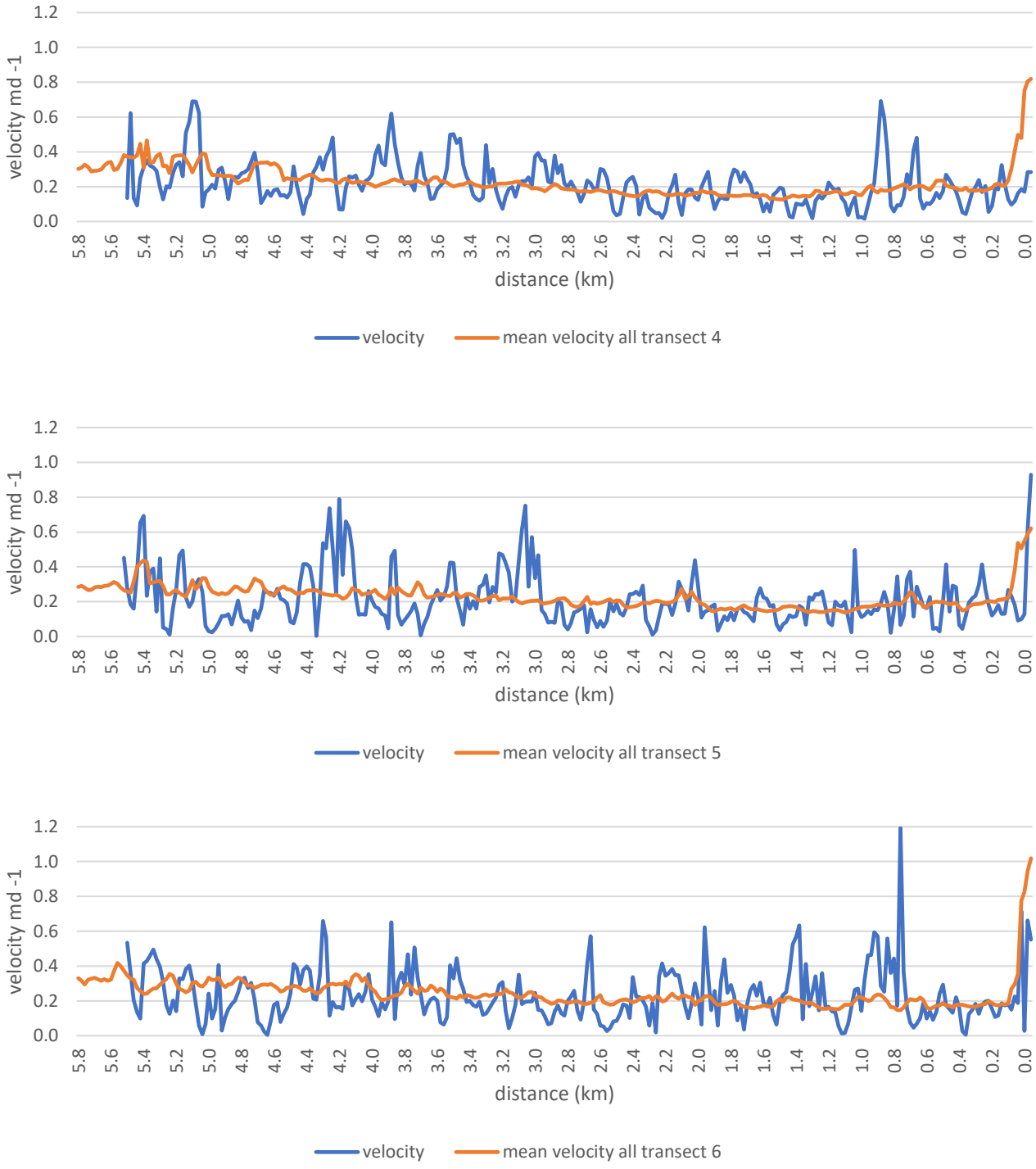

Appendix 25A: Longitudinal velocity profiles from 18/11/2017 – 28/11/2017 (time period of 20 days) The orange line indicates the surface velocity values extracted from all surface velocity images. The blue line is the surface velocity values extracted from each profile. Profiles run from A near the Ball Glacier confluence down to B at the terminus.

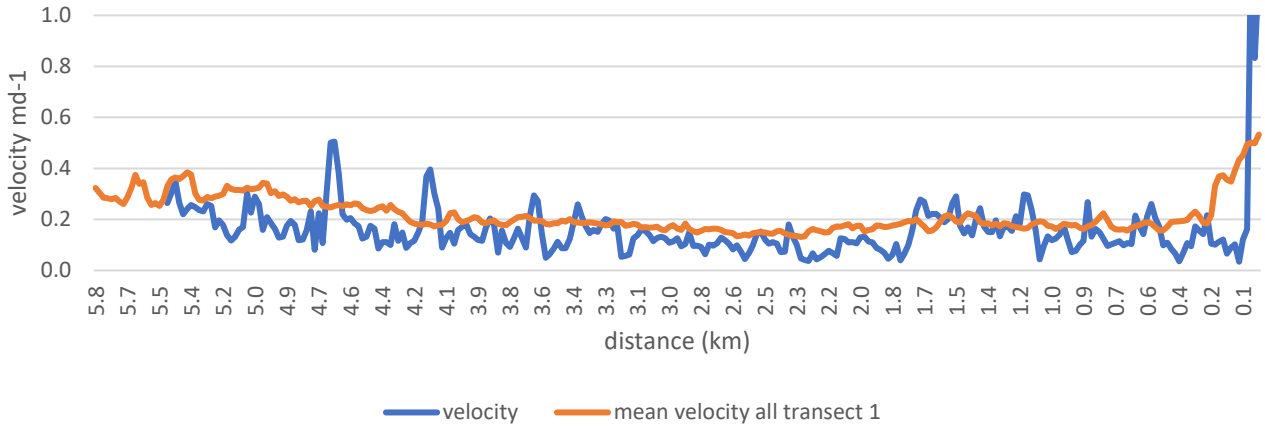
velocity md-1
1.0
0.8
0.6
0.4
0.2
0.0
5.8 5.7 5.5 5.4 5.2 5.0 4.9 4.7 4.6 4.4 4.2 4.1 3.9 3.8 3.6 3.4 3.3 3.1 3.0 2.8 2.6 2.5 2.3 2.2 2.0 1.8 1.7 1.5 1.4 1.2 1.0 0.9 0.7 0.6 0.4 0.2 0.1
distance (km)
velocity
mean velocity all transect 1

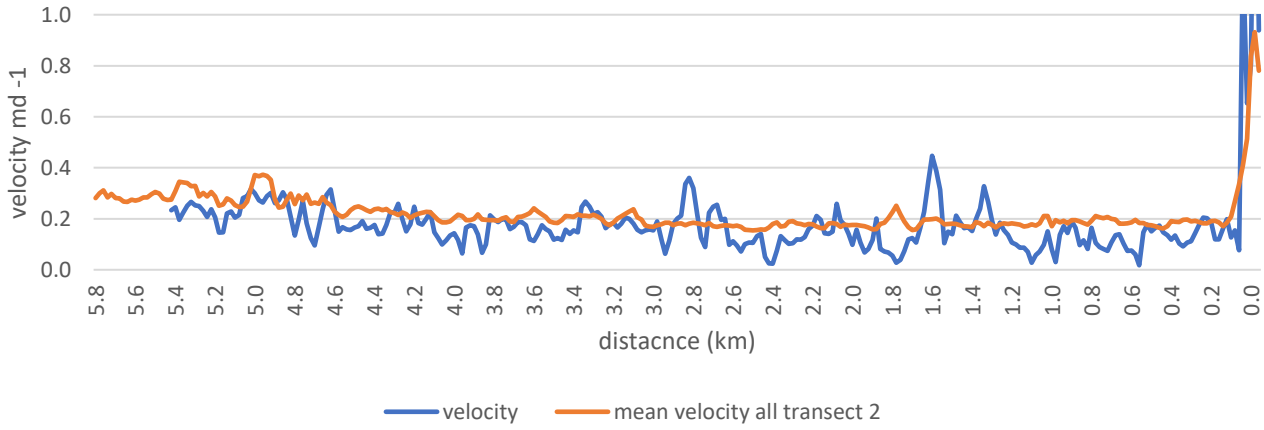
velocity md -1
1.0
0.8
0.6
0.4
0.2
0.0
5.8 5.6 5.4 5.2 5.0 4.8 4.6 4.4 4.2 4.0 3.8 3.6 3.4 3.2 3.0 2.8 2.6 2.4 2.2 2.0 1.8 1.6 1.4 1.2 1.0 0.8 0.6 0.4 0.2 0.0
distacnce (km)
velocity
mean velocity all transect 2

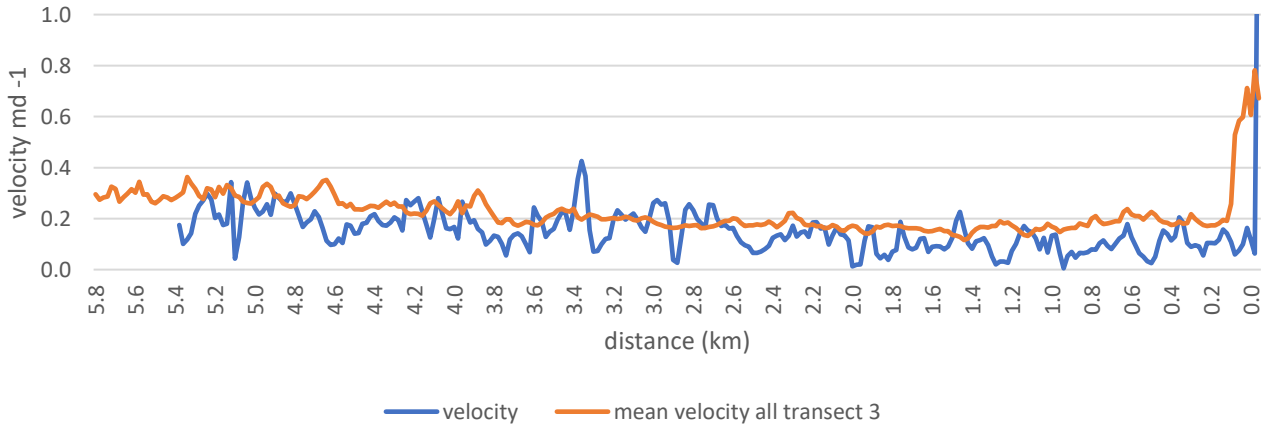
velocity md -1
1.0
0.8
0.6
0.4
0.2
0.0
5.8 5.6 5.4 5.2 5.0 4.8 4.6 4.4 4.2 4.0 3.8 3.6 3.4 3.2 3.0 2.8 2.6 2.4 2.2 2.0 1.8 1.6 1.4 1.2 1.0 0.8 0.6 0.4 0.2 0.0
distance (km)
velocity
mean velocity all transect 3

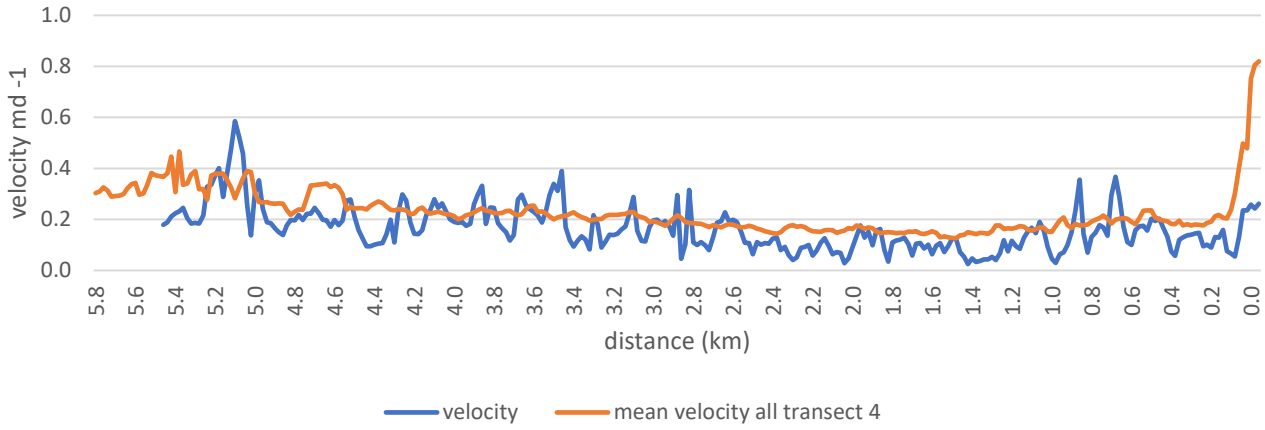

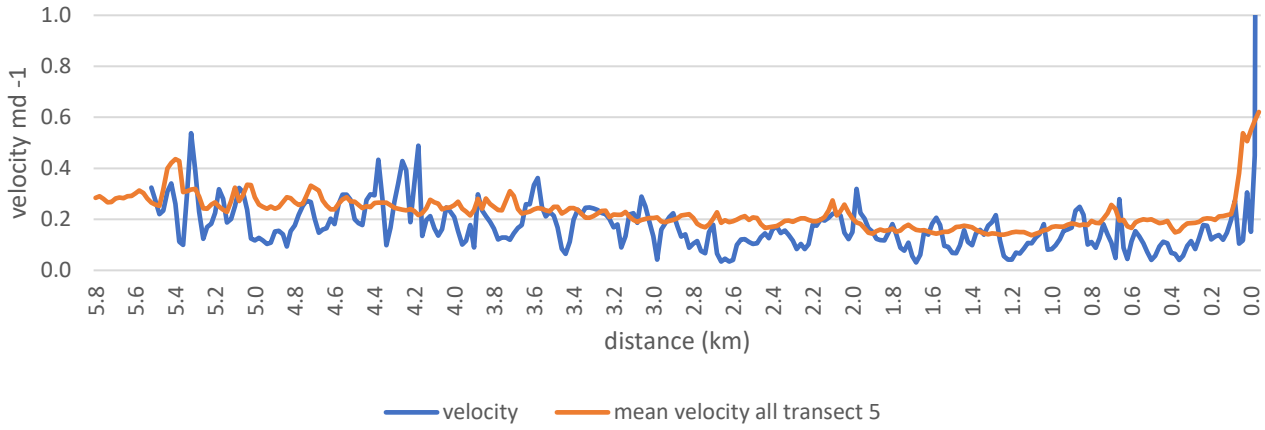

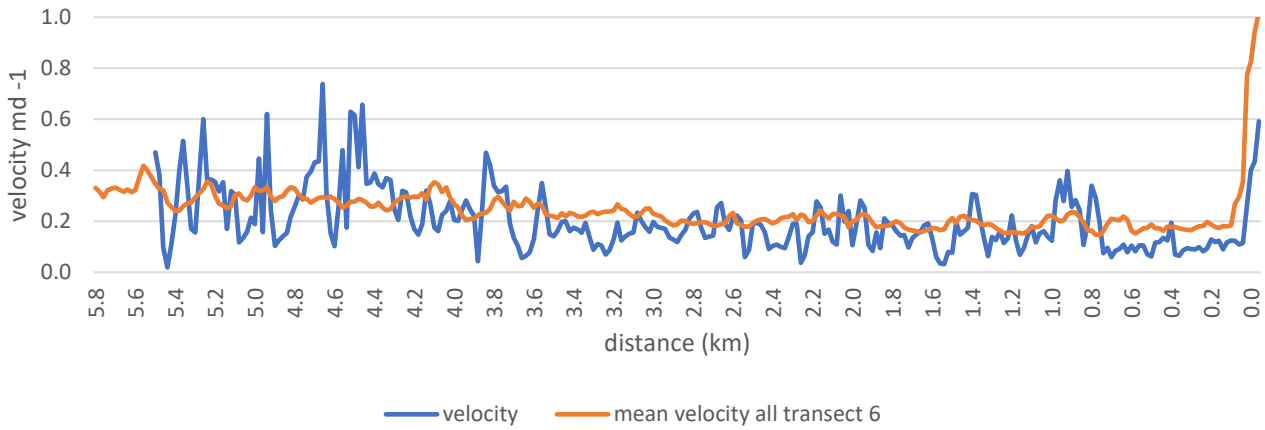

Appendix 26A: Longitudinal velocity profiles from 18/11/2017 – 13/12/2017 (time period of 25 days) The orange line indicates the surface velocity values extracted from all surface velocity images. The blue line is the surface velocity values extracted from each profile. Profiles run from A near the Ball Glacier confluence down to B at the terminus.

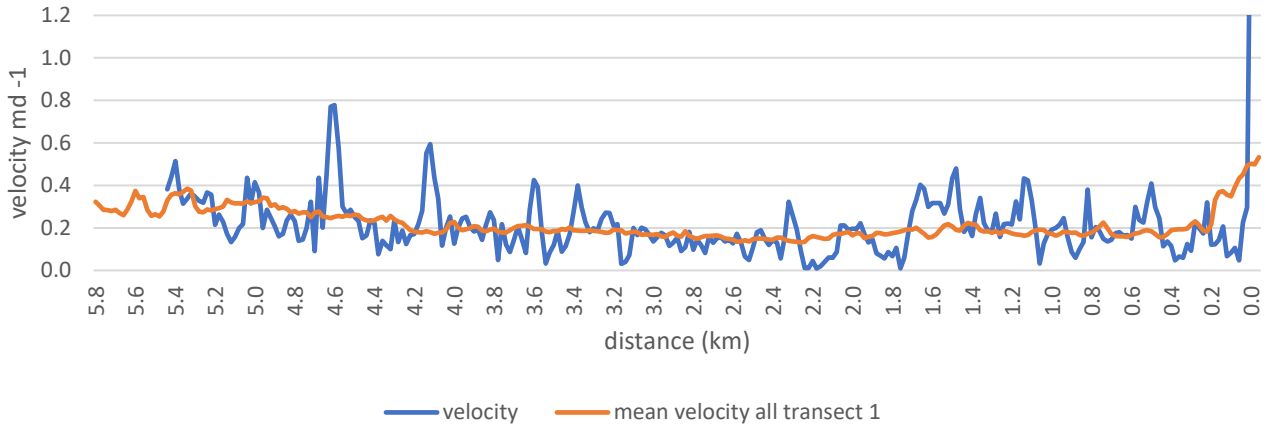
velocity md -1
1.2
1.0
0.8
0.6
0.4
0.2
0.0
5.8 5.6 5.4 5.2 5.0 4.8 4.6 4.4 4.2 4.0 3.8 3.6 3.4 3.2 3.0 2.8 2.6 2.4 2.2 2.0 1.8 1.6 1.4 1.2 1.0 0.8 0.6 0.4 0.2 0.0
distance (km)
velocity
mean velocity all transect 1

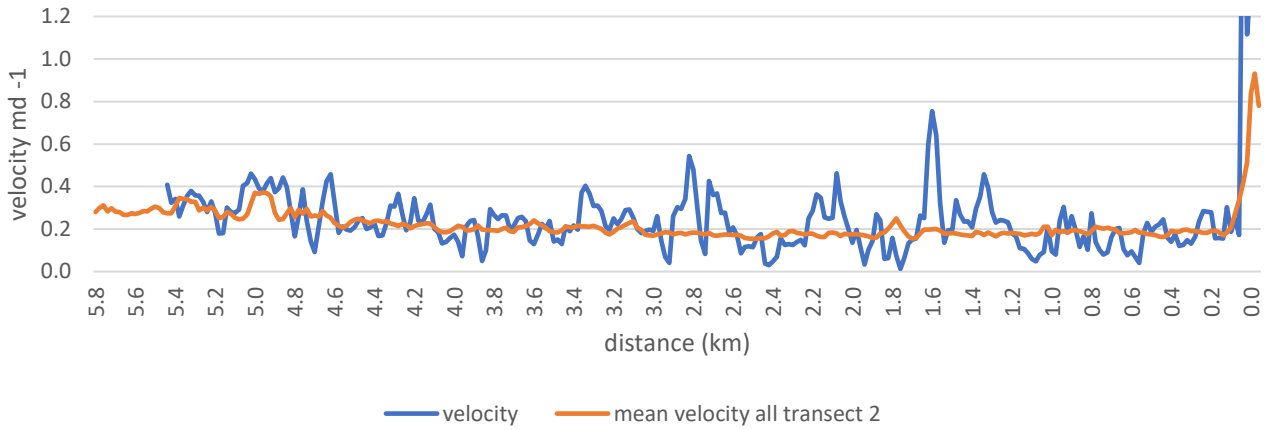
velocity md -1
1.2
1.0
0.8
0.6
0.4
0.2
0.0
5.8 5.6 5.4 5.2 5.0 4.8 4.6 4.4 4.2 4.0 3.8 3.6 3.4 3.2 3.0 2.8 2.6 2.4 2.2 2.0 1.8 1.6 1.4 1.2 1.0 0.8 0.6 0.4 0.2 0.0
distance (km)
velocity
mean velocity all transect 2

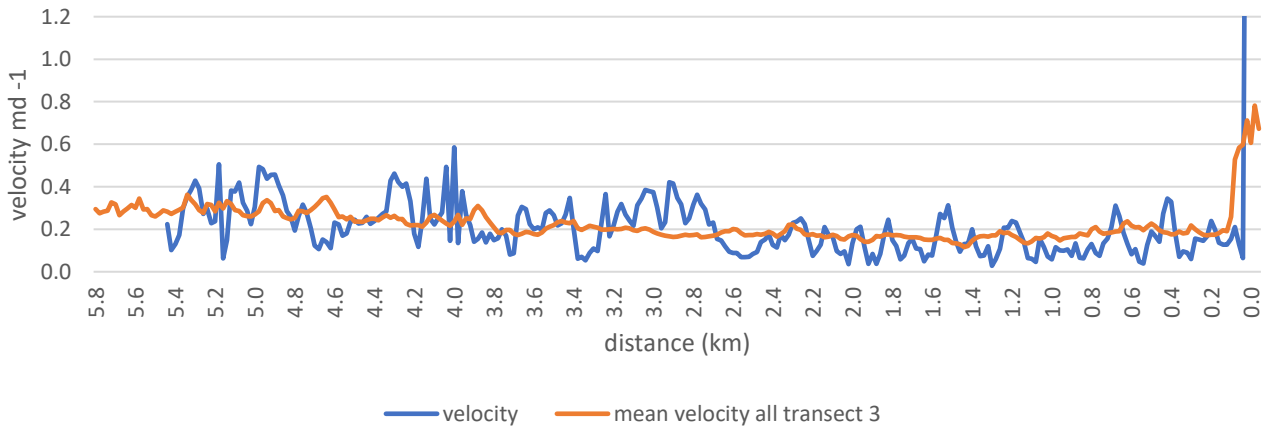
velocity md -1
1.2
1.0
0.8
0.6
0.4
0.2
0.0
5.8 5.6 5.4 5.2 5.0 4.8 4.6 4.4 4.2 4.0 3.8 3.6 3.4 3.2 3.0 2.8 2.6 2.4 2.2 2.0 1.8 1.6 1.4 1.2 1.0 0.8 0.6 0.4 0.2 0.0
distance (km)
velocity
mean velocity all transect 3

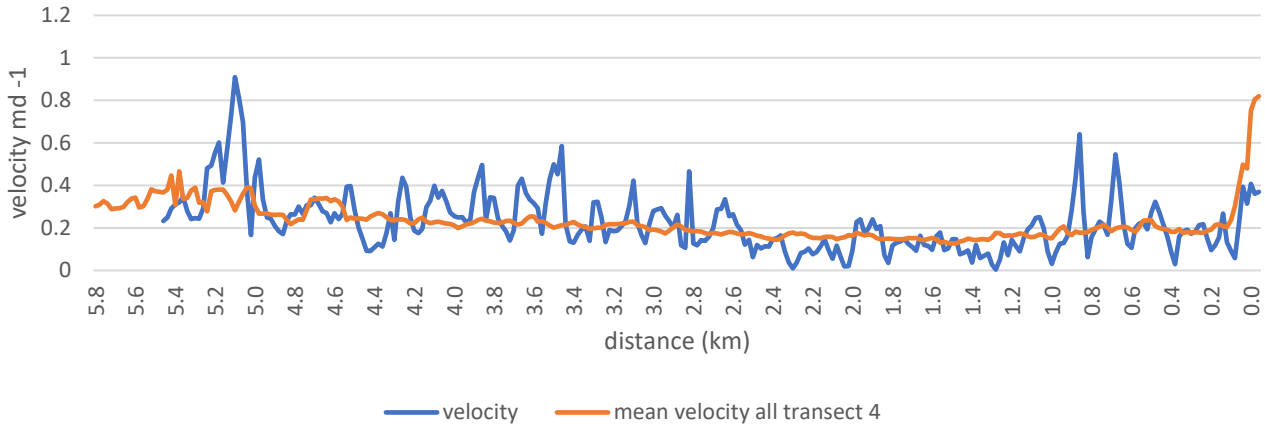

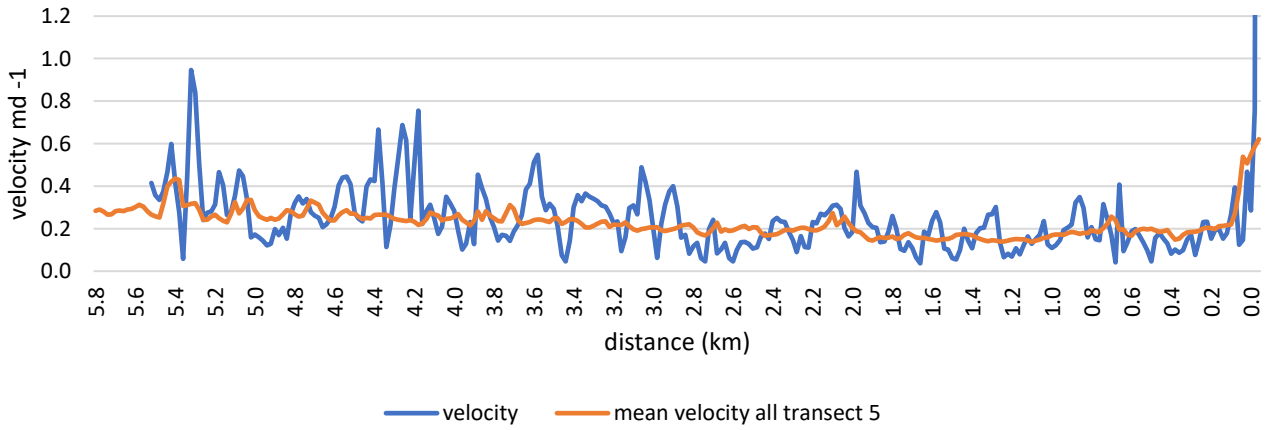

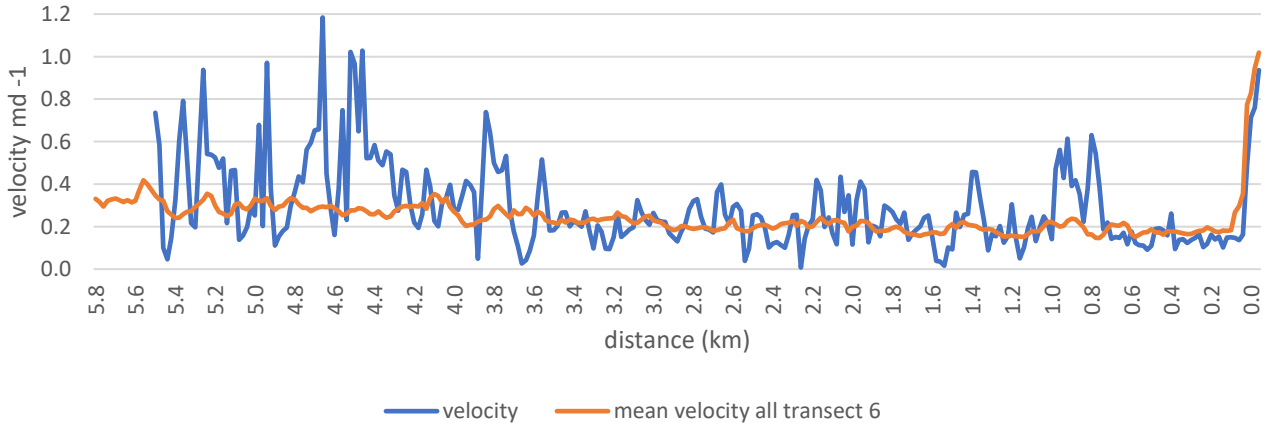

Appendix 27A: Longitudinal velocity profiles from 28/11/2017 – 13/12/2017 (time period of 15 days) The orange line indicates the surface velocity values extracted from all surface velocity images. The blue line is the surface velocity values extracted from each profile. Profiles run from A near the Ball Glacier confluence down to B at the terminus.

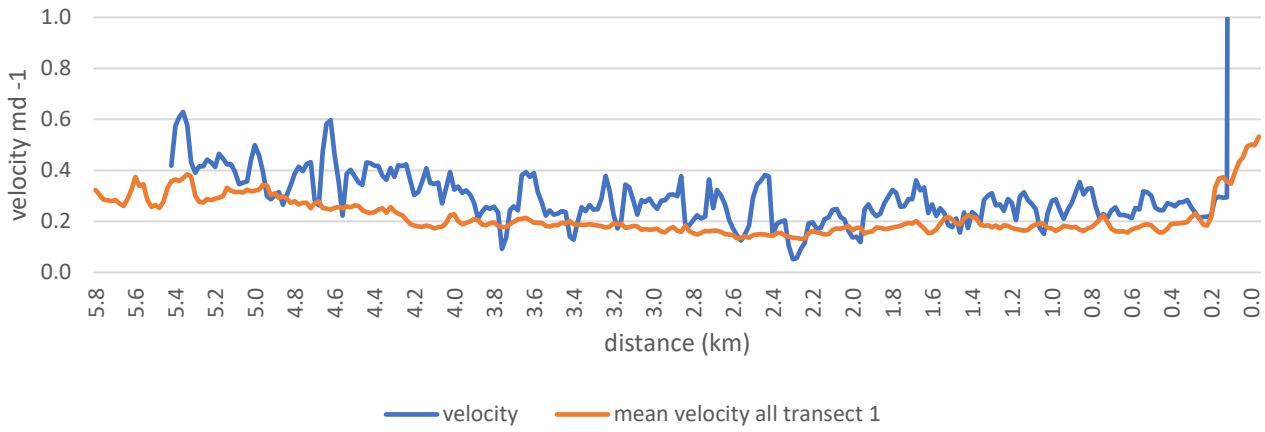
velocity md -1
1.0
0.8
0.6
0.4
0.2
0.0
5.8 5.6 5.4 5.2 5.0 4.8 4.6 4.4 4.2 4.0 3.8 3.6 3.4 3.2 3.0 2.8 2.6 2.4 2.2 2.0 1.8 1.6 1.4 1.2 1.0 0.8 0.6 0.4 0.2 0.0
distance (km)
velocity
mean velocity all transect 1

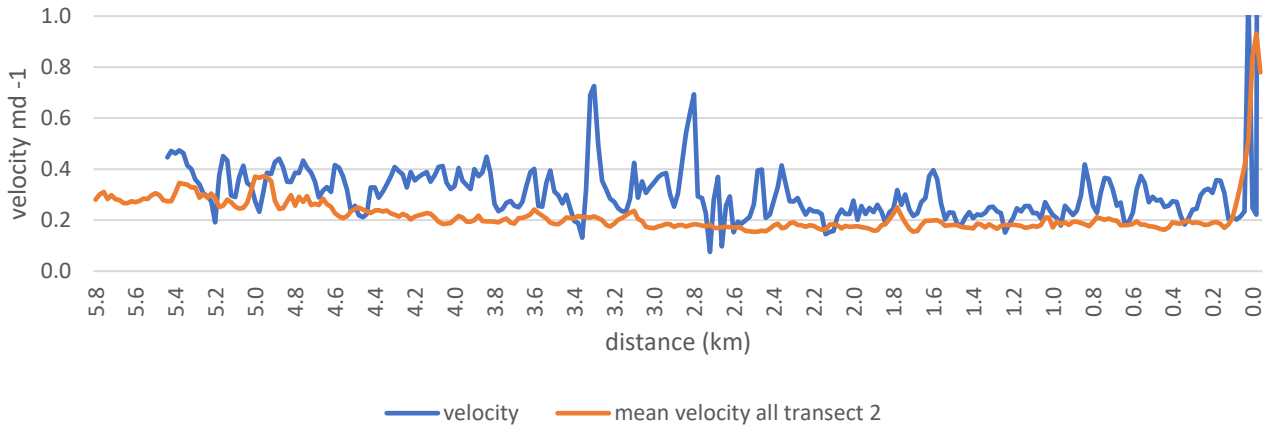
velocity md -1
1.0
0.8
0.6
0.4
0.2
0.0
5.8 5.6 5.4 5.2 5.0 4.8 4.6 4.4 4.2 4.0 3.8 3.6 3.4 3.2 3.0 2.8 2.6 2.4 2.2 2.0 1.8 1.6 1.4 1.2 1.0 0.8 0.6 0.4 0.2 0.0
distance (km)
velocity
mean velocity all transect 2

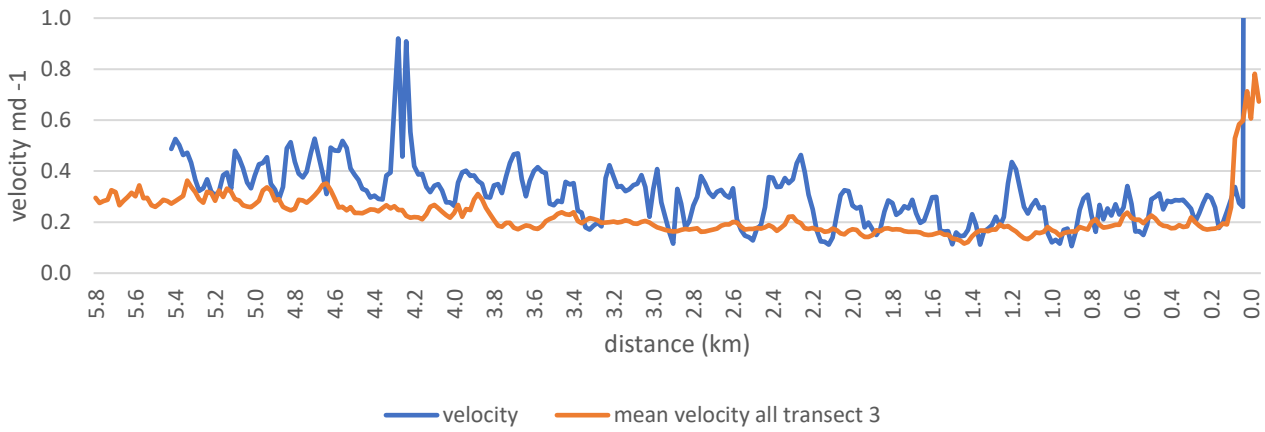
velocity md -1
1.0
0.8
0.6
0.4
0.2
0.0
5.8 5.6 5.4 5.2 5.0 4.8 4.6 4.4 4.2 4.0 3.8 3.6 3.4 3.2 3.0 2.8 2.6 2.4 2.2 2.0 1.8 1.6 1.4 1.2 1.0 0.8 0.6 0.4 0.2 0.0
distance (km)
velocity
mean velocity all transect 3

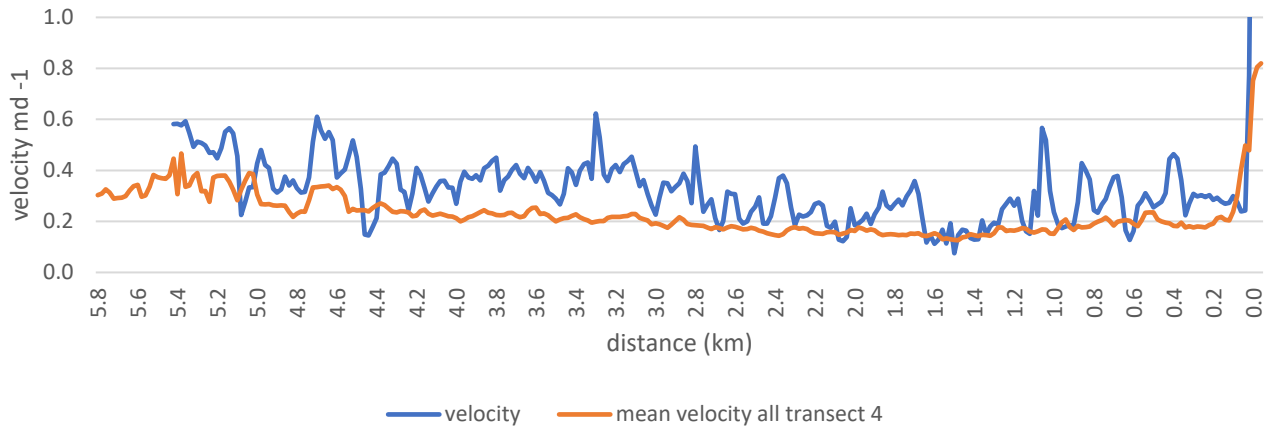

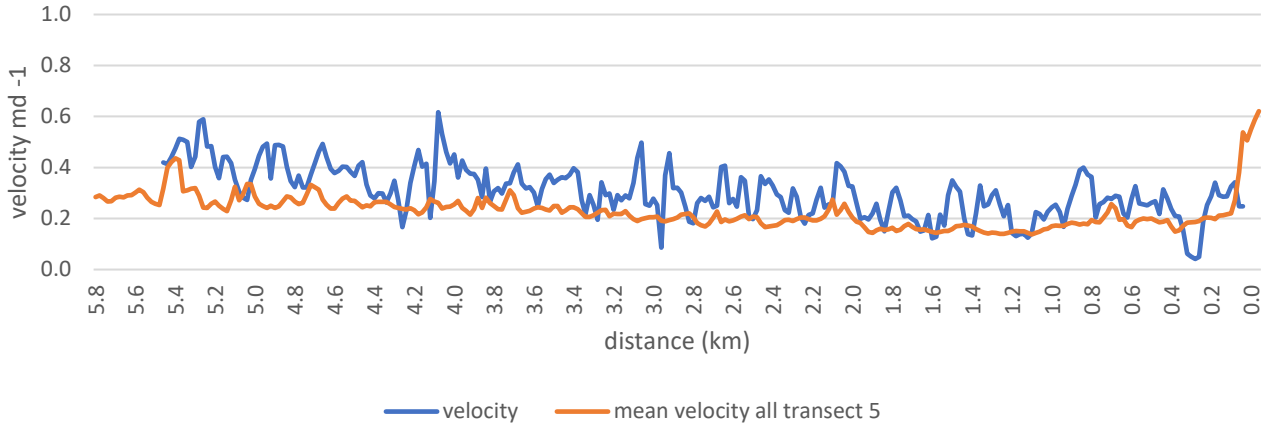

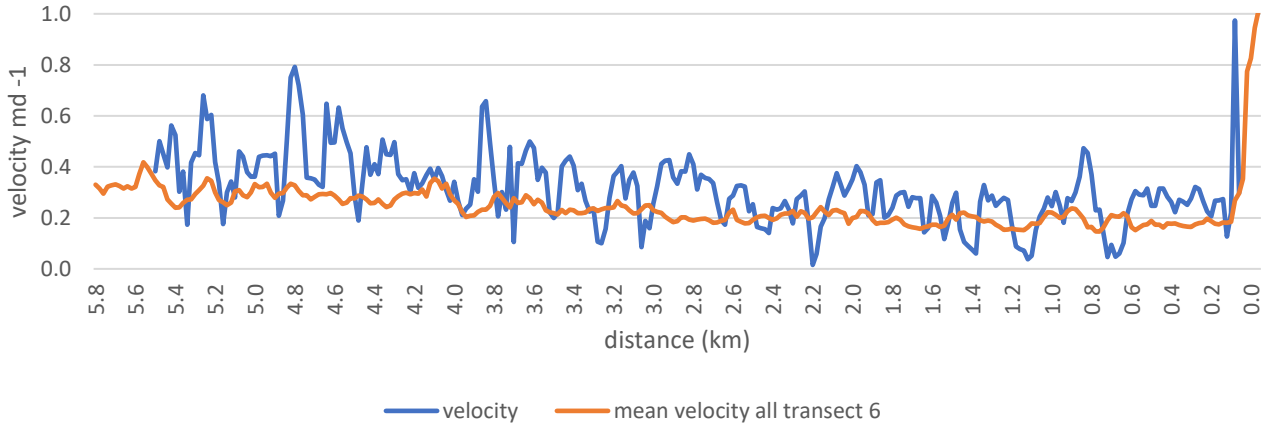

Appendix 28A: Longitudinal velocity profiles from 13/12/2017 – 22/01/2018 (time period of 15 days) The orange line indicates the surface velocity values extracted from all surface velocity images. The blue line is the surface velocity values extracted from each profile. Profiles run from A near the Ball Glacier confluence down to B at the terminus.

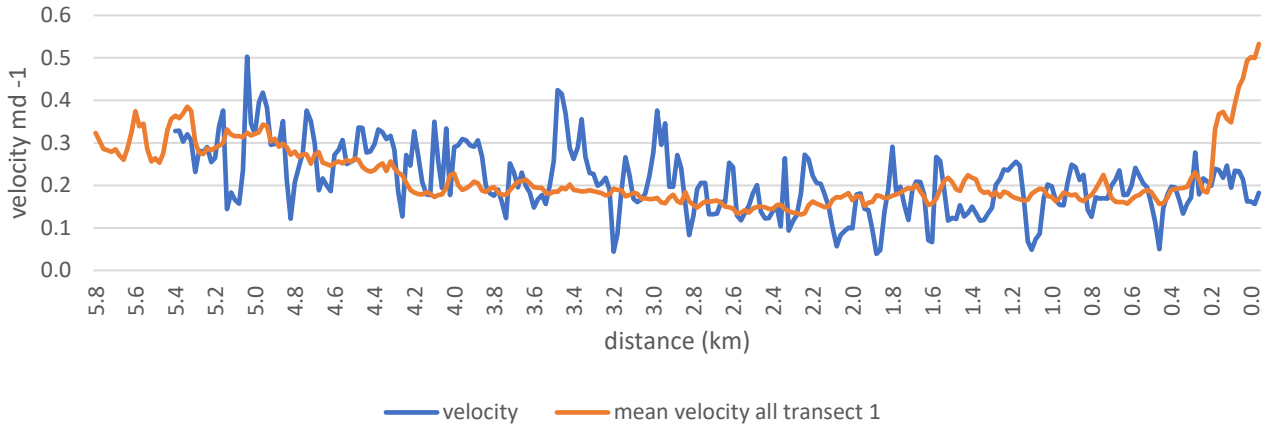
velocity md -1
0.6
0.5
0.4
0.3
0.2
0.1
0.0
5.8 5.6 5.4 5.2 5.0 4.8 4.6 4.4 4.2 4.0 3.8 3.6 3.4 3.2 3.0 2.8 2.6 2.4 2.2 2.0 1.8 1.6 1.4 1.2 1.0 0.8 0.6 0.4 0.2 0.0
distance (km)
velocity
mean velocity all transect 1

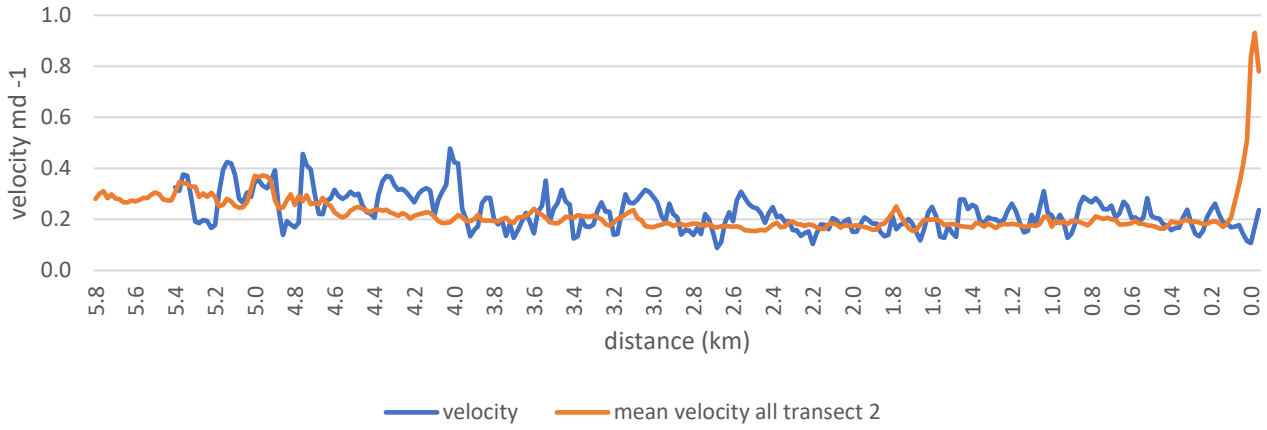
velocity md -1
1.0
0.8
0.6
0.4
0.2
0.0
5.8 5.6 5.4 5.2 5.0 4.8 4.6 4.4 4.2 4.0 3.8 3.6 3.4 3.2 3.0 2.8 2.6 2.4 2.2 2.0 1.8 1.6 1.4 1.2 1.0 0.8 0.6 0.4 0.2 0.0
distance (km)
velocity
mean velocity all transect 2

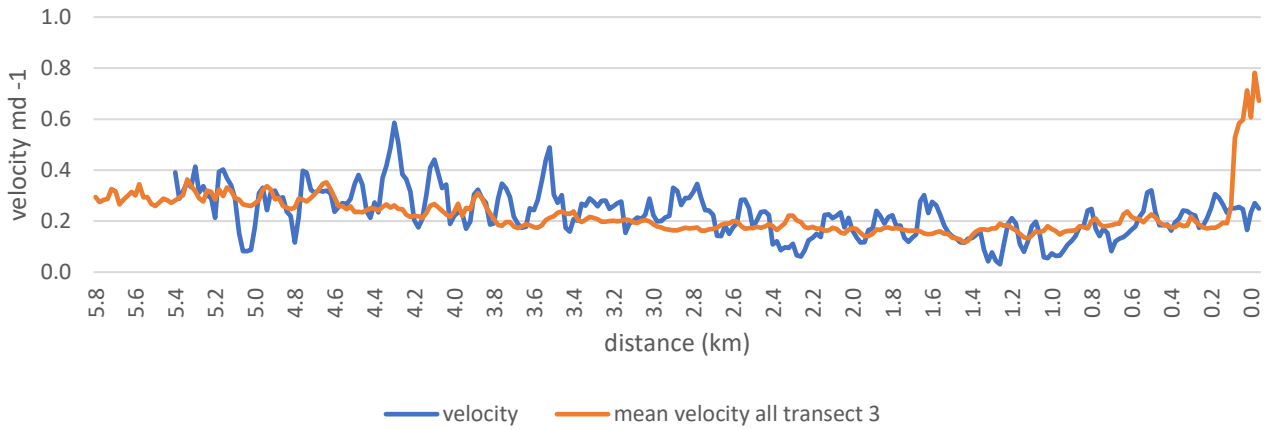
velocity md -1
1.0
0.8
0.6
0.4
0.2
0.0
5.8 5.6 5.4 5.2 5.0 4.8 4.6 4.4 4.2 4.0 3.8 3.6 3.4 3.2 3.0 2.8 2.6 2.4 2.2 2.0 1.8 1.6 1.4 1.2 1.0 0.8 0.6 0.4 0.2 0.0
distance (km)
velocity
mean velocity all transect 3

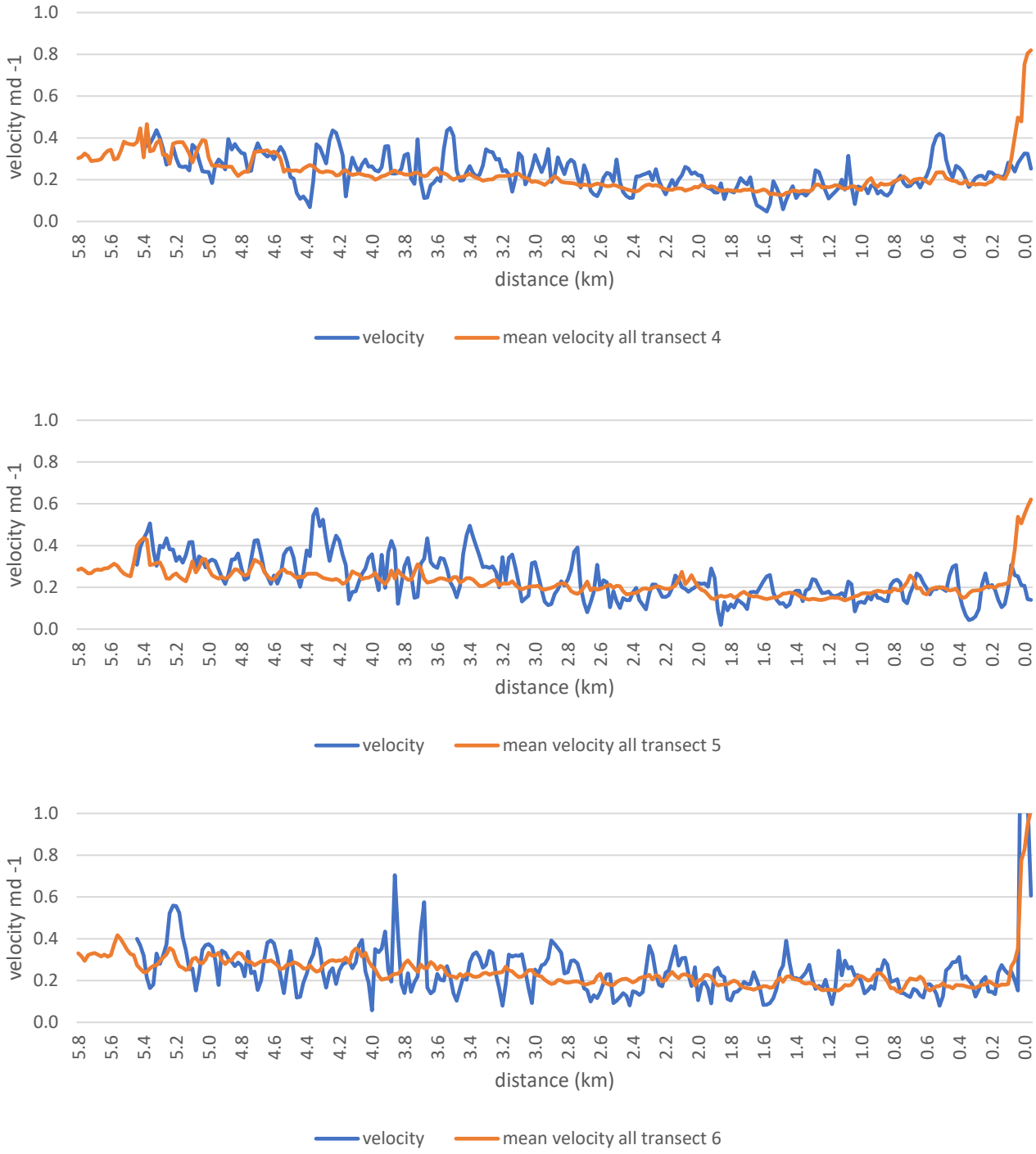

Appendix 29A: Longitudinal velocity profiles from 22/01/2018 – 21/02/2018 (time period of 30 days) The orange line indicates the surface velocity values extracted from all surface velocity images. The blue line is the surface velocity values extracted from each profile. Profiles run from A near the Ball Glacier confluence down to B at the terminus.

Appendix B: Longitudinal velocity profile – buoyant terminus

Longitudinal velocity profiles from different times of the year showing an acceleration at the near terminus, suggesting a buoyant terminus.

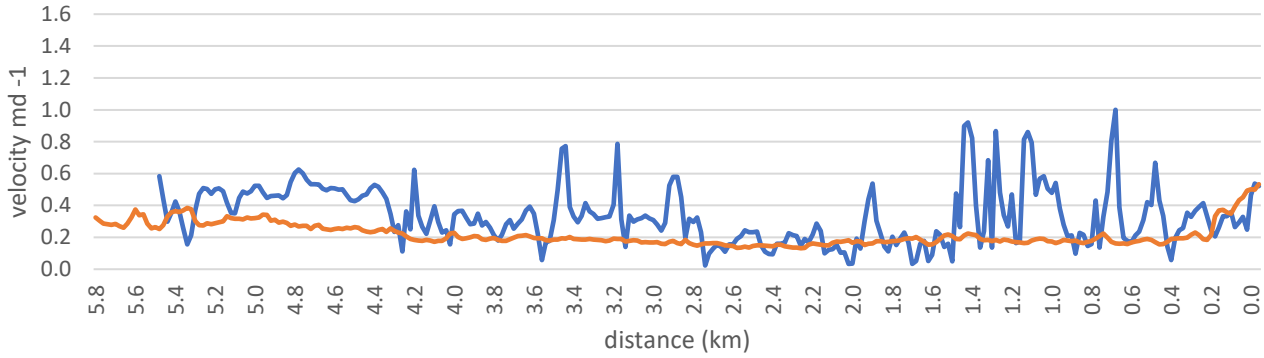

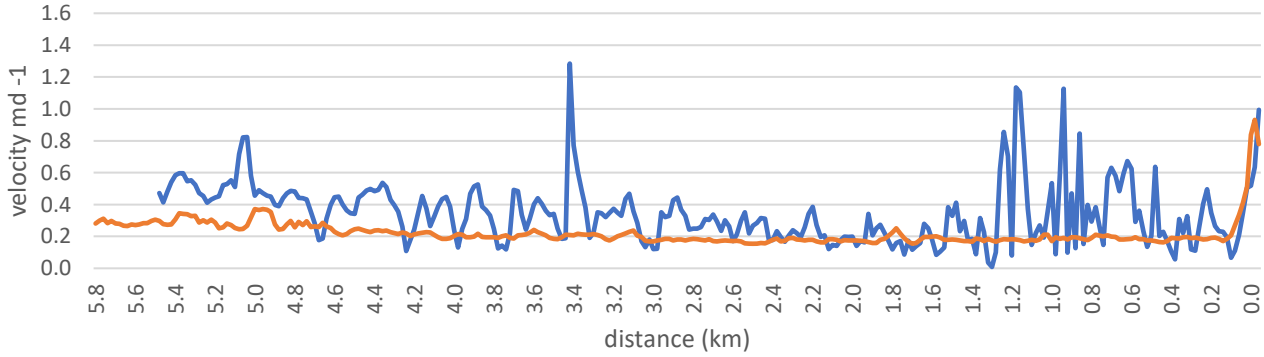

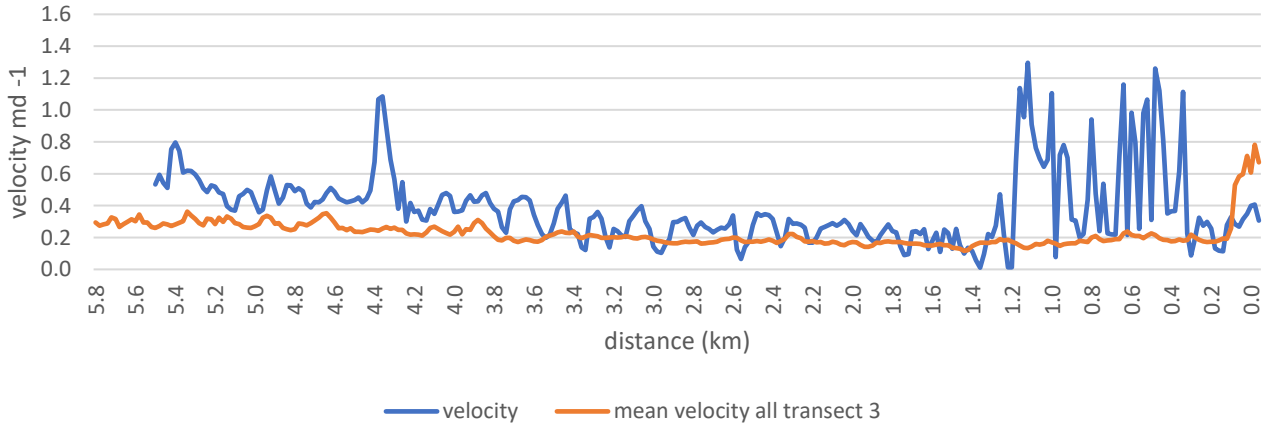

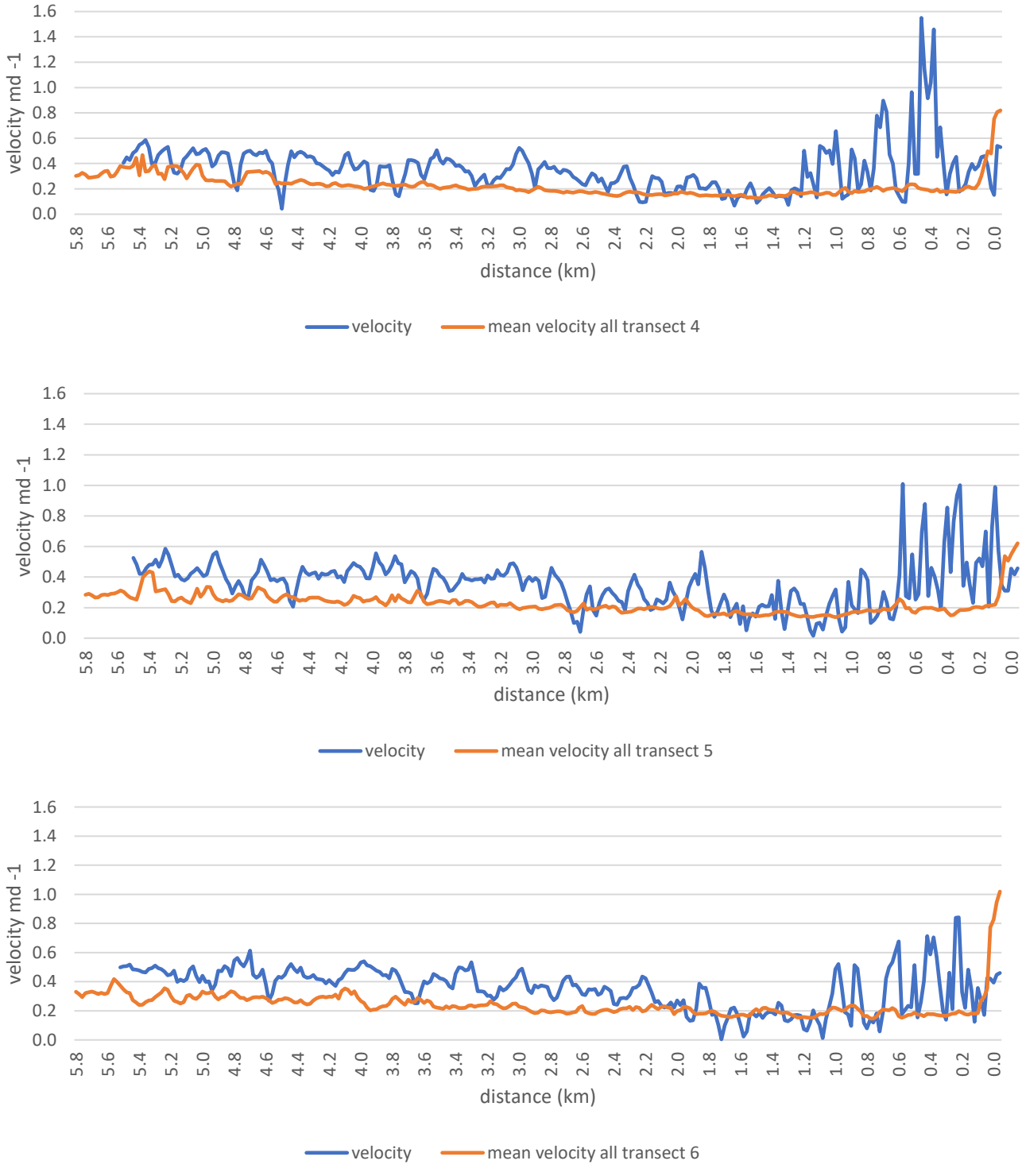

Appendix 1B: Longitudinal velocity profiles from 06/07/2017 – 16/07/2017 (time period of 10 days) The orange line indicates the surface velocity values extracted from all surface velocity images. The blue line is the surface velocity values extracted from each profile. Profiles run from A near the Ball Glacier confluence down to B at the

terminus.

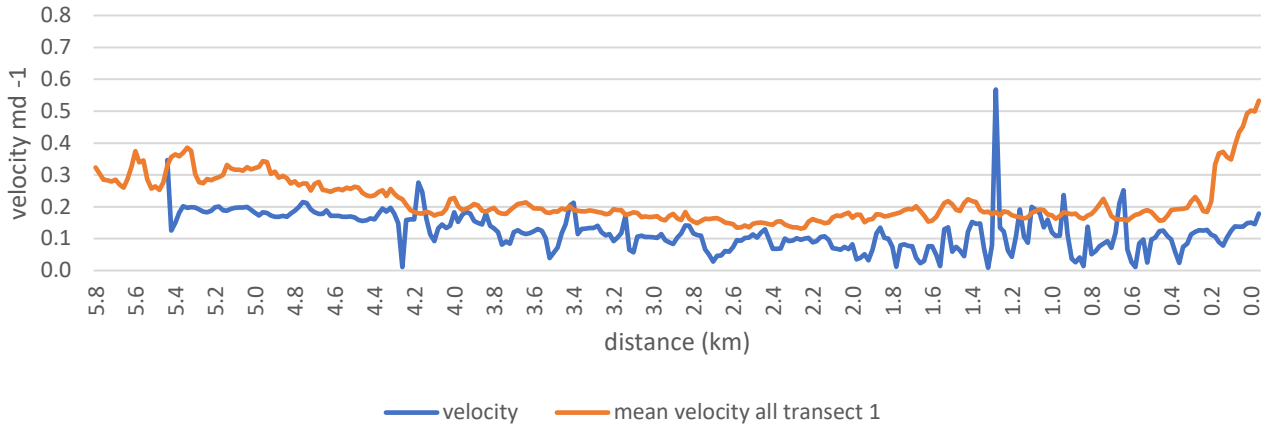
velocity md -1
0.8
0.7
0.6
0.5
0.4
0.3
0.2
0.1
0.0
5.8 5.6 5.4 5.2 5.0 4.8 4.6 4.4 4.2 4.0 3.8 3.6 3.4 3.2 3.0 2.8 2.6 2.4 2.2 2.0 1.8 1.6 1.4 1.2 1.0 0.8 0.6 0.4 0.2 0.0
distance (km)
velocity
mean velocity all transect 1

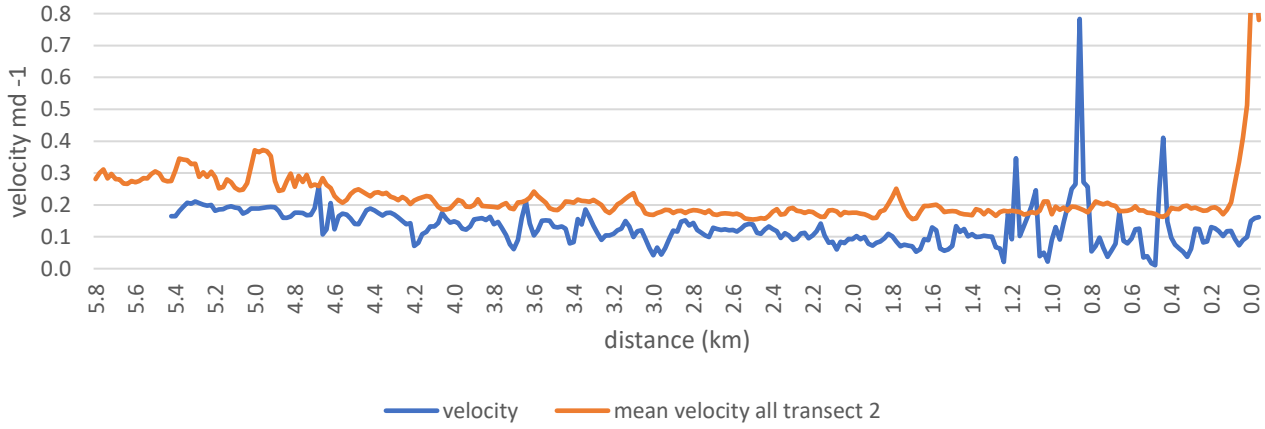
velocity md -1
0.8
0.7
0.6
0.5
0.4
0.3
0.2
0.1
0.0
5.8 5.6 5.4 5.2 5.0 4.8 4.6 4.4 4.2 4.0 3.8 3.6 3.4 3.2 3.0 2.8 2.6 2.4 2.2 2.0 1.8 1.6 1.4 1.2 1.0 0.8 0.6 0.4 0.2 0.0
distance (km)
velocity
mean velocity all transect 2

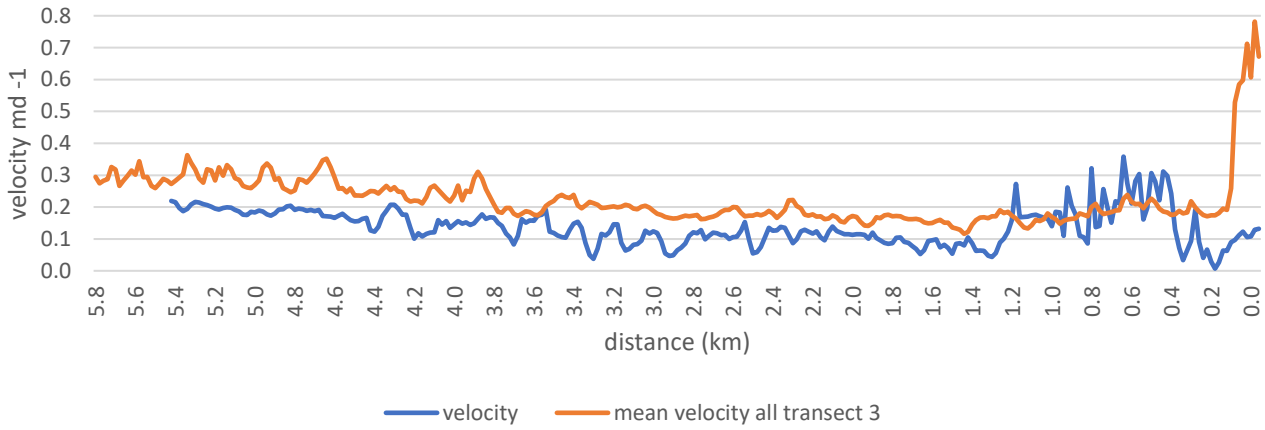
velocity md -1
0.8
0.7
0.6
0.5
0.4
0.3
0.2
0.1
0.0
5.8 5.6 5.4 5.2 5.0 4.8 4.6 4.4 4.2 4.0 3.8 3.6 3.4 3.2 3.0 2.8 2.6 2.4 2.2 2.0 1.8 1.6 1.4 1.2 1.0 0.8 0.6 0.4 0.2 0.0
distance (km)
velocity
mean velocity all transect 3

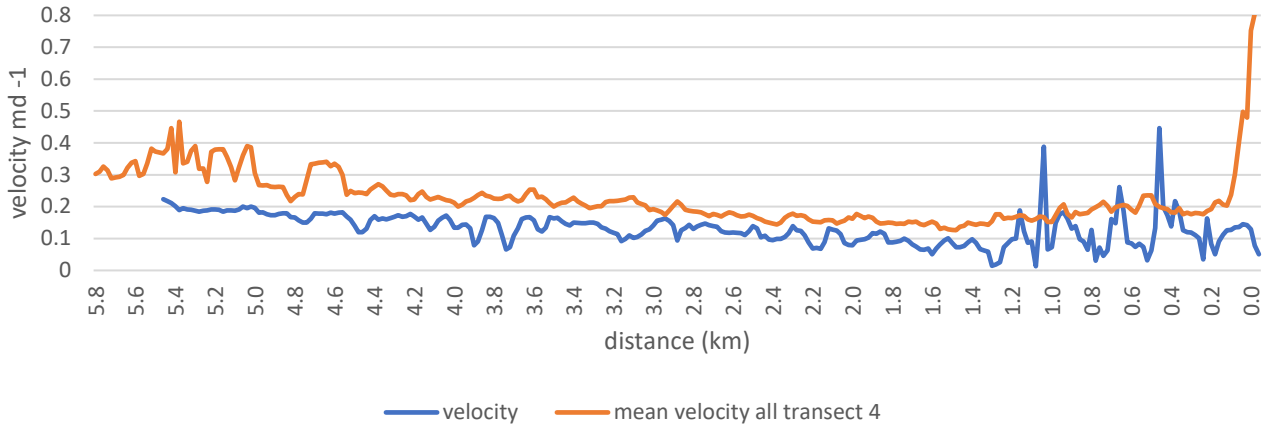

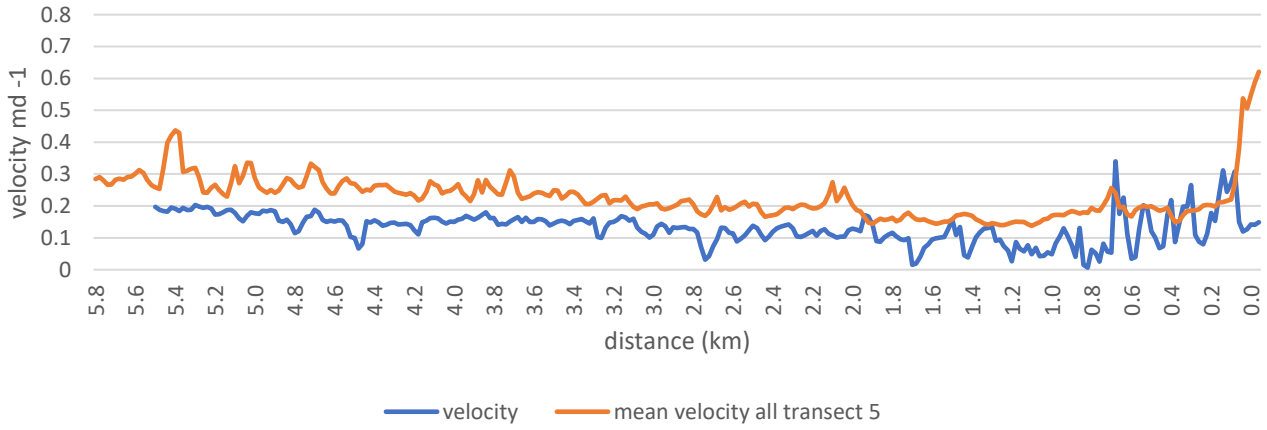

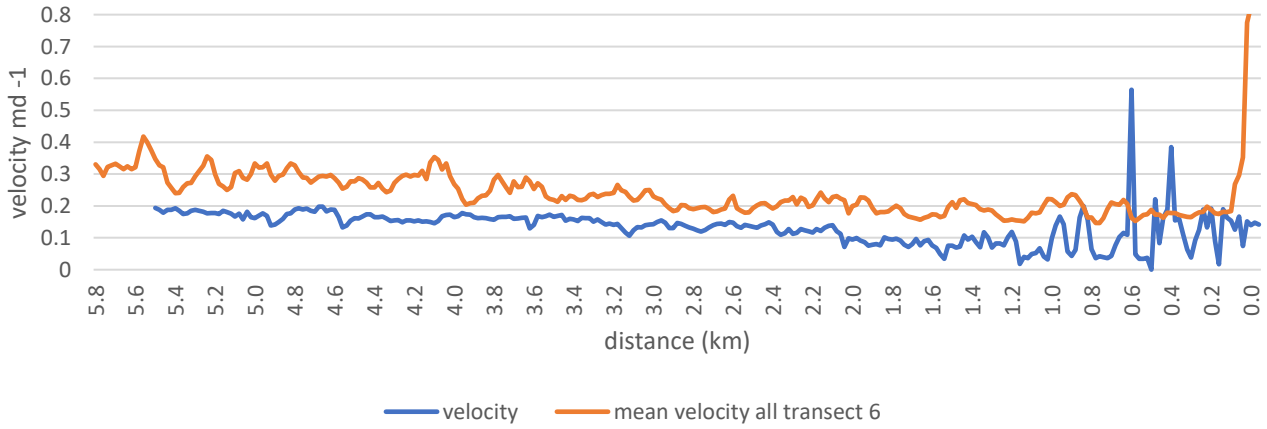

Appendix 2B: Longitudinal velocity profiles from 06/07/2017 – 15/08/2017 (time period of 30 days) The orange line indicates the surface velocity values extracted from all surface velocity images. The blue line is the surface velocity values extracted from each profile. Profiles run from A near the Ball Glacier confluence down to B at the terminus.

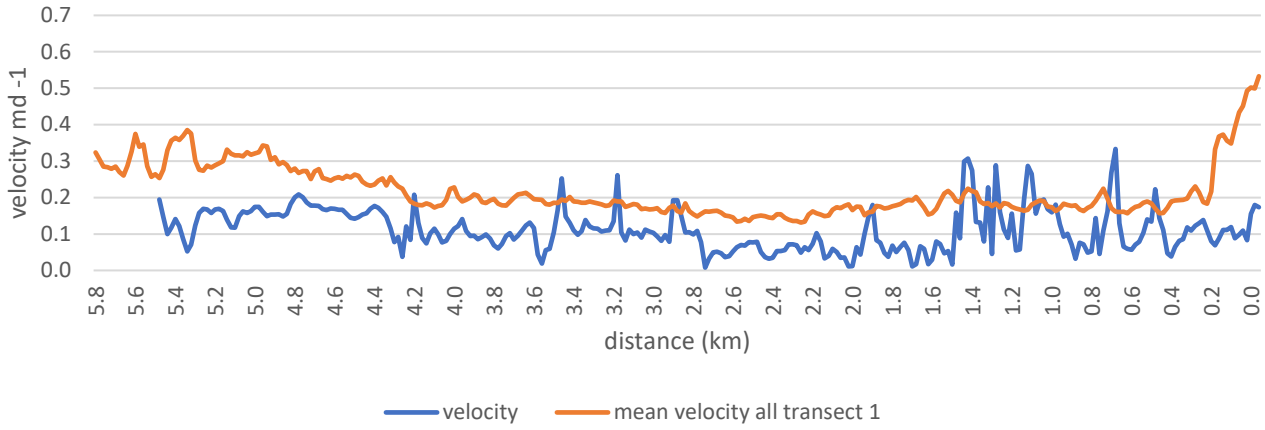
velocity md -1
0.7
0.6
0.5
0.4
0.3
0.2
0.1
0.0
5.8 5.6 5.4 5.2 5.0 4.8 4.6 4.4 4.2 4.0 3.8 3.6 3.4 3.2 3.0 2.8 2.6 2.4 2.2 2.0 1.8 1.6 1.4 1.2 1.0 0.8 0.6 0.4 0.2 0.0
distance (km)
velocity
mean velocity all transect 1

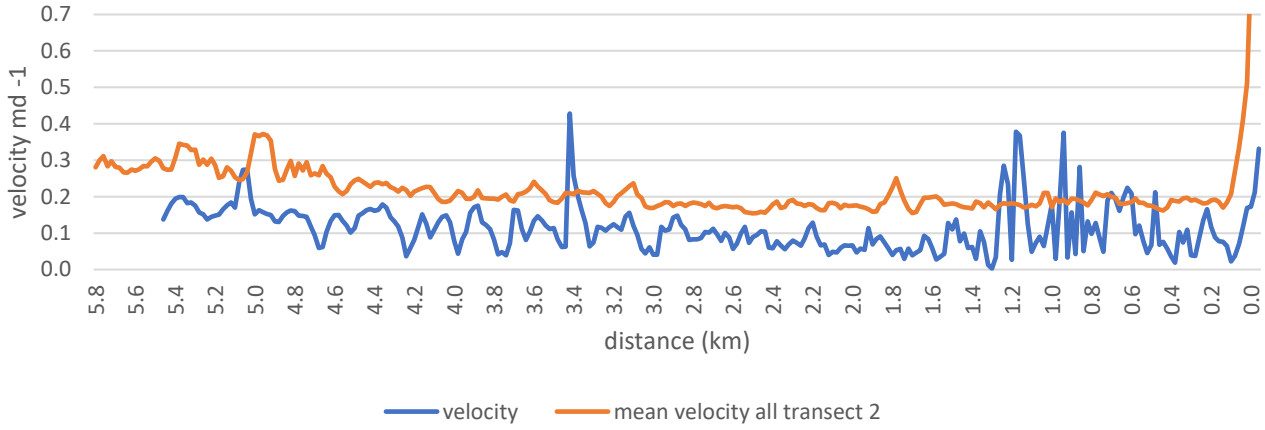
velocity md -1
0.7
0.6
0.5
0.4
0.3
0.2
0.1
0.0
5.8 5.6 5.4 5.2 5.0 4.8 4.6 4.4 4.2 4.0 3.8 3.6 3.4 3.2 3.0 2.8 2.6 2.4 2.2 2.0 1.8 1.6 1.4 1.2 1.0 0.8 0.6 0.4 0.2 0.0
distance (km)
velocity
mean velocity all transect 2

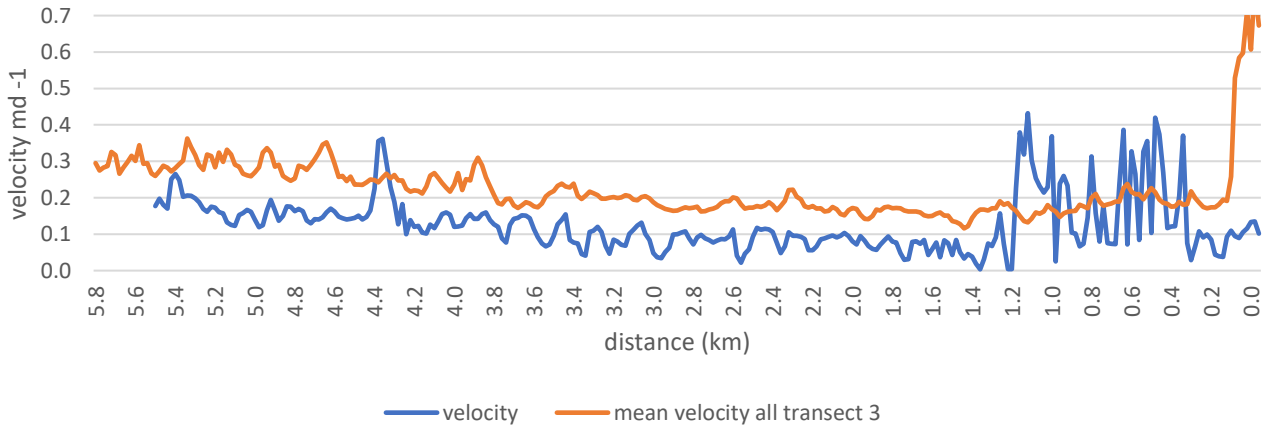
velocity md -1
0.7
0.6
0.5
0.4
0.3
0.2
0.1
0.0
5.8 5.6 5.4 5.2 5.0 4.8 4.6 4.4 4.2 4.0 3.8 3.6 3.4 3.2 3.0 2.8 2.6 2.4 2.2 2.0 1.8 1.6 1.4 1.2 1.0 0.8 0.6 0.4 0.2 0.0
distance (km)
velocity
mean velocity all transect 3

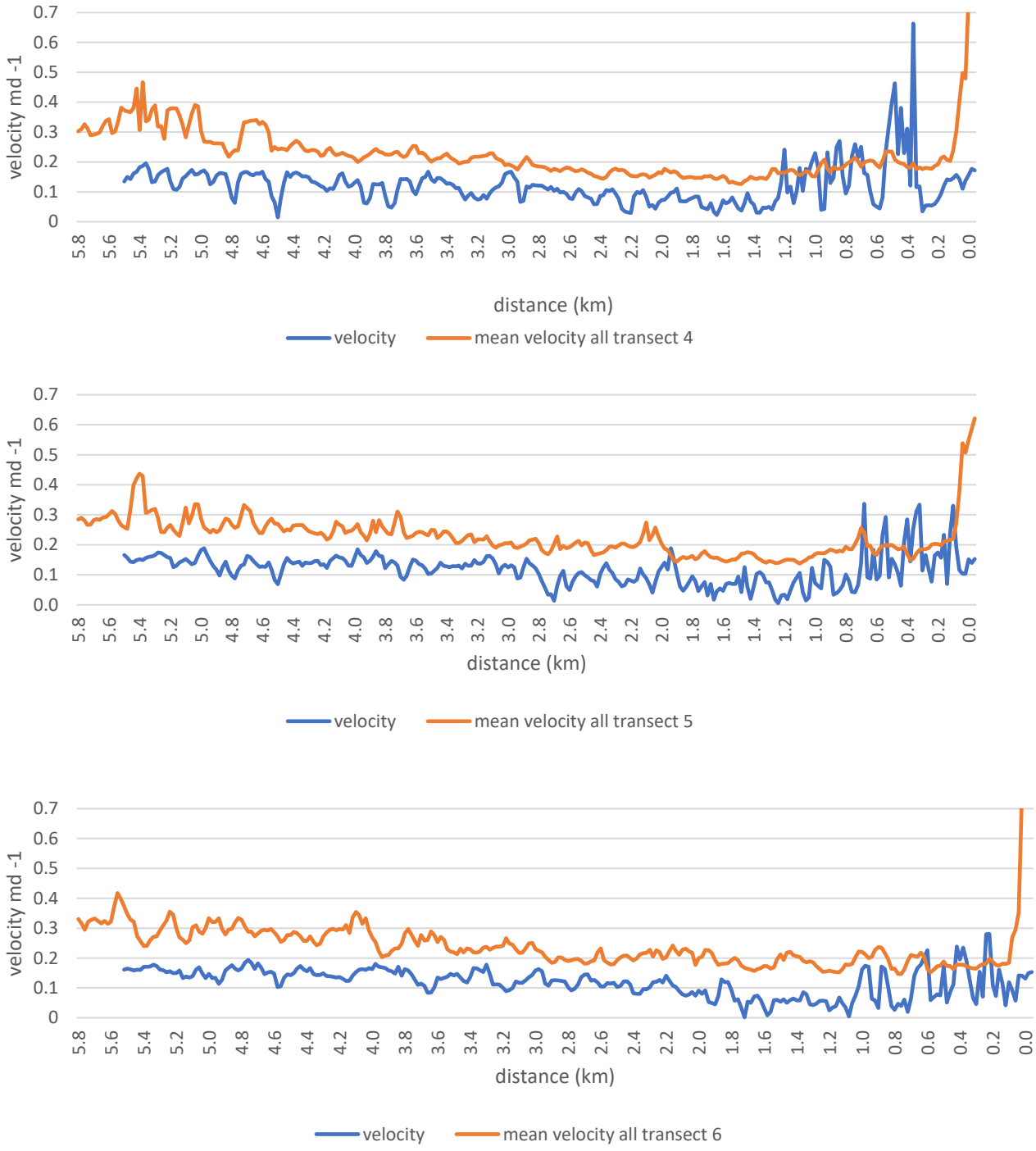

Appendix 3B: Longitudinal velocity profiles from 16/07/2017 – 15/08/2017 (time period of 30 days) The orange line indicates the surface velocity values extracted from all surface velocity images. The blue line is the surface velocity values extracted from each profile. Profiles run from A near the Ball Glacier confluence down to B at the terminus.

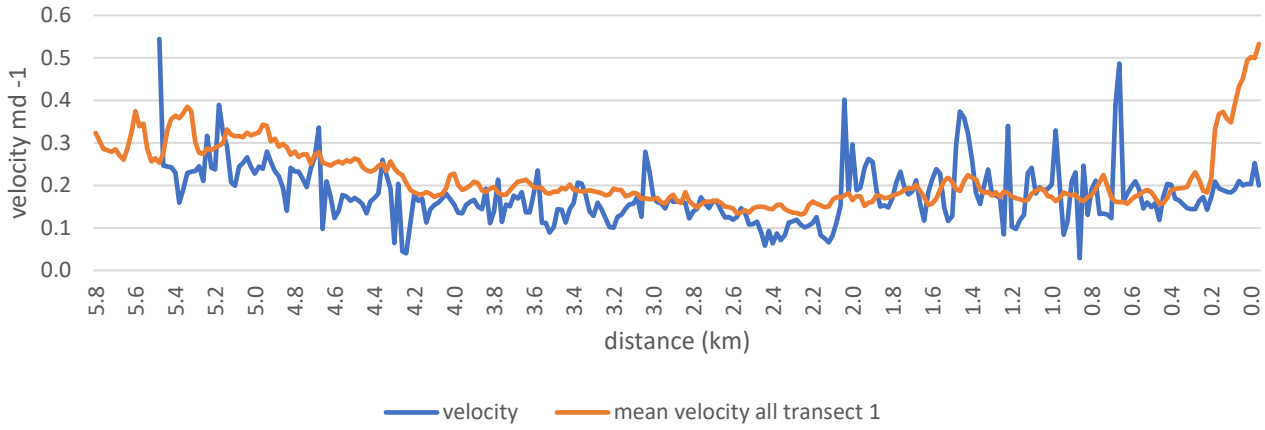
velocity md -1
0.6
0.5
0.4
0.3
0.2
0.1
0.0
5.8 5.6 5.4 5.2 5.0 4.8 4.6 4.4 4.2 4.0 3.8 3.6 3.4 3.2 3.0 2.8 2.6 2.4 2.2 2.0 1.8 1.6 1.4 1.2 1.0 0.8 0.6 0.4 0.2 0.0
distance (km)
velocity
mean velocity all transect 1

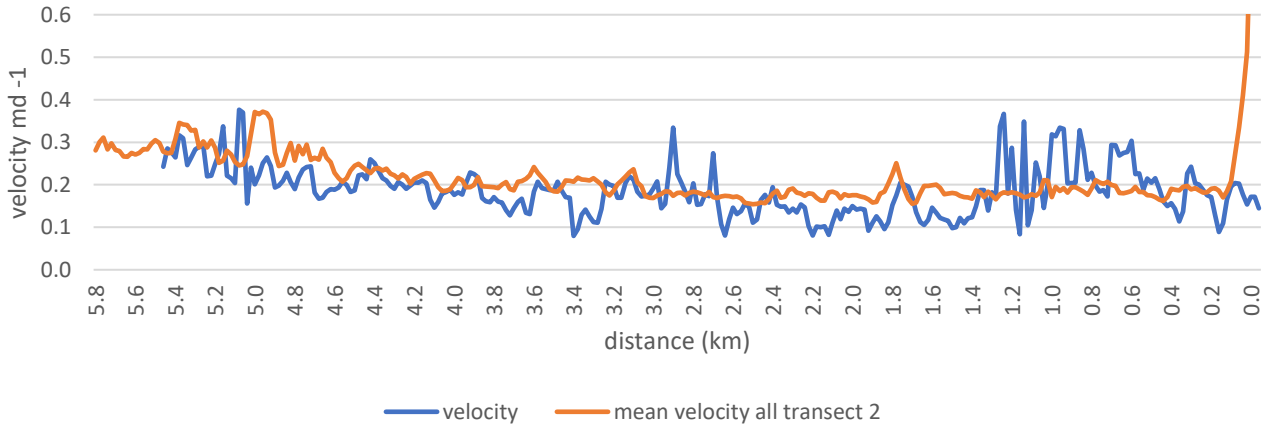
velocity md -1
0.6
0.5
0.4
0.3
0.2
0.1
0.0
5.8 5.6 5.4 5.2 5.0 4.8 4.6 4.4 4.2 4.0 3.8 3.6 3.4 3.2 3.0 2.8 2.6 2.4 2.2 2.0 1.8 1.6 1.4 1.2 1.0 0.8 0.6 0.4 0.2 0.0
distance (km)
velocity
mean velocity all transect 2

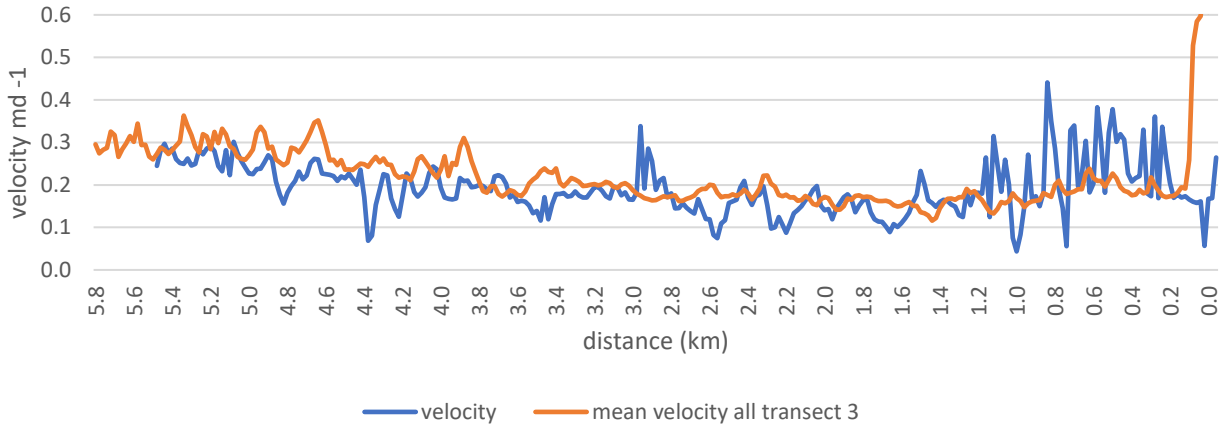
velocity md -1
0.6
0.5
0.4
0.3
0.2
0.1
0.0
5.8 5.6 5.4 5.2 5.0 4.8 4.6 4.4 4.2 4.0 3.8 3.6 3.4 3.2 3.0 2.8 2.6 2.4 2.2 2.0 1.8 1.6 1.4 1.2 1.0 0.8 0.6 0.4 0.2 0.0
distance (km)
velocity
mean velocity all transect 3

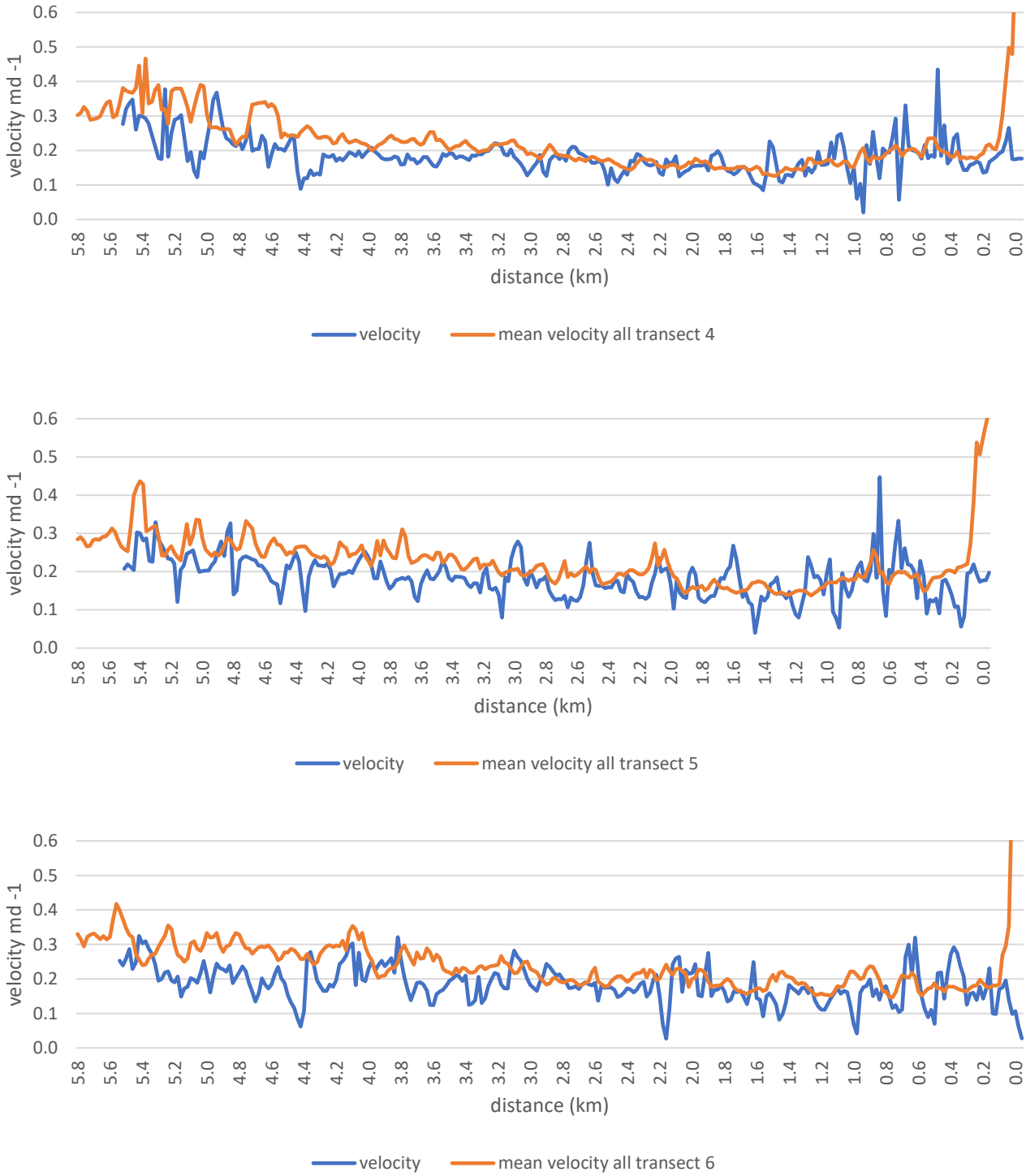

Appendix 4B: Longitudinal velocity profiles from 15/08/2017 – 04/10/2017 (time period of 30 days) The orange line indicates the surface velocity values extracted from all surface velocity images. The blue line is the surface velocity values extracted from each profile. Profiles run from A near the Ball Glacier confluence down to B at the terminus.

Appendix C: Gridded velocity surface

Seasonal surface velocity was determined for the region of the glacier below the Hochstetter confluence for 35 surface velocity images. The below images show how the surface velocity varies across time throughout the study period from 2016 – 2018.

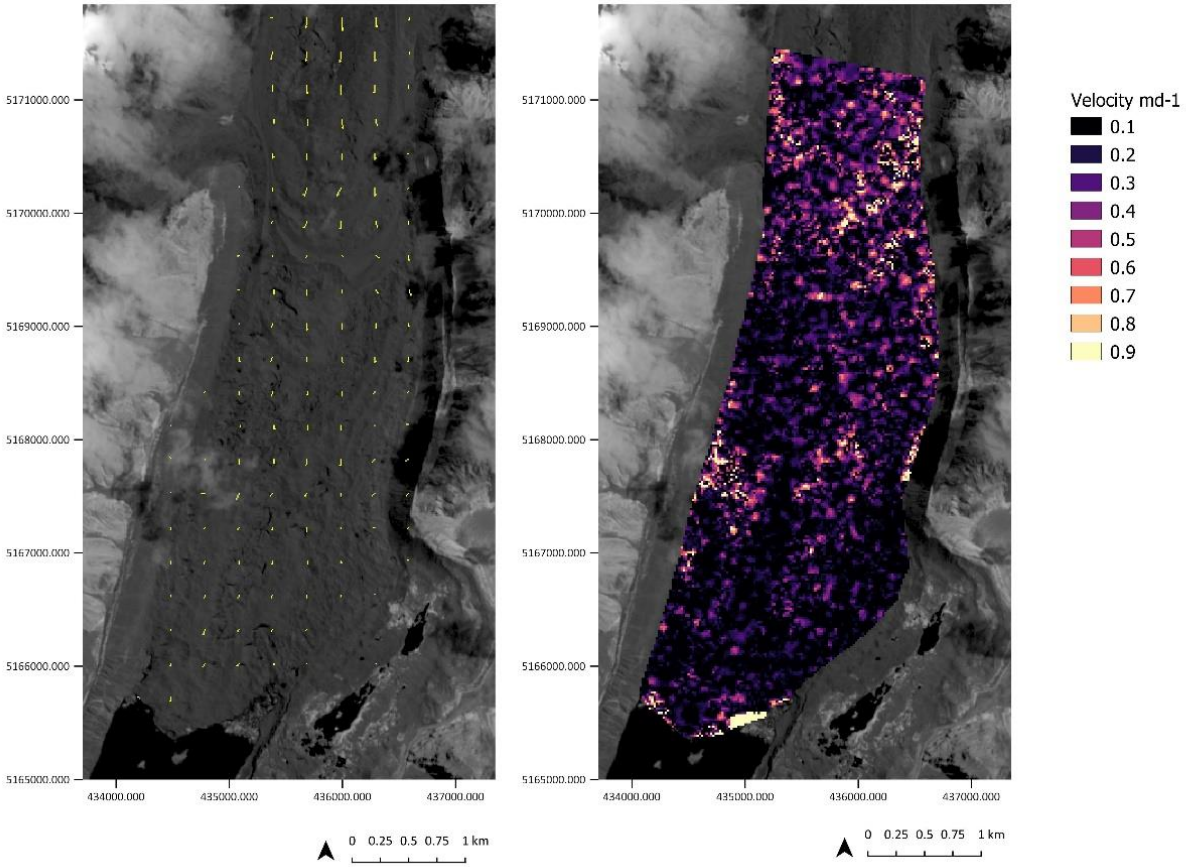

Appendix 1C Surface velocity during summer over a 10-day time interval from 24/12/2015 – 03/01/2016, left image shows the vector arrows showing the direction of displacement. Right images shows the surface velocity in md^{-1}.

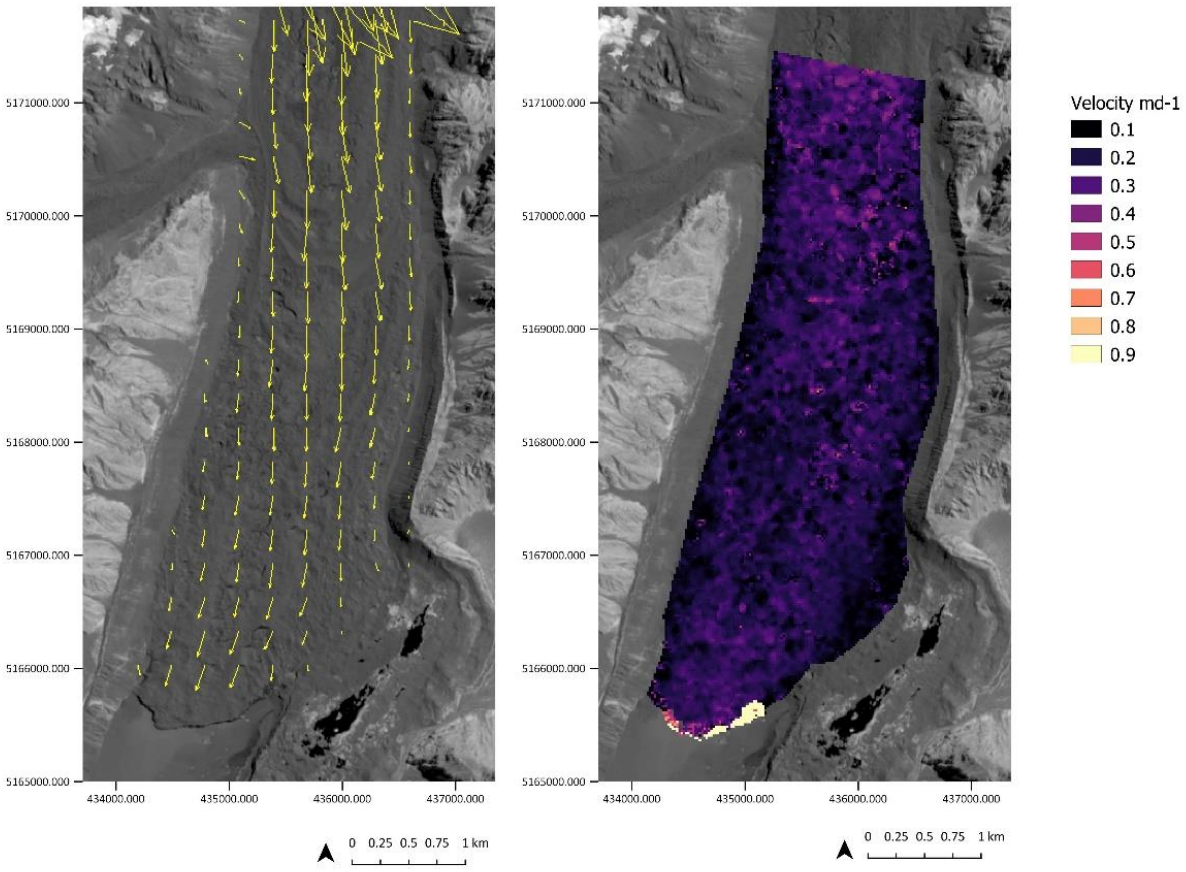

Appendix 2C Surface velocity during summer over a 40-day time interval from 24/12/2015 – 02/02/2016, left image shows the vector arrows showing the direction of displacement. Right images shows the surface velocity in md^{-1}.

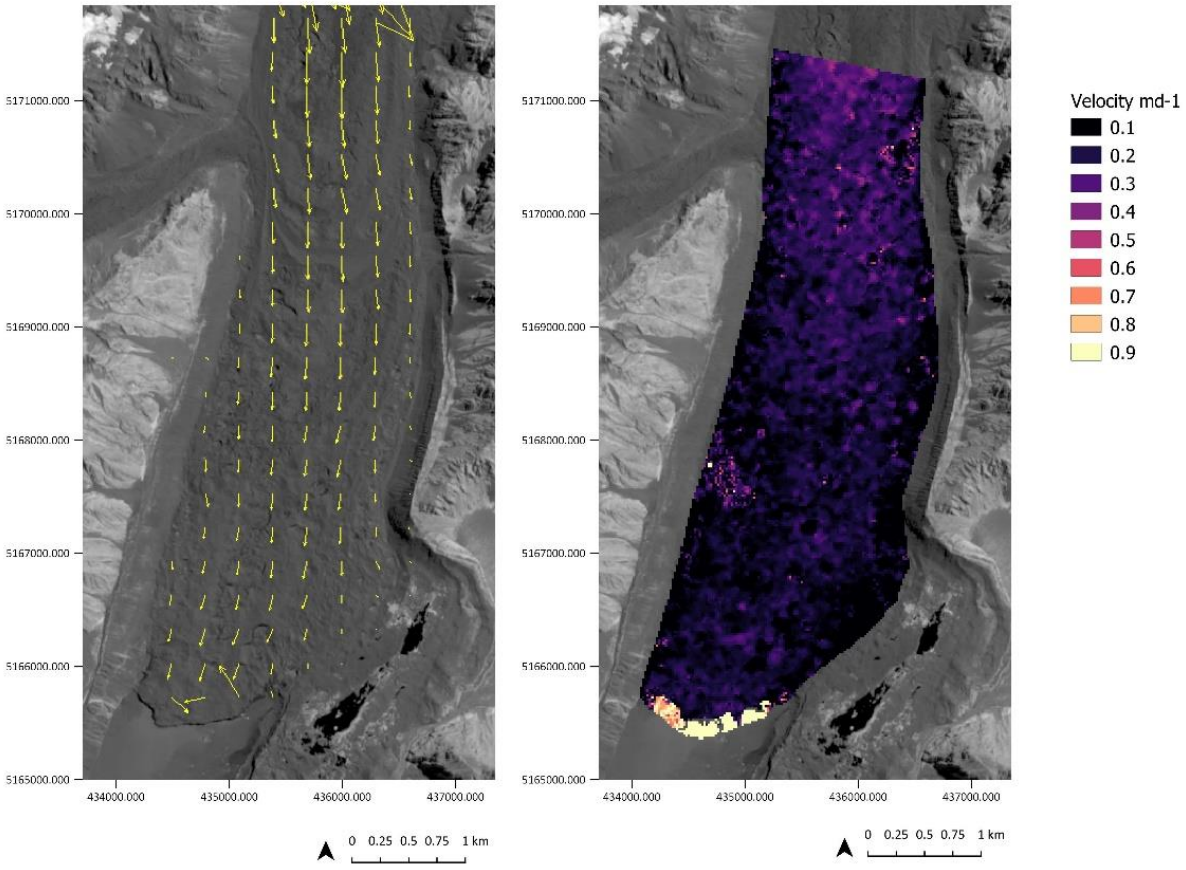

Appendix 3C Surface velocity during summer over a 40-day time interval from 03/01/2016–02/02/2016, left image shows the vector arrows showing the direction of displacement. Right images shows the surface velocity in md^{-1}.

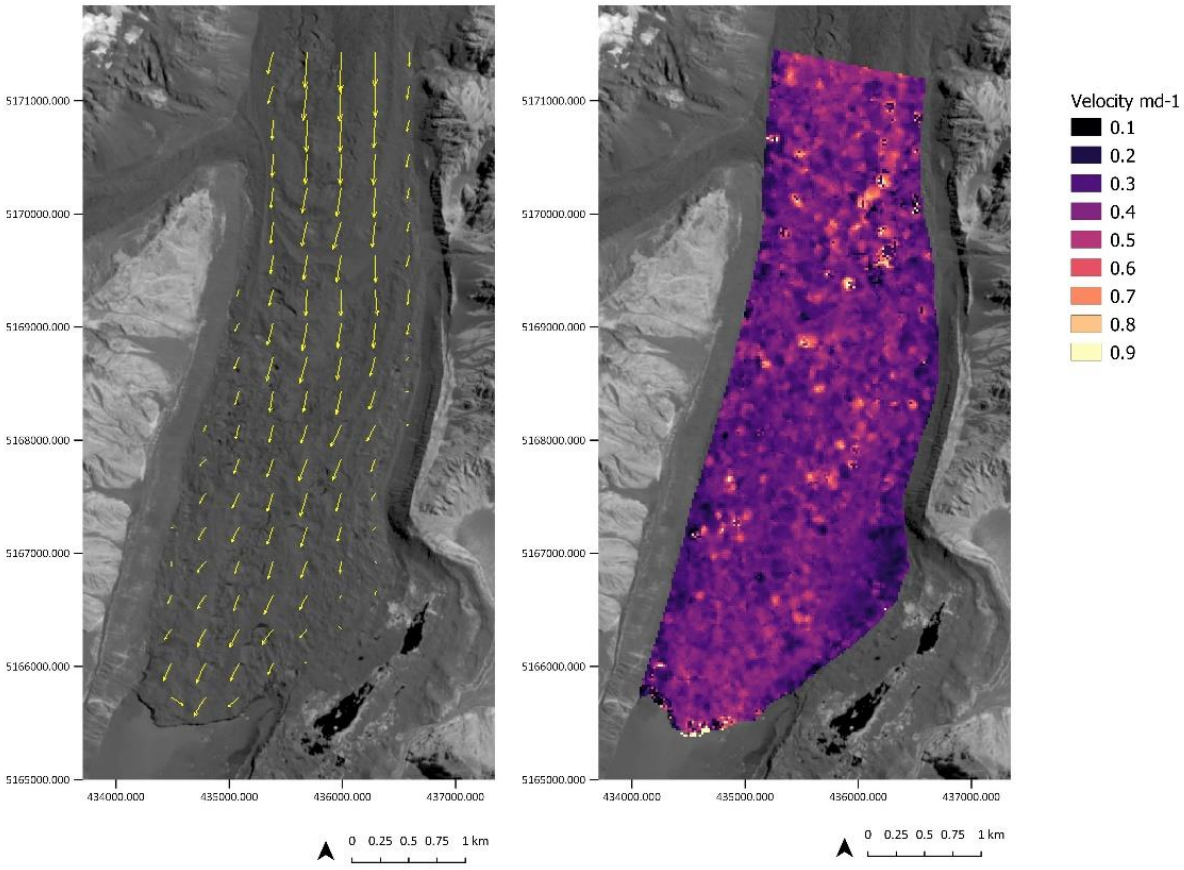

Appendix 4C Surface velocity during summer over a 20-day time interval from 13/01/2016–02/02/2016, left image shows the vector arrows showing the direction of displacement. Right images shows the surface velocity in md^{-1}.

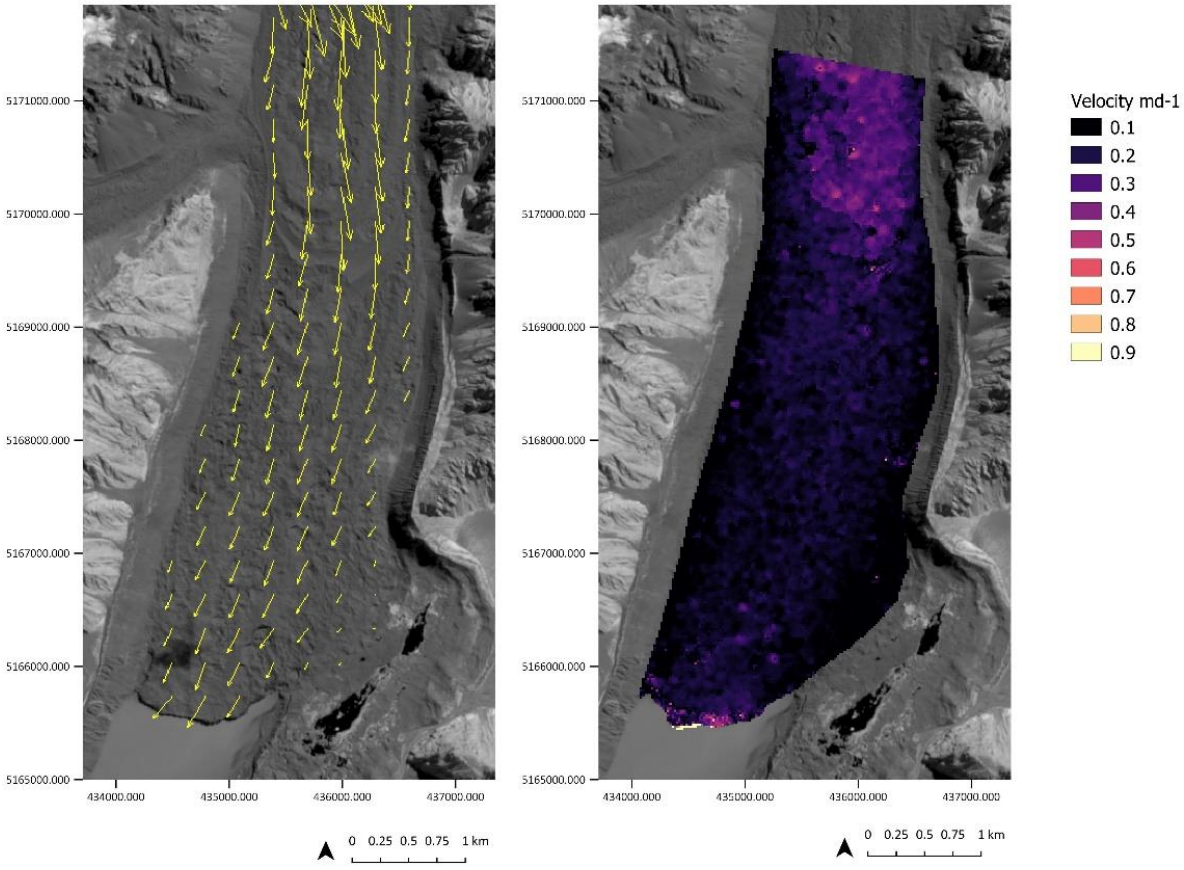

Appendix 5C Surface velocity during summer over a 40-day time interval from 02/02/2016–13/03/2016, left image shows the vector arrows showing the direction of displacement. Right images shows the surface velocity in md^{-1}.

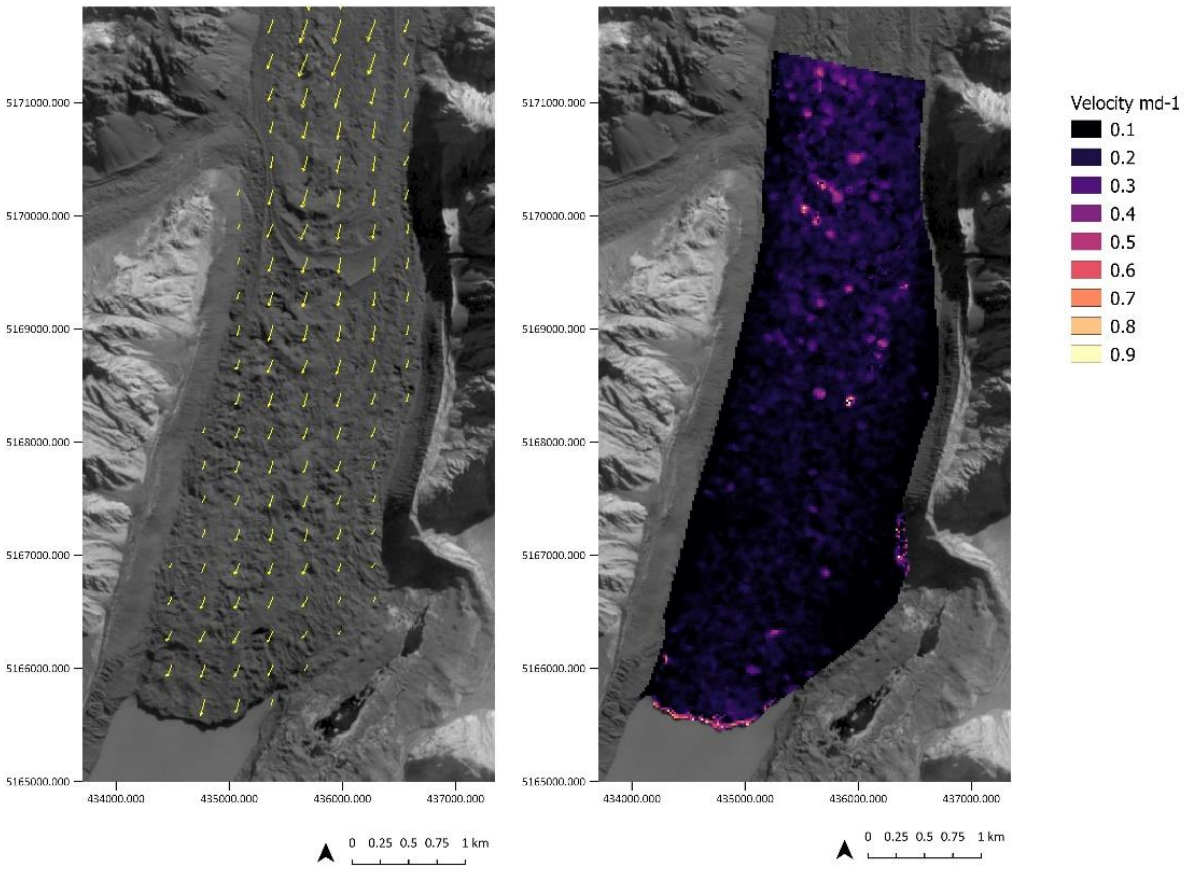

Appendix 6C Surface velocity during summer over a 20-day time interval from 12/04/2016–02/05/2016, left image shows the vector arrows showing the direction of displacement. Right images shows the surface velocity in md^{-1}.

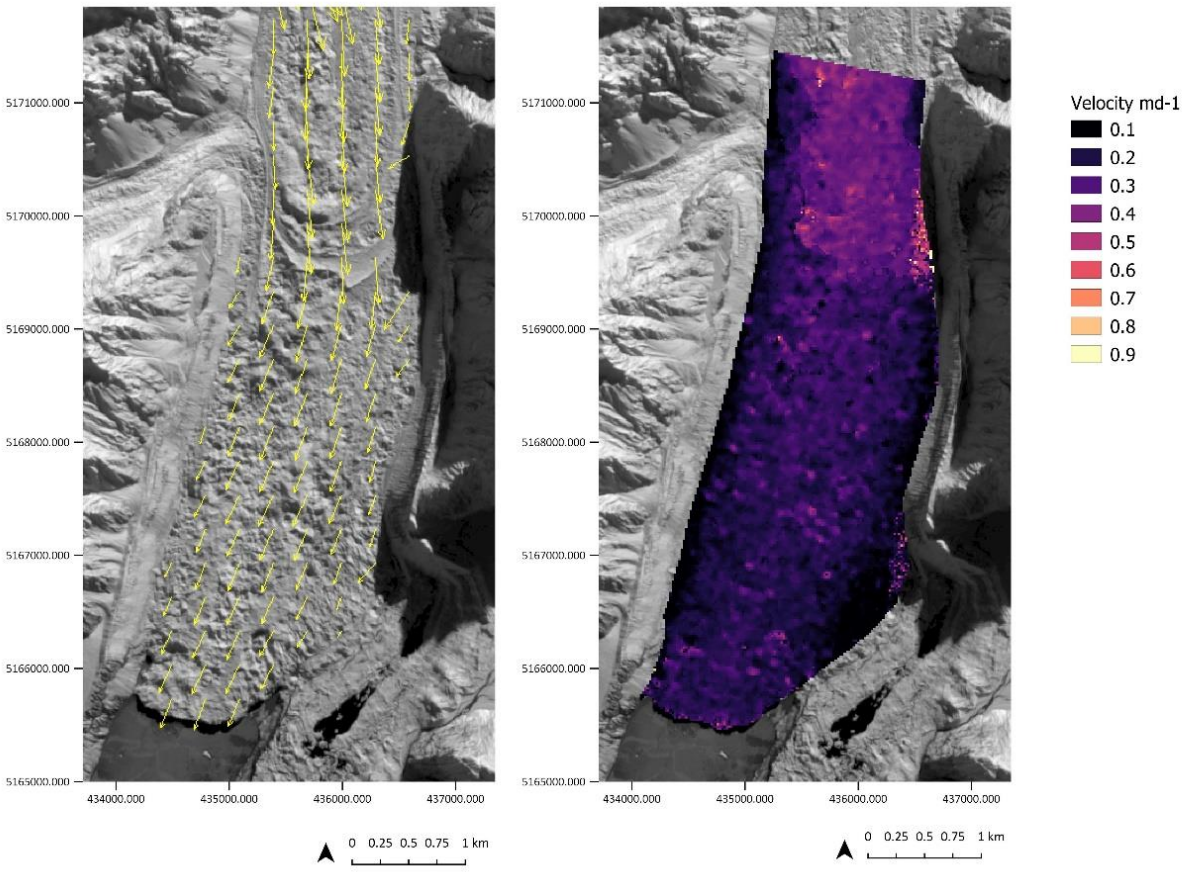

Appendix 7C Surface velocity during summer over a 30-day time interval from 02/05/2016–01/06/2016, left image shows the vector arrows showing the direction of displacement. Right images shows the surface velocity in md^{-1}.

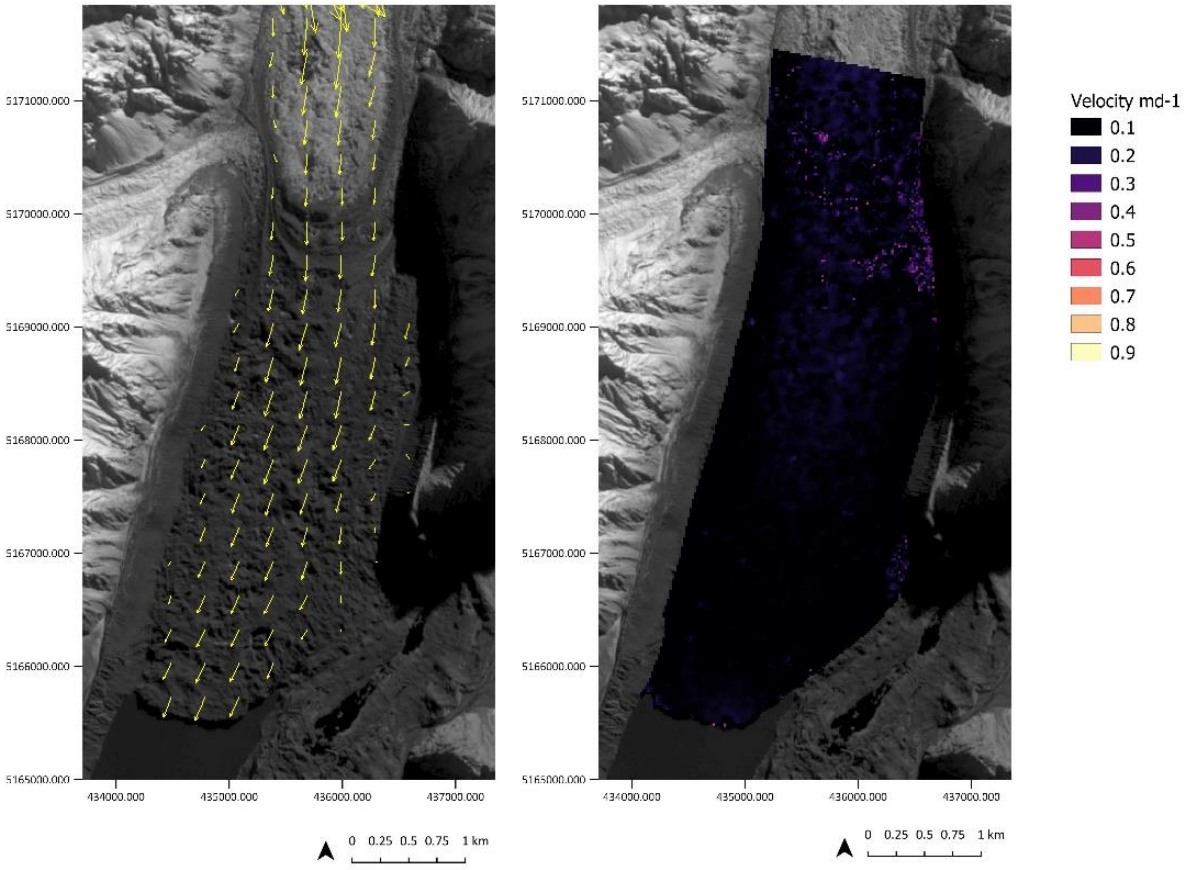

Appendix 8C Surface velocity during summer over a 50-day time interval from 01/06/2016–21/07/2016, left image shows the vector arrows showing the direction of displacement. Right images shows the surface velocity in md^{-1}.

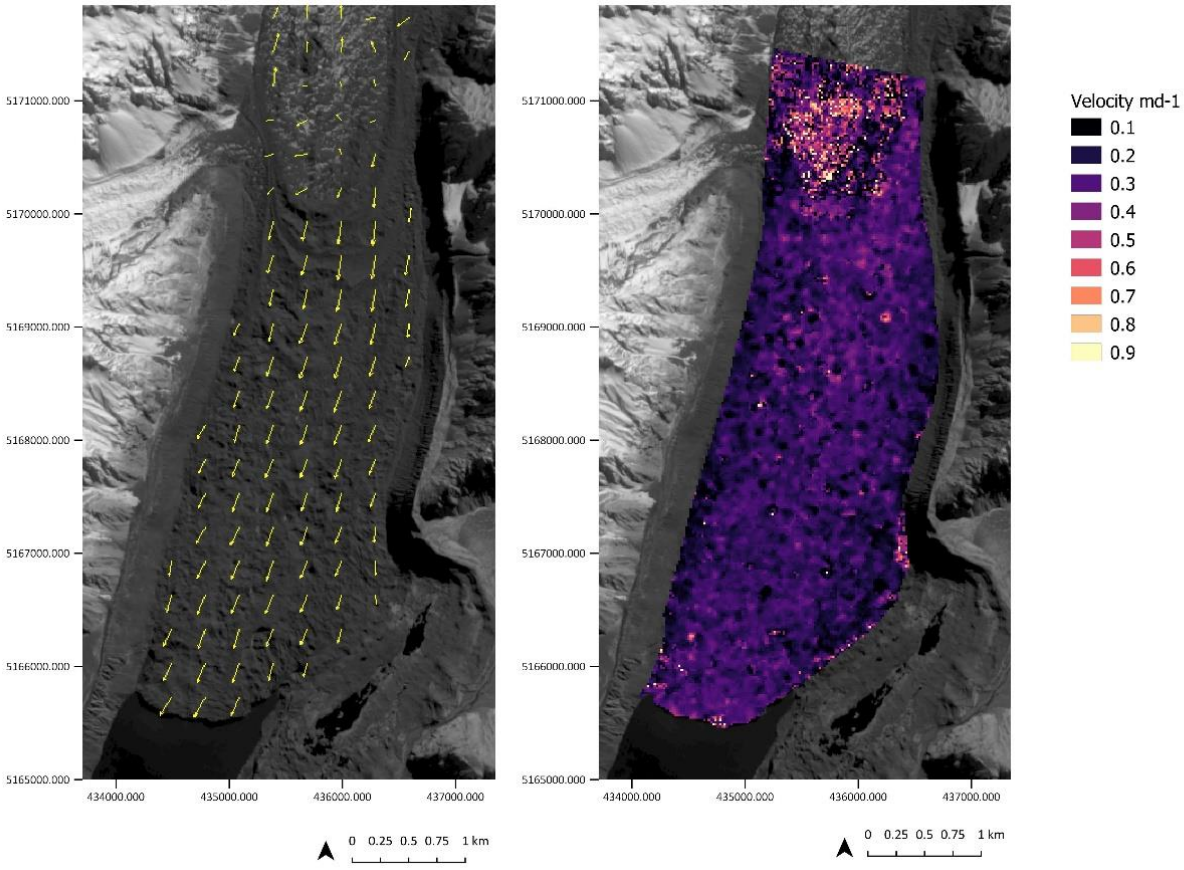

Appendix 9C Surface velocity during summer over a 20-day time interval from 10/08/2016–30/08/2016, left image shows the vector arrows showing the direction of displacement. Right images shows the surface velocity in md^{-1}.

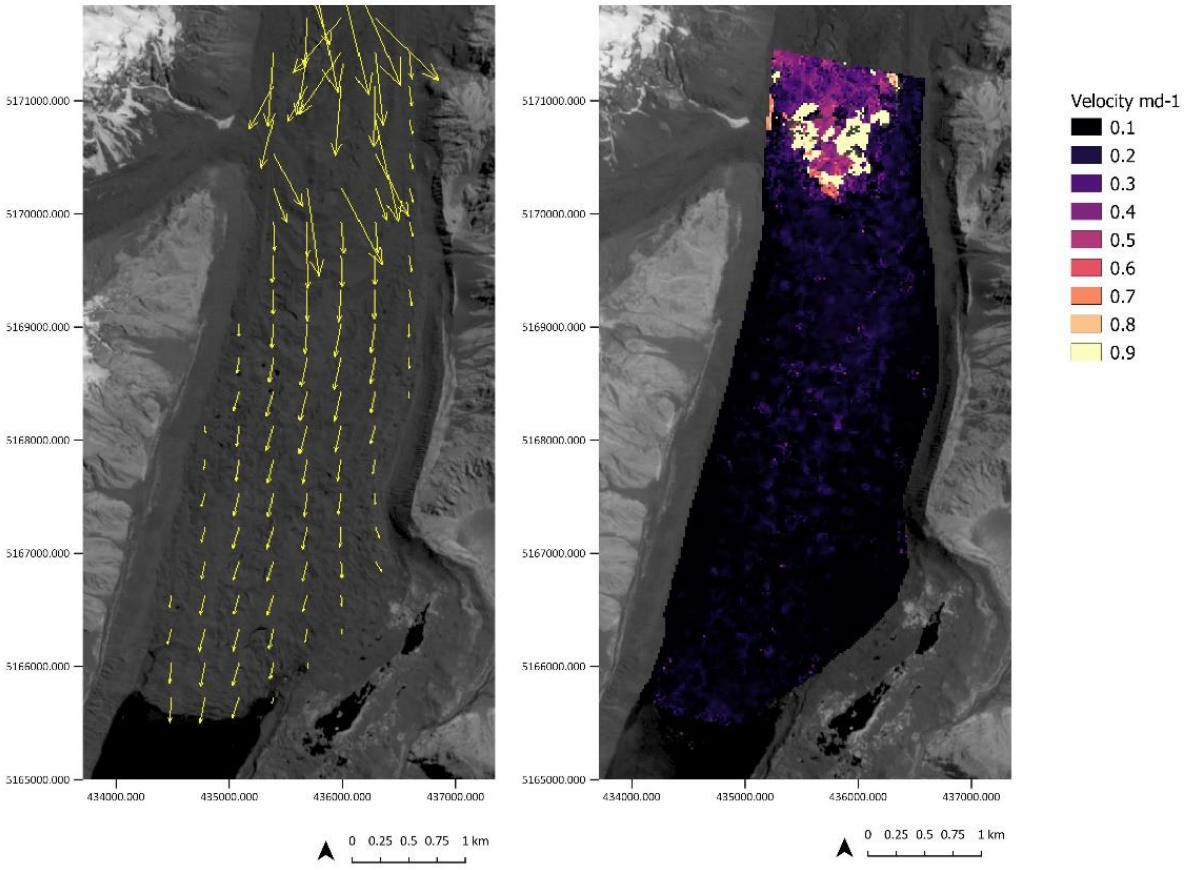

Appendix 10C Surface velocity during summer over a 60-day time interval from 30/08/2016–29/10/2016, left image shows the vector arrows showing the direction of displacement. Right images shows the surface velocity in md^{-1}.

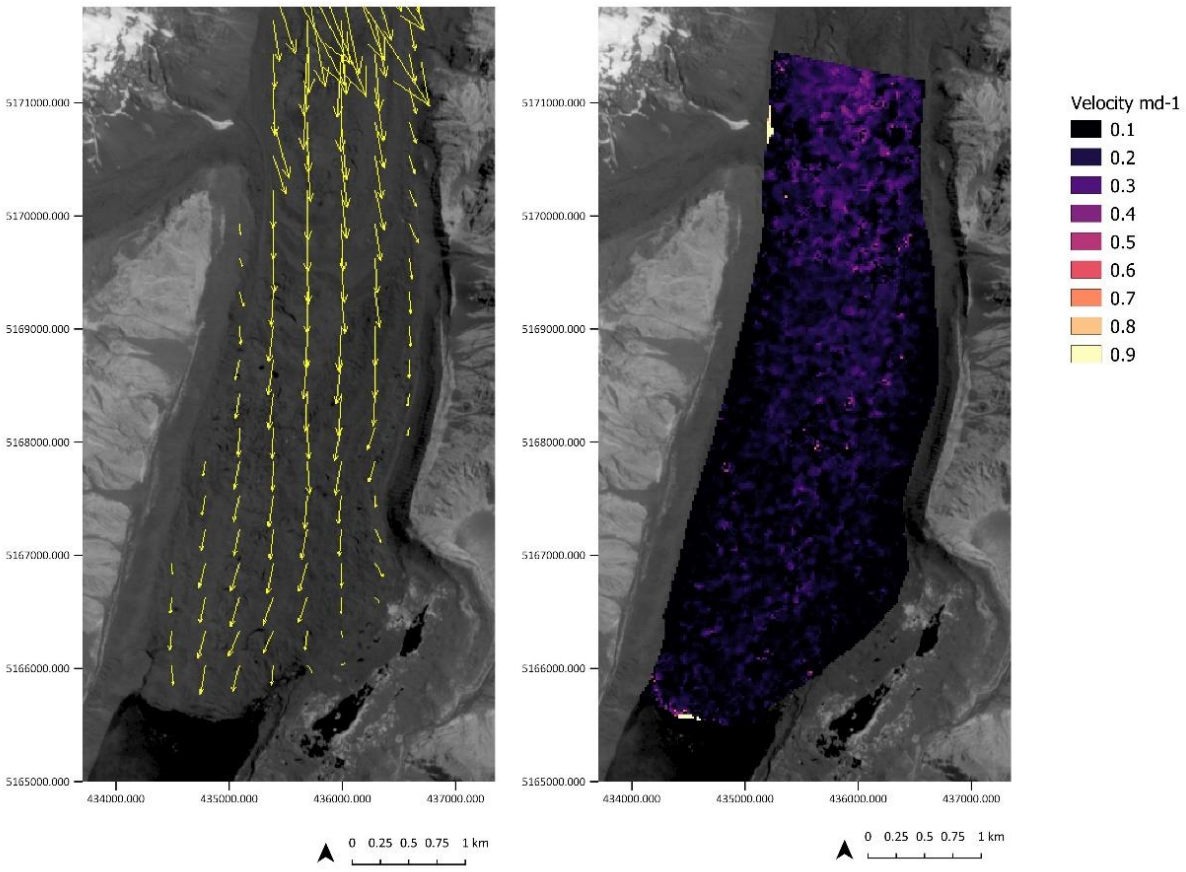

Appendix 11C Surface velocity during summer over a 40-day time interval from 29/10/2016–08/12/2016, left image shows the vector arrows showing the direction of displacement. Right images shows the surface velocity in md^{-1}.

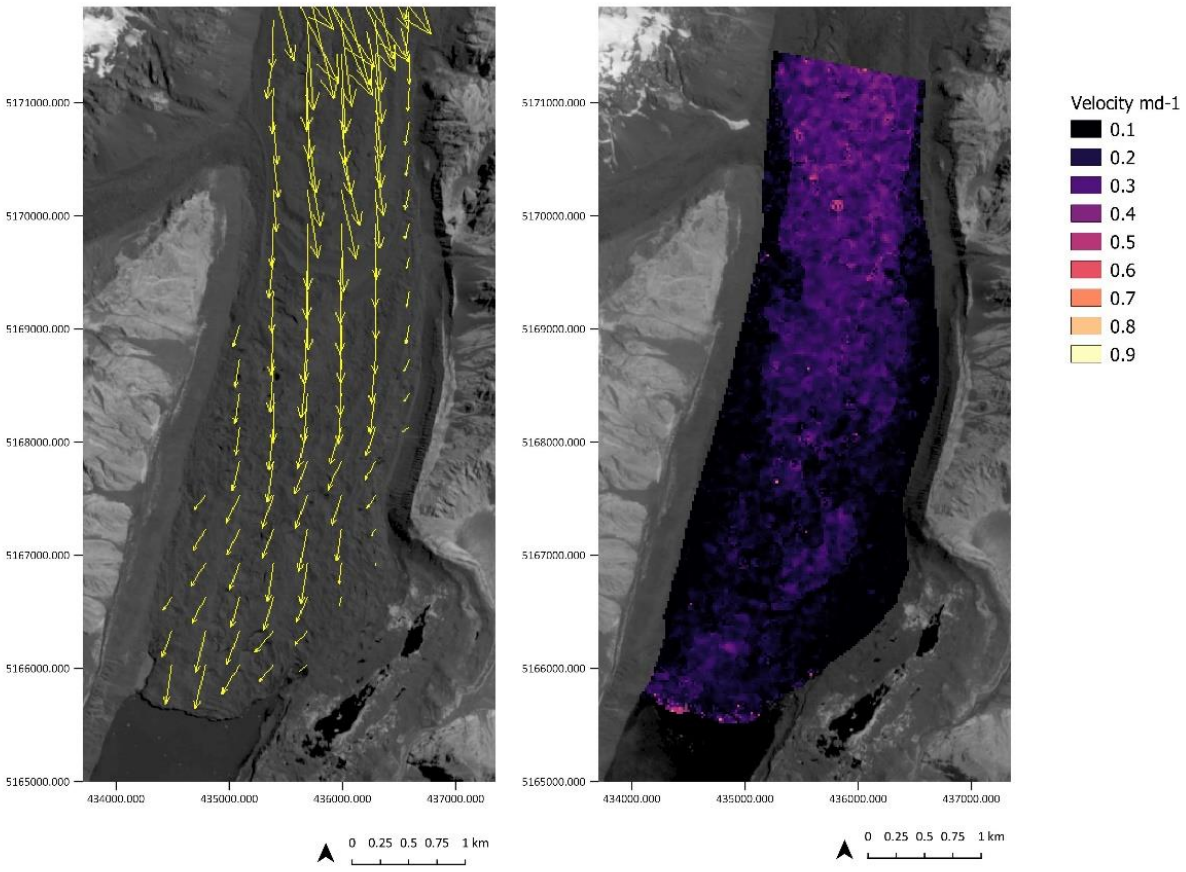

Appendix 12C Surface velocity during summer over a 40-day time interval from 08/12/2016–27/07/2017, left image shows the vector arrows showing the direction of displacement. Right images shows the surface velocity in md^{-1}.

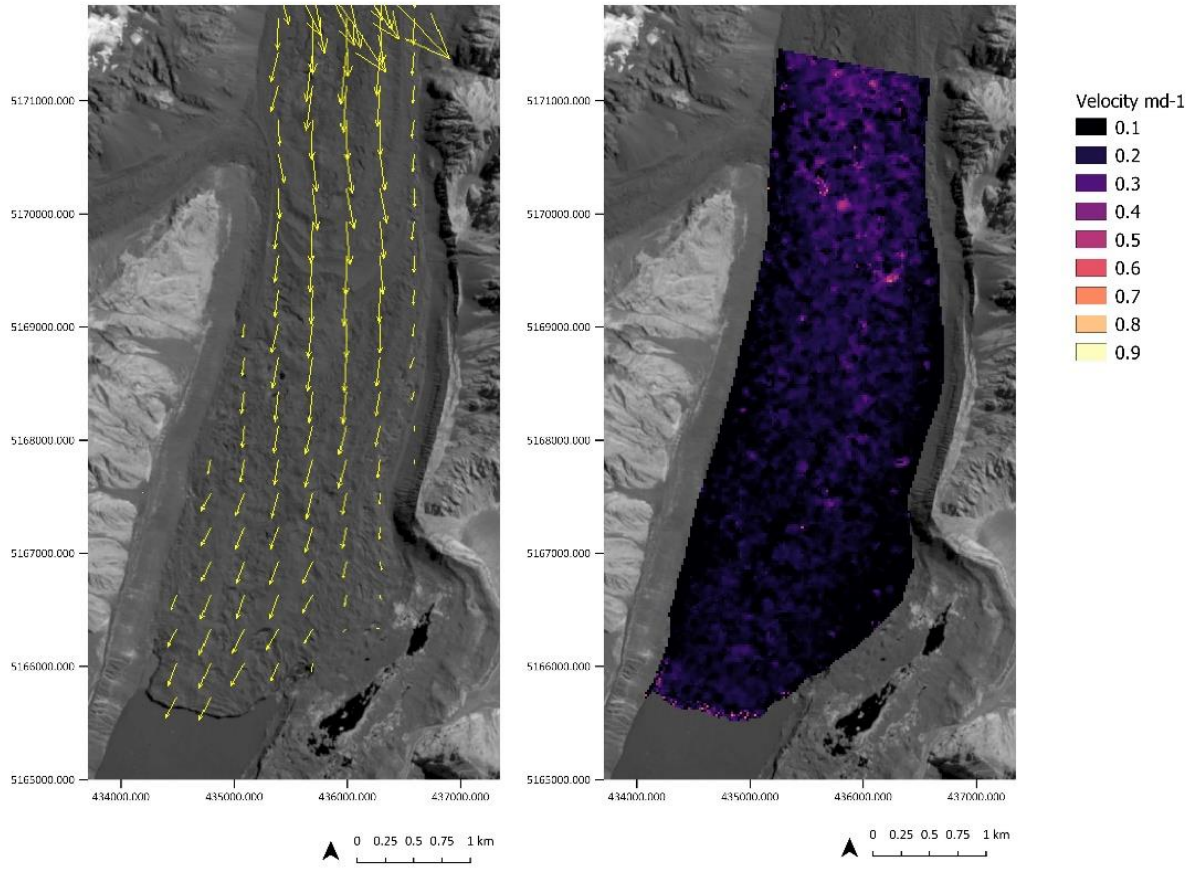

Appendix 13C Surface velocity during summer over a 30-day time interval from 27/01/2016–26/02/2017, left image shows the vector arrows showing the direction of displacement. Right images shows the surface velocity in md^{-1}.

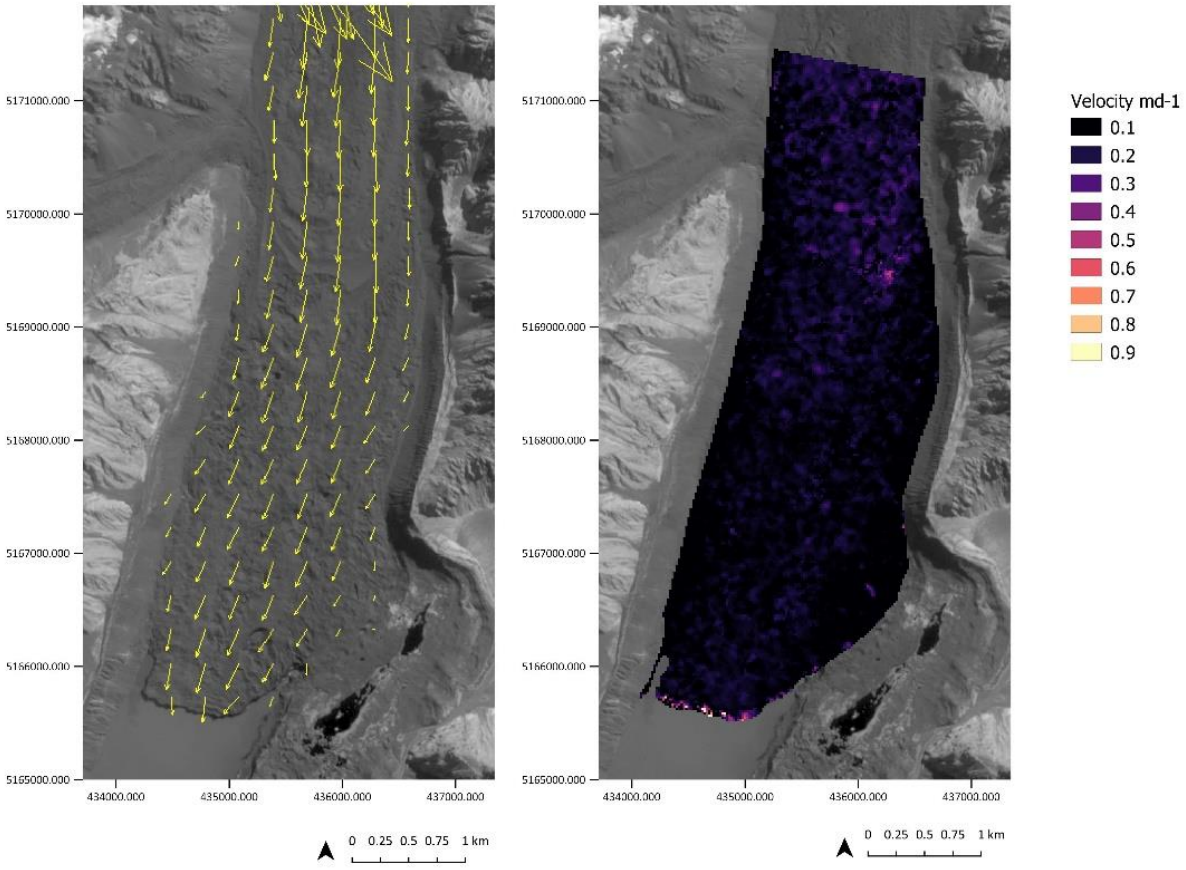

Appendix 14C Surface velocity during summer over a 20-day time interval from 26/06/2017–18/03/2017, left image shows the vector arrows showing the direction of displacement. Right images shows the surface velocity in md^{-1}.

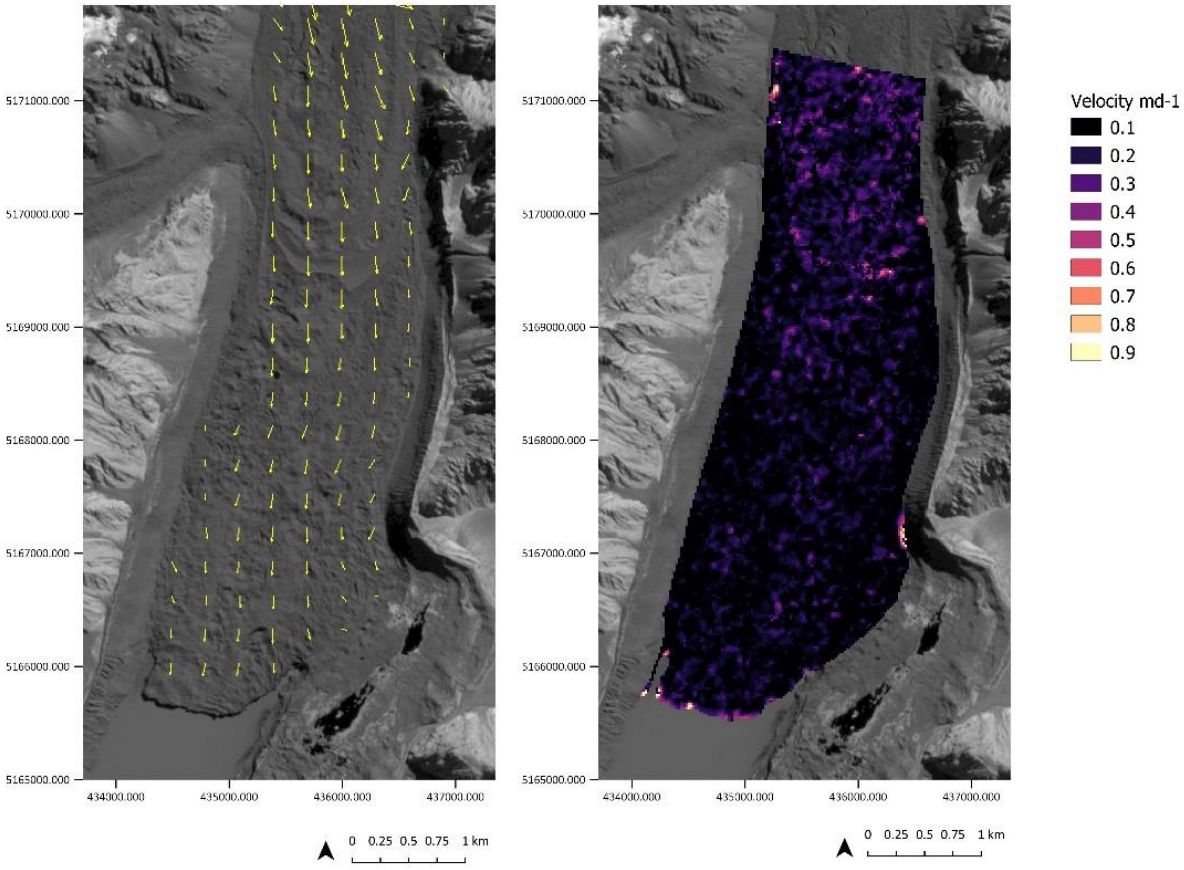

Appendix 15C Surface velocity during summer over a 10-day time interval from 18/03/2017–28/03/2017, left image shows the vector arrows showing the direction of displacement. Right images shows the surface velocity in md^{-1}.

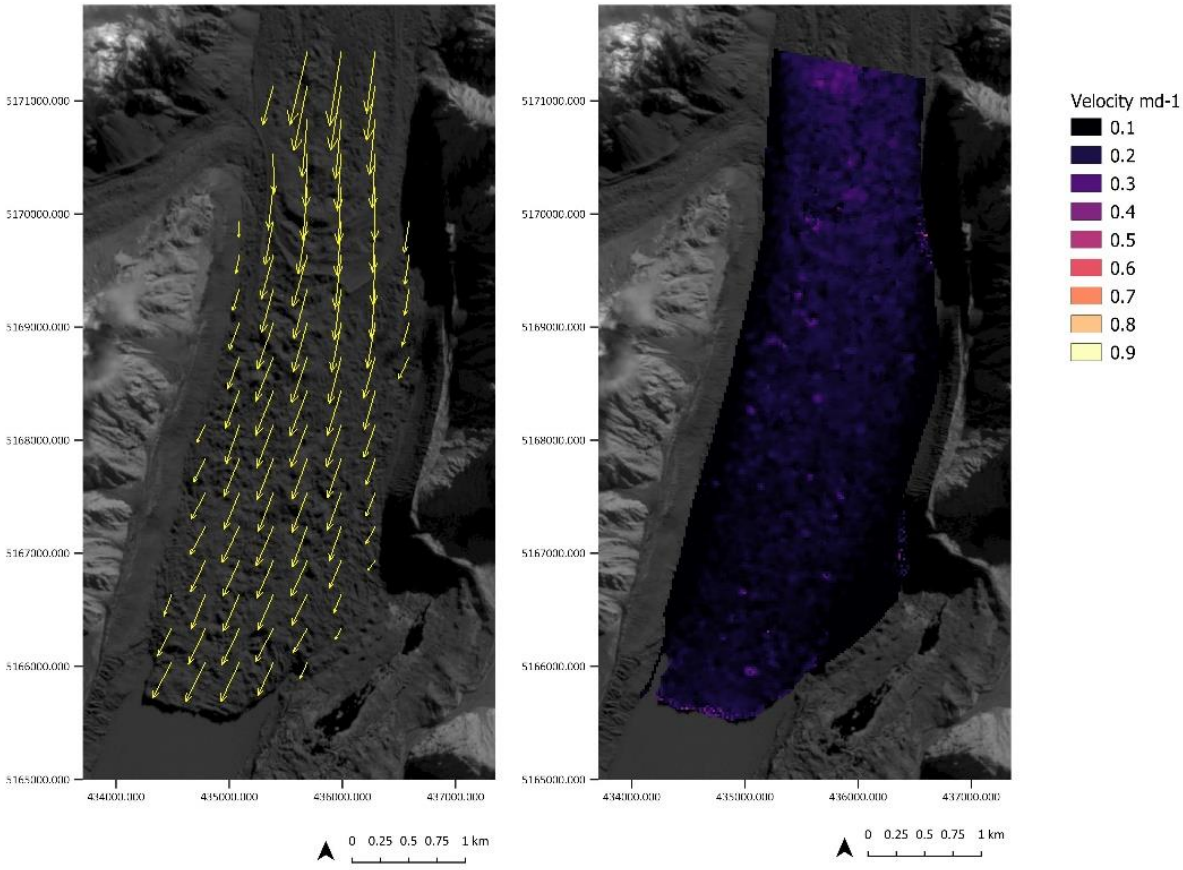

Appendix 16C Surface velocity during summer over a 50-day time interval from 28/03/2017–17/05/2017, left image shows the vector arrows showing the direction of displacement. Right images shows the surface velocity in md^{-1}.

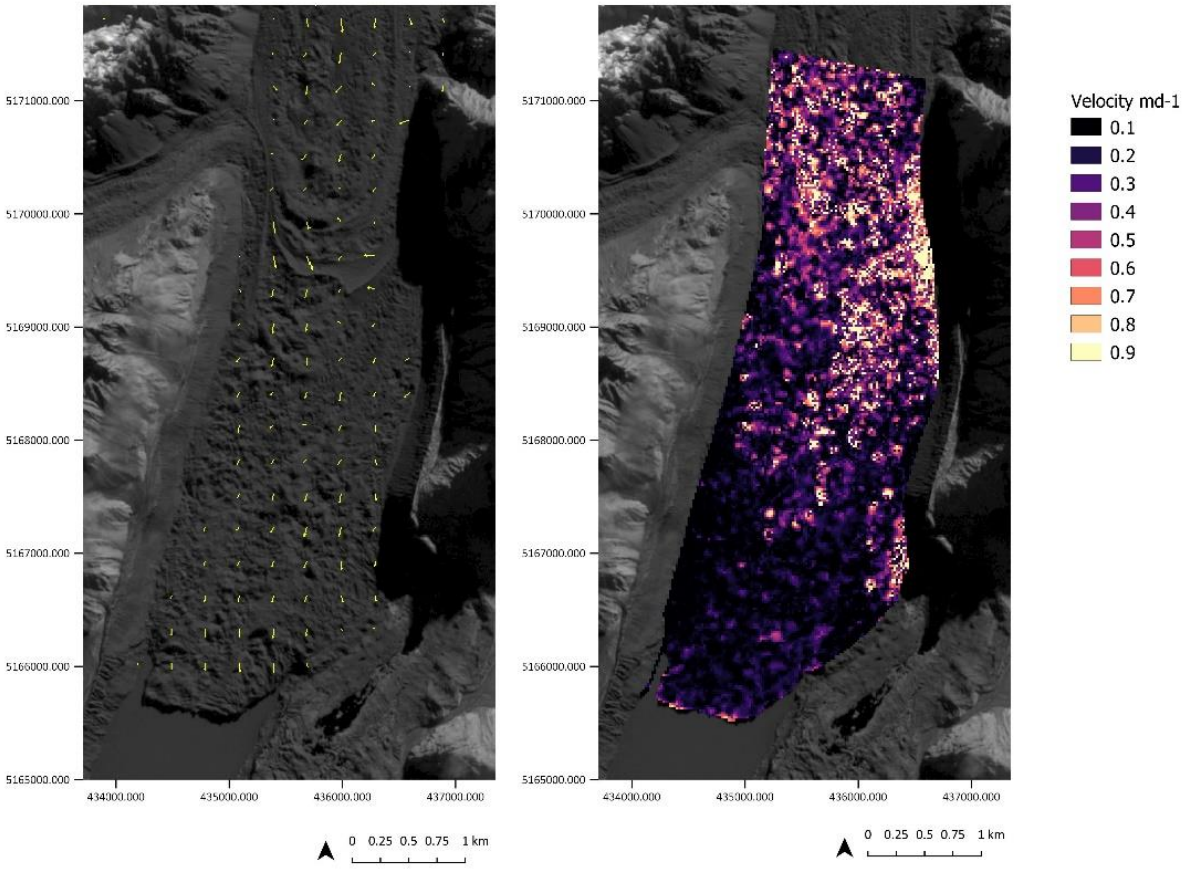

Appendix 16C Surface velocity during summer over a 10-day time interval from 17/05/2017–27/05/2017, left image shows the vector arrows showing the direction of displacement. Right images shows the surface velocity in md^{-1}.

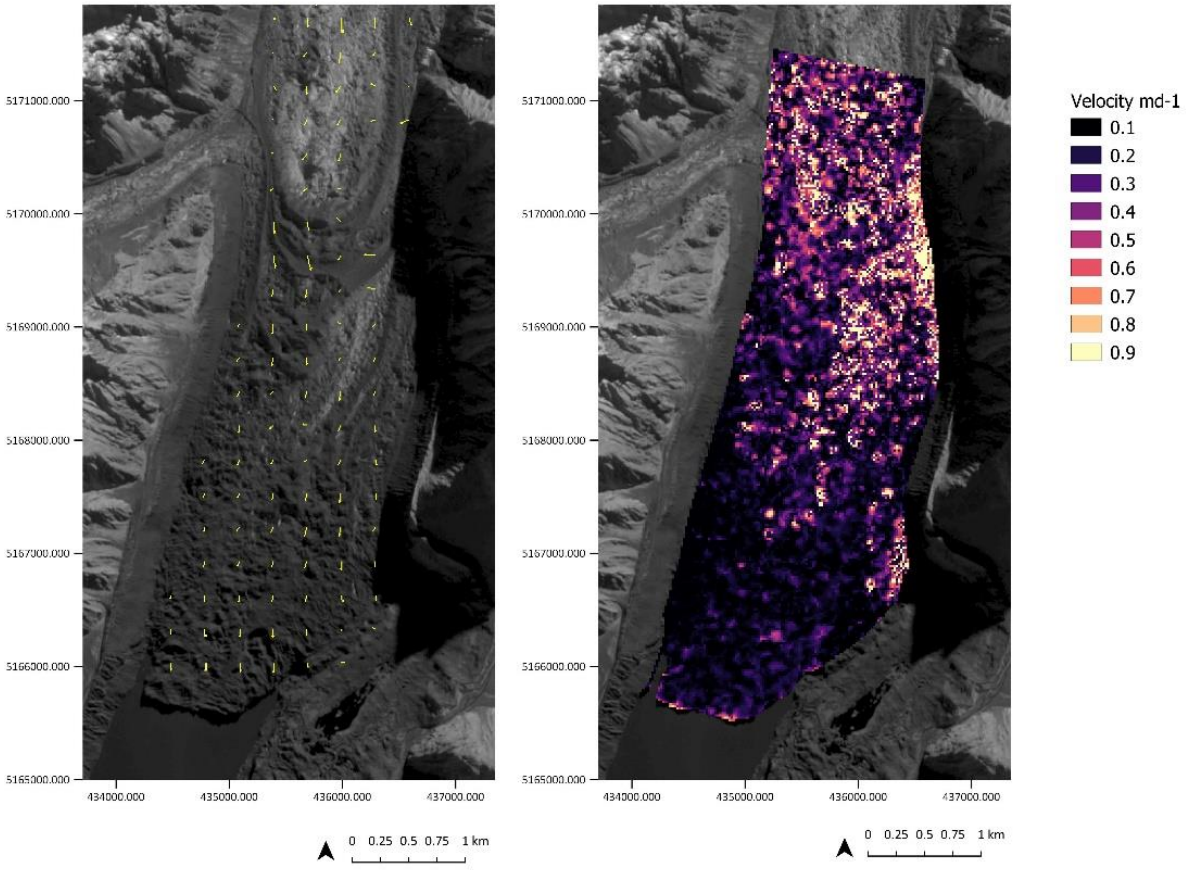

Appendix 16C Surface velocity during summer over a 10-day time interval from 27/05/2017–06/06/2017, left image shows the vector arrows showing the direction of displacement. Right images shows the surface velocity in md^{-1}.

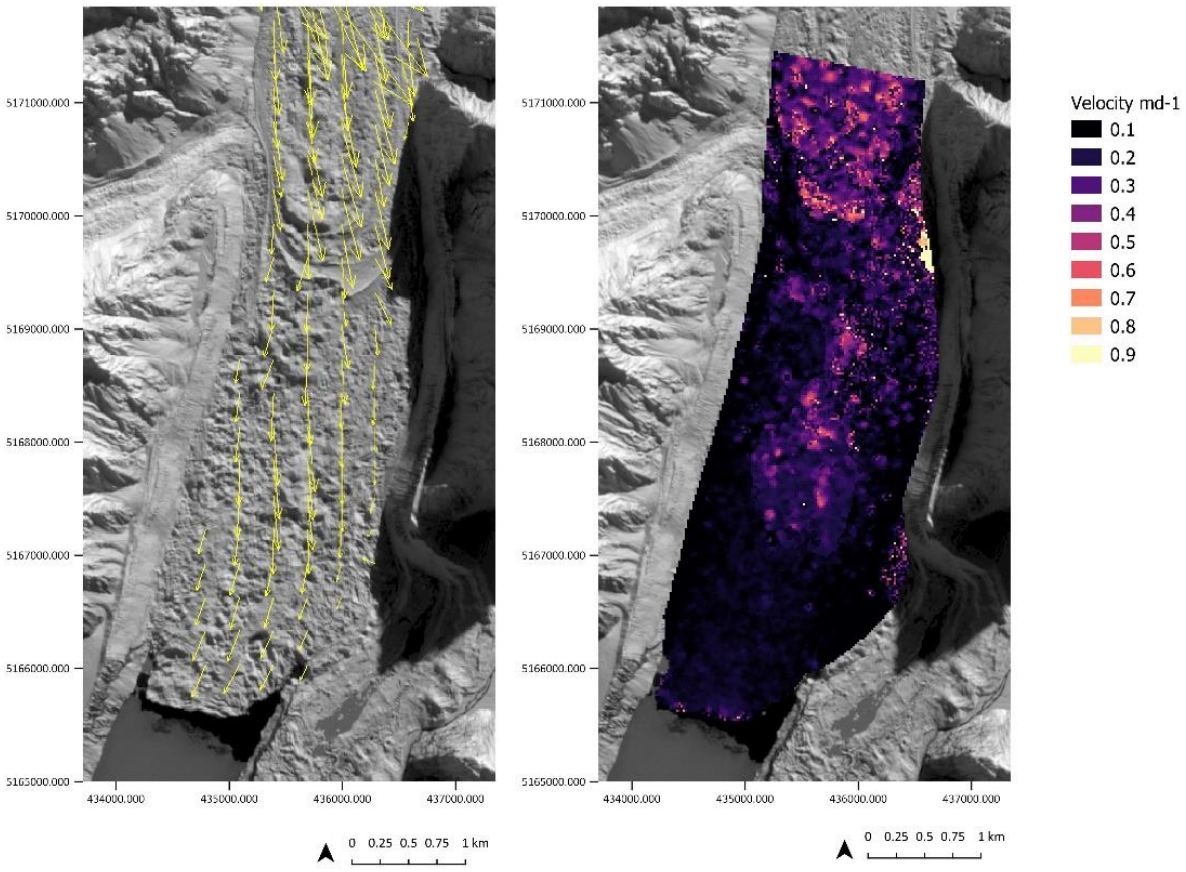

Appendix 17C Surface velocity during summer over a 30-day time interval from 06/06/2017–06/07/2017, left image shows the vector arrows showing the direction of displacement. Right images shows the surface velocity in md^{-1}.

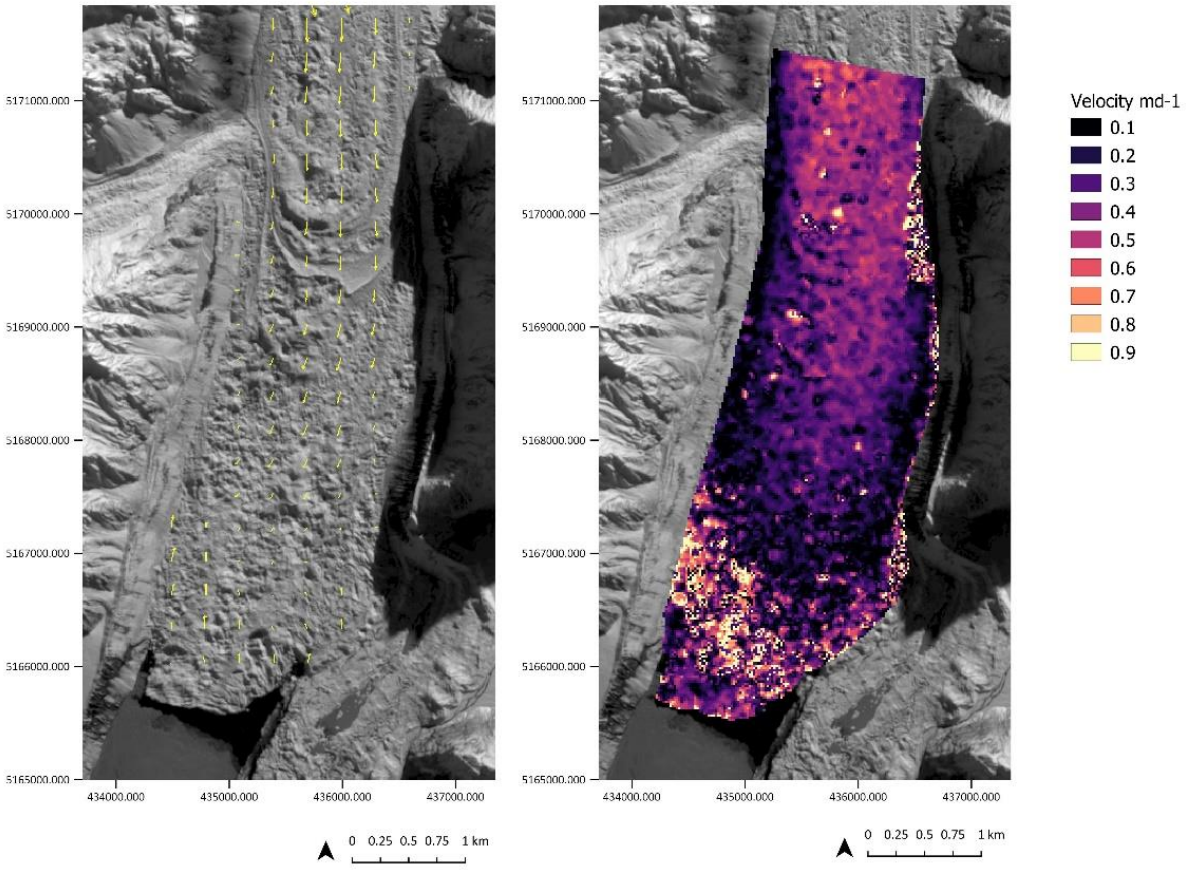

Appendix 18C Surface velocity during summer over a 10-day time interval from 06/07/2017–16/07/2017, left image shows the vector arrows showing the direction of displacement. Right images shows the surface velocity in md^{-1}.

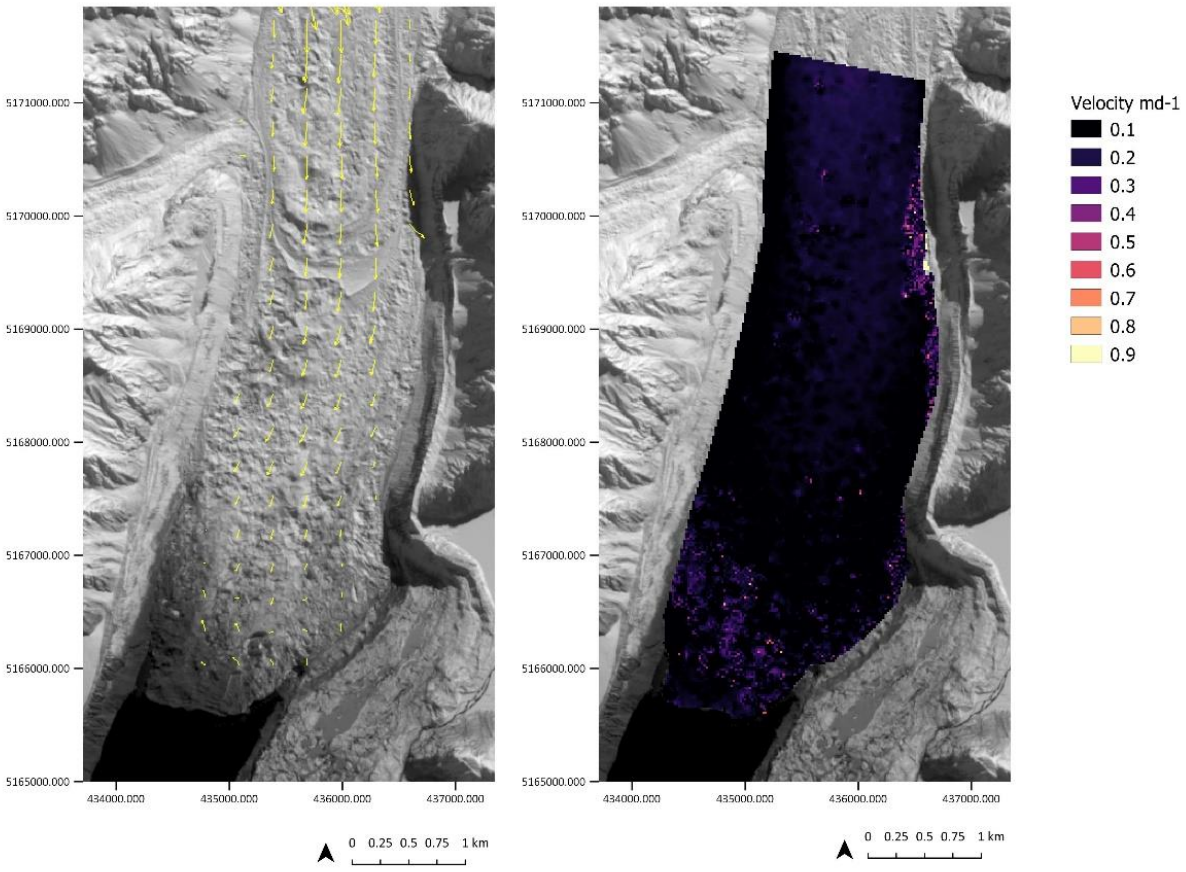

Appendix 19C Surface velocity during summer over a 30-day time interval from 06/07/2017–15/08/2017, left image shows the vector arrows showing the direction of displacement. Right images shows the surface velocity in md^{-1}.

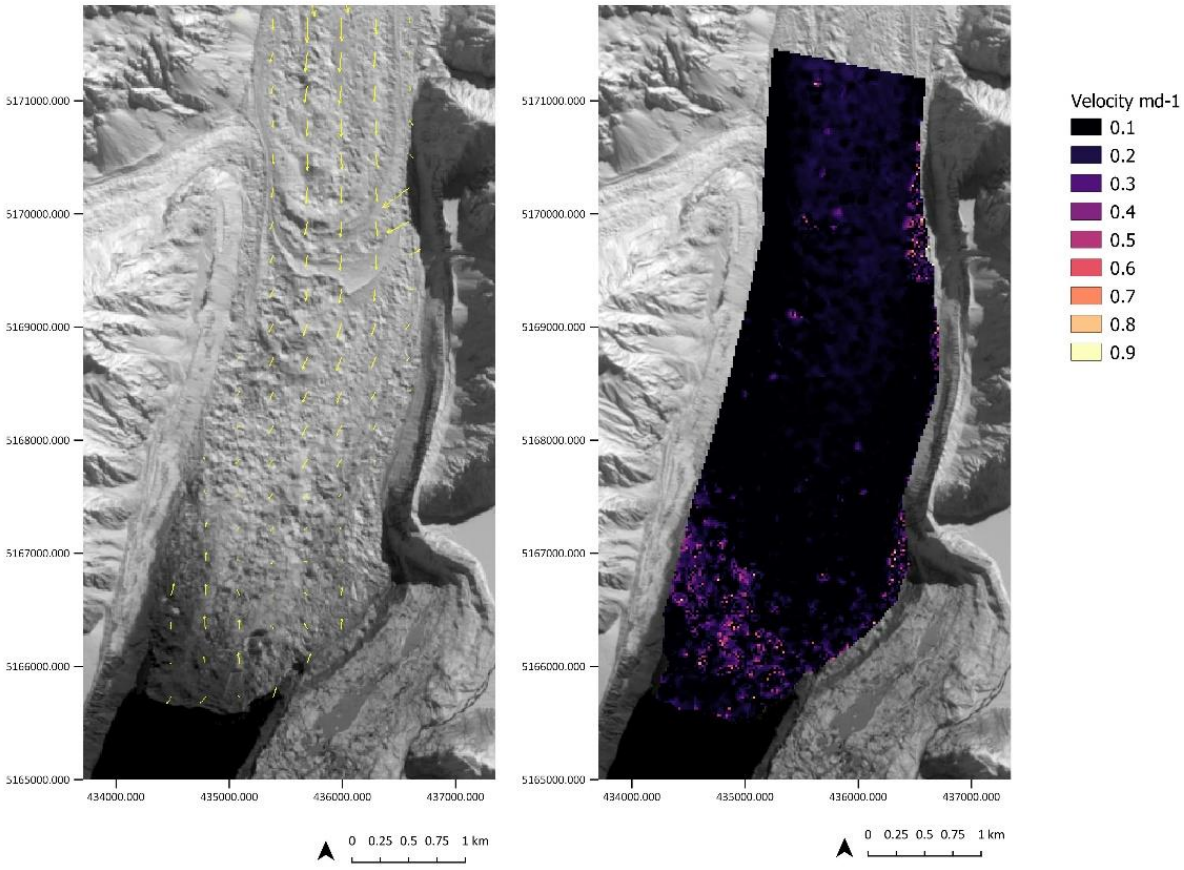

Appendix 20C Surface velocity during summer over a 30-day time interval from 16/07/2017–15/08/2017, left image shows the vector arrows showing the direction of displacement. Right images shows the surface velocity in md^{-1}.

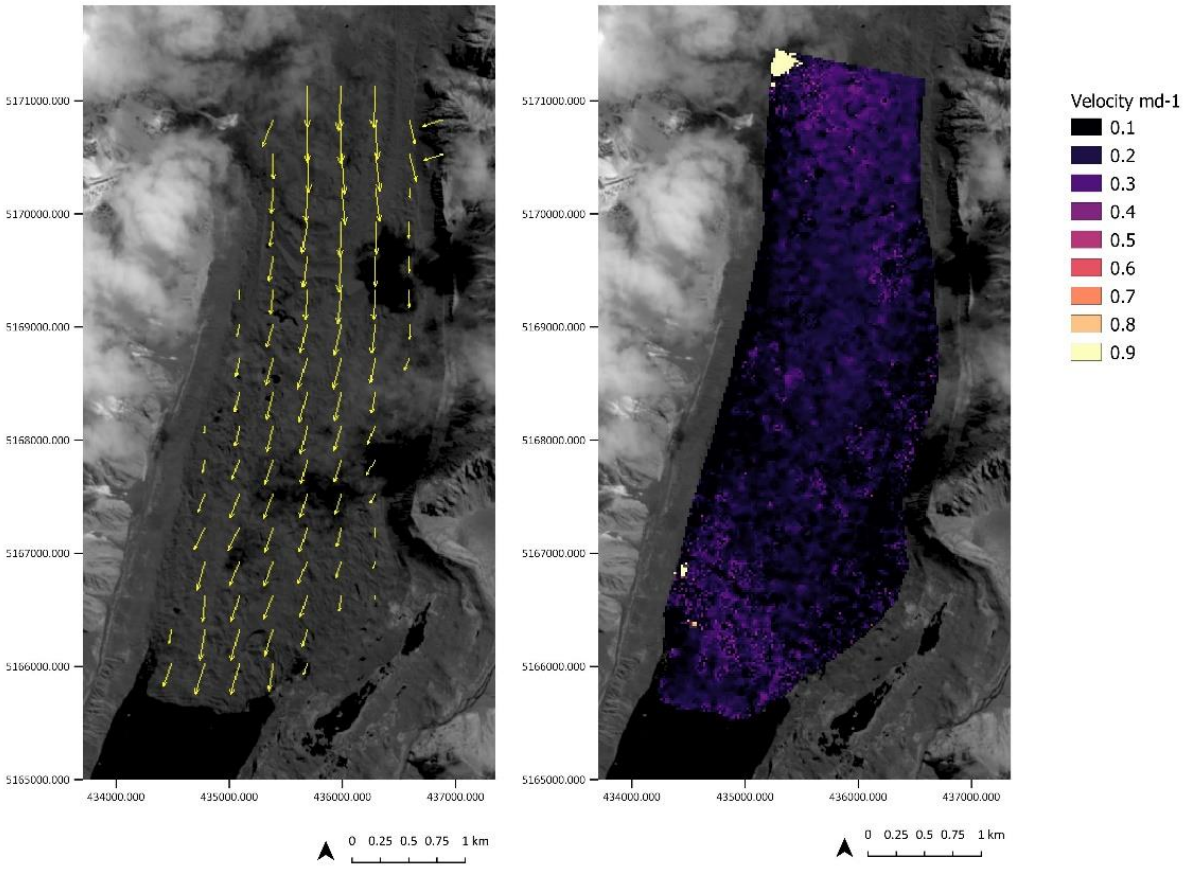

Appendix 21C Surface velocity during summer over a 50-day time interval from 15/08/2017–04/10/2017, left image shows the vector arrows showing the direction of displacement. Right images shows the surface velocity in md^{-1}.

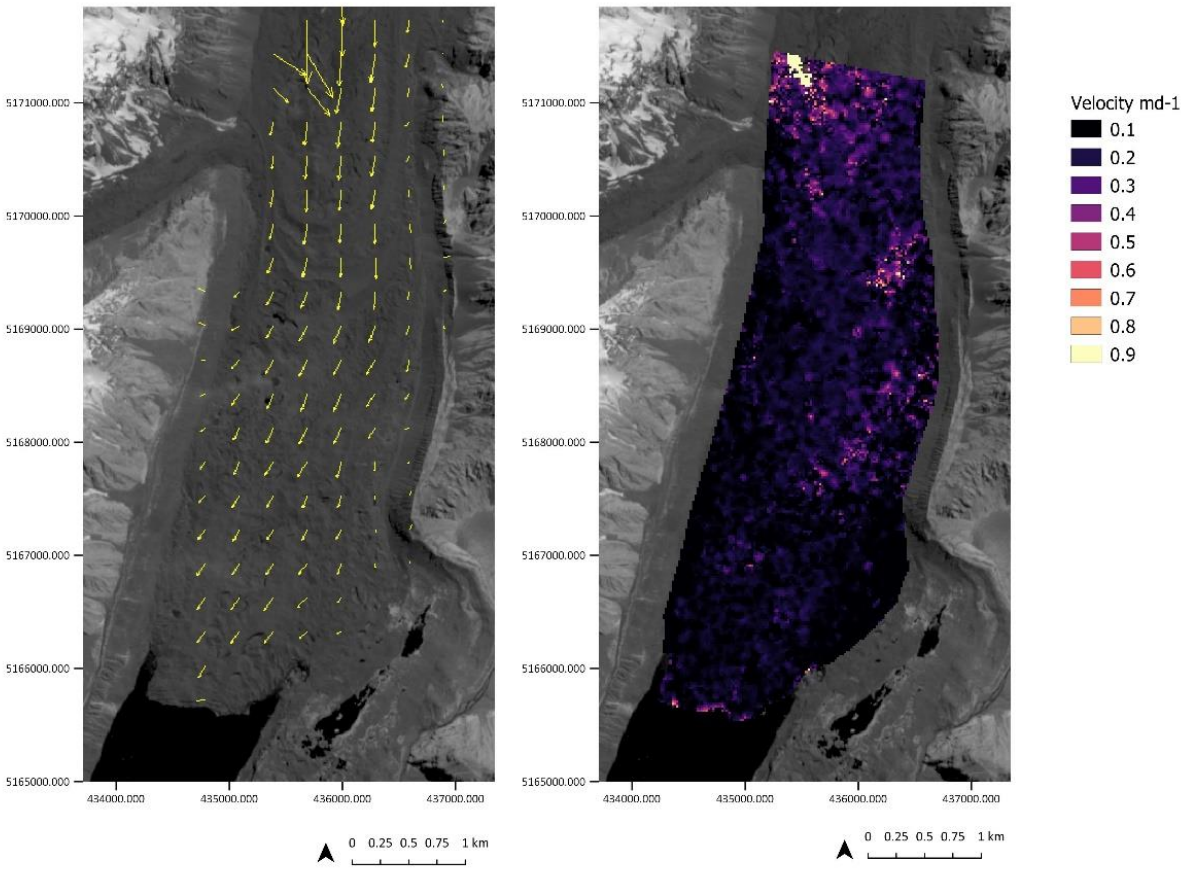

Appendix 22C Surface velocity during summer over a 25-day time interval from 04/10/2017–29/10/2017, left image shows the vector arrows showing the direction of displacement. Right images shows the surface velocity in md^{-1}.

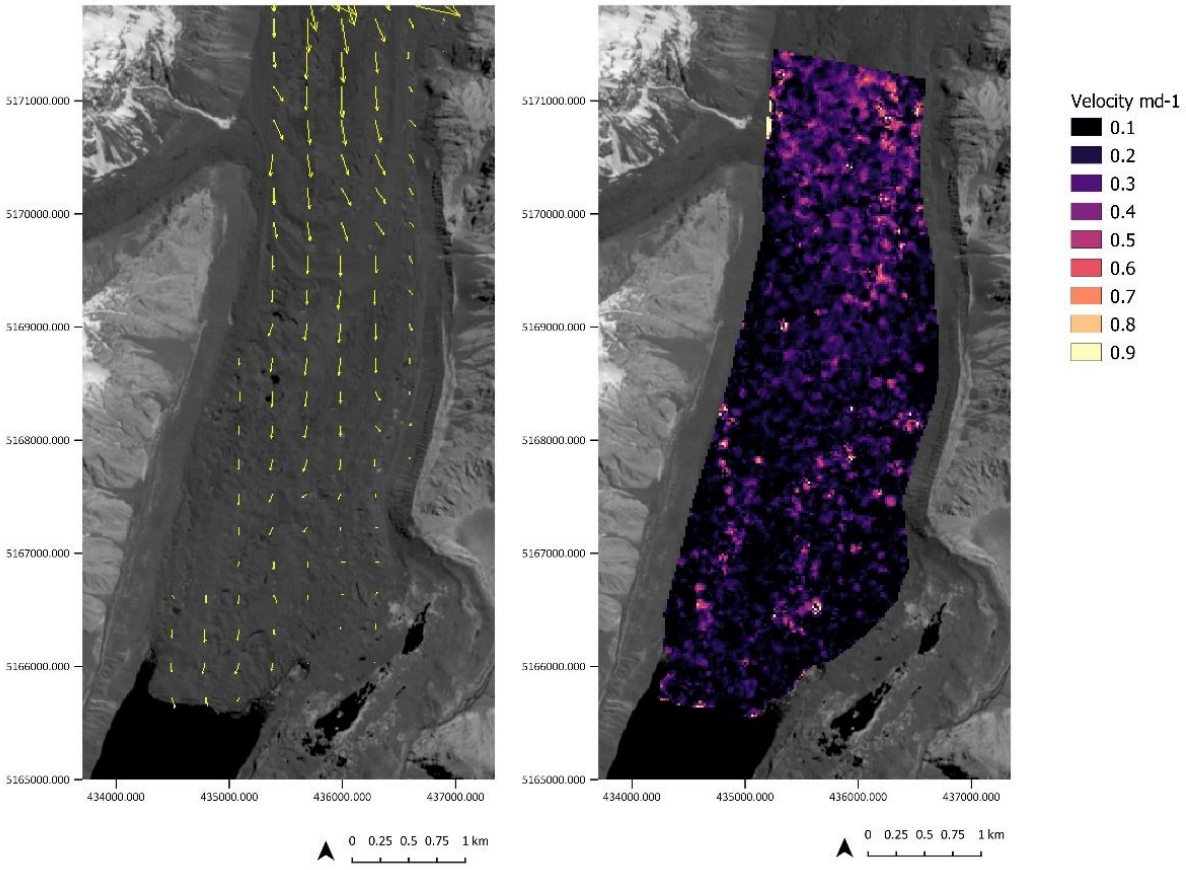

Appendix 23C Surface velocity during summer over a 15-day time interval from 29/10/2017–13/11/2017, left image shows the vector arrows showing the direction of displacement. Right images shows the surface velocity in md^{-1}.

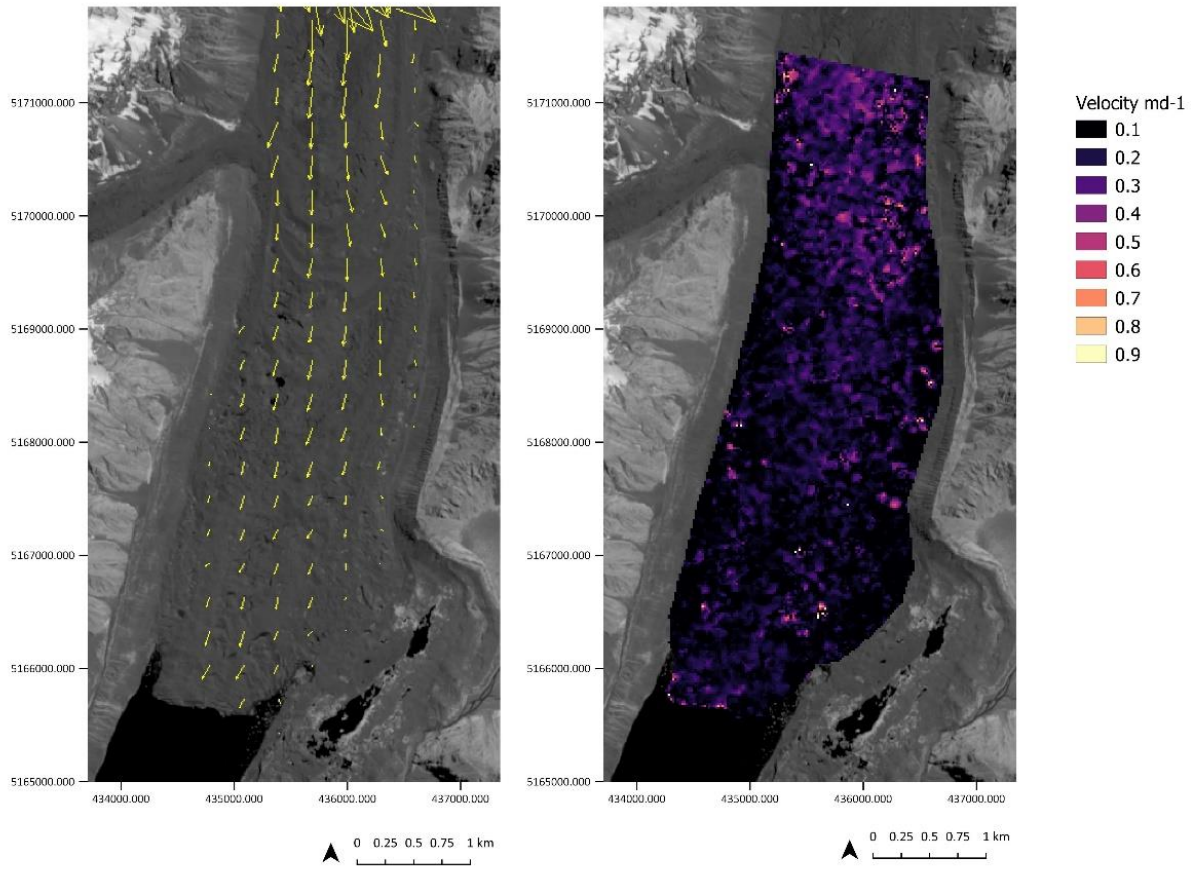

Appendix 24C Surface velocity during summer over a 40-day time interval from 29/10/2017– 18/11/2017, left image shows the vector arrows showing the direction of displacement. Right images shows the surface velocity in md^{-1}.

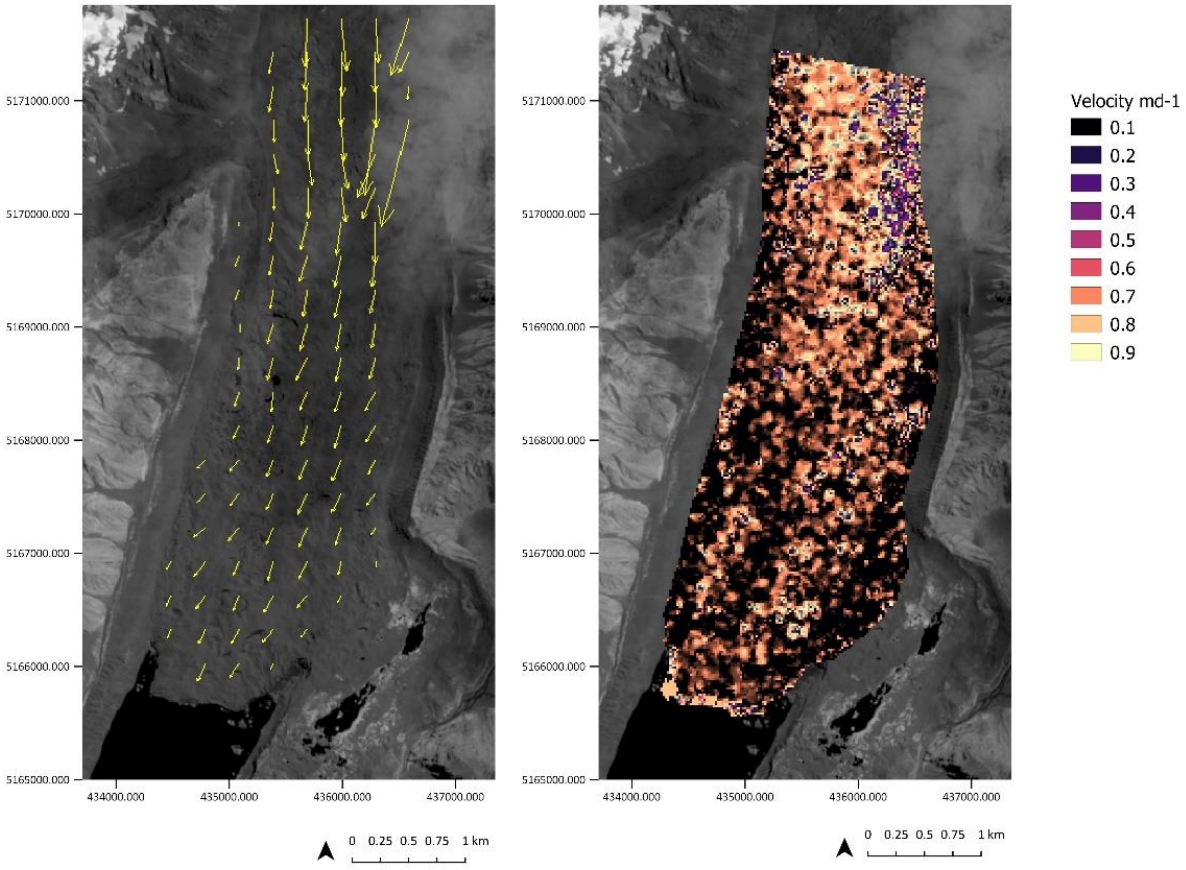

Appendix 25C Surface velocity during summer over a 10-day time interval from 18/11/2017–13/12/2017, left image shows the vector arrows showing the direction of displacement. Right images shows the surface velocity in md^{-1}.

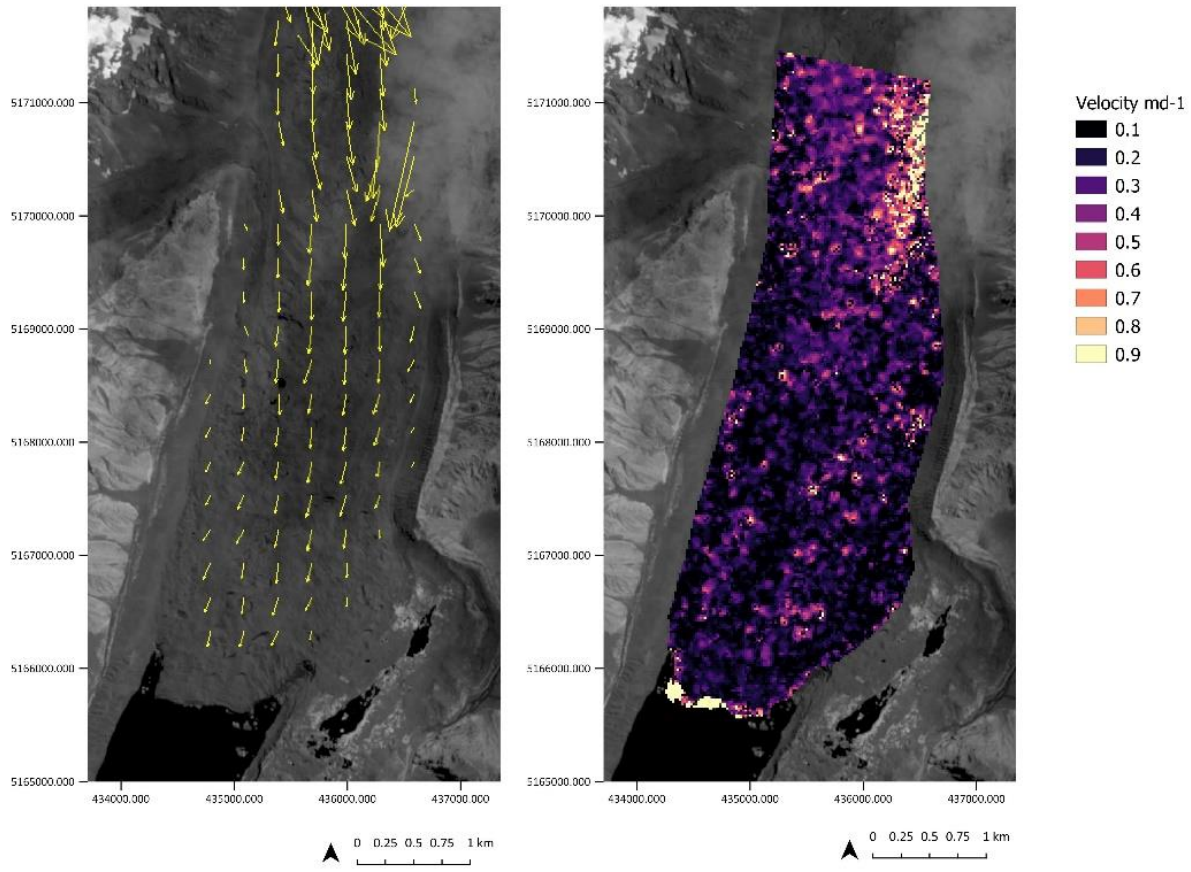

Appendix 26C Surface velocity during summer over a 25-day time interval from 17/05/2017– 27/05/2017, left image shows the vector arrows showing the direction of displacement. Right images shows the surface velocity in md^{-1}.

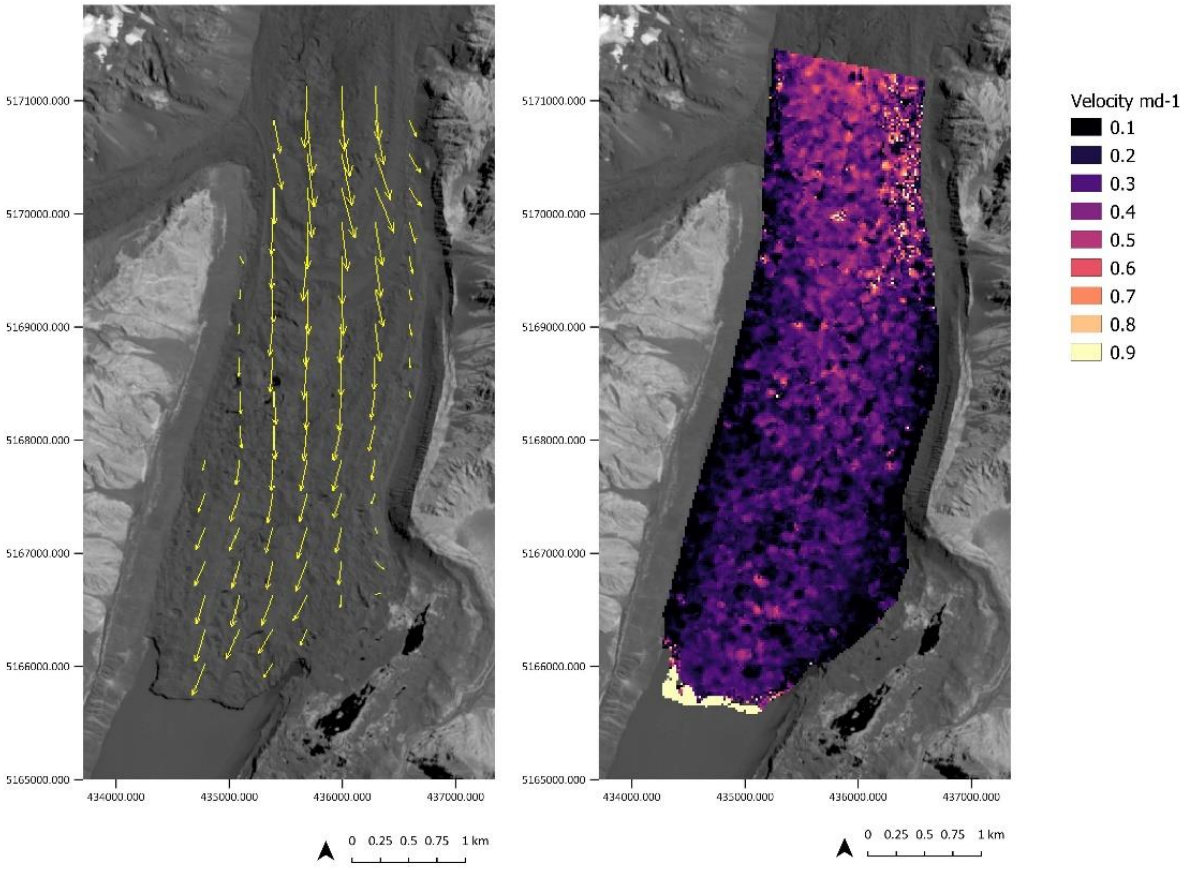

Appendix 27C Surface velocity during summer over a 20-day time interval from 13/12/2017–22/01/2017, left image shows the vector arrows showing the direction of displacement. Right images shows the surface velocity in md^{-1}.

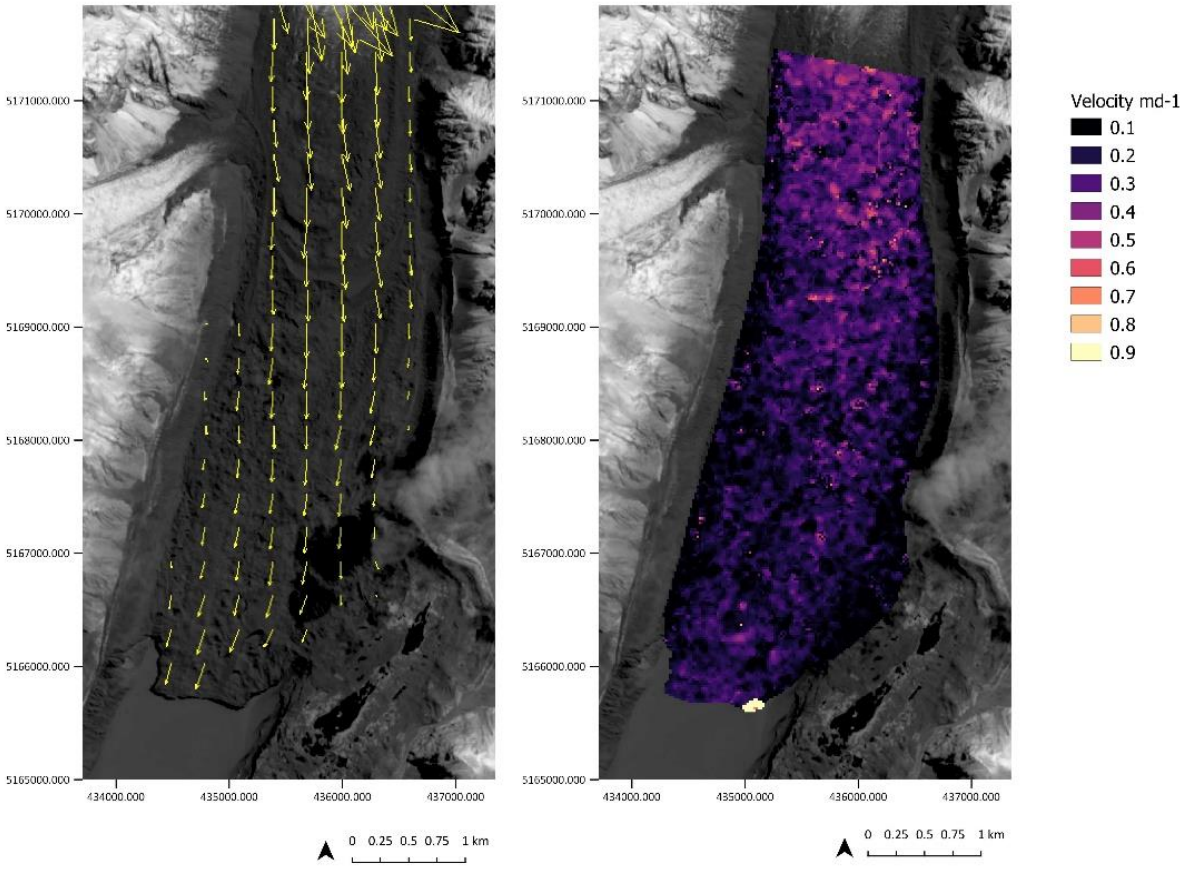

Appendix 16C Surface velocity during summer over a 30-day time interval from 22/01/2017–21/02/2017, left image shows the vector arrows showing the direction of displacement. Right images shows the surface velocity in md^{-1}.